Laboratoire d'Étude du Rayonnement et de la Matière en Astrophysique

CENTRE NATIONAL DE LA
RECHERCHE SCIENTIFIQUE

OBSERVATOIRE DE PARIS

ECOLE DOCTORALE
ASTRONOMIE ET ASTROPHYSIQUE D'ILE-DE-FRANCE

Doctorat
ASTRONOMIE ET ASTROPHYSIQUE

AUTHOR: CELIA ANAHI VERDUGO SALGADO

STAR FORMATION IN LOW GAS DENSITY AND LOW METALLICITY ENVIRONMENTS

Thesis supervised by FRANÇOISE COMBES

Defended on July 21st 2015, in Paris

Jury:

Eva Schinnerer (examiner)
Samuel Boissier (examiner)
Pierre-Alain Duc
Nicolas Bouché
Matthew Lehnert
David Valls-Gabaud

Laboratoire d'Étude du Rayonnement et de la Matière en Astrophysique

CENTRE NATIONAL DE LA
RECHERCHE SCIENTIFIQUE

OBSERVATOIRE DE PARIS

ECOLE DOCTORALE
ASTRONOMIE ET ASTROPHYSIQUE D'ILE-DE-FRANCE

Doctorat
ASTRONOMIE ET ASTROPHYSIQUE

AUTEUR: CELIA ANAHI VERDUGO SALGADO

FORMATION DES ÉTOILES DANS LES ENVIRONNEMENTS DE BASSE DENSITÉ DE GAZ ET BASSE MÉTALLICITÉ

Thèse dirigée par FRANÇOISE COMBES

Soutenue à Paris le 21 Juillet 2015

Jury:

Eva Schinnerer (rapporteur)
Samuel Boissier (rapporteur)
Pierre-Alain Duc
Nicolas Bouché
Matthew Lehnert
David Valls-Gabaud

Abstract

In nearby galaxies, an empirical relation has been established between star formation and gas surface densities, the Kennicutt-Schmidt relation (K-S). The relation is nearly linear when molecular gas (H_2) is considered, while is less tight with atomic hydrogen (HI). These low gas density regions are of a key importance in the field of star formation, since the are also low metallicity environments, resembling the conditions of a younger universe. This thesis summarizes the observational work done with the IRAM 30mt telescope in two kinds of such regions: disk galaxies with extended ultra-violet emission (XUV), and the interstellar medium going into the hot intra-cluster medium (ICM) under ram-pressure stripping in the Virgo Cluster. The GALEX telescope has unveiled in Far Ultra-Violet (FUV) star formation in the outer parts of some disk galaxies that was not traced by Ha. To determine the presence of H_2 and analyze the K-S relation in these regions, CO observations were done in the outskirts of several XUV disk galaxies, finding both detections and upper limits. These K-S relations showed a broken power law at low gas densities, below the HI-H_2 threshold. In the Virgo Cluster, similar CO observations were done along the HI tidal arm connecting NGC4388 and M86, where no H_2 is expected. Two detections were found, showing very low star formation efficiencies (depleting less than 0.1% of the gas reservoir per 10^8 yr), and showing again a discontinuity of the K-S relation at low gas densities, probing that the process of gas consumption into stars well known at high densities cannot be extrapolated to lower densities, and that H_2 can survive a certain time in the hostile ICM.

Abstract

Dans les galaxies proches la relation empirique de Kennicutt-Schmidt (K-S) a été établie entre la densité surfacique de formation d'étoiles et la densité surfacique de gaz. Elle est forte et presque linéaire quand on considère le gaz moléculaire (H_2) mais devient moins valable lorsque l'hydrogène n'est qu'atomique (HI). Ces régions de densité de gaz faible sont d'une importance cruciale dans le domaine de la formation d'étoiles, car elles possèdent les mêmes conditions que dans les galaxies de Univers jeune, de faible métallicité. Cette thèse compile les données observationnelles obtenues au télescope de 30m de l'IRAM sur deux types de régions distinctes: les galaxies à disque ayant une émission ultra-violet étendue (XUV), et le milieu interstellaire déplacé dans le milieu intra-amas (ICM) chaud sous l'effet du balayage de la pression dynamique dans l'amas de la Vierge. Pour déterminer la présence de molécules H_2 et afin d'étudier la relation K-S dans ces régions, des observations de CO ont été faites dans les parties externes des galaxies XUV, et nous avons à la fois des détections et des limites supérieures. Les relations K-S ont montré une loi de puissance discontinue pour des densités de gaz faibles, en dessous du seuil de la transition de phase HI-H_2. Dans l'amas de la Vierge, des observations similaires de CO ont été faites le long des bras de marée qui relient NGC4388 et M86, où aucune présence de H_2 n'est attendue. Nous avons effectué des détections, montrant une efficacité de formation d'toiles très faible, et montrant de nouveau une discontinuité de la relation K-S pour des densités de gaz faibles, prouvant que les processus bien connus de consommation du gaz à forte densité ne peuvent être généralisés aux densités plus faibles. D'autre part, nos résultats montrent que le gaz H_2 peut survivre un temps plus long que prévu dans l'ICM hostile.

Acknowledgements

Throughout these three years of PhD I have a lot of people to thank for, that have made my life just wonderful. It wasn't easy to spend such a long time abroad, leaving friends, family... well, an entire life, on the other side of the ocean. At moments I felt very lonely and homesick, but thanks to the unconditional devotion of my loved ones in Chile, regardless of the distance, and also to the wonderful people I met here, my situation transformed up-side-down and became one of the most wonderful experiences in my life. I know I will never stop thanking you all for everything, but this is a start.

First of all I would like to thank my family for always supporting me in every decision I have made, especially during my career. Even when the path I decided to take was so uncommon, I never felt anything else but support and pride from my entire family, and I will always cherish that. I just hope someday I will be able to do everything you have done for me in return.

And of course, many thanks are ought to Françoise, for the constant guidance throughout this work, and the permanent availability for any question, any day at any time. I feel extremely lucky to have had such a remarkable investigator as my tutor, and I conclude my PhD with a great feeling of knowledge and achievement. I especially thank her her kind comprehension and patience on every difficult aspect I found in this period. And also part of my guidance, I'd like to thank Mónica Rubio and Alberto Bolatto for all their kind help and support in my work throughout these last five years.

I also want to thank my friends in Chile, my friends from childhood, that regardless of the time or distance, never forget about me and always keep me in their minds. Thank you so much for so many years of friendship, laughter and good times. We have shared so much that we are soul mates for life.

But of course my experience here in France wouldn't have been the same without the friends I made here. A beautiful group of people, most of the from Chile, but from other countries as well, that have become my family here. They are the main reason of my happiness here, and I will never forget them. Some of them I'll meet again in Chile, and others will be forever in my heart.

And finally, but most important, I thank my boyfriend, my best friend and my soul mate for making my life so wonderful. You have not only been my major pillar during this thesis, but changed my life forever. You were my best friend and then became my soul mate, always there for me, no matter what. Your faith in my doing this successfully is amazing. No one understands like you the heavy road this has been, and I'm sure we only have happiness ahead.

Additionally, special acknowledgments are ought to the IRAM staff for their support during the observations for this thesis, and to both the Centre National de la Recherche Scientifique (CNRS) and the Comisión Nacional de Investigación Científica y Tecnológica (CONICYT) for supporting my financially during the three years of my PhD, through agreement signed on December 11, 2007.

Contents

1 Introduction **12**
- 1.1 Observing molecular gas 15
- 1.2 Molecular gas mass 16
- 1.3 Kennicutt-Schmidt relation 17
- 1.4 Low gas density environments 20
- 1.5 Instrumentation 21

2 XUV **23**
- 2.1 M63 24
  - 2.1.1 Observations 26
  - 2.1.2 Results 27
  - 2.1.3 Analysis 33
  - 2.1.4 Summary and conclusions 48
  - 2.1.5 Publication 50
- 2.2 2013 observations 63
  - 2.2.1 Data reduction and Results 63
  - 2.2.2 Stacking 67
- 2.3 M83 68
  - 2.3.1 Instrumentation and Observations 69
  - 2.3.2 Results 70
  - 2.3.3 Star formation rate 72

3 Ram-Pressure stripping **76**
- 3.1 Virgo cluster 78
- 3.2 Observations 80
- 3.3 Data Reduction and spectral line fitting 80
- 3.4 Results 85
- 3.5 Star formation efficiency 85
  - 3.5.1 HI photometry 87
  - 3.5.2 Hα data 87
  - 3.5.3 K-S relation 92
- 3.6 Publication 93

4 Summary and Conclusions **102**
- A.1 CO in low metallicity galaxies 108
  - A.1.1 Introduction 108

A.1.2 Results 110
A.1.3 Publication 112

List of Figures

1.1 H_2 energy levels diagram 15
1.2 Kennicutt-Schmidt relation in nearby galaxies. 18
1.3 IRAM 30-mt single dish radio telescope. 21
1.4 Atmospheric transmission at Pico Veleta. 22

2.1 NUV-FUV color image of M63. 26
2.2 Observing pointings for M63. 28
2.3 Mosaic of CO spectra obtained along the major axis of M63. 32
2.4 CO spectrum for UV region in M63. 33
2.5 Maps of complementary data for M63. 35
2.6 Multiwavelength views of the UV region in M63. 36
2.7 Image processing in complementary data for M63. 37
2.8 Radial profiles of CO observations and complementary data for M63. 40
2.9 Radial profiles of SFE and H_2/HI for M63. 43
2.10 Comparison of radial profiles of $\Sigma_{\rm SFR}$, $\Sigma_{\rm HI}$ and $\Sigma_{\rm H_2}$ between this work and Leroy et al. (2008). 44
2.11 HI map of M63. 45
2.12 Kennicutt-Schmidt relations of M63. 46
2.13 XUV galaxies observed in 2013. 64
2.14 Spectra results for XUV observatons 2013. 66
2.15 CO stacked spectra for NGC3344. 68
2.16 ALMA observatory at Llano Chajnantor in Chile. 69
2.17 Atmospheric transmissions and spectral bands for ALMA. 70
2.18 M83 UV map. 71
2.19 ALMA CO(2–1) intensity for M83. 72
2.20 Hint of a possible clump in the CO(2–1) data cube of M83. 73
2.21 ALMA continuum map for M83. 74
2.22 Complementary data for M83. 74
2.23 $\Sigma_{\rm SFR}$ maps for M83. 75

3.1 $H\alpha + \rm NII$ image of the Virgo cluster from Kenney et al. (2008). . . . 79
3.2 Targets observed in the Virgo Cluster. 81
3.3 CO detection for NGC4388, Source-1and HaR-2. 83
3.4 CO detection for second run of observations in the Virgo Cluster . . . 84
3.5 HI column density map from Oosterloo & van Gorkom (2005) 88
3.6 $H\alpha$ map of the Virgo cluster from Kenney et al. (2008). 90

3.7 K-S relation for sources observed in the Virgo cluster. 91

1 Color composite image of the WLM galaxy. 109
2 Example of a modified blackbody fit. 111

List of Tables

2.1 CO mapping along the major axis of the M63 disk. 30
2.2 CO mapping over the bright UV region at $1.36\,r_{25}$. 31
2.3 Public ancillary data for M63. 34
2.4 Photometry results obtained for the complementary data of M63 in its radial cut. 38
2.5 Photometry results obtained for the complementary data of M63 in its UV region. 39
2.6 Best-fitting bisector linear Kennicutt-Schmidt relations obtained for M63 in log space. 47
2.7 Galaxies selected for XUV observations in 2013. 64
2.8 Targets description for XUV observations 2013. 65
2.9 Line parameters for detections in XUV observations 2013. 65
2.10 3σ upper limits of CO(1–0) emission for sources with no detection in 2013 observations. 67

3.1 Targets and Observations. 82
3.2 CO(1–0) upper limits at 3σ for sources with no detection. 85
3.3 CO detections in the Virgo Cluster. 86
3.4 K-S relation values. 89

Chapter 1

Introduction

Contents

1.1 Observing molecular gas 15
1.2 Molecular gas mass 16
1.3 Kennicutt-Schmidt relation 17
1.4 Low gas density environments 20
1.5 Instrumentation 21

The process in which stars are born in the Universe holds one of the key answers to our origins. It sheds light on the different conditions needed for the formation of all types of stars, including ours and our planetary system. However, it is also the root of astrophysics on its largest scales, since it is a principal agent of galaxy formation and evolution. This is why in astronomy, the field of star formation has never lost interest throughout the decades.

Thanks to many years of research (Kennicutt & Evans 2012 and references therein), we now know that, on large scales, star formation events are determined by a hierarchy of physical processes (e,g. Elmegreen & Elmegreen 2014, Drazinos et al. 2013) spanning a vast range of physical scales. We could roughly describe it as a first accretion of gas onto disks from satellite object and the intergalactic medium (megaparsec scale) (e.g Combes 2014, Bouché et al. 2013, Sánchez Almeida et al. 2014), followed by the cooling of this gas to form a cool neutral phase (kiloparsec scale), then the formation of molecular clouds (tens of parsecs) (e.g Dobbs et al. 2014), the fragmentation and accretion of this molecular gas to form progressively denser structures such as clumps ($\sim$1 pc) (Zhang 2014) and cores ($\sim$0.1 pc) (Gong & Ostriker 2015, Zhang et al. 2015), to finally initiate the contraction of the cores to form stars (solar radius) and planets ($\sim$astronomical units). Because these processes involve physical scales and local conditions so different from each other, they have been studied by different teams who have specialized in each one of them, to parameterize the best possible way these various processes.

Consequently, these groups have grown separately, and enormous efforts have been made to bring closer the community studying individual star-forming regions and stars in the Milky Way, and the large extragalactic community that attempts to characterize the star formation process on galactic and cosmological scales.

Of course, the historical distance between these two fields lies on observational restrictions. The key physical processes that determine how molecular clouds contract and fragment into clumps and cores and finally clusters and individual stars can be probed up close only in our Galaxy, and much of the progress in this subject has come from in-depth case studies of individual star forming regions. Such detailed observations have been impossible to obtain outside our galaxy, even relatively nearby galaxies (with the exception of the Magellanic Clouds). The spatial resolution required for that is too high, and hence those observations have been restricted to a large scale only.

However, the past decade has witnessed an unprecedented stream of new observational information on star formation on all scales, thanks to the very successful space mission telescopes, like the Galaxy Evolution Explorer (GALEX), the Spitzer Space Telescope, and the Herschel space Observatory, as well as the state-of-the-art ground based telescopes, like the Atacama Large Millimeter Array (ALMA), the Institut de Radioastronomie millimétrique (IRAM), or the Very Large Telescope (VLT), just to name a few. These facilities have not only provided key and detailed information on the physical processes leading to the formation of individual stars in interstellar clouds, but also mapped for the first time entire galaxies and ensembles of galaxies, denoting evidences of star formation processes going on, and even more fascinating, the interactions of these processes with their extragalactic medium, and how they influence the evolution of their host galaxies.

With this instrumentation, the extragalactic branch of the field has focused on the collective effects of star formation, integrated over entire star-forming regions or, often, over entire galaxies (e.g Gil de Paz et al. 2007a, Kennicutt et al. 2011, Dale et al. 2009, Walter et al. 2008). This collective conversion of baryons from interstellar gas to stars and the emergent radiation and mechanical energy from the stellar populations is most relevant to the formation and evolution of galaxies. Consequently, much of the empirical knowledge of star formation on these scales consists of scaling laws and other parametric descriptions, in place of rigorous, physically based characterizations. Improving our knowledge of large-scale star formation and its attendant feedback processes is essential to understand the formation and evolution of galaxies.

A lot of the work done in star formation beyond our Milky Way (MW), in the nearby Universe, involves the analysis of different star formation tracers present in local and normal spiral disk galaxies. The new generation of telescopes has provided maps of entire galaxies at different wavelengths, including ultra-violet (UV), Hα, atomic gas (HI), molecular gas (H_2) and infrared. These emissions can be directly correlated with the amount of ongoing star formation, and more precisely, quantify it. It has been shown that in these galaxies the amount of star formation depends directly on the amount of molecular gas present, in a more or less linear relation, and the gas consumption times are fairly constant, between $\sim$2 and 3 Gyrs (Leroy et al. 2008). But very little is known about the efficiency of this process on other types of galaxies and environments, including irregular galaxies and mediums of low gas density and/or low metallicity. Such regions seem more difficult to observe since their emission is much colder and fainter than in normal galaxies, but they are not devoided of star formation, and to understand in detail the processes they go through and to quantify their efficiencies to form stars is of a key importance to someday fully understand star formation at all its levels.

This thesis explores the extragalactic branch of star formation, focusing on the regions of galaxies in the local universe, where star forming events can interact with the surrounding environments of the host galaxies. Such regions involve particularly the outer parts of nearby disk galaxies with evidences of recent star formation, and the intergalactic medium of galaxies that belong to a cluster and interact with each other. It is an observational work done with ground-based telescopes, and complemented with space telescope data. The aim of this work is to shed light on the star formation processes taking place in regions where it is more difficult to form stars, due to extreme conditions, such as low metallicity, low gas density, and physical interaction with the surrounding environments. The study of star formation in these regions not only help us to constrain boundaries on the conditions needed to form stars, but also help us to better understand the past of our cosmos, since they resemble the conditions of a younger universe.

The thesis is structured as follows. The present chapter gives a description of the typical regions observed in this work, characterized by their low gas densities and low metallicities. It also explains how we observe these regions and how we can estimate the amount of molecular gas out of which stars can form. The Kennicutt-Schmidt relation is also introduced, to quantify the star formation rate (SFR) and star formation efficiency (SFE) as a function of the gas density. Finally, the instrumentation used in this work is explained. Chapter 2 explains the first observational work done for this thesis, on nearby galaxies with extended disks of ultra-violet emission (XUV), including radio observations, and analysis with complementary data. It contains the work done on the M63 galaxy, with the results of successful carbon monoxide (CO) observations and the first Kennicutt-Schmidt relation ever done on a XUV disk galaxy, with its corresponding publication in the A&A Journal. It also encompasses more CO observations on other XUV galaxies, with both the IRAM and ALMA telescopes, and their preliminary results. Chapter 3 describes the second part of this thesis, on a tail of gas stripped from the NGC4388 galaxy, going under ram-pressure stripping in the Virgo Cluster. It includes successful CO detections in the intergalactic medium, were molecular gas is unexpected. A Kennicutt-Schmidt analysis was also done in this part, with extremely low values of star formation efficiencies, not reported before, and a submitted publication to A&A. Chapter 4 presents the final analysis and conclusion of this thesis. Also, in the appendix I present an additional work, that started during my master thesis, but finished during the first year of this PhD thesis, on CO observations at extremely low metallicities. It is the first CO detection ever found on a galaxy of such a low metallicity (O/H abundance less than 20%). The successful work published in the Nature Journal is included here.

1.1 Observing molecular gas

The best way to analyze the star formation activity in a region and quantify its efficiency, is to measure the amount of gas available to be converted into stars, which as we know, are formed inside molecular clouds. These regions are constituted mainly of hydrogen (H), which at the typical low temperatures of molecular clouds ($\sim$10 K) tends to be molecular (i.e H_2). Hence the molecular gas holds the key answer to the efficiency of any star formation process, however, is extremely difficult to observe.

Even though hydrogen is the most abundant element in the universe, observing molecular hydrogen (H_2) is highly difficult in the interstellar medium (ISM). For H_2, the first excited state, the J = 1 rotational state, is 100 - 200 K above ground state (Figure 1.1), whereas typical molecular clouds have temperatures of a few tens, making this transition highly unlikely. Even more, since the H_2 is a homonuclear molecule, it is practically impossible to detect because it has no electric dipole transitions that can change J by 1 (therefore no $J = 1 \rightarrow 0$ emission). Instead, the lowest-lying transition is the $J = 2 \rightarrow 0$ quadrupole, very weak and unlikely, since the J = 2 state is 511 K above ground state.

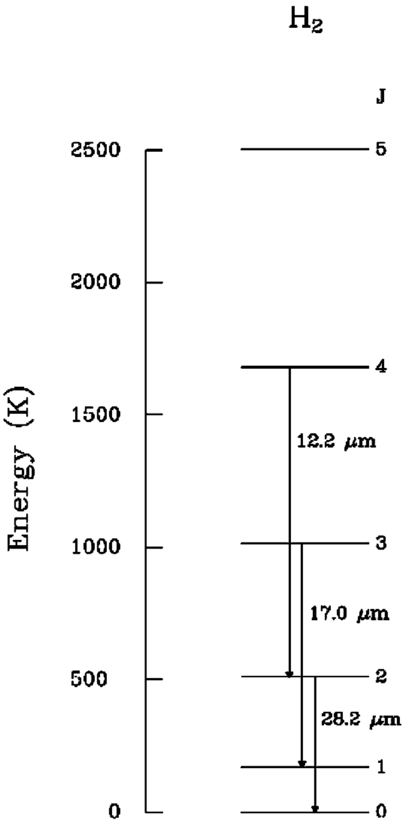

Figure 1.1: H_2 energy levels diagram

The basic reason of why it is so difficult to observe H_2 is its low mass (3.34×10^{-27}

kg). For a quantum oscillator or rotor the level spacing varies with reduced mass as $m^{-1/2}$, making it so difficult to go from one transition to another.

For these reasons we turn to other tracers to determine the amount of H_2. The most common one is the CO molecule, thanks to its dipole moment and its bright emission line. Carbon and oxygen are two of the most common elements in the ISM after H and He, and since the CO molecule is much more massive than H_2, its lowest rotational state is only 5.5 K above ground state, making CO molecules abundant with bright emission lines, easy to detect. As a consequence, CO has long been used as the preferred molecular gas tracer.

1.2 Molecular gas mass

As we know, stars form out of molecular gas, due to gravitational collapse inside molecular clouds. Therefore, in star formation analysis, including star formation rates (SFRs) and star formation efficiencies (SFEs), it is of crucial importance to measure the amount of molecular gas available to form stars.

As explained in the previous section, it is extremely difficult to detect molecular gas, i.e H_2, in low gas density environments and the cold ISM. In these cases we need to turn to CO(1–0) emission to detect H_2 and measure its mass.

The H_2 column density, which corresponds to the amount of H_2 particles per unit area,

$$\mathrm{N_{H2}} = \frac{\mathrm{M_{H_2}}}{\mu \mathrm{m_{H_2}} \pi \mathrm{R}^2} \tag{1.1}$$

has a simple and linear relation with the observed intensity of the CO(1–0) line through so called CO-to-H_2 conversion factor, or X_{CO}:

$$\mathrm{N_{H_2}} = \mathrm{X_{CO} I_{CO(1-0)}} \tag{1.2}$$

So by comparing the two previous equations we can clear a relation between the molecular gas mass and the intensity of the CO line:

$$\mathrm{M_{H_2}} = \mathrm{X_{CO}} \mu \mathrm{m_{H_2}} \pi \mathrm{R}^2 \mathrm{I_{CO(1-0)}} \tag{1.3}$$

where m_{H_2} is the mass of one H_2 molecule and μ is the correction factor for the contribution of heavy elements by mass, mainly dominated by the He molecular weight.

The radius R in Equation 1.1 is the radius of the area taken into account for calculating the column density, when assuming a spherical symmetry in molecular clouds. In practical terms, as we can see in Equation 1.3, this radius is restricted to the CO observations (otherwise Equation 1.3 would not make much sense). So the radius R in Equation 1.3 is the radius in which the CO line intensity I_{CO} was measured. As we will see in the following chapters, due to the nature of our CO observations in this particular work, this radius corresponds to the CO(1–0) beamsize or Full Width at Half Maximum (FWHM).

Now, if we assume a Galactic value for the CO conversion factor, $X_{CO} = 2 \times 10^{20}$ [cm^{-2}(K km/s)$^{-1}$] = 1.9×10^{57} [pc^{-2}(K km/s)$^{-1}$] (Dickman et al. 1986), a correction factor for heavy elements of 1.36 (based on cosmological abundances, Bolatto et al. 2013), and a mass of the H_2 molecule of $1.7 \times 10^{-57} M_\odot$, a simpler expression for the molecular mass is obtained:

$$M_{H_2}[M_\odot] = 4.4\pi R^2 [pc] I_{CO(1-0)} [K\ km/s] \tag{1.4}$$

where R is the radius of the CO(1-0) beamsize in parsecs, so it depends on the distance of the source. This formula for calculating the mass of H_2 from the CO line intensity will be used throughout this entire work.

1.3 Kennicutt-Schmidt relation

From the moment we acknowledge that stars form due to the gravitational collapse of gas inside molecular clouds, a first and direct conclusion can be established: the star formation *must* depend on the amount of gas available. And to parameterize this relation is of key importance to begin to understand the physics of the process and its evolution throughout time. This is how in nearby galaxies, an empirical relation has been established between star formation and gas surface densities, the Kennicutt-Schmidt (K-S) relation, that compares the SFR surface density (Σ_{SFR}) versus the gas surface density (Σ_{gas}), which, depending on the analysis, can be molecular gas (H_2), atomic gas (HI), or both (HI+H_2). The first work done on this topic was by Schmidt (1959), setting for the first time the concept of a power-law relation between the SFR and gas densities. On physical grounds, we may expect the most fundamental relation to be between the volume densities of star formation and gas, but because most observations of external galaxies can measure only surface densities integrated along the line of sight, the most commonly used K-S relation in terms of densities is:

$$\Sigma_{SFR} = A \Sigma_{gas}^{N} \tag{1.5}$$

which in log-space translates into a constant slope plot. The coefficient A traces the absolute SFE (Kennicutt 1998b), and the slope N relates the star formation

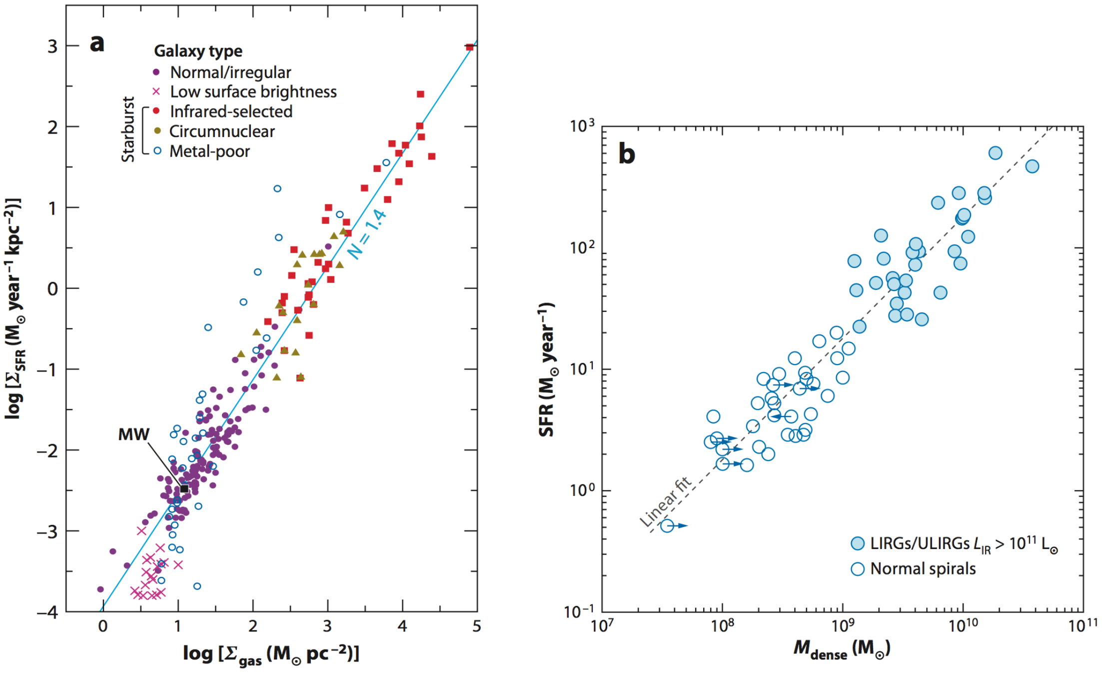

Figure 1.2: (a) Relationship between the disk-averaged surface densities of star formation and gas (atomic and molecular) for different classes of star-forming galaxies. Each point represents an individual galaxy, with the SFRs and gas masses normalized to the radius of the main star-forming disk. For this plot, a constant X_{CO} factor was applied to all galaxies. The light blue line shows a fiducial relation with slope $N = 1.4$ (not intended as a fit to these data). (b) Corresponding relation between the total (absolute) SFR and the mass of dense molecular gas as traced in HCN. The dashed gray line is a linear fit, which contrasts with the nonlinear fit in panel a. Figure adapted from Gao & Solomon (2004).

rate to the gas density present and tells us how close are the two variables from a linearity. The relation is nearly linear when Σ_{gas} considers molecular gas (H_2), while is less tight with atomic hydrogen (HI).

Kennicutt (1998a) presented a review of observations of the K-S relation up to the time, and nearly all that work characterized the relation between the disk-averaged SFR and gas surface densities in galaxies. Figure 1.2 presents an updated version of the global K-S in nearby galaxies, taken from Kennicutt & Evans (2012). Each point is an individual galaxy with the surface density defined as the total gas mass (molecular plus atomic) or SFR normalized to the radius of the main star-forming disk, as measured from Hα, Paα, or IR maps.

Most of the galaxies form a tight relation, and the dispersion of the normal galaxies overall from the average relation (± 0.30 dex rms) is considerably higher than can be attributed to observational uncertainties, which suggests that much of the dispersion is physical. The form of this integrated K-S relation appears to be surprisingly insensitive to the SFR environment and parameters such as the atomic versus molecular fraction. However, some metal-poor galaxies (defined as $Z < 0.3\ Z_\odot$) deviate systematically from the main relation (Figure 1.2a). These deviations could arise from a physical change in the star-formation relation, but more likely reflect a breakdown in the application of a constant X_{CO} factor (Leroy et al. 2011, and references therein). Adopting higher values of X_{CO} for metal-poor galaxies brings the galaxies much more into accord with the main relation in Figure 1.2a. Observations of low-surface-brightness spiral galaxies by Wyder et al. (2009) extend the measurements of the integrated star-formation relation to even lower mean surface densities (Figure 1.2a), where a clear turnover is present. The slope of the integrated K-S relation is nonlinear, with N $\sim$ 1.4–1.5 (Kennicutt 1998b) when a constant X_{CO} factor is applied. This uncertainty range does not include all possible systematic errors, arising, for example, from changes in X_{CO} or the initial mass function (IMF) with increasing surface density or SFR. Major systematic changes in either of these could easily change the derived value of N by as much as 0.2–0.3, which is what would happen if we would change X_{CO} to a value five times lower in the dense starburst galaxies: the slope N of the overall K-S relation would increase from 1.4–1.5 to 1.7–1.9 (Narayanan et al. 2011).

Usually, the K-S relation is parameterized in terms of the total (HI+H_2) gas surface density, but one can also explore the dependences of the disk-averaged SFR densities on the mean HI and H_2 surface densities individually. Among galaxies with relatively low mean surface densities, the SFR density is not particularly well correlated with either component, though variations in X_{CO} could partly explain the poor correlation between SFR and derived H_2 densities (e.g., Kennicutt 1998b).

The dependence of the SFR on dense molecular gas mass is markedly different, however. The right panel of Figure 1.2, taken from Gao & Solomon (2004), shows the relation between the integrated SFRs and the dense molecular gas masses, as derived from HCN $J = 1 \rightarrow 0$ measurements for a sample of normal and starburst galaxies. In contrast to the correlation with total molecular mass from CO $J = 1 \rightarrow 0$, this relation is linear, implying a strong coupling between the masses of dense molecular clumps and stars formed, which is largely independent of the galactic star-forming environment. Wu et al. (2005) have subsequently shown that this linear relation extends down to the scales of individual star-forming molecular clouds and dense clumps in the Galaxy. Combined with the MW studies, these dense gas relations for galaxies suggest that dense clumps are plausible fundamental star-forming units. If so, the mass fraction of the ISM (and fraction of the total molecular gas) residing in dense clumps must increase systematically with the SFR.

Finally, the K-S relation gives one more extra piece of information, used throughout this entire work: the efficiency of the star-forming process. The SFE can be directly measured as

$$\mathrm{SFE} = \frac{\Sigma_{\mathrm{SFR}}}{\Sigma_{\mathrm{gas}}} \tag{1.6}$$

where Σ_{gas} can consider either just the atomic gas (HI), the molecular gas (H_2) or the combination of both (HI+H_2). The inverse of this quantity (i,e. $\Sigma_{\mathrm{gas}}/\Sigma_{\mathrm{SFR}}$) is called the depletion time τ_{dep}, and tell us exactly how long will the process take to convert all the amount of gas taken under consideration, into stars. For nearby spiral galaxies these depletion times are often found to be between 2 and 3 Gyrs

(Bigiel et al. 2011, Leroy et al. 2008). As we will see in the following chapters, the efficiency of the star-forming processes in low gas density regions is much lower, implying longer depletion times.

1.4 Low gas density environments

This thesis focuses on star formation in low gas density regimes, where the typical gas surface density is less than 10 $M_{\odot}pc^{-2}$ and the gas is mostly atomic. These regions can be found in the outer disks of spirals, early-type, low surface brightness (LSB) and dwarf galaxies, and the characterize for having a very low and sparse star formation, low metallicities and dust abundances, relatively high shear, low total gas column densities spread over significant scale heights, a preponderance of HI compared to H_2, and a comparatively weak stellar potential well (Kennicutt & Evans 2012).

But even though the cold gas in this regime is predominantly atomic, small and local concentrations of molecular gas are often found. Star formation is highly dispersed, with young clusters and HII regions observed only in regions of unusually high cold-gas densities. The SFE in these places is very low and seems to be uncorrelated with Σ_{gas}, where the SFR has a much larger dynamic range than the local gas density. Such are the results found in the outer parts of spiral galaxies (Bigiel et al. 2008, 2010).

Observations in such environments are indeed difficult, due to the weakness of the emission, but extremely important in the field of star formation. A robust, quantitative picture of how the the environment in the outer disks affects star formation is crucial if we want to understand the origins of galaxy structure. Many galaxies sustain a large reservoir of (low column density) gas in their outer disks over evolutionary timescales. To measure the gas consumption timescale in this regime for many galaxies and compare it to the gas consumption time found for the inner parts of galaxies provides valuable clues regarding the role of outer disk gas for fueling star formation over cosmological times (Shlosman et al. 1989, Bauermeister et al. 2010). Additionally, star formation at large galactocentric radii will affect how chemical enrichment varies across a galaxy (Gil de Paz et al. 2007b) and plays a critical role in determining the location and form of the break in the exponential stellar disk (Pohlen & Trujillo 2006)

But evidences of star formation activity in low gas density mediums are not found only in the outer parts of galaxies. This thesis also studies regions even farther away from the central parts of galaxies, where typical star formation occurs, and involves the intergalactic medium in the Virgo Cluster, where galaxies interact with each other, affecting their structure and further evolution. The dynamics of these galaxies are dominated by the gravitational potential of the entire cluster, and thus not only interact with each other through collisional processes, but also with the cluster as a whole, and with the intra-cluster medium (ICM), which strips the gas content from them. This effect is most likely to be the result of ram-pressure, i.e the force that any body, in this case a galaxy, feels when moving through a fluid, like the ICM. The ram-pressure can strip large amounts of atomic gas from galaxies, up to thousands of parsecs away, forming large tails of atomic gas, the initial fuel of star formation. The ICM is a very hostile environment, with temperatures of $\sim10^7$-10^8 K (Roediger & Hensler 2005), and destructive X-rays (e.g., Machacek et al. 2004; Fabian et al. 2006; Tamura et al. 2009), and yet surprisingly there has been evidence of molecular gas clumps, most likely formed in situ, since ram-pressure is not expected to be able to drag such a dense gas. Furthermore, evidence of recent star formation has also been observed through Hα emission. Active star formation in such unusual, hostile and isolated environments makes an ideal laboratory to study star formation under extreme conditions, and help us to define the limiting conditions for the process to take place, as well as to disentangle what are the determining factors that can trigger such an unlikely event.

1.5 Instrumentation

The main data for this thesis were obtained through observations at the IRAM 30 mt single dish radio telescope (Figure 1.3). Located at 2850 meters of altitude in Pico Veleta in the Spanish Sierra Nevada, this telescope is one of the most sought-after radio telescopes in the world.

Figure 1.3: IRAM 30-mt single dish radio telescope at Pico Veleta in Sierra Nevada, Spain.

Thanks to its heterodyne Eight MIxer Receiver (EMIR), four double sidebands are available to cover the millimeter spectral range from 83 to 360 GHz (Carter et al. 2012). These bands cover the four main atmospheric windows in the millimeter range, at 3, 2, 1.3 and 0.9 mm (Figure 1.4), and are ideal to study the cold interstellar matter in its molecular form. Furthermore, these bands are built in a technology that offers 8 GHz instantaneous bandwidth per sideband and polarization (horizontal and vertical), and allows three possible combination of dual and simultaneous band observations.

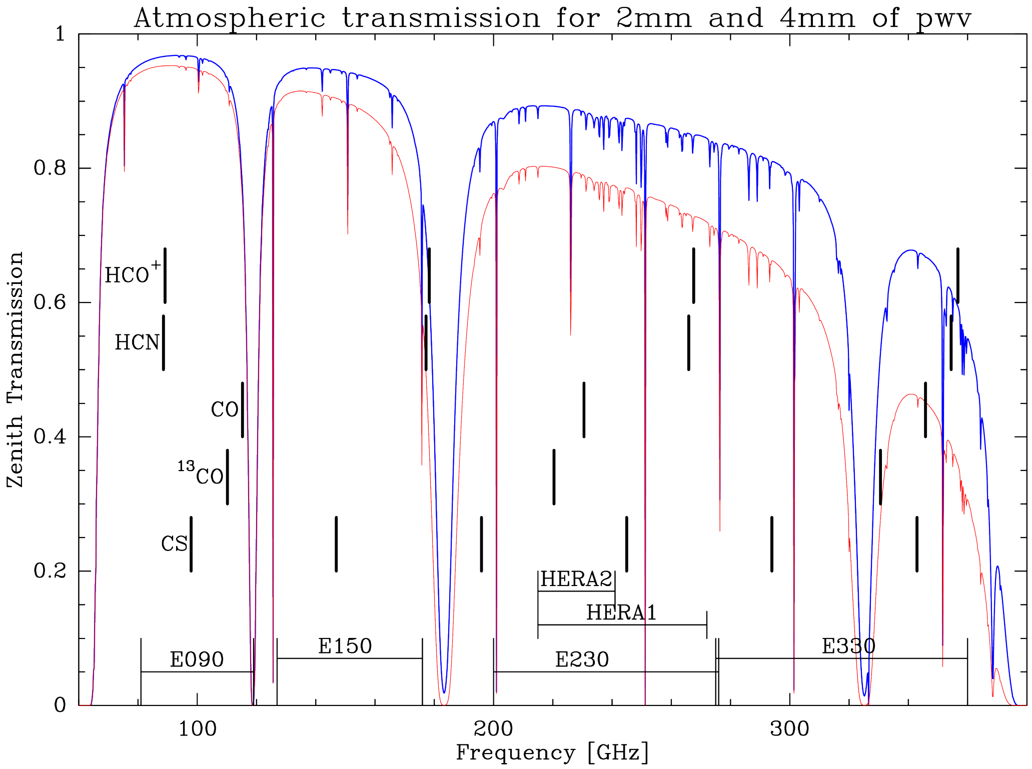

Figure 1.4: Atmospheric transmission between 60 and 400GHz for two precipitable water vapors, modeled with the ATM model. Additionally the EMIR bands: E090, E150, E230 and E330 (named after their approximated central frequencies), covering the 3, 2, 1.3 and 0.9 mm atmospheric windows respectively, and a few important molecular transitions

All the observations done in this thesis were done with the E0/E2 configuration, which allows simultaneous observations of CO(1–0) and CO(2–1) at 115.271 and 230.538 GHz respectively, in both polarization. The telescope half-power beam widths at these frequencies are 22″ and 11″ respectively.

Finally, to achieve the spectral resolution needed, both the Wideband Line Multiple Autocorrelator (WILMA) and the Fast Fourier Transform Spectrometer(FTS) backends were used, which give an spectral resolution of 2 MHz and 195 kHz respectively. At 115 GHz, these resolutions translate into 5.2 km/s for WILMA and 0.5 km/s for FTS, and at 230 GHz, the corresponding values are 2.6 km/s and 0.25 km/s respectively.

Chapter 2

XUV

Contents

2.1 M63 24
  2.1.1 Observations 26
  2.1.2 Results 27
  2.1.3 Analysis 33
  2.1.4 Summary and conclusions 48
  2.1.5 Publication 50
2.2 2013 observations 63
  2.2.1 Data reduction and Results 63
  2.2.2 Stacking 67
2.3 M83 68
  2.3.1 Instrumentation and Observations 69
  2.3.2 Results 70
  2.3.3 Star formation rate 72

Ever since the Galaxy Evolution Explorer (GALEX) telescope was launched in 2003 it has mapped numerous galaxies in our local Universe, in both near ultraviolet (NUV) at 2267Å, and far ultraviolet (FUV) at 1516Å. With its 1.25 degree field of view, a spatial resolution of $5''$, and a sensitivity to stellar populations younger than a few hundred Myrs, the GALEX telescope is ideal to resolve the spiral structure of nearby galaxies and map with great detail the ultra-violet (UV) emission coming from young O and B stars, characterized by ages from a few Myr up to 400 Myr. During the first years of the mission, the GALEX telescope made a major discovery, by surprisingly unveiling large disks of UV emission in several nearby spiral galaxies, that can go up to 3 to 4 times their optical radii (Gil de Paz et al. 2007a). Such disks of extended ultraviolet (XUV) emission are present in $\sim$30% of spiral galaxies, and in many cases go further than the Hα emission, the typical star formation tracer. The most remarkable examples of XUV disks are present in M63, M83, NGC2841 and NGC4625 (Thilker et al. 2005, Gil de Paz et al. 2005, 2007a), and they cover a significant fraction of the area detected at 21 cm wavelength, with some correspondence between the position of the brightest UV complexes and peak of atomic gas distribution. With these XUV disk of emission, the GALEX telescope has demonstrated that Hα observations are not always good tracers of star formation, and can fail to detect a significant population of moderate-age stars in the outermost disks of spiral galaxies, since Hα traces more recent episodes of star formation. In these scenarios, UV emission is a much better tracer of star formation, and can be used to estimate the efficiency of this process.

These XUV regions in the outer parts of spiral galaxies have gained interest in the past few years in the field of star formation, since the are low metallicity environments (Henry & Worthey 1999), resembling the conditions of early stages of spiral galaxies and high-redshift galaxies. These regions are also known to have low star formation rates (Dong et al. 2008, Bigiel et al. 2010, Alberts et al. 2011). Moreover, there is growing evidence of cold gas accretion in the local Universe, both through the arrival and merging of gas-rich satellites and through gas infall from the intergalactic medium. This new gas could be deposited in the outer regions of galaxies and form reservoirs for replenishing the inner parts and feeding star formation (Sancisi et al. 2008), making outer regions good laboratories for scanning the interface between galaxies and the surrounding intergalactic gas.

The importance of the occurrence of recent and ongoing star formation in the outer disks of normal spiral galaxies has several important implications. First of all, it supports the presence of molecular gas in the outskirts of spirals, since stars are formed within molecular clouds. Furthermore, this suggests the presence of large reservoirs of hydrogen in the form of H_2, which may contribute to the baryonic dark matter of spiral galaxies. It also offers the ideal place to study the unresolved issue of the atomic hydrogen gas origin: is HI mainly a product of the star formation process; i.e, does it result from the photodissociation of H_2 by the UV flux from newly formed stars (Allen et al. 1986, 2004, Smith et al. 2000), rather than mainly being a precursor of it? Additionally, the presence of recently formed stellar complexes at large galactocentric radii also provides a simplified laboratory for determining the star formation to occur spontaneously (Kennicutt 1989, Martin & Kennicutt 2001). And finally, it allows us to investigate the star formation in quiescent and low metallicity environments that may affect the star formation density and the initial mass function.

The aim of the work presented in this chapter is demonstrate the presence of molecular gas in the outer parts of a few XUV disk galaxies in the nearby universe, and use it to study the star formation efficiency of the process at extremely low gas densities, where little is known about the topic.

2.1 M63

For this thesis, the first galaxy studied in the XUV topic was M63 (NGC5055), by resuming a work started in 2007 with CO observations from the IRAM 30-m telescope. This section presents the results of those observations and the analysis done in the CO data, in combination with complementary UV and infrared data, to quantify the SFR and study its efficiency.

M63 is a SA(rs)bc galaxy located at 10.1 Mpc (Leroy et al. 2009), and looks like a typical spiral galaxy, representative of a large class of local spirals, with no immediate neighbor, which excludes the potentiality of an object in interaction. However, M63 is not so ordinary, as it is a remarkable example of a nearby spiral with a bright and extended XUV disk. In Fig. 2.1 is shown the GALEX NUV and FUV color-composite image of M63, where an extensive population of UV-bright star-forming regions and stellar clusters (tracing the O and B stars) is revealed. The major axis radius of the B-band 25 mag arcsec^{-2} isophote, the so-called isophotal or optical radius, is equal to $r_{25} = 354'' = 17.4$ kpc in M63. Its NUV and FUV surface-brightness profiles show a smooth decrease of the XUV emission out to 2.5 times the optical radius (Gil de Paz et al. 2007a).

The 21 cm observations of M63 (see Figure 2.11) also show the presence of a very large, warped gaseous disk extending out to 40 kpc in the major axis radius (e.g., Battaglia et al. 2006). The warp starts around r_{25} and is exceptionally extended and symmetric, suggesting a stable dynamics. The measured H I column densities are larger than 10^{20} cm^{-2} up to 70% of the XUV disk. These large H I column densities plus the extended XUV emission, both suggest the presence of molecular gas out to large galactocentric radii. Indeed, recent studies have demonstrated that strong H I emission is on average a good tracer of regions rich in molecular gas (e.g., Crosthwaite et al. 2002, Nieten et al. 2006), and the XUV emission undeniably betrays the presence of stars and hence of molecular gas necessary for their formation.

Molecular gas in M63 has been searched in the past in the context of the BIMA/SONG survey, the first systematic imaging survey of ^{12}CO(1–0) emission from the centers and disks of nearby galaxies (Helfer et al. 2003, see their Fig. 43). The reported high-resolution CO measurements are confined to the very central area of the M63 optical disk, $r_{\rm gal} = 96'' = 0.3\,r_{25}$ along the major axis, because of the lack of sensitivity of these data at the border of the map with a primary beam gain drop by a factor of 2. Single-dish spectra from the FCRAO Extragalactic CO Survey (Young et al. 1995, see their Fig. 87), despite their moderate sensitivity and low-resolution, show that the CO emission extends over a larger area than that mapped by BIMA/SONG, reaching a two times larger galactocentric radius, but still not extending up to the optical disk limit r_{25}. The signal measured at $r_{\rm gal} = 180''$ is equal to ~ 2 K km s^{-1}, which leaves place for a CO line intensity decrease by a factor of 10 to 20 in the outermost XUV disk (depending on the CO line width), when aiming at signals as weak as 10 mK, or weaker, in these extreme regions. More recently, M63 was also observed by Schruba et al. (2011), but in this work, once again beyond the galactocentric radius $r_{\rm gal} = 0.8\,r_{25}$, only upper limits are reported for $3\,\sigma$ detections, still lacking of high enough sensitivity. Finally, Leroy et al. (2009) mapped the CO(2–1) line in M63 over the full optical disk, as part as the HERACLES survey on the IRAM 30 m telescope, and obtained reliable measurements out to $r_{\rm gal} = 0.68\,r_{25}$.

The aim of the present work was to go further than all these observations, and achieve a good sensitivity beyond the r_{25} limit, to confirm the presence of H_2 suggested by the extended HI and FUV-NUV emission.

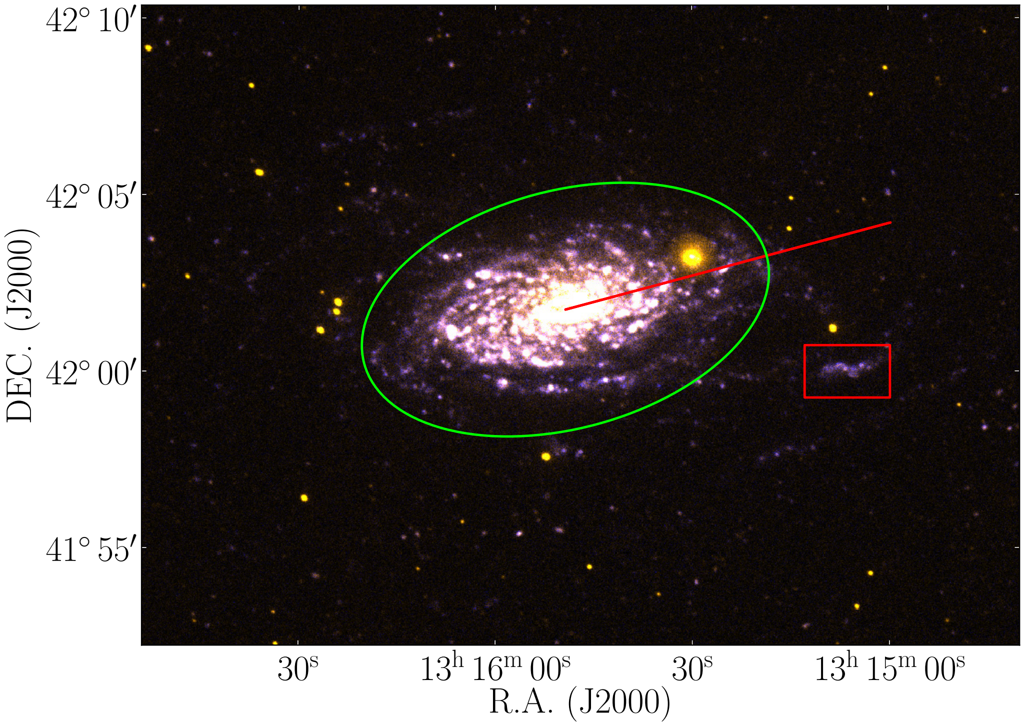

Figure 2.1: False-color RGB image of M63. The image was produced using the *arcsinh* function, which allows to show faint structures while simultaneously preserving brighter structures in the field, such as the spiral arms of large galaxies (Lupton et al. 2004). The GALEX NUV and FUV emissions are plotted in red and blue, respectively, and the composition of NUV (80%) and FUV (20%) is plotted in green. The green ellipse represents the B-band 25 mag arcsec^{-2} isophote limit, r_{25}, or optical limit. The red solid line shows the CO mapping we performed along the major axis of M63 from the center out to $r_{\rm gal} = 572'' = 1.6\,r_{25}$. The red box encloses the chosen bright UV region, located at $r_{\rm gal} = 483'' = 1.36\,r_{25}$.

2.1.1 Observations

The observations were performed with the IRAM 30-m telescope at Pico Veleta, Spain, during a first run on September 10–17, 2007 under poor weather conditions, and during a second run on November 2, 16 and 27 and December 1, 2007 under good-to-excellent weather conditions.

Simultaneous CO(1–0) and CO(2–1) observations were done with the now decommissioned single pixel heterodyne receivers, with two of them centered on the

^{12}CO(1–0) line at 115.271 GHz, and two on the ^{12}CO(2–1) line at 230.538 GHz. The telescope half-power beam widths at these two frequencies are $22''$ and $11''$, respectively. The data were recorded using the VESPA autocorrelator with 640 MHz bandwidth and 1.25 MHz resolution at 3 mm, and two 1 MHz filter banks (512 channels each) at 1 mm. The resulting velocity coverage at 115.271 GHz is 1665 km s^{-1} with a spectral resolution of 3.2 km s^{-1}. The corresponding values at 230.538 GHz are 666 km s^{-1} and 1.3 km s^{-1}.

The observing strategy for this work was of key importance to achieve the necessary sensitivity. For this, an arrange of single ON+OFF positions was created, instead of doing a raster mapping, which requires much more integration time to reach a good S/N. First, a CO mapping was performed along the major axis of the M63 disk from the center of the galaxy located at (J2000) RA = $13^{\rm h}\,15^{\rm m}\,49.3^{\rm s}$, Dec = $+42^\circ\,01^{\rm m}\,45.4^{\rm s}$ out to the galactocentric radius $r_{\rm gal} = 572'' = 1.6\,r_{25}$ by aligning 27 single pointings with a spatial sampling of $22''$ in the radial direction sustaining a position angle PA = 105°. This alignment of pointings is shown in Figure 2.2. Second, a bright UV region was mapped in the outer regions of the M63 disk centered on (J2000) RA = $13{\rm h}\,15^{\rm m}\,07.0^{\rm s}$, Dec = $+42^\circ\,00^{\rm m}\,00.0^{\rm s}$ and located at the galactocentric radius $r_{\rm gal} = 483''$ with $6\times 2 = 12$ pointings following the sequence from $(-66''; 0'')$ to $(+44''; +22'')$ offsets relative to the central coordinates with a $22''$ spatial sampling in the right ascension direction and same in the declination direction. In Figure 2.2 we can see the positions of these 12 pointings in the UV region. Observations were performed in wobbler switching mode with the maximum symmetrical azimuthal wobbler throw of $240''$ allowed, corresponding, for this spiral galaxy located at a distance of 10.1 Mpc, to 11.8 kpc in projected distance.

2.1.2 Results

The data were reduced with the CLASS software from the GILDAS package. All the spectra obtained with the two receivers tuned on the ^{12}CO(1–0) line and corresponding to scans at the same pointings were summed up without any smoothing. On the other hand, the spectra obtained with the two receivers tuned on the ^{12}CO(2–1) line were first Hanning smoothed to a resolution of 2.6 km s^{-1}, since the expected average CO line width is of the order of 10 km s^{-1}, before being summed up when corresponding to scans at the same pointings. No baseline subtraction was performed on individual spectra before summing, as we simply did a linear sum. In Tables 2.1 and 2.2 (columns 4 and 7) we list the achieved $1\,\sigma$ rms in mK at 115 GHz (or 3 mm) and 230 GHz (1 mm) for each pointing of the M63 disk map and the UV region map, respectively[1]. These rms values were obtained with a baseline subtraction of degree 0, and with windows set to $300 - 400$ km s^{-1}, both at 3 mm and 1 mm, as defined by the velocity positions of detected CO(1–0) and CO(2–1)

---

[1] The efficiencies of the ABCD receivers on the IRAM 30 m telescope are 5.9 Jy K^{-1} at 3 mm and 7.2 Jy K^{-1} at 1 mm (see the online IRAM wiki pages at http://www.iram.es/IRAMES/mainWiki/Iram30mEfficiencies).

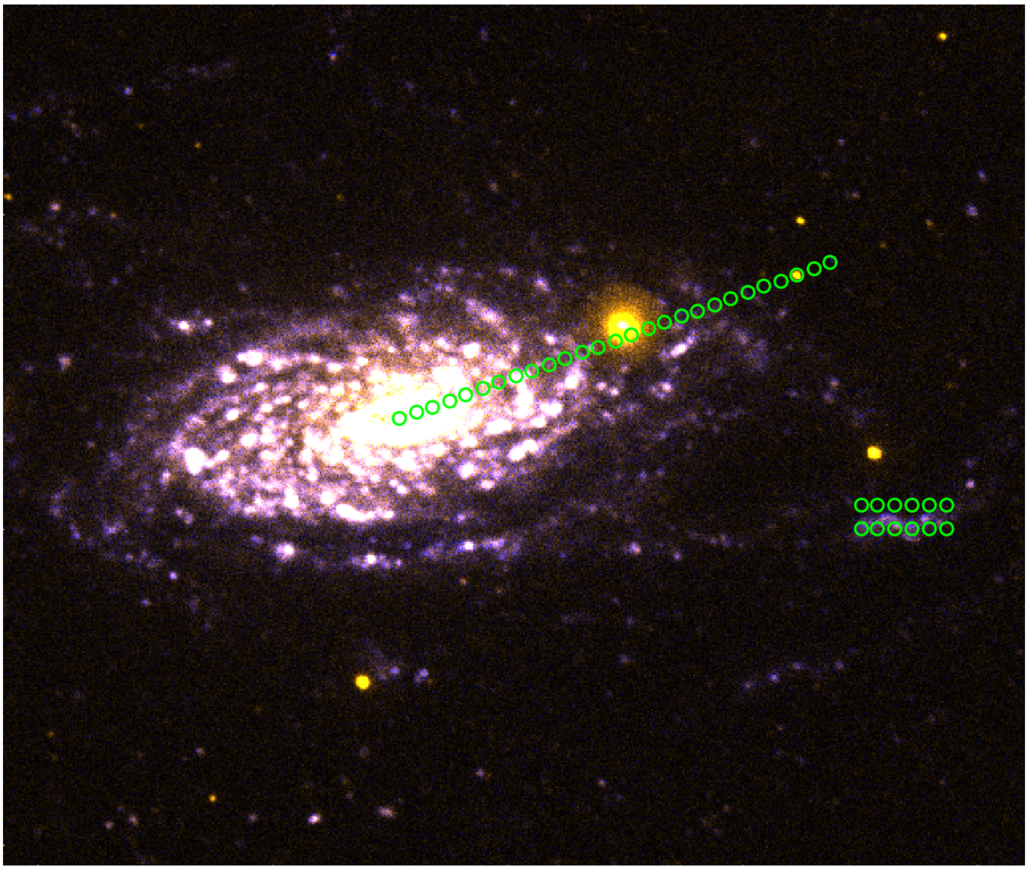

Figure 2.2: Positions of observing pointings to map the radial axis of M63, as well as its bright UV region, overlaid in the same NUV-FUV composite image of Figure 2.18. Mapping CO through individual beam pointings, has proben to be a very efficient technique to obtain deep observations of specific, not extended areas of a galaxy. To better visualize the spatial resolution of our data, pointings circles have been drawn with a 11″ width, same as the CO(2–1) FWHM.

lines[2]. At 3 mm we obtained on average rms values between 4 and 21 mK in the M63 disk map, while for seven pointings around the isophotal radius, r_{25}, and for all the pointings of the UV region map we pushed the rms limit down to 4 to 7 mK.

The results of our CO emission mapping of M63 along the major axis of its disk and over the bright UV region at $r_{\rm gal} = 1.36\,r_{25}$ are presented in Tables 2.1 and 2.2, respectively. We provide the CO(1–0) and CO(2–1) line full widths at half maximum, FWHM (columns 5 and 8) and the integrated CO(1–0) and CO(2–1) line fluxes (columns 6 and 9) at each pointing of the mapping, as determined from fitting Gaussian functions to the CO profiles obtained by summing up all spectra corresponding to all scans per pointing. The CO(1–0) and CO(2–1) line FWHM are in the range from 9 to 53 km $\rm s^{-1}$ and from 6 to 39 km $\rm s^{-1}$, respectively. They are greater than those expected for individual giant molecular clouds (GMCs) that have typical line widths of $\sim$ 10.4 km $\rm s^{-1}$ (Solomon et al. 1987), except for a few pointings around r_{25} and over the UV region. This implies that mostly an ensemble of molecular clouds is emitting per beam of $\sim$ 1 and 0.5 kpc at 3 and 1 mm, respectively.

In Table 2.1 we also list the molecular gas masses per pointing (column 11), through Eq. 1.4, using the "standard" Galactic CO(1–0)-to-$\rm H_2$ conversion factor $X_{\rm CO} = 2 \times 10^{20}$ $\rm cm^{-2}(K\ km\ s^{-1})^{-1}$ (Dickman et al. 1986) and including a correction for helium. The inferred masses are in the range $M_{\rm H_2} = (1.5 - 322) \times 10^6$ $\rm M_\odot$. Figure 2.3 shows the summed-up spectra of all scans *per* pointing of the M63 disk map along the major axis, while Fig. 2.4 shows the resulting spectrum obtained by summing up all spectra of all scans at the 12 pointings used to map the UV region.

The radial mapping (Fig. 2.3) clearly shows a detection of the CO(1–0) emission out to the galactocentric radius $r_{\rm gal} = 352''$, namely out to the isophotal radius $r_{25} = 354'' = 17.4$ kpc defined as the radius of the B-band 25 mag $\rm arcsec^{-2}$ isophote. A severe drop of the CO flux is nevertheless observed as a function of the galactocentric radius. Beyond r_{25} and out to $1.62\,r_{25}$, the limit of our CO search along the M63 major axis, no CO emission is detected anymore (Table 2.1). Even by summing up all the spectra corresponding to all scans at the 10 outermost pointings and by smoothing the resulting spectrum to a resolution of 9.7 km $\rm s^{-1}$, corresponding to the typical FWHM of the CO(1–0) lines detected at the outermost pointings, no CO emission is observed. We do, however, derive a stringent $3\,\sigma$ upper limit on the integrated CO(1–0) line flux at $r_{\rm gal} > r_{25}$ of $F_{\rm CO(1-0)} < 0.06$ K km $\rm s^{-1}$, when assuming a line width of 10 km $\rm s^{-1}$. This is equivalent to a molecular gas mass of $M_{\rm H_2} < 3.9 \times 10^5$ $\rm M_\odot$. On the other hand, the CO(2–1) emission is securely detected out to $r_{\rm gal} = 242''$ only, i.e. $0.68\,r_{25}$, in agreement with the CO(2–1) mapping by Leroy et al. (2009), while there are two very tentative detections at $2\,\sigma$ at the pointings $r_{\rm gal} = 0.93\,r_{25}$ and r_{25} (Table 2.1). The CO(2–1) line thus appears to be excited over about 2/3 of the optical disk. The corresponding CO luminosity ratios, $r_{2,1} = L'_{\rm CO(2-1)}/L'_{\rm CO(1-0)}$, can be found in Table 2.1 (Col. 10). They varie randomly

---

[2] Except for the very few inner pointings at $r_{\rm gal} = 0$, $22''$, and $44''$ for which a larger window was set, given the larger widths of the CO(1–0) and CO(2–1) lines.

Table 2.1. CO mapping along the major axis of the M63 disk.

				CO(1–0)			CO(2–1)				
$r_{\rm gal}$ [$''$]	$r_{\rm gal}$ [r_{25}]	Time [min]	rms[a] [mK]	FWHM[b] [km s^{-1}]	F[c] [K km s^{-1}]	rms[a] [mK]	FWHM[b] [km s^{-1}]	F[c] [K km s^{-1}]	$r_{2,1}$[d]	M$_{H_2}$[e] [10^6M$_\odot$]	Σ_{H_2}[f] [$M_\odot$pc^2]
0	0	31	11.	200	49.8 ± 2.2	16.	192	39.8 ± 3.1	0.24	321.8 ± 14.2	125.7 ± 5.6
22	0.06	8	18.	53	24.5 ± 0.9	28.	27	12.6 ± 0.8	0.16	158.3 ± 5.8	61.8 ± 2.3
44	0.12	8	19.	41	16.4 ± 0.8	33.	21	9.0 ± 0.7	0.17	106.0 ± 5.2	41.4 ± 2.0
66	0.19	8	19.	23	9.8 ± 0.4	32.	16	4.2 ± 0.5	0.13	63.3 ± 2.6	24.7 ± 1.0
88	0.25	8	18.	20	6.3 ± 0.4	32.	20	3.4 ± 0.6	0.17	40.7 ± 2.6	15.9 ± 1.0
110	0.31	8	19.	26	12.6 ± 0.5	30.	21	8.2 ± 0.6	0.20	81.4 ± 3.2	31.8 ± 1.3
132	0.37	8	21.	22	5.1 ± 0.5	35.	20	2.6 ± 0.7	0.16	33.0 ± 3.2	12.9 ± 1.3
154	0.44	23	13.	29	5.3 ± 0.4	22.	39	2.5 ± 0.9‡	0.15	34.3 ± 2.6	13.4 ± 1.0
176	0.50	23	13.	19	5.4 ± 0.2	24.	27	2.8 ± 0.6	0.16	34.9 ± 1.3	13.6 ± 0.5
198	0.56	23	13.	21	1.8 ± 0.3	22.	18	0.82 ± 0.40‡	0.14	11.6 ± 1.9	4.5 ± 0.8
220	0.62	31	11.	16	0.98 ± 0.17	11.†	10	< 0.33	< 0.11	6.3 ± 1.1	2.5 ± 0.4
242	0.68	101	6.	11	0.30 ± 0.06	8.	6	0.17 ± 0.05	0.17	1.9 ± 0.4	0.76 ± 0.15
264	0.75	101	6.	14	0.45 ± 0.08	4.†	10	< 0.12	< 0.08	2.9 ± 0.5	1.1 ± 0.2
286	0.81	55	10.	21	0.88 ± 0.21	9.†	10	< 0.27	< 0.10	5.7 ± 1.4	2.2 ± 0.5
308	0.87	47	11.	14	0.81 ± 0.15	11.†	10	< 0.33	< 0.13	5.2 ± 1.0	2.0 ± 0.4
330	0.93	63	7.	22	0.85 ± 0.15	9.	34	0.38 ± 0.31‡	0.14	5.5 ± 1.0	2.1 ± 0.4
352	0.99	155	5.	9	0.23 ± 0.04	6.	34	0.29 ± 0.21‡	0.38	1.5 ± 0.3	0.58 ± 0.10
374	1.06	109	4.†	10	< 0.12	4.†	10	< 0.12	···	···	···
396	1.12	117	4.†	10	< 0.12	3.†	10	< 0.09	···	···	···
418	1.18	93	5.†	10	< 0.15	5.†	10	< 0.15	···	···	···
···	···	···	···	···	···	···	···	···	···	···	
473	1.34	381	2.†	10	< 0.06	2.†	10	< 0.06	···	< 0.39	< 0.15

Note. — The radius of the B-band 25 mag arcsec^{-2} isophote, the so-called isophotal radius, is equal to $r_{25} = 354'' = 17.4$ kpc in M63. It is often used as a reference to express the relative galactocentric radius, $r_{\rm gal}$. The last separate line of the Table gives the values obtained when summing all scans at the 10 outermost pointings with no CO detection from $1.06\,r_{25}$ to $1.62\,r_{25}$ and by smoothing the resulting 3 mm and 1 mm spectra to a resolution of 9.7 and 10.4 km s^{-1}, respectively.

[a] Rms noises at, respectively, 3 and 1 mm, measured per channel of 3.2 and 1.3 km s^{-1}. The values marked with † correspond to rms noises measured per smoothed channel of 9.7 and 10.4 km s^{-1}, respectively.

[b] Full widths at half maximum of, respectively, CO(1–0) and CO(2–1) lines as determined from fitting Gaussian profiles.

[c] Integrated CO(1–0) and CO(2-1) line intensities as determined from fitting Gaussian profiles. The values marked with ‡ correspond to potentially less reliable measurements, because of a CO line detection at $2\,\sigma$ only. Upper limits are $3\,\sigma$ and are calculated assuming a 10 km s^{-1} line width.

[d] CO luminosity correction factor defined as $r_{2,1} = L'_{\rm CO(2-1)}/L'_{\rm CO(1-0)}$, needed to correct the lower Rayleigh-Jeans brightness temperature of the 2–1 transition relative to 1–0.

[e] H_2 mass calculated from the CO(1–0) luminosity and by adopting the "Galactic" CO-to-H_2 conversion factor, $X_{\rm CO} = 2 \times 10^{20}$ cm^{-2} (K km s^{-1})$^{-1}$ (Dickman et al. 1986). The applied formula is: $M_{\rm H_2}$ (M$_\odot$) $= 4.4 L'_{\rm CO(1-0)}$ (K km s^{-1} pc^2), where a factor of 1.36 is included to account for helium.

[f] H_2 surface density calculated from the integrated CO(1–0) line intensity and by adopting the CO-to-H_2 conversion factor given under $^{(e)}$. The applied formula is: $\Sigma_{\rm H_2}$ (M$_\odot$ pc^{-2}) $= 4.4\cos(i) I_{\rm CO(1-0)}$ (K km s^{-1}), where $i = 55°$ is the inclination of M63 (Leroy et al. 2008).

Table 2.2. CO mapping over the bright UV region at $1.36\,r_{25}$.

			CO(1–0)			CO(2–1)					
Offsets ($''$)	($''$)	Time (min)	rms[a] (mK)	FWHM[b] (km s^{-1})	F[c] (K km s^{-1})	rms[a] (mK)	FWHM[b] (km s^{-1})	F[c] (K km s^{-1})	$r_{2,1}$[d]	M_{H_2}[e] (10^6 $M_\odot$)	Σ_{H_2}[f] ($M_\odot$ pc^2)
−66	0	118	5	10	< 0.15	6	10	< 0.18	⋯	< 0.97	< 0.38
−66	+22	117	5	11	0.14 ± 0.06‡	6	10	< 0.18	< 0.39	0.90 ± 0.39	0.35 ± 0.15
−44	0	186	4	10	< 0.12	4	10	< 0.12	⋯	< 0.78	0.30
−44	+22	164	4	10	< 0.12	6	10	< 0.18	⋯	< 0.78	0.30
−22	0	171	4	14	0.21 ± 0.06	5	10	< 0.15	< 0.22	1.36 ± 0.39	0.53 ± 0.15
−22	+22	148	4	10	< 0.12	6	10	< 0.18	⋯	< 0.78	< 0.30
0	0	164	4	10	< 0.12	5	10	< 0.15	⋯	< 0.78	< 0.30
0	+22	148	5	10	< 0.15	6	10	< 0.18	⋯	< 0.97	< 0.38
+22	0	123	5	10	< 0.15	7	10	< 0.21	⋯	< 0.97	< 0.38
+22	+22	116	5	10	< 0.15	8	10	< 0.24	⋯	< 0.97	< 0.38
+44	0	63	7	10	< 0.21	9	10	< 0.27	⋯	< 1.36	< 0.53
+44	+22	62	7	10	< 0.21	8	10	< 0.24	⋯	< 1.36	< 0.53
all offsets		1932	1	23	0.11 ± 0.02	2	10	< 0.06	< 0.17	0.71 ± 0.13	0.28 ± 0.05

Note. — The last separate line gives the values obtained when summing all scans at the 12 offset pointings.

[a] Rms noises at, respectively, 3 and 1 mm, measured per channel of 3.2 and 1.3 km s^{-1}.

[b] Full widths at half maximum of, respectively, CO(1–0) and CO(2–1) lines as determined from fitting Gaussian profiles.

[c] Integrated CO(1–0) and CO(2–1) line intensities as determined from fitting Gaussian profiles. The values marked with ‡ correspond to potentially less reliable measurements, because of a CO line detection at $2\,\sigma$ only. Upper limits are $3\,\sigma$ and are calculated assuming a 10 km s^{-1} line width.

[d,e,f] CO luminosity correction factor, H_2 mass, and H_2 surface density, respectively, calculated using the same prescriptions as in Table 2.1.

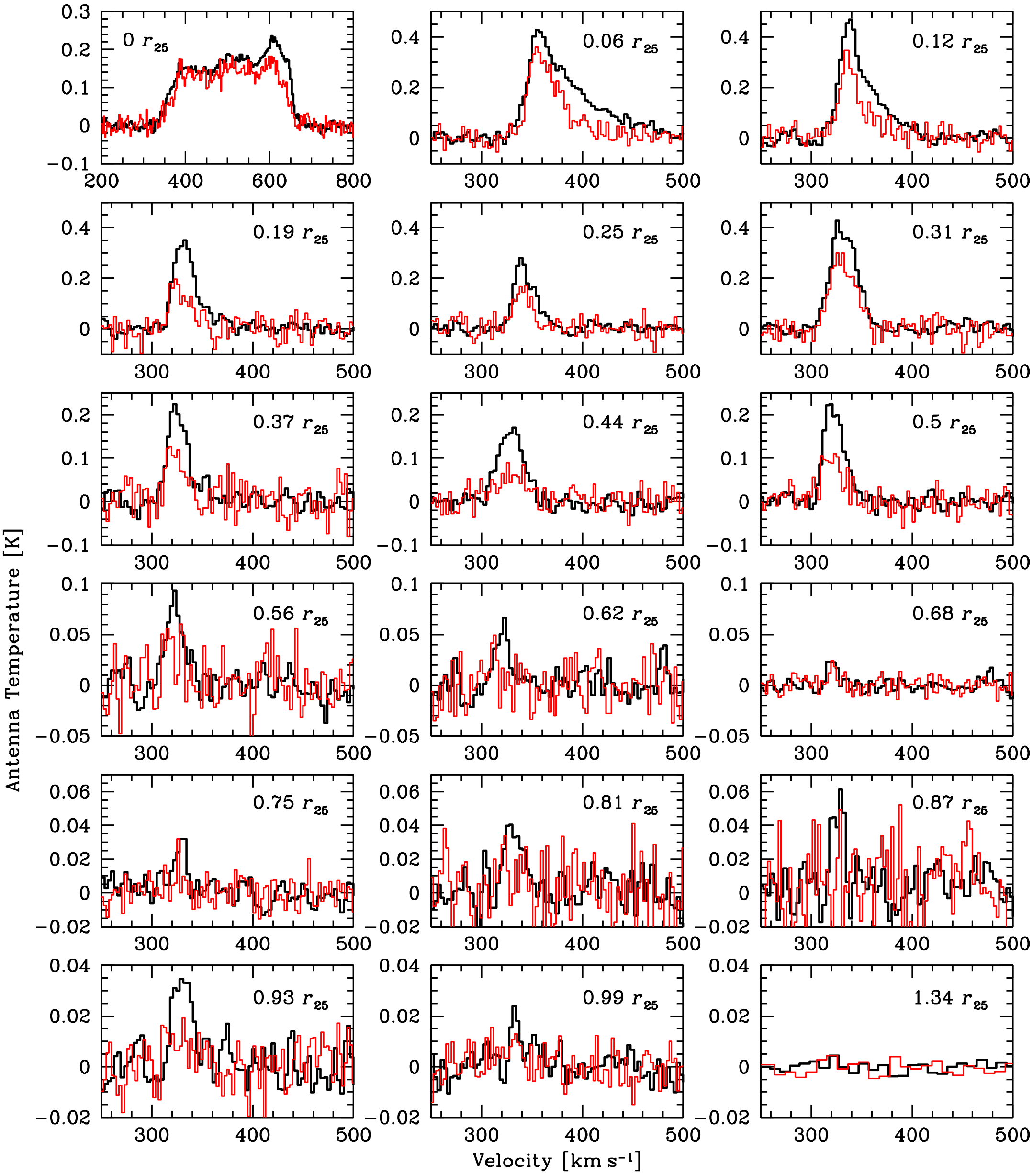

Figure 2.3: Mosaic of CO spectra obtained when mapping the M63 disk along its major axis from the center of the galaxy out to the isophotal radius, r_{25}. The CO(2–1) spectra (red thin line) are overplotted on the CO(1–0) spectra (black thick line). While the CO(1–0) emission is clearly detected out the optical radius, the CO(2–1) appears to be confined to $r_{\rm gal} \lesssim 0.68\,r_{25}$. The bottom-right panel shows the CO(1–0) and CO(2–1) spectra obtained when summing all scans at the 10 outermost pointings from $r_{\rm gal} = 1.06\,r_{25}$ to $1.62\,r_{25}$ and smoothed to a resolution of 9.7 and 10.4 km s^{-1}, respectively. No CO emission is detected at these outermost pointings.

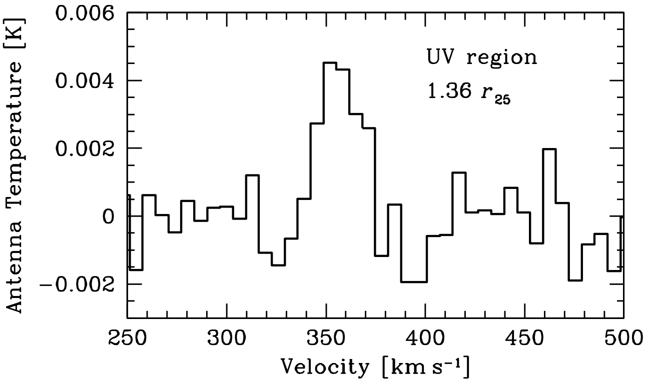

Figure 2.4: CO(1–0) spectrum obtained by summing up all spectra at the 12 pointings done to map the bright UV region at $r_{\rm gal} = 1.36\,r_{25}$. There is a clear CO emission detection in this region of M63 well beyond the optical radius. CO(2–1) remains undetected.

between 0.13 and 0.24 (in the center of M63) along the galactocentric radius, without showing any radial evolution. The absence of a clear detection of the CO(2–1) line beyond $r_{\rm gal} = 0.68\,r_{25}$ suggests that the subthermal excitation sets in around this galactocentric radius. However, this has to be considered with caution, because the major axis pointings probe only a small portion of the M63 disk at each radius and the Leroy et al. (2009) CO(2–1) map of the entire M63 disk is not very deep, and because there seems still to be plenty of star forming regions at $r_{\rm gal} > 0.68\,r_{25}$ with high enough densities (locally) to thermalize the CO(2–1) line (see Fig. 2.1).

Whereas our survey for CO emission along the major axis of the M63 disk seems to indicate that the molecular gas is confined to the isophotal radius r_{25} of the galaxy, we find a convincing CO(1–0) detection in the selected bright UV region at $r_{\rm gal} = 1.36\,r_{25}$. The sum of all spectra corresponding to all scans at the 12 pointings done to map the UV region leads to a CO(1–0) detection at $5.5\,\sigma$ with an integrated line flux $F_{\rm CO(1-0)} = 0.11 \pm 0.02$ K km s^{-1} (Fig. 2.4). This corresponds to a molecular gas mass of $M_{\rm H_2} = 7.1 \times 10^7$ M$_\odot$. The CO(1–0) emission appears to be maximal at the offset ($-22''$; $0''$), where it is detected at $3-4\,\sigma$ (Table 2.2). The CO(2–1) emission is, on the other hand, not detected down to an integrated line flux $F_{\rm CO(2-1)} < 0.06$ K km s^{-1}, obtained when summing up all the spectra corresponding to all scans at the 12 pointings.

2.1.3 Analysis

A few hundreds of nearby galaxies have been the object of intensive surveys for molecular gas (e.g., Young & Scoville 1991, Young et al. 1995, Helfer et al. 2003, Leroy et al. 2009). However, for very few only, deep CO searches in their outer disk regions have been undertaken. Here, we show the existence of molecular gas up to the isophotal radius, r_{25}, and beyond in the nearby spiral galaxy M63. This is the fourth of such a detection of molecular gas in the outskirts after the spiral galaxies NGC 4414 (Braine & Herpin 2004), NGC 6946 (Braine et al. 2007), and M33 (Braine et al. 2010). To analyse the impact of our observations in the

Table 2.3. Public ancillary data for M63.

Band or line	Telescope	FWHM [arcsec]	Reference
CO(2–1)	IRAM	13.4	Leroy et al. (2009)
FUV	GALEX	4.3	Gil de Paz et al. (2007a)
NUV	GALEX	5.3	Gil de Paz et al. (2007a)
Hα	KPNO	0.38	Kennicutt et al. (2008)
24 μm	Spitzer	6	Dale et al. (2009)
H I (21 cm)	VLA	6	Walter et al. (2008)

context of star formation in the outer disk of M63, we present the radial profiles of our CO observations along with complementary data of other star formation tracers (FUV, NUV, Hα, 24 μm) and H I, and we investigate the behaviour of the Kennicutt-Schmidt relation across the galaxy and beyond r_{25} in the bright UV region. Characterizing the Kennicutt-Schmidt relation in the outer disk regions, namely in environments with low metallicities, gas temperatures, excitations, and gas densities, all properties hostile to star formation, is of our main interest.

Radial profiles

In order to compare the CO distribution in M63 along the major axis of its disk to H I and other star formation tracers' distributions, we built comparative radial profiles of the CO, H I, FUV, NUV, Hα, and 24 μm emission. All together, they provide a complete view of the past and on-going star formation that took or takes place in the galaxy and of the ingredients needed to sustain the star formation: molecular and atomic gas. The respective data are taken from the literature and are described in Table 2.3. All these images are presented in Figure 2.5, where it can be appreciated the size of the area mapped in each one of them, as well as the extent of the emission of each tracer. A close look at the bright UV region at $r_{\rm gal} = 1.36\, r_{25}$ is shown in Fig. 2.6, through multiwavelength panels, from left to right, of the NUV, 24 μm, and H I 21 cm emission.

As these complementary data were obtained with different instruments and hence at various FWHM resolutions, we first convolved all these data to the resolution of our CO(1–0) data which is equal to the half-power beam width of the IRAM 30 m telescope at 3 mm, i.e. 22″. The images were then rotated by 20° in a north-to-west direction to have the major axis in the horizontal axis, and deprojected by correcting for a 55° inclination angle to bring the galaxy face-on. As an example, the corresponding convolved, rotated and deprojected images of M63 for 24μm, FUV and HI are shown in Figure 2.7. Finally, we made aperture photometry on these processed images inside apertures of 22″ diameter using the 'qphot' task of the 'digiphot.apphot' package of IRAF[3], and we subtracted an average sky value

---

[3] IRAF is distributed by the National Optical Astronomy Observatories, which are operated by the Association of Universities for Research in Astronomy, Inc., under cooperative agreement with the national Science Foundation.

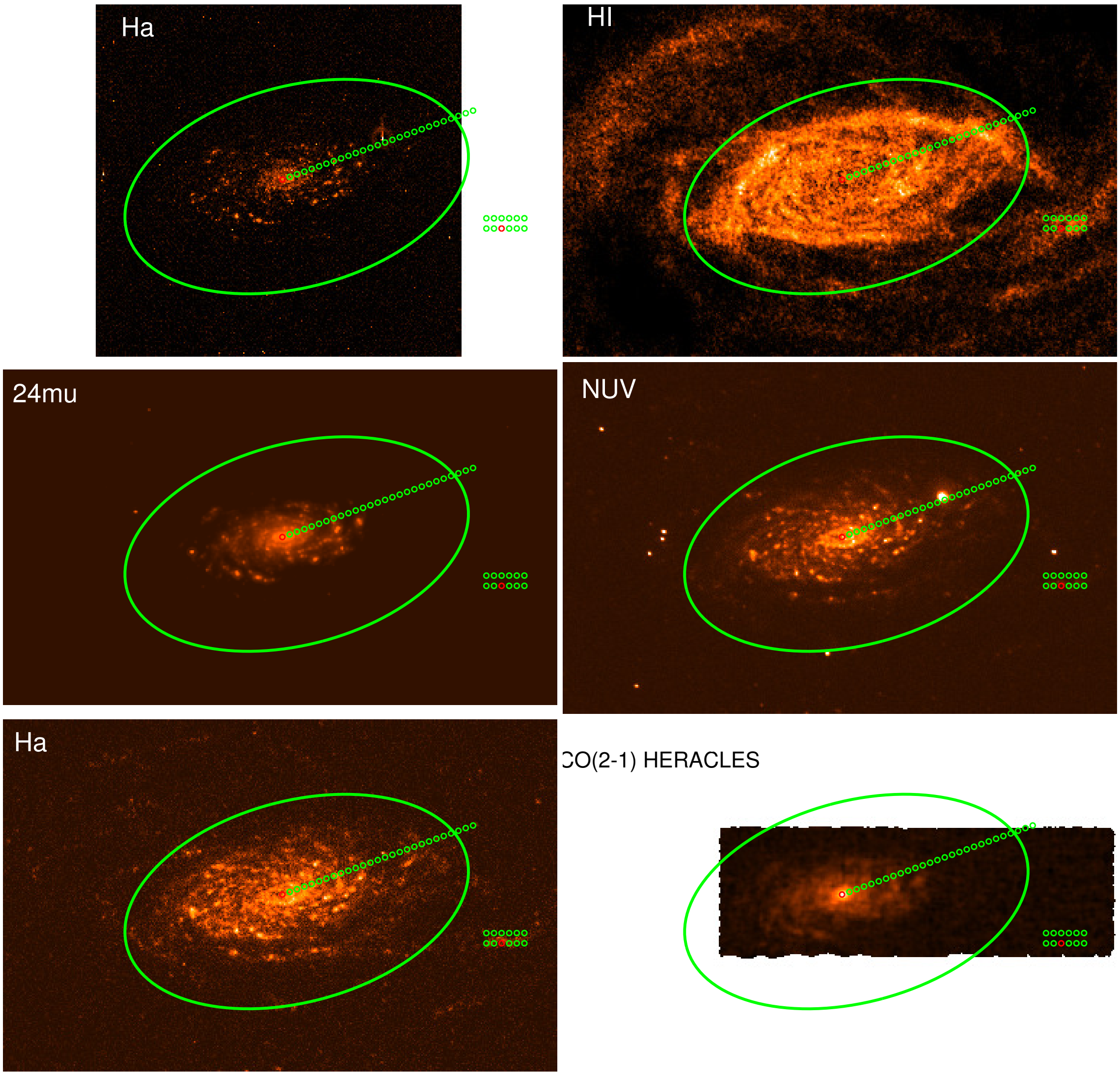

Figure 2.5: Maps of complemetary data for M63, taken from the literature (Table 2.3). The r_{25} or optical limit is drawn as a green ellipse, as well as the 27 single pointings of our observations along the radial axis of the galaxy, and the 12 pointings for the UV region (in the same way as in Figure 2.2).

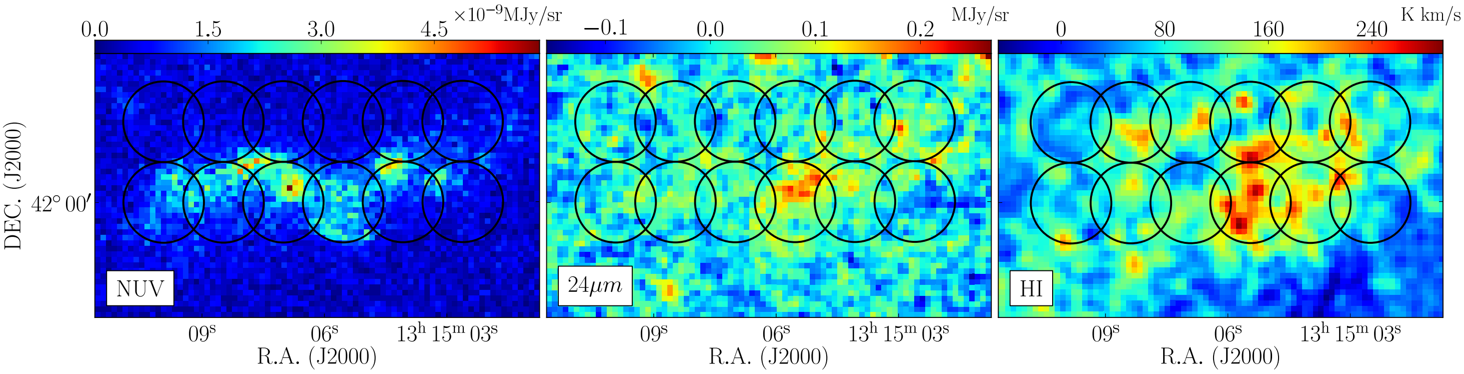

Figure 2.6: Multiwavelength views of the bright UV region at $r_{\rm gal} = 1.36\,r_{25}$, showing from left to right the NUV, 24 μm, and H I 21 cm emission in flux units of 10^{-9} MJy sr^{-1}, MJy sr^{-1}, and K km s^{-1}, respectively, as indicated by the color bars. The circles of 22″ diameter refer to the positions of the 12 pointings used to map the CO(1–0) emission. The Hα emission is undetected in this external region of the M63 galaxy.

measured away from the galaxy. The photometric measurements were performed inside 22″ width apertures (same as our CO(1–0) data FWHM) at the 27 positions of the radial cut along the M63 major axis used for the CO radial mapping, as well as at the 12 positions used to map CO in the external bright UV region, following the same spacing and pointings exactly as in our observations . These photometric results are presented in Table 2.4 for the pointings a long the radial axis, and in Table 2.5 for the UV region, including our CO(1–0) observations and the complementary data described in Table 2.3.

Using the results of Tables 2.4 and 2.5, we created radial profiles for the CO(1–0), CO(2–1), FUV, NUV, H I, Hα, and 24 μm emission, including both, the radial axis and the UV region. This is presented in Fig. 2.8 (connected data points), where the measured fluxes are plotted in a normalized flux scale in order to allow relative comparisons. The dashed vertical line represents the r_{25} limit. All the profiles nicely follow the spiral structure observed at galactocentric radii $r_{\rm gal} \simeq 130$, 200, and probably 260″. They all show a severe drop with the galactocentric radius, except the profile of the atomic gas which has a completely different behaviour. We observe that close to the r_{25} limit the star formation tracers and CO begin to considerably vanish and, beyond the r_{25} limit, they all are practically absent with the exception of the faint XUV emission. The H I emission is very strong beyond the r_{25} limit. This shows the importance of looking for molecular gas beyond the optical limit, where evidence of star formation is clearly brought by the UV emission.

While the CO emission is not detected beyond the r_{25} limit in the M63 major axis map, it is again detected in the external UV region at $r_{\rm gal} = 1.36\,r_{25}$. The corresponding CO(1–0) fluxes, multiplied by a factor of 40 to make them visible (this shows the deepness of our data), with H I and other star formation tracer fluxes as measured in the UV region are also shown in Fig. 2.8 (dashed box). The FUV and NUV emissions are observed in all pointings over the external UV region, while the Hα emission is undetected and a faint 24 μm emission, whose fluxes are multiplied by a factor of 200 to make them visible, is observed in only 8 pointings

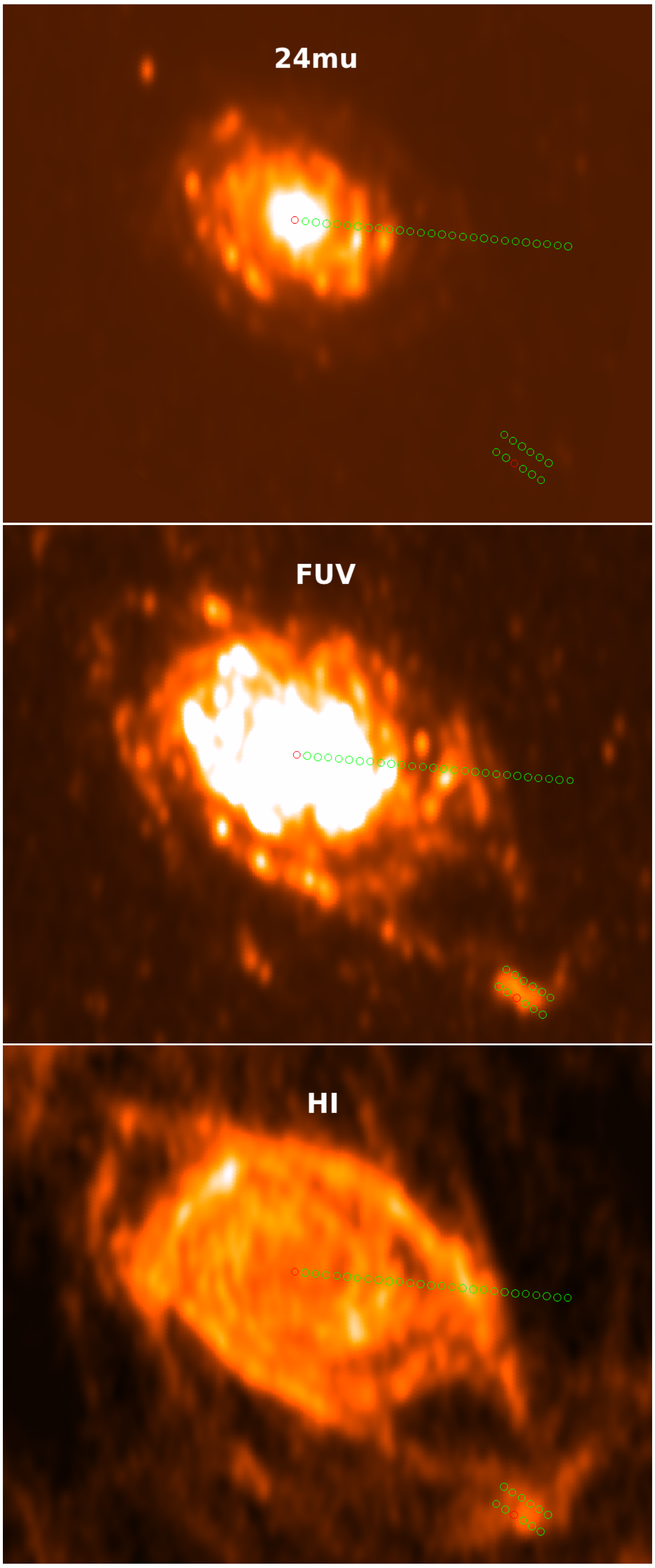

Figure 2.7: Convolved, rotated and deprojected images of M63 corresponding to the 24μm, FUV and HI emission. Our observing CO pointings are overlaid in the same way as in Figure 2.2.

Table 2.4. Photometry results obtained for the complementary data of M63 in its radial cut.

	r_{gal} [arcsec]	r_{gal} [kpc]	CO(1–0) † [K km/s]	CO(2–1) ‡ [K km/s]	FUV [MJy/sr]	NUV [MJy/sr]	HI [K km/s]	Hα [erg/sec]	24μm [MJy/sr]	Σ_{SFR} (FUV) [$M_\odot$ yr^{-1} kpc^{-2}]	Σ_{SFR} (24μm) [$M_\odot$ yr^{-1} kpc^{-2}]	Σ_{HI} [$M_\odot$ pc^{-2}]	Σ_{H_2} [$M_\odot$ pc^{-2}]
1	0	0.0	49.8	79.3	2.8E-08	3.6E-08	230.5	2.2E-10	33.5	2.3E-09	1.07E-01	4.6	125.7
2	22	1.1	24.5	46.0	3.7E-08	4.3E-08	267.5	2.2E-10	28.6	3.0E-09	9.2E-02	5.3	61.8
3	44	2.2	16.4	42.1	3.6E-08	3.6E-08	255.4	1.6E-10	18.8	2.9E-09	6.0E-02	5.1	41.4
4	66	3.2	9.8	16.6	2.6E-08	2.5E-08	247.9	1.1E-10	12.9	2.2E-09	4.1E-02	5.0	24.7
5	88	4.3	6.3	15.7	1.6E-08	1.4E-08	183.9	3.7E-11	6.7	1.3E-09	2.1E-02	3.7	15.9
6	110	5.4	12.6	10.9	1.0E-08	9.0E-09	249.7	2.9E-11	5.7	8.4E-10	1.8E-02	5.0	31.8
7	132	6.5	5.1	11.9	1.6E-08	1.1E-08	343.8	6.1E-11	8.9	1.3E-09	2.9E-02	6.9	12.9
8	154	7.5	5.3	11.1	1.1E-08	8.3E-09	288.8	2.4E-11	4.0	9.3E-10	1.3E-02	5.8	13.4
9	176	8.6	5.4	8.9	8.4E-09	5.5E-09	313.1	2.8E-11	3.6	6.8E-10	1.2E-02	6.3	13.6
10	198	9.7	1.8	9.5	1.2E-08	6.6E-09	358.9	2.9E-11	4.2	9.4E-10	1.3E-02	7.2	4.5
11	220	10.8	1.0	4.6	4.2E-09	3.7E-09	261.3	7.3E-12	1.4	3.4E-10	4.5E-03	5.2	2.5
12	242	11.9	0.3	0.7	1.8E-09	4.5E-09	177.8	2.3E-11	0.6	1.5E-10	1.8E-03	3.6	0.8
13	264	12.9	0.5	0.2	1.6E-09	5.9E-09	153.2	2.0E-11	0.3	1.3E-10	1.1E-03	3.1	1.1
14	286	14.0	0.9	0.6	2.0E-09	3.4E-09	179.4	7.7E-12	0.2	1.7E-10	7.2E-04	3.6	2.2
15	308	15.1	0.8	0.9	5.2E-09	3.0E-09	220.3	8.6E-12	0.3	4.3E-10	1.1E-03	4.4	2.0
16	330	16.2	0.9	1.4	4.9E-09	2.7E-09	283.6	4.1E-12	0.3	4.0E-10	1.0E-03	5.7	2.2
17	352	17.2	0.2	0.7	2.7E-09	1.8E-09	433.2	2.3E-12	0.4	2.2E-10	1.2E-03	8.7	0.6
18	374	18.3	0.0	0.4	1.9E-09	1.1E-09	423.8	3.1E-12	0.3	1.6E-10	8.6E-04	8.5	0.0
19	396	19.4	0.0	0.6	1.1E-09	6.1E-10	312.5	7.1E-13	0.1	9.1E-11	2.4E-04	6.3	0.0
20	418	20.5	0.0	0.5	1.1E-09	5.6E-10	191.9	2.5E-12	0.0	8.6E-11	5.1E-05	3.8	0.0
21	440	21.5	0.0	0.0	5.9E-10	3.4E-10	67.8	4.4E-12	0.0	4.7E-11	0.0	1.4	0.0
22	462	22.6	0.0	0.0	9.0E-11	5.0E-11	5.9	···	0.0	7.3E-12	0.0	0.1	0.0
23	484	23.7	0.0	0.0	1.4E-10	-4.2E-12	0.0	···	0.0	1.1E-11	0.0	0.0	0.0
24	506	24.8	0.0	0.0	1.4E-10	2.8E-11	0.0	···	0.0	1.1E-11	0.0	0.0	0.0
25	528	25.9	0.0	0.0	0.0	-1.3E-11	0.0	···	0.0	0.0	0.0	0.0	0.0
26	550	26.9	0.0	0.0	2.3E-11	-6.1E-11	0.0	···	0.0	1.9E-12	0.0	0.0	0.0
27	572	28.0	0.0	0.0	4.0E-11	-7.5E-11	0.0	···	0.0	3.3E-12	0.0	0.0	0.0

Note. — † CO(1–0) data from this work. ‡CO(2–1) data from HERACLES (Leroy et al. 2009). The Hα map from (Kennicutt et al. 2008) does not fully cover the mapping along the radial axis (see Figure 2.5).

Table 2.5. Photometry results obtained for the complementary data of M63 in its UV region.

	offsets		CO(1–0) †	CO(2–1) ‡	FUV	NUV	HI	Hα	24μm	$\Sigma_{\rm SFR}$ (FUV)	$\Sigma_{\rm SFR}$ (24μm)	$\Sigma_{\rm HI}$	$\Sigma_{\rm H_2}$
	[arcsec]	[arcsec]	[K km/s]	[K km/s]	[MJy/sr]	[MJy/sr]	[K km/s]	[erg/sec]	[MJy/sr]	[M$_\odot$ yr^{-1} kpc^{-2}]	[M$_\odot$ yr^{-1} kpc^{-2}]	[M$_\odot$ pc^{-2}]	[M$_\odot$ pc^{-2}]
1	0	22	<0.15	0	2.14E-09	7.40E-10	170.0	···	0.011	1.74E-10	3.56E-05	3.40	<0.38
2	0	0	<0.12	0	3.60E-09	1.76E-09	180.4	···	0.030	2.91E-10	9.57E-05	3.61	<0.30
3	-22	0	0.21	0	3.57E-09	1.76E-09	237.8	···	0.069	2.89E-10	2.20E-04	4.76	0.53
4	-22	22	<0.12	0	2.21E-09	7.16E-10	198.5	···	0.039	1.79E-10	1.25E-04	3.97	<0.30
5	22	0	<0.15	0	3.30E-09	1.59E-09	143.2	···	0.003	2.67E-10	1.07E-05	2.86	<0.38
6	-44	22	<0.12	0	2.00E-09	8.64E-10	179.2	···	0.041	1.62E-10	1.33E-04	3.59	<0.30
7	22	22	<0.15	0	2.63E-09	8.04E-10	153.1	···	0.000	2.13E-10	0.00	3.06	<0.38
8	44	0	<0.21	0	2.54E-09	1.21E-09	113.7	···	0.000	2.06E-10	0.00	2.27	<0.53
9	44	22	<0.21	0	1.75E-09	4.58E-10	111.5	···	0.000	1.42E-10	0.00	2.23	<0.53
10	-44	0	<0.12	0	1.90E-09	8.88E-10	180.3	···	0.018	1.54E-10	5.84E-05	3.61	<0.30
11	-66	22	0.14	0	1.21E-09	6.44E-10	123.4	···	0.020	9.77E-11	6.34E-05	2.47	0.35
12	-66	0	<0.15	0	7.22E-10	2.18E-10	88.8	···	0.000	5.84E-11	0.00	1.78	<0.38

Note. — † CO(1–0) data from this work. ‡CO(2–1) data from HERACLES (Leroy et al. 2009). Offsets are relative to position number 2, marked as a red circle in the UV region in each panel of Figure 2.5. The Hα map from (Kennicutt et al. 2008) does not cover the UV region (see Figure 2.5).

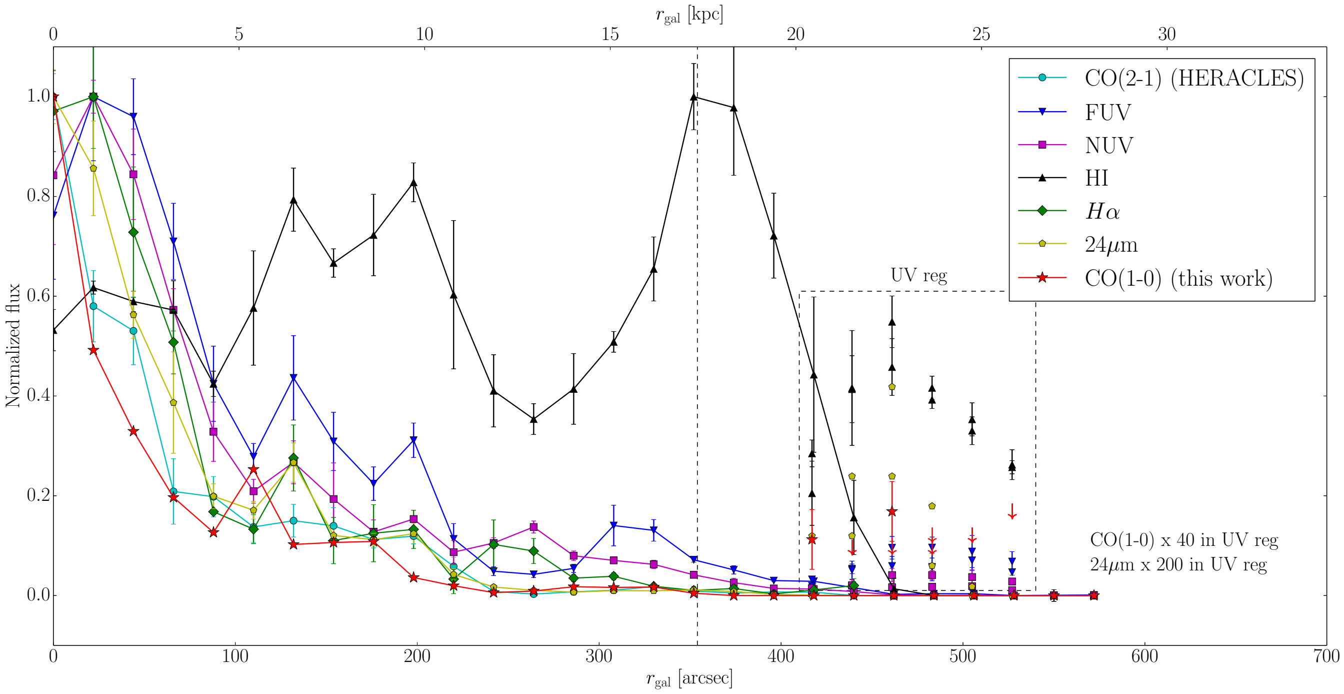

Figure 2.8: Radial profiles of FUV, NUV, Hα, 24 μm, different star formation tracers, and H I taken from the literature (see Table 2.3), as measured along the major axis of the M63 disk, and which we compare to our CO(1–0) radial profile (red stars) and to the CO(2–1) radial profile from the HERACLES survey (Leroy et al. 2009). The measured fluxes are plotted in a normalized flux scale in order to allow relative comparisons. All the star formation tracers nicely follow the spiral arm structure at $r_{\rm gal} \simeq 130$, 200, and probably 260″. We observe a severe drop with the galactocentric radius for all star formation tracers, as well as for CO, such that close to the r_{25} limit (dashed line) and beyond all tracers and CO are practically absent with the exception of XUV and H I. The CO emission is again detected in the external bright UV region. The measurements obtained in this UV region are shown in the dashed box at the correct galactocentric radii. We multiply the CO(1–0) fluxes by a factor of 40 to make them visible. The double data points plotted at each $r_{\rm gal}$ correspond to the parallel pointings used to map the UV region (see Table 2.2). This external UV region has relatively high FUV and NUV emissions and is dominated by H I.

(see also Fig. 2.6). It is interesting to point out that the FUV and NUV fluxes in the external UV region are similar to those at the pointing at r_{25}, the galactocentric limit where CO is still detected along the M63 major axis. Beyond r_{25} the FUV and NUV fluxes decrease and get weaker than in the external UV region. This suggests a tight correlation between the XUV flux, namely the intensity of star formation, and the CO flux which should trace the amount of molecular gas, since the CO emission starts to be detected at a given XUV flux level. If correct, the CO emission is not detected beyond r_{25} along the major axis mapping, because the amount of CO, corresponding to the molecular gas needed to sustain the star formation which is taking place there, falls below our detection threshold. Consequently, it is likely that molecular gas is present in the outer regions of the M63 disk, at least as long as the XUV emission is present.

The considerably larger amount of H I observed in the external UV region relative to CO leads to speculate that H I is more likely a precursor of H_2 rather than a product of photo-dissociation due to UV radiation. However, the situation might be more complicated in reality. The main complication we may invoke is the reliability of CO as a proxy of H_2. As previously discussed, and also shown in Fig. 2.8, the absence of a clear CO(2–1) line detection beyond $r_{\mathrm{gal}} = 0.68\,r_{25}$ may betray a decrease in the excitation temperature with the galactocentric radius. If this is the case, it may be that even if substantial H_2 is present in the outer regions of the M63 disk, the CO lines may be quite weak, hence remain undetected.

Star formation rate, efficiency, and Kennicutt-Schmidt relation

Our acquired CO measurements offer the opportunity to analyse the Kennicutt-Schmidt relations across the optical disk of the M63 galaxy, and, in particular, close to and beyond the isophotal radius, r_{25}. This exercise especially is of interest in the bright UV region located in the outer disk of M63 at the galactocentric radius $r_{\mathrm{gal}} = 1.36\,r_{25}$, whose stellar emission is solely dominated by the UV emission, so where the star formation rate (SFR) metallicity, excitation, and gas density are potentially lower. For this purpose, we use the photometric measurements obtained for the FUV, 24 μm, and H I data. At each pointing defined for the CO radial mapping and the CO mapping of the bright UV region, we compute the star formation rate surface density, Σ_{SFR}, the atomic gas surface density, $\Sigma_{\mathrm{H\,I}}$, and the molecular gas surface density, $\Sigma_{\mathrm{H_2}}$.

The SFR surface density is determined using the calibration from Leroy et al. (2008):

$$\Sigma_{\mathrm{SFR}}(\mathrm{M_\odot\ yr^{-1}\ kpc^{-2}}) = 8.1 \times 10^{-2} F_{\mathrm{FUV}}(\mathrm{MJy\ sr^{-1}}) + 3.2 \times 10^{-3} F_{24\mu\mathrm{m}}(\mathrm{MJy\ sr^{-1}}) \tag{2.1}$$

which includes the FUV flux to measure the unobscured and recent star formation through the emission of O and B stars, and the 24 μm flux that traces the obscured FUV emission that is re-emitted in the FIR by dust grains.

The atomic gas surface density is measured with the calibration of Bigiel et al. (2010):

$$\Sigma_{\mathrm{H\,I}}(\mathrm{M_\odot\ pc^{-2}}) = 0.020 F_{\mathrm{H\,I}}(\mathrm{K\ km\ s^{-1}}) \tag{2.2}$$

which includes a factor of 1.36 to reflect the presence of helium.

Finally, the molecular gas surface density (see Tables 2.1 and 2.2) is calculated with our integrated CO(1–0) line fluxes using the calibration of Leroy et al. (2008):

$$\Sigma_{\mathrm{H_2}}(\mathrm{M_\odot\ pc^{-2}}) = 4.4\cos(i) F_{\mathrm{CO(1-0)}}(\mathrm{K\ km\ s^{-1}}) \tag{2.3}$$

where the "standard" Galactic CO-to-H_2 conversion factor, $X_{\mathrm{CO}} = 2 \times 10^{20}$ cm^{-2} (K km s^{-1})$^{-1}$ (Dickman et al. 1986), as well as the factor of 1.36 to account for helium are adopted. The inclination correction by an angle $i = 55°$ is taken into account. This correction is also considered in the computation of the SFR and atomic gas surface densities when deprojecting the FUV, 24 μm, and H I images (Figure 2.7).

In Fig. 2.9, we plot the radial profiles of the star formation efficiency (SFE) and the H_2-to-H I surface density ratio. The SFE is the star formation rate (SFR) per unit of molecular gas, or the inverse of the gas depletion timescale, i.e. the time required for present-day star formation to consume the gas reservoir. It is calculated here as SFE $= \Sigma_{\mathrm{SFR}}/\Sigma_{\mathrm{H_2}}$. The various surface densities are computed using Eqs. (2.1) to (2.3). The blue squares correspond to the pointings done to map CO along the M63 major axis (the radial cut), and the red circles to those done to map CO over the bright UV region in the outer disk of M63.

In the radial cut we consider only the pointings up to the isophotal radius, r_{25}, where we obtained convincing CO detections (17 pointings), and in the UV region we retain pointings with 24 μm detections only (8 pointings) in order to have an accurate estimation of the Σ_{SFR}. We observe that the SFE, as measured over the radial cut of M63, is roughly constant as a function of the galactocentric radius out to the r_{25} limit. This is in line with the findings by Leroy et al. (2008) which we now extend out to the isophotal radius. Beyond r_{25}, the two SFE detections tend to show a drop of the SFE in the bright UV region, but upper limits in the other data points prevent us from drawing definitive conclusions. The H_2-to-H I surface density ratio shows a smooth decrease with the galactocentric radius, such that the inner regions of the M63 disk are H_2-dominated, while the regions at $r_{\mathrm{gal}} > 0.5\, r_{25}$ end up to be H I-dominated. This transition between a "mostly-H_2" and a "mostly-H I" interstellar medium (ISM) is found to be a well-defined function of local conditions according to Leroy et al. (2008), occurring at characteristic galactocentric radius, stellar and gas surface densities, hydrostatic gas pressure, and orbital timescale. At the r_{25} limit, we observe a further and more severe drop of the H_2-to-HI surface density ratio. Nevertheless, the behaviour of the radial profiles of the SFE and the H_2-to-H I surface density ratio may well be inverted, if the trend toward an increasing CO-to-H_2 conversion factor with the galactocentric radius, as shown by Sandstrom et al. 2013 (see their Fig. 7) for M63 over the radial cut out to $r_{\mathrm{gal}} \sim 0.7\, r_{25}$, is confirmed.

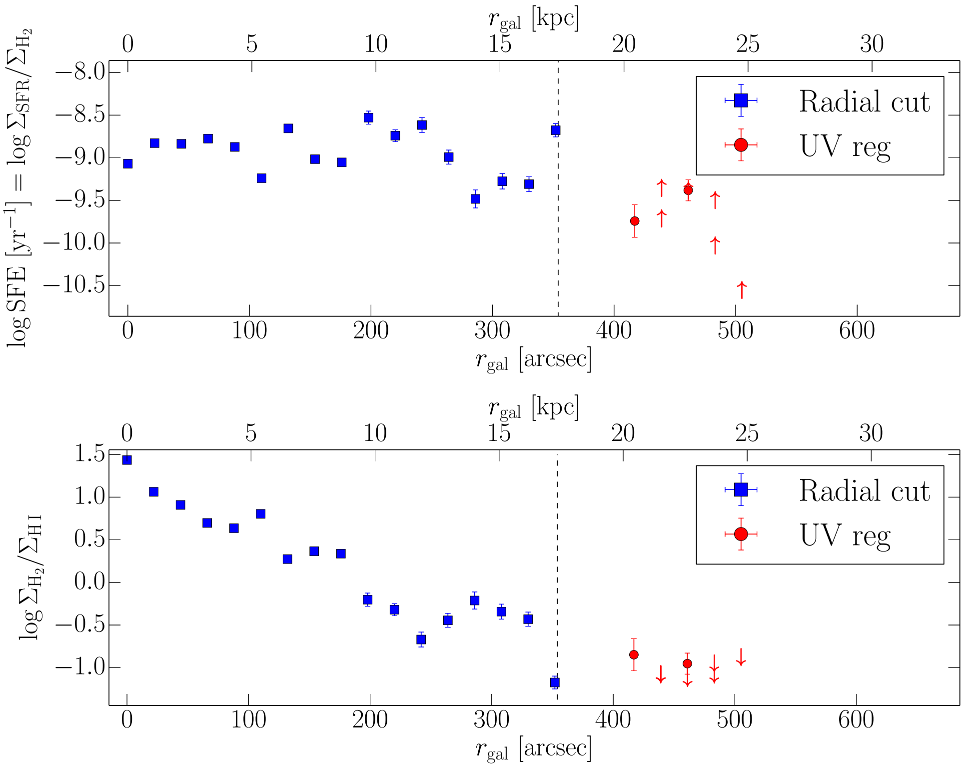

Figure 2.9: Radial profiles of the star formation efficiency (upper panel) and the H$_2$-to-H I surface density ratio (bottom panel). The SFE is defined here as the star formation rate per unit of molecular gas. The blue squares correspond to the 17 pointings done to map CO along the M63 major axis (the radial cut) out to the isophotal radius, r_{25} (dashed line), and the red circles correspond to the 8 pointings with 24 μm emission detection done to map CO over the bright UV region at $r_{\rm gal} = 1.36\, r_{25}$. The double data points plotted for the UV region at each $r_{\rm gal}$ correspond to the parallel pointings used to map this region (see Table 2.2).

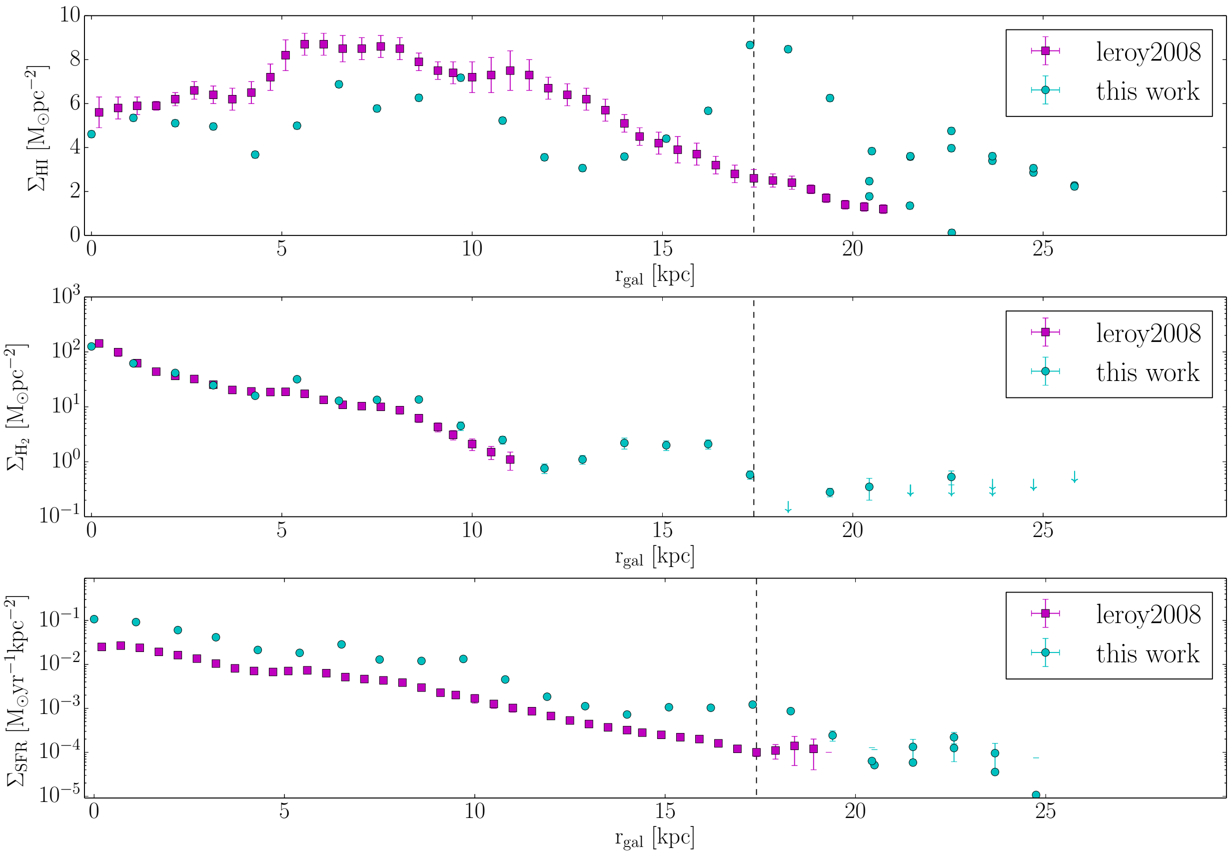

Figure 2.10: Comparison of Σ_{SFR}, Σ_{HI} and Σ_{H_2} between this work and Leroy et al. (2008), as a function of the galactocentric radius. Data points of this work correspond to each one of the pointings used to maps the major axis of M63, and its UV region, whereas Leroy's points correspond to azimuthal averages over the entire disk.

Now, concerning the Σ_{SFR}, Σ_{HI} and Σ_{H_2}, we can question how these surface densities determined over single pointings along the radial major axis cut are representative of surface densities that Leroy et al. (2008) obtained by performing azimuthal averages over the entire disk of M63. Such comparison is presented in Figure 2.10

The comparison of the respective molecular gas surface densities as a function of the galactocentric radius is excellent. The SFR surface densities for the radial cut show an offset toward higher values, but the respective Σ_{SFR} radial profiles are the same. Only the atomic gas surface density measurements seem to severely diverge between the radial cut and the azimuthal averages. This difference comes from the fact that the radial cut along the major axis crosses a spiral arm like structure, which is very bright in H I and covers an H I emission peak in the outer parts of the radial profile (see Figure 2.11). This certainly also explains the higher Σ_{SFR} we observe for the radial cut, where the star formation activity is slightly enhanced.

Finally, we compare the star formation rate surface densities with the atomic and molecular gas surface densities, separately, in Kennicutt-Schmidt plots, in the two top panels of Fig. 2.12. The blue squares correspond to the pointings done to map CO along the M63 major axis, and the red circles to those done to map CO over the

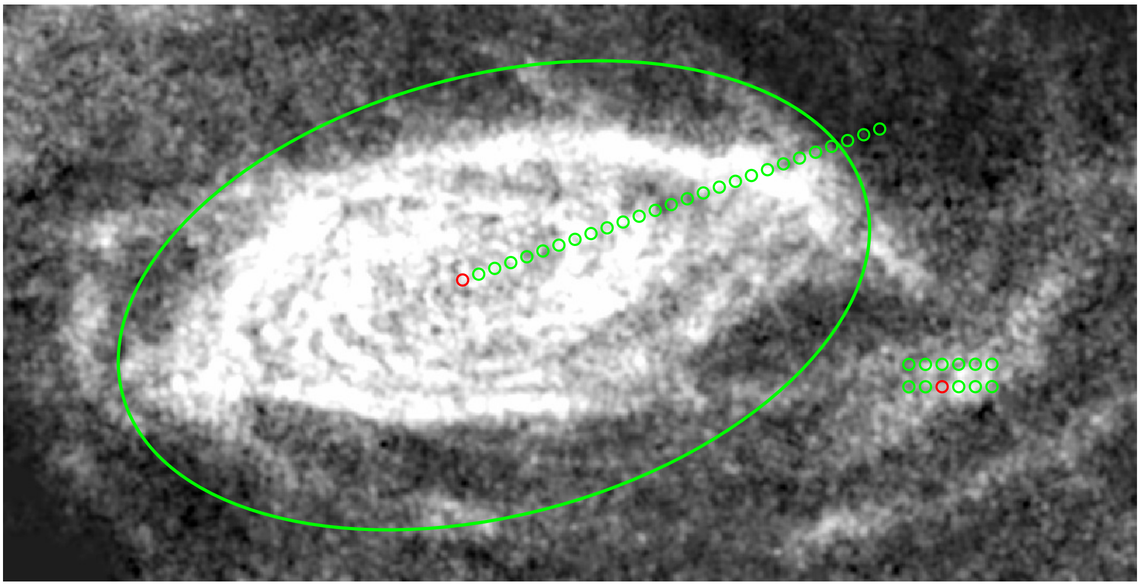

Figure 2.11: HI map of M63 from Walter et al. (2008), with the observing CO pointings overlaid. The radial cut along the major axis crosses a spiral arm like structure, very bright in HI.

bright UV region in the outer disk of M63 (similarly to Fig. 2.9). The two plots show that the gas surface density of M63 in its radial cut is dominated by the molecular gas, whereas the bright UV region is strongly dominated by the atomic gas, as also observed in Fig. 2.9 (bottom panel). Interestingly, the H I surface density of the UV region is very similar to the one observed along the radial cut, on the contrary to its molecular gas surface density which is significantly lower. Finally, in the bottom panel of Fig. 2.12 we show the star formation rate surface density as a function of the total gas surface density, $\Sigma_{\mathrm{H\,I+H_2}}$, namely the sum of both $\Sigma_{\mathrm{H\,I}}$ and $\Sigma_{\mathrm{H_2}}$.

To characterize the star formation in M63, we use the Kennicutt-Schmidt (K-S) relation that relates the SFR surface density to the gas surface density. In all plots of Fig. 2.12, we fit a power-law of the form $\Sigma_{\mathrm{SFR}} = \mathrm{A}(\Sigma_{\mathrm{gas}})^{\mathrm{N}}$, which in a log-space translates into a simple linear relation. The coefficient A traces the absolute star formation efficiency (Kennicutt 1998b), and the slope N relates the star formation rate to the gas density present and tells us how close are the two variables from a linearity. We use the least-square bisector method, suitable for two independent variables (Isobe et al. 1990), for the fit in the log-space and leave log A and N as free parameters. It is important to note that for the fitting procedure only (not the plotting), we re-scaled Σ_{gas} by a factor of 10, such that $\Sigma_{\mathrm{gas}}/10\ \mathrm{M}_\odot\ \mathrm{pc}^{-2}$. We made this rescaling to minimize the covariance of log A and N in the fit[4], and to make our results comparable to those of Bigiel et al. (2008) for M63. In their work they used the same FUV and H I data as we did, but the CO data were taken from the HERACLES CO(2–1) database (Leroy et al. 2009) with a 11″ resolution and a CO(2–1)/CO(1–0) line ratio of 0.8. Our CO(1–0) data reach a much deeper sensitivity than the HERACLES CO(2–1) data, which is essential to properly characterize the K-S relation all over the optical disk and especially beyond the r_{25} limit.

---

[4] This rescaling has no influence on the results of the slope N, only the coefficient A will need to be corrected by the factor of 10.

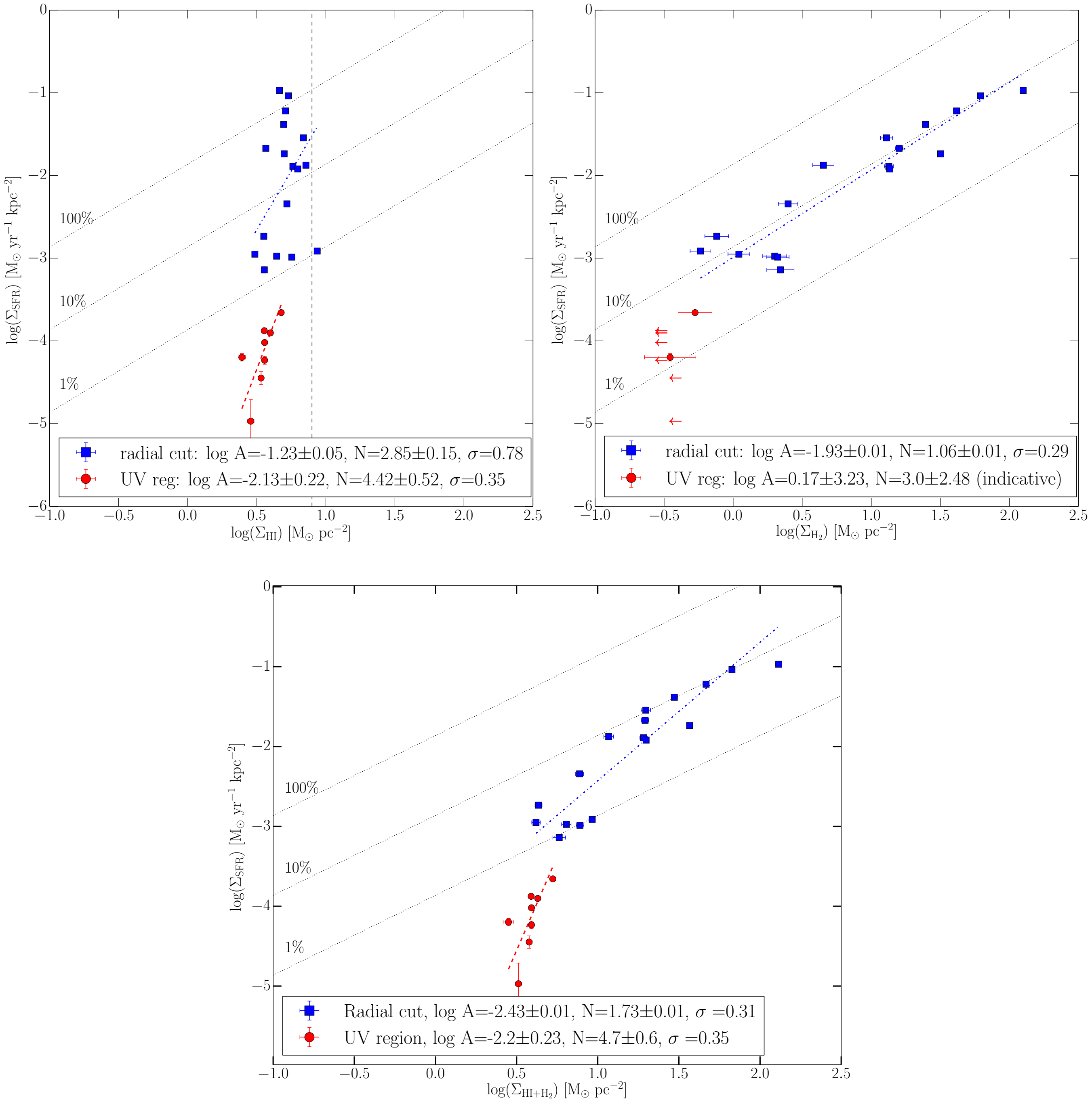

Figure 2.12: Kennicutt-Schmidt relations that relate the SFR surface density to the gas surface density plotted for $\Sigma_{\rm H\,I}$ (top-left panel), $\Sigma_{\rm H_2}$ (top-right panel), and $\Sigma_{\rm H\,I+H_2}$ (bottom panel). The blue squares correspond to the 17 pointings done to map CO along the M63 major axis (the radial cut) out to the isophotal radius, r_{25}, and the red circles correspond to the 8 pointings with 24 μm emission detection done to map CO over the bright UV region at $r_{\rm gal} = 1.36\,r_{25}$. The K-S relation is best parametrized by a power-law of the form $\Sigma_{\rm SFR} = {\rm A}(\Sigma_{\rm gas})^{\rm N}$, which in a log-space translates into a simple linear relation. The best-fitting bisector linear K-S relations are derived separately for the radial cut (blue dashed-dotted lines) and for the UV region (red dashed lines). The corresponding coefficients log A and slopes N can be found in the labels of each panel. The black dotted lines represent “isochrones” of constant star formation efficiencies, indicating the level of $\Sigma_{\rm SFR}$ needed to consume 100%, 10%, and 1% of the total amount of gas within 10^8 years. The vertical dashed line in the top-left panel corresponds to the $\Sigma_{\rm H\,I} \sim 9$ M$_\odot$ pc^{-2} threshold at which the atomic gas saturates (Bigiel et al. 2008).

Table 2.6. Best-fitting bisector linear Kennicutt-Schmidt relations obtained for M63 in log space.

	This work						Bigiel et al. 2008		
	Radial cut out to r_{25}			UV region at $1.36\,r_{25}$			Radial cut out to $0.68\,r_{25}$		
	log A	N	σ	log A	N	σ	log A	N	σ
H_2	-1.93	1.06	0.29	0.17†	3.0†	···	-2.22	0.92	0.10
HI+H_2	-2.43	1.73	0.31	-2.20	4.7	0.35	-2.63	1.58	0.22

Note. — The Kennicutt-Schmidt relations are best parametrized by power-laws of the form $\Sigma_{\rm SFR} = {\rm A}(\Sigma_{\rm gas})^{\rm N}$, which in log space translates into linear relations. † Only indicative log A and N values, since they rely on two data points only, which makes them very uncertain.

The best-fitting bisector linear relations, $\log \Sigma_{\rm SFR} = \log A + N \log \Sigma_{\rm gas}$, obtained independently for the K-S relation all over the radial cut out to r_{25} and the UV region in the outer disk of M63 are shown in Fig. 2.12. The errors we provide on log A and N are $1\,\sigma$ quotes of the nearly Gaussian distributions of log A and N obtained through Monte-Carlo simulations of 5000 data sets created from the original data, with random values generated within their error bars. The scatter (σ) in our fits typically are of the order of 0.3 dex. The corresponding K-S relation results are presented in Table 2.6 for both $\Sigma_{\rm gas} = \Sigma_{\rm H_2}$ and $\Sigma_{\rm gas} = \Sigma_{\rm H\,I+H_2}$, and are compared to the K-S relations found by Bigiel et al. (2008) over the radial cut of the M63 disk out to $r_{\rm gal} = 0.68\,r_{25}$ only. The respective K-S relations obtained over the radial cut have very comparable slopes N$\sim$ 1.0 for $\Sigma_{\rm H_2}$ and N$\sim$ 1.65 for $\Sigma_{\rm H\,I+H_2}$, with our slopes being systematically slighly steeper. They also have comparable coefficients $\log {\rm A} \sim -2.0$ for $\Sigma_{\rm H_2}$ and $\log A \sim -2.5$ for $\Sigma_{\rm H\,I+H_2}$, with our coefficients being systematically higher by about $0.2 - 0.3$ dex, but still within the fit scatter. The one-to-one linearity of the K-S relation, between the SFR surface density and the molecular gas surface density is really solid, meaning that the gas is being consumed at a nearly constant rate, as expected for $\Sigma_{\rm H_2}$.

On the other hand, when comparing these results to the K-S relations of the UV region in the outer disk of M63, at the galactocentric radius $r_{\rm gal} = 1.36\,r_{25}$, we note that they are significantly different. The slope N = 4.7 of the K-S relation for $\Sigma_{\rm H\,I+H_2}$ is considerably steeper in the external UV region. A similar trend is observed for $\Sigma_{\rm H_2}$. It is true that it relies on two data points, but if we trust our $3\,\sigma$ upper limits on $\Sigma_{\rm H_2}$, we can hardly expect to reconcile these external UV region measurements with the K-S relation observed over the radial cut, more especially as the derived star formation rate surface densities are very reliable. It is very likely that the CO-to-H_2 conversion factor adopted over the external UV region is underestimated, given the low metallicity expected in the outskirts of M63, as supported by the metallicity gradient inferred in M63, and the observed trend for an increase in $X_{\rm CO}$ with decreasing metallicity (Sandstrom et al. 2013, Bolatto et al. 2013). While this may induce a shift of the external UV region data points towards larger gas surface densities, the slope of the K-S relation will remain unchanged, unless there is a significant $X_{\rm CO}$ gradient over the external UV region. As a result, a broken K-S power-law between the inner and outer regions of the M63 disk seems to robustly emerge. It suggests that the regime of star formation drastically changes beyond the isophotal radius, r_{25}. Indeed, the slopes observed for the K-S relations in the external UV region show a non-linear SFR regime, in clear contrast with the quasi-linear SFR regime in the inner regions of the disk. What triggers the "quenching" of the star formation in the outer regions of the M63 disk and, consequently, the severe deviation from the commonly accepted SF relation as traced by the K-S relation observed along the radial cut of M63? We can invoke the flaring of the outer gas layers or, more speculative, the possible presence of high turbulence providing support against gravitational collapse as suggested by Longmore et al. (2013).

To better appreciate the change in the star formation regime between the inner and outer regions of the M63 disk, in Fig. 2.12 we also plot "isochrones" of constant star formation efficiencies, indicating the levels of $\Sigma_{\rm SFR}$ needed to consume 100%, 10%, and 1% of the total amount of gas (corrected by a factor of 1.36 to account for helium) within 10^8 years. These isochrones can also be interpreted as constant gas depletion timescales (i.e., the time needed to consume the total amount of gas) of 10^8, 10^9, and 10^{10} years from top to bottom. We can see that when the total gas is considered (H I + H_2), for the radial cut of M63 the SFE settles the gas consumption within 10^8 years to 1 to 10%, whereas the external UV region has a much lower SFE with less than 1% of the gas being converted into stars within 10^8 years. The drop of the star formation efficiency beyond the isophotal radius, r_{25}, can also be appreciated in Fig. 2.9 (upper panel). The SFE could even be lower in the external UV region, as the CO-to-H_2 conversion factor may, in reality, be up to 100 times larger (in the extreme case) than the "Galactic" value (Bolatto et al. 2013), and so are the computed $\Sigma_{\rm H_2}$ values, depending on the metallicity of the external UV region which may well be as low as $10 - 20\%$ of the local Galactic ISM[5]. Consequently, the star formation still occurs in the outer regions of the M63 disk, but at a very low efficiency, significantly lower than in the inner regions of the disk.

2.1.4 Summary and conclusions

Deep CO(1–0) and CO(2–1) observations obtained on the IRAM 30 m telescope of the M63 spiral galaxy characterized by a large XUV disk extending out to 2.5 times the optical equivalent radius are presented. We performed both a CO mapping along the major axis of the M63 disk from the center out to the galactocentric radius $r_{\rm gal} = 572'' = 1.6\, r_{25}$ and over a bright UV region in the outer disk of M63 at the galactocentric radius $r_{\rm gal} = 1.36\, r_{25}$. Our objective was to search for CO emission and hence for molecular gas in the outer regions of the M63 disk beyond the optical radius, where evidence of star formation is brought by both the XUV emission and high H I column densities observed in these regions. We highlight the importance of a CO detection in regions far away from the center of the galaxy, where the metallicity, excitation, and gas density are supposed to be lower, and stars have

---

[5] When extrapolating the metallicity gradient determined for M63, we get a metallicity of 20% of the local Galactic ISM at $r_{\rm gal} = 1.36\, r_{25}$, the galactocentric radius of the bright UV region.

more difficulty to form. To complement our CO observations, we used FUV, NUV, Hα, 24 μm, and H I data from the literature. This allowed us to investigate the Kennicutt-Schmidt relation across the galaxy and beyond the isophotal radius, r_{25}, in the bright UV region. Our main results are as follows:

The CO(1–0) emission is clearly detected along the major axis of the M63 disk out to the isophotal radius, r_{25}, but not beyond. However, the CO(1–0) is again detected in the bright UV region in the outer disk of M63 at $r_{\rm gal} = 1.36\, r_{25}$. This is the fourth molecular gas detection in the outskirts of nearby spiral galaxies. The CO(2–1) emission is, on the other hand, confined to $r_{\rm gal} = 0.68\, r_{25}$, and thus suggests subthermal excitation in the outer regions of the M63 disk.

The radial profiles of the CO emission and other star formation tracers (Fig. 2.8) show a severe drop with the galactocentric radius, on the contrary of the atomic gas. Close to the r_{25} limit, CO and the star formation tracers begin to considerably vanish and, beyond r_{25}, they all are practically absent with the exception of the faint UV emission and H I. The UV region at $r_{\rm gal} = 1.36\, r_{25}$, in which the CO emission is detected, is characterized by FUV and NUV emission fluxes similar to the fluxes observed at r_{25}, but stronger than the fluxes observed at $r_{\rm gal} > r_{25}$ along the M63 major axis. This likely reflects a tight correlation between the CO and UV fluxes, namely between the intensity of star formation and the amount of molecular gas, and hence strongly suggests that the absence of CO detection at $r_{\rm gal} > r_{25}$, where the XUV is weaker, is simply the result of the still too high CO detection threshold.

The external UV region is characterized by a very high H I flux with respect to the measured CO flux. This leads us to speculate that H I is more likely the precursor of H_2 rather than the product of UV photo-dissociation, since it seems to dominate in quantity. This is, however, true as long as substantial H_2 is not hidden in the outer disk regions of M63, which may be the case as we observe hints for an excitation temperature decrease with the galactocentric radius, which may lead to very weak CO lines.

With the integrated CO line flux measurements and the complementary data from the literature, we derive SFR, H I, and H_2 surface densities all along the major axis of the M63 disk and in the external UV region. We observe that the gas surface density along the radial cut is dominated by the molecular gas, whereas the UV region is dominated by the atomic gas. The best-fit Kennicutt-Schmidt relations, $\log \Sigma_{\rm SFR} = \log {\rm A} + {\rm N} \log \Sigma_{\rm gas}$, show a broken power-law from the inner to the outer regions of the M63 disk (Fig. 2.12). Indeed, the almost linear K-S relation (with a slope of nearly 1 in log space) observed over the radial cut, in the inner regions of the disk characterized by high gas densities, cannot be extrapolated to the outer disk regions. The later are characterized by a non-linear SFR regime (with a K-S slope much higher than 1 in log space), perhaps owing to the flaring of the outer gas layers. This is the first time that the K-S relation is quantified in the outskirts of a spiral galaxy, i.e, in low gas density environments. At a molecular gas surface density as low as $\Sigma_{\rm H_2} = 0.35$ M$_\odot$ pc^{-2}, well below all the determined H_2 surface densities referenced in spiral galaxies so far (Bigiel et al. 2008, 2011), star formation still occurs spontaneously.

The change in the star formation regime between the inner and outer regions of the M63 disk can also be appreciated by the difference in star formation efficiencies. Indeed, along the major axis of the disk out to the isophotal radius the SFE settles the gas consumption within 10^8 years to 1% to 10%, whereas in the UV region much less than 1% of the gas is converted into stars within 10^8 years. Consequently, star formation still occurs in the outer regions of the disk, but at a very low efficiency.

2.1.5 Publication

This entire work done on M63 was submitted to A& A in December 2013, and accepted for its publication in April 2014. The final publication is presented here.

A&A 566, A147 (2014)
DOI: 10.1051/0004-6361/201323330
© ESO 2014

Astronomy & Astrophysics

CO map and steep Kennicutt-Schmidt relation in the extended UV disk of M 63[⋆]

M. Dessauges-Zavadsky[1], C. Verdugo[2], F. Combes[2], and D. Pfenniger[1]

[1] Observatoire de Genève, Université de Genève, 51, Ch. des Maillettes, 1290 Sauverny, Switzerland
e-mail: `[miroslava.dessauges;daniel.pfenniger]@unige.ch`
[2] Observatoire de Paris, LERMA, 61 Av. de l'Observatoire, 75014 Paris, France
e-mail: `[celia.verdugo;francoise.combes]@obspm.fr`

Received 23 December 2013 / Accepted 5 April 2014

ABSTRACT

Results from the UV satellite GALEX revealed surprisingly large extensions of disks in some nearby spiral galaxies. While the Hα emission, the usual tracer of star formation, drops down at the border of the isophotal radius, r_{25}, the UV emission extends out to 3 to 4 times this radius and often covers a significant fraction of the H I area. M 63 is a remarkable example of a spiral galaxy with one of the most extended UV disks, so it offers the opportunity to search for the molecular gas and characterize the star formation in outer disk regions as revealed by the UV emission. We obtained deep CO(1–0) and CO(2–1) observations on the IRAM 30 m telescope along the major axis of the M 63 disk from the center out to the galactocentric radius $r_{\rm gal} = 1.6\,r_{25}$ and over a bright UV region at $r_{\rm gal} = 1.36\,r_{25}$. CO(1–0) is detected all along the M 63 major axis out to r_{25}, and CO(2–1) is confined to $r_{\rm gal} = 0.68\,r_{25}$, which may betray lower excitation temperatures in the outer disk. CO(1–0) is also detected in the external bright UV region of M 63. This is the fourth molecular gas detection in the outskirts of nearby spirals. The radial profiles of the CO emission and of the Hα, 24 μm, NUV and FUV star formation tracers and H I taken from the literature show a severe drop with the galactocentric radius, such that beyond r_{25} they are all absent with the exception of a faint UV emission and H I. The CO emission detection in the external UV region, where the UV flux is higher than the UV flux observed beyond r_{25}, highlights a tight correlation between the CO and UV fluxes, namely the amount of molecular gas and the intensity of star formation. This external UV region is dominated by the atomic gas, suggesting that H I is more likely the precursor of H_2 rather than the product of UV photodissociation. A broken power law needs to be invoked to describe the Kennicutt-Schmidt (K-S) relation of M 63 from the center of the galaxy out to $r_{\rm gal} = 1.36\,r_{25}$. While all along the major axis out to r_{25}, the K-S relation is almost linear (with a slope of nearly 1 in log space), in the external UV region the SFR regime is highly nonlinear and characterized by a steep K-S relation (with a slope much higher than 1 in log space) and very low star formation efficiency.

Key words. galaxies: star formation – ultraviolet: galaxies – galaxies: ISM – submillimeter: ISM – galaxies: evolution

1. Introduction

The study of star formation in the outer regions of disks of normal spiral galaxies has gained interest in the past few years, mainly because they are low-metallicity environments (Henry & Worthey 1999), resembling the conditions of early stages of spiral galaxies and high-redshift galaxies. These regions are also known to have low star formation rates (Dong et al. 2008; Bigiel et al. 2010; Alberts et al. 2011). Moreover, there is growing evidence of cold gas accretion in the local Universe, both through the arrival and merging of gas-rich satellites and through gas infall from the intergalactic medium. This new gas could be deposited in the outer regions of galaxies and form reservoirs for replenishing the inner parts and feeding star formation (Sancisi et al. 2008), making outer regions good laboratories for scanning the interface between galaxies and the surrounding intergalactic gas.

With its 1.25 degree field of view and sensitivity to stellar populations younger than a few hundred Myr, the UV satellite GALEX (Galaxy Evolution Explorer) is well suited to address the question of star formation in spiral galaxies at large galactocentric radii. Recent star formation within such environments was detected in Hα (the principal star formation tracer over the years) and broad-band observations for a few galaxies: NGC 628, NGC 1058, NGC 6946 (Ferguson et al. 1998), M 31 (Cuillandre et al. 2001), and NGC 6822 (de Blok & Walter 2003). However, the GALEX far-UV (FUV) and near-UV (NUV) data demonstrate that Hα observations still fail to detect a significant population of moderate-age stars in the outermost disks of spiral galaxies, since Hα traces more recent star formation episodes. Indeed, UV-bright disks extending up to 3 to 4 times the optical radius have been reported in about 30% of spiral galaxies, with the most remarkable examples: M 63, M 83, NGC 2841, and NGC 4625 (Thilker et al. 2005; Gil de Paz et al. 2005, 2007). These extended UV emission (XUV) disks cover a significant fraction of the area detected at 21 cm wavelength, with some correspondence between the position of the brightest UV complexes and peaks in the atomic gas distribution. The measured FUV – NUV colors are generally consistent with young populations of O, and predominantly B stars, characterized by ages from a few Myr up to 400 Myr.

The confirmed occurrence of recent and ongoing star formation in the outer disks of normal spiral galaxies has several important implications. First, it supports the presence of molecular gas in the outskirts of spirals, since stars are formed within

---

[⋆] Based on observations carried out with the IRAM 30 m telescope. IRAM is supported by INSU/CNRS (France), MPG (Germany), and IGN (Spain).

molecular clouds. Second, this suggests the presence of large reservoirs of hydrogen in the form of H_2, which may contribute to the baryonic dark matter of spiral galaxies. Third, it offers the ideal place to study the unresolved issue of the atomic hydrogen gas origin: is H I mainly a product of the star formation process; i.e., does it result from the photodissociation of H_2 by the UV flux radiation emanated from newly formed stars (Allen et al. 1986, 2004; Smith et al. 2000), rather than mainly being a precursor to it? Fourth, the presence of recently formed stellar complexes at large galactocentric radii also provides a simplified laboratory for determining the star formation threshold, namely the minimum gas surface density required for star formation to occur spontaneously (Kennicutt 1989; Martin & Kennicutt 2001). Fifth, it allows investigating the star formation in quiescent and low-metallicity environments that may affect the star formation density and the initial mass function.

In this paper we aim to detect the molecular gas expected in the outskirts of spiral galaxies because of the star formation discovered from the XUV observations. The M 63 spiral galaxy, known to have an XUV disk, is selected for this work. The search for molecular gas in galaxies is difficult, since we cannot detect cold H_2 directly. Instead, the second most common molecule, CO, is used as a proxy. Molecular gas has been detected in many galaxies from the mapping of the CO emission. It is now well established that the CO emission is the strongest in the central regions of spiral galaxies (e.g., Young & Scoville 1991), but then falls off, as does the blue stellar light, with the galactocentric radius (e.g., Young & Scoville 1982; Young et al. 1995). The questions "is this CO emission drop real, or does it reflect the difficulty of detecting the molecular gas in the outer regions of spiral galaxies" remain open. For example, CO emission lines are known to be weaker in media characterized by low metallicities, low gas temperatures, low excitations, and low gas densities, even if substantial molecular gas is present (e.g., Allen 1996; Combes & Pineau Des Forets 2000), and thus in media that may well be potentially representative of outer disk regions.

Schruba et al. (2011) used a very effective stacking technique on HERACLES CO(2–1) data of nearby spiral galaxies, where they stack CO spectra across many sightlines by assuming that the mean H I and CO velocities are similar, to highlight the presence of the faintest CO emission. They focused their analysis on data stacked in bins of galactocentric radius and found that the CO radial profile follows a remarkably uniform exponential decline with a scale length of $\sim 0.2\, r_{25}$. But even though this has been shown to be a very effective technique, it still fails to detect CO in the farthest out regions of galactic disks, where they only reach 3σ upper limits. Specific very deep CO observations are thus required to trace the molecular gas in the outer disk regions of spiral galaxies, which is precisely the objective of this work.

In Sect. 2 we present the characteristics of the M 63 spiral galaxy, selected for deep CO observations in the outer disk regions. We qualify the advantages of M 63 in the context of XUV galaxies and cite the previous works done on M 63. In Sect. 3 we describe the CO observations performed on the IRAM 30 m telescope and show the corresponding results in Sect. 4. In Sect. 5 we discuss the radial profiles obtained for the acquired CO measurements in comparison to other star formation tracers (FUV, NUV, Hα, 24 μm) and H I, and investigate the Kennicutt-Schmidt relations across the galaxy and beyond the optical radius. Summary and conclusions are given in Sect. 6. Throughout the paper we adopt the "standard" Galactic CO(1–0)-to-H_2 conversion factor $X_{\rm CO} = 2 \times 10^{20}$ cm^{-2}(K km s^{-1})$^{-1}$ (Dickman et al. 1986) and include a correction for helium.

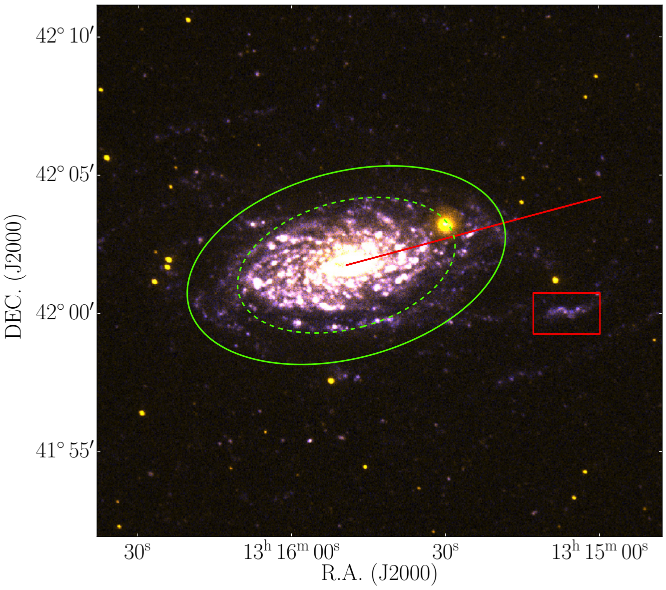

Fig. 1. False three-color (red/green/blue) composite image of M 63 from Gil de Paz et al. (2007). The image was produced using the *arcsinh* function, which allows showing faint structures while simultaneously preserving brighter structures in the field, such as the spiral arms of large galaxies (Lupton et al. 2004). The green ellipse represents the *B*-band 25 mag arcsec^{-2} isophote limit, r_{25}. The red solid line shows the CO mapping we performed along the major axis of M 63 from the center out to $r_{\rm gal} = 572'' = 1.6\, r_{25}$, where 27 single pointings were aligned with a spatial sampling of 22″. The red box encloses the bright UV region at $r_{\rm gal} = 483'' = 1.36\, r_{25}$ which we mapped with $6 \times 2 = 12$ pointings with the same spatial sampling. The CO(1–0) emission is observed out to the isophotal radius along the radial cut and in the bright UV region, while the CO(2–1) emission is confined to $0.68\, r_{25}$ (dashed green ellipse).

2. M 63 characteristics

Classified as SA(rs)bc and located at 10.1 Mpc (Leroy et al. 2009), M 63 (or NGC 5055) looks like a typical spiral galaxy, representative of a large class of local spirals, with no immediate neighbour, which excludes the potentiality of a galaxy in interaction. However, M 63 is not very ordinary, since it is a remarkable example of a nearby spiral with a bright and XUV disk. In Fig. 1 we show the GALEX NUV and FUV color-composite image of M 63, where an extensive population of UV-bright star-forming regions and stellar clusters (tracing the O and B stars) is revealed. The M 63 NUV and FUV surface-brightness profiles show a smooth decrease in the UV emission out to 700″ in the equivalent radius (defined as the square root of the product of the half-minor axis times the half-major axis), namely out to 2.5 times the optical equivalent radius (Gil de Paz et al. 2007). The major axis radius of the *B*-band 25 mag arcsec^{-2} isophote, the so-called isophotal radius, is equal to $r_{25} = 354'' = 17.4$ kpc in M 63. About 30% of local spiral galaxies have XUV disks as compared to their optical r_{25} disks, among which M 63 is one of the most extreme cases (Thilker et al. 2005; Gil de Paz et al. 2005, 2007). A metallicity gradient of -0.59 dex r_{25}^{-1} was reported by Moustakas et al. (2010) for the calibration of Pilyugin & Thuan (2005), which gives $12 + \log({\rm O/H}) = 8.59 \pm 0.07$ for the central metallicity of M 63.

The 21 cm observations of M 63 also show the presence of a very large, warped gaseous disk extending out to 40 kpc in the major axis radius (e.g., Battaglia et al. 2006). The warp starts around r_{25} and is exceptionally extended and symmetric. The measured H I column densities are higher than 10^{20} cm^{-2} up to 70% of the XUV disk. These high H I column densities plus the extended UV emission, both suggest the presence of molecular gas out to large galactocentric radii. Indeed, recent studies have demonstrated that strong H I emission is on average a good tracer of regions rich in molecular gas (e.g., Crosthwaite et al. 2002; Nieten et al. 2006), and the extended UV emission undeniably betrays the presence of relatively young stars, hence of the molecular gas necessary for their formation.

Molecular gas was looked for in M 63 in the context of the BIMA/SONG survey, the first systematic imaging survey of CO(1–0) emission from the centers and disks of nearby galaxies (Helfer et al. 2003, see their Fig. 43). The reported high-resolution CO measurements are confined to the very central area of the M 63 optical disk, $r_{\rm gal} = 96'' = 0.3\,r_{25}$ along the major axis, because of the lack of sensitivity of these data at the border of the map with a primary beam gain drop by a factor of 2. Single-dish spectra from the FCRAO Extragalactic CO Survey (Young et al. 1995, see their Fig. 87), despite their moderate sensitivity and low resolution, show that the CO emission extends over a larger area than mapped by BIMA/SONG, reaching a two times larger galactocentric radius, but still not extending up to the optical disk limit r_{25}. The signal measured at $r_{\rm gal} = 180''$ is equal to ~2 K km s^{-1}, which leaves room for a CO line flux decrease by a factor of 10 to 20 in the outermost XUV disk (depending on the CO line width), when aiming at signals as weak as 10 mK, or weaker, in these extreme regions. More recently, Leroy et al. (2009) mapped the CO(2–1) line in M 63 over the full optical disk, as part as the HERACLES survey on the IRAM 30 m telescope, and obtained reliable measurements out to $r_{\rm gal} = 0.68\,r_{25}$.

3. Observations and data reduction

The CO observations were performed with the IRAM 30 m millimeter-wave telescope at Pico Veleta, Spain, during a first run on September 10–17, 2007 under poor weather conditions, and during a second run on November 2, 16, and 27 and December 1, 2007 under good-to-excellent weather conditions. We used four single-pixel heterodyne receivers, simultaneously, two centered on the ^{12}CO(1–0) line at 115.271 GHz, and two on the ^{12}CO(2–1) line at 230.538 GHz. The telescope half-power beam widths at these two frequencies are 22″ and 11″, respectively. The data were recorded using the VESPA autocorrelator with 640 MHz bandwidth and 1.25 MHz resolution at 3 mm, and two 1 MHz filter banks (512 channels each) at 1 mm. The resulting velocity coverage at 115.271 GHz is 1665 km s^{-1} with a spectral resolution of 3.2 km s^{-1}. The corresponding values at 230.538 GHz are 666 km s^{-1} and 1.3 km s^{-1}.

First, we performed a CO mapping along the major axis of the M 63 disk from the center of the galaxy located at (J2000) RA = 13h15m49.3s, Dec = +42°01m45.4s out to the galactocentric radius $r_{\rm gal} = 572''$ by aligning 27 single pointings with a spatial sampling of 22″ in the radial direction sustaining a position angle PA = 105°. Second, we mapped a bright UV region in the outer regions of the M 63 disk centered on (J2000) RA = 13h15m07.0s, Dec = +42°00m00.0s and located at the galactocentric radius $r_{\rm gal} = 483''$ with $6 \times 2 = 12$ pointings following the sequence from (−66″; 0″) to (+44″; +22″) offsets relative to the central coordinates with a 22″ spatial sampling in the right-ascension direction and the same in the declination direction. In Fig. 1 we show the false-color GALEX image of M 63 on top of which the regions targeted for CO emission are plotted. Observations were performed in wobbler-switching mode with the maximum symmetrical azimuthal wobbler throw of 240″ allowed, corresponding to 11.8 kpc in projected distance for this spiral galaxy located at a distance of 10.1 Mpc. The total on-source exposure time obtained per pointing in the M 63 disk map and the UV region map is listed in Tables 1 and 2 (Col. 3), respectively. Only scans with a system temperature lower than 400 K at 3 mm were retained for analysis.

The data were reduced with the CLASS software from the GILDAS package. All the spectra obtained with the two receivers tuned on the ^{12}CO(1–0) line and corresponding to scans at the same pointings were summed up without any smoothing. On the other hand, the spectra obtained with the two receivers tuned on the ^{12}CO(2–1) line were first Hanning-smoothed to a resolution of 2.6 km s^{-1}, since the expected average CO line full width half maximum is approximately 10 km s^{-1}, before being summed up when corresponding to scans at the same pointings. No baseline subtraction was performed on individual spectra before summing because we simply did a linear sum. In Tables 1 and 2 (Cols. 4 and 7), we list the achieved 1σ rms in mK at 3 mm and 1 mm for each pointing of the M 63 disk map and the UV region map, respectively[1]. These rms values were obtained with a baseline subtraction of degree 0 and with windows set to 300−400 km s^{-1}, both at 3 mm and 1 mm, as defined by the velocity positions of detected CO(1–0) and CO(2–1) lines[2]. At 3 mm we obtained on average rms values between 4 mK and 21 mK in the M 63 disk map, while for seven pointings around the isophotal radius, r_{25}, and for all the pointings of the UV region map, we pushed the rms limit down to 4 mK to 7 mK.

4. Results

As summarized in Sect. 2, the CO(1–0) and CO(2–1) lines were previously mapped over the full optical disk of M 63 in the context of various CO surveys of nearby galaxies. However, none of these observations reaches the sensitivity of our data, in particular around the isophotal radius, r_{25}, and beyond. High sensitivity can be achieved by mapping CO through individual beam pointings, which is a technique that proves to be very efficient for obtaining deep observations of specific, not extended, areas of a galaxy.

The results of our CO emission mapping of M 63 along the major axis of its disk and over the bright UV region at $r_{\rm gal} = 1.36\,r_{25}$ are presented in Tables 1 and 2, respectively. We provide the CO(1–0) and CO(2–1) line full widths half maximum, FWHM (Cols. 5 and 8) and the integrated CO(1–0) and CO(2–1) line fluxes (Cols. 6 and 9) at each pointing of the mapping, as determined from fitting Gaussian functions to the CO profiles obtained by summing up all spectra corresponding to all scans per pointing. The CO(1–0) and CO(2–1) line FWHM are in the range from 9 km s^{-1} to 53 km s^{-1} and from 6 km s^{-1} to 39 km s^{-1}, respectively. They are greater than those expected for individual giant molecular clouds (GMCs) that have typical line widths of 10.4 km s^{-1} (Solomon et al. 1987), except for a few pointings around r_{25} and over the UV region. This implies that mostly an ensemble of molecular clouds is emitting per beam of 1 kpc and 0.5 kpc at 3 mm and 1 mm, respectively.

---

[1] The efficiencies of the ABCD receivers on the IRAM 30 m telescope are 5.9 Jy K^{-1} at 3 mm and 7.2 Jy K^{-1} at 1 mm (see the online IRAM wiki pages at `http://www.iram.es/IRAMES/mainWiki/Iram30mEfficiencies`).

[2] Except for the very few inner pointings at $r_{\rm gal} = 0$, 22″, and 44″, for which a larger window was set, given the larger widths of the CO(1–0) and CO(2–1) lines.

Table 1. CO mapping along the major axis of the M 63 disk.

			CO(1–0)			CO(2–1)					
$r_{\rm gal}$ ($''$)	$r_{\rm gal}$ (r_{25})	Time (min)	rms^a (mK)	*FWHM*^{b} (km s^{-1})	F^c (K km s^{-1})	rms^a (mK)	*FWHM*^{b} (km s^{-1})	F^c (K km s^{-1})	$r_{2,1}{}^d$	$M_{\rm H_2}{}^e$ (10^6 $M_\odot$)	$\Sigma_{\rm H_2}{}^f$ ($M_\odot$ pc^2)
0	0	31	11	200	49.8 ± 2.2	16	192	39.8 ± 3.1	0.24	321.8 ± 14.2	125.7 ± 5.6
22	0.06	8	18	53	24.5 ± 0.9	28	27	12.6 ± 0.8	0.16	158.3 ± 5.8	61.8 ± 2.3
44	0.12	8	19	41	16.4 ± 0.8	33	21	9.0 ± 0.7	0.17	106.0 ± 5.2	41.4 ± 2.0
66	0.19	8	19	23	9.8 ± 0.4	32	16	4.2 ± 0.5	0.13	63.3 ± 2.6	24.7 ± 1.0
88	0.25	8	18	20	6.3 ± 0.4	32	20	3.4 ± 0.6	0.17	40.7 ± 2.6	15.9 ± 1.0
110	0.31	8	19	26	12.6 ± 0.5	30	21	8.2 ± 0.6	0.20	81.4 ± 3.2	31.8 ± 1.3
132	0.37	8	21	22	5.1 ± 0.5	35	20	2.6 ± 0.7	0.16	33.0 ± 3.2	12.9 ± 1.3
154	0.44	23	13	29	5.3 ± 0.4	22	39	2.5 ± 0.9‡	0.15	34.3 ± 2.6	13.4 ± 1.0
176	0.50	23	13	19	5.4 ± 0.2	24	27	2.8 ± 0.6	0.16	34.9 ± 1.3	13.6 ± 0.5
198	0.56	23	13	21	1.8 ± 0.3	22	18	0.82 ± 0.40‡	0.14	11.6 ± 1.9	4.5 ± 0.8
220	0.62	31	11	16	0.98 ± 0.17	11†	10	<0.33	<0.11	6.3 ± 1.1	2.5 ± 0.4
242	0.68	101	6	11	0.30 ± 0.06	8	6	0.17 ± 0.05	0.17	1.9 ± 0.4	0.76 ± 0.15
264	0.75	101	6	14	0.45 ± 0.08	4†	10	<0.12	<0.08	2.9 ± 0.5	1.1 ± 0.2
286	0.81	55	10	21	0.88 ± 0.21	9†	10	<0.27	<0.10	5.7 ± 1.4	2.2 ± 0.5
308	0.87	47	11	14	0.81 ± 0.15	11†	10	<0.33	<0.13	5.2 ± 1.0	2.0 ± 0.4
330	0.93	63	7	22	0.85 ± 0.15	9	34	0.38 ± 0.31‡	0.14	5.5 ± 1.0	2.1 ± 0.4
352	0.99	155	5	9	0.23 ± 0.04	6	34	0.29 ± 0.21‡	0.38	1.5 ± 0.3	0.58 ± 0.10
374	1.06	109	4†	10	<0.12	4†	10	<0.12			
396	1.12	117	4†	10	<0.12	3†	10	<0.09			
418	1.18	93	5†	10	<0.15	5†	10	<0.15			
...	...										
473	1.34	381	2†	10	<0.06	2†	10	<0.06		<0.39	<0.15

Notes. The radius of the *B*-band 25 mag arcsec^{-2} isophote, the so-called isophotal radius, is equal to r_{25} = 354$''$ = 17.4 kpc in M 63. It is often used as a reference to express the relative galactocentric radius, $r_{\rm gal}$. The last separate line of the Table gives the values obtained when summing all scans at the 10 outermost pointings from 1.06 r_{25} to 1.6 r_{25} with no CO detection and by smoothing the resulting 3 mm and 1 mm spectra to a resolution of 9.7 km s^{-1} and 10.4 km s^{-1}, respectively. $^{(a)}$ Rms noises at, respectively, 3 mm and 1 mm, measured per channel of 3.2 km s^{-1} and 1.3 km s^{-1}. The values marked with † correspond to rms noises measured per smoothed channel of 9.7 km s^{-1} and 10.4 km s^{-1}, respectively. $^{(b)}$ Full widths at half maximum of, respectively, CO(1–0) and CO(2–1) lines as determined from fitting Gaussian profiles. $^{(c)}$ Integrated CO(1–0) and CO(2–1) line fluxes as determined from fitting Gaussian profiles. The values marked with ‡ correspond to potentially less reliable measurements, because of a CO line detection at 2σ only. Upper limits are 3σ and are calculated assuming a 10 km s^{-1} line width. $^{(d)}$ CO luminosity ratios defined as $r_{2,1} = L'_{\rm CO(2-1)}/L'_{\rm CO(1-0)}$, needed to correct the lower Rayleigh-Jeans brightness temperature of the 2–1 transition relative to 1–0. We would like, however, to stress that CO(1–0) and CO(2–1) do not exactly map the same regions, because the CO(1–0) beam area equals 4× the CO(2–1) beam area. The CO luminosity is calculated using the formula (3) from Solomon et al. (1997). $^{(e)}$ H$_2$ masses calculated from the CO(1–0) luminosity and by adopting the "standard" Galactic CO-to-H$_2$ conversion factor, $X_{\rm CO}$ = 2 × 10^{20} cm^{-2} (K km s^{-1})$^{-1}$ (Dickman et al. 1986). The applied formula is: $M_{\rm H_2}$ ($M_\odot$) = $4.4L'_{\rm CO(1-0)}$ (K km s^{-1} pc^2), where a factor of 1.36 is included to account for helium. $^{(f)}$ H$_2$ surface densities calculated from the integrated CO(1–0) line flux and by adopting the CO-to-H$_2$ conversion factor given under. $^{(e)}$ The applied formula is: $\Sigma_{\rm H_2}$ ($M_\odot$ pc^{-2}) = $4.4\cos(i)F_{\rm CO(1-0)}$ (K km s^{-1}), where i = 55° is the inclination of M 63 (Leroy et al. 2008).

Table 2. CO mapping over the bright UV region at 1.36 r_{25}.

Offsets			CO(1–0)			CO(2–1)					
($''$)	($''$)	Time (min)	rms^a (mK)	*FWHM*^{b} (km s^{-1})	F^c (K km s^{-1})	rms^a (mK)	*FWHM*^{b} (km s^{-1})	F^c (K km s^{-1})	$r_{2,1}{}^d$	$M_{\rm H_2}{}^e$ (10^6 $M_\odot$)	$\Sigma_{\rm H_2}{}^f$ ($M_\odot$ pc^2)
−66	0	118	5	10	<0.15	6	10	<0.18		<0.97	<0.38
−66	+22	117	5	11	0.14 ± 0.06‡	6	10	<0.18	<0.39	0.90 ± 0.39	0.35 ± 0.15
−44	0	186	4	10	<0.12	4	10	<0.12		<0.78	0.30
−44	+22	164	4	10	<0.12	6	10	<0.18		<0.78	0.30
−22	0	171	4	14	0.21 ± 0.06	5	10	<0.15	<0.22	1.36 ± 0.39	0.53 ± 0.15
−22	+22	148	4	10	<0.12	6	10	<0.18		<0.78	<0.30
0	0	164	4	10	<0.12	5	10	<0.15		<0.78	<0.30
0	+22	148	5	10	<0.15	6	10	<0.18		<0.97	<0.38
+22	0	123	5	10	<0.15	7	10	<0.21		<0.97	<0.38
+22	+22	116	5	10	<0.15	8	10	<0.24		<0.97	<0.38
+44	0	63	7	10	<0.21	9	10	<0.27		<1.36	<0.53
+44	+22	62	7	10	<0.21	8	10	<0.24		<1.36	<0.53
All offsets		1932	1	23	0.11 ± 0.02	2	10	<0.06	<0.17	0.71 ± 0.13	0.28 ± 0.05

Notes. The last separate line gives the values obtained when summing all scans at the 12 offset pointings. $^{(a)}$ Rms noises at, respectively, 3 mm and 1 mm, measured per channel of 3.2 km s^{-1} and 1.3 km s^{-1}. $^{(b)}$ Full widths at half maximum of, respectively, CO(1–0) and CO(2–1) lines as determined from fitting Gaussian profiles. $^{(c)}$ Integrated CO(1–0) and CO(2–1) line fluxes as determined from fitting Gaussian profiles. The value marked with ‡ corresponds to a potentially less reliable measurement, because of the CO line detection at barely 3σ. Upper limits are 3σ and are calculated assuming a 10 km s^{-1} line width. $^{(d)}$ $^{+(e)}$ $^{+(f)}$ CO luminosity ratios, H$_2$ masses, and H$_2$ surface densities, respectively, calculated using the same prescriptions as in Table 1.

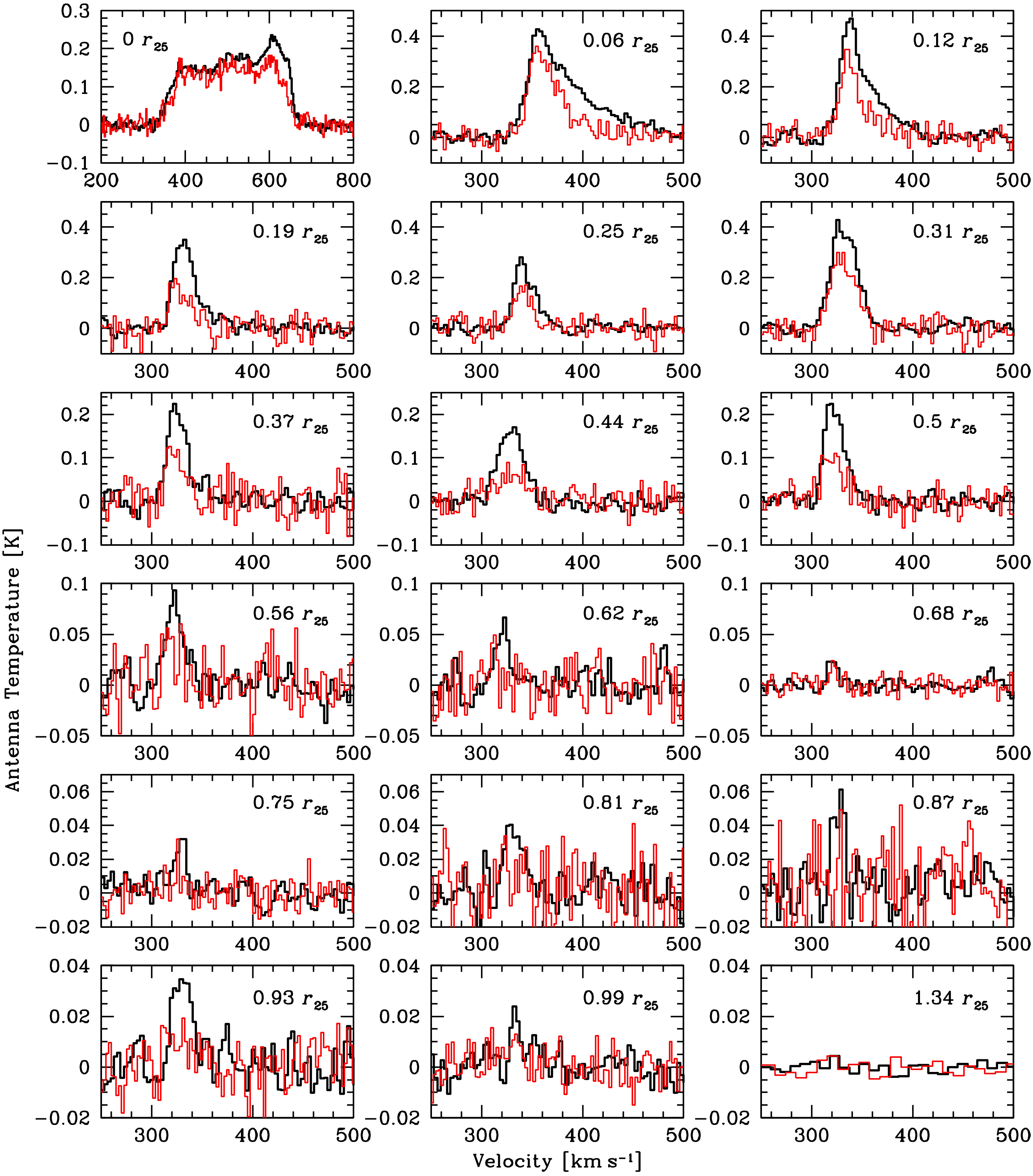

Fig. 2. Mosaic of CO spectra obtained when mapping the M 63 disk along its major axis from the center of the galaxy out to the isophotal radius, r_{25}. The CO(2–1) spectra (red thin line) are overplotted on the CO(1–0) spectra (black thick line). While CO(1–0) is clearly detected up to the optical radius, CO(2–1) appears to be confined to $r_{\rm gal} \lesssim 0.68\,r_{25}$. The *bottom right hand panel* shows the CO(1–0) and CO(2–1) spectra obtained when summing all scans at the ten outermost pointings from $r_{\rm gal} = 1.06\,r_{25}$ to $1.6\,r_{25}$ and smoothed to a resolution of 9.7 km s^{-1} and 10.4 km s^{-1}, respectively. No CO emission is detected at these outermost pointings.

In Tables 1 and 2 we also list the molecular gas masses per pointing (Col. 11), as derived using the "standard" Galactic CO(1–0)-to-H$_2$ conversion factor $X_{\rm CO} = 2 \times 10^{20}$ cm^{-2}(K km s^{-1})$^{-1}$ (Dickman et al. 1986) and including a correction factor of 1.36 for helium. The inferred masses are in the range $M_{\rm H_2} = (1.5{-}322) \times 10^6\ M_\odot$. Figure 2 shows the summed-up spectra of all scans *per* pointing of the M 63 disk map along the major axis, while Fig. 3 shows the resulting spectrum obtained by summing up all spectra of all scans at the 12 pointings used to map the external UV region.

The radial mapping (Fig. 2) clearly shows a detection of the CO(1–0) emission out to the galactocentric radius $r_{\rm gal} = 352''$,

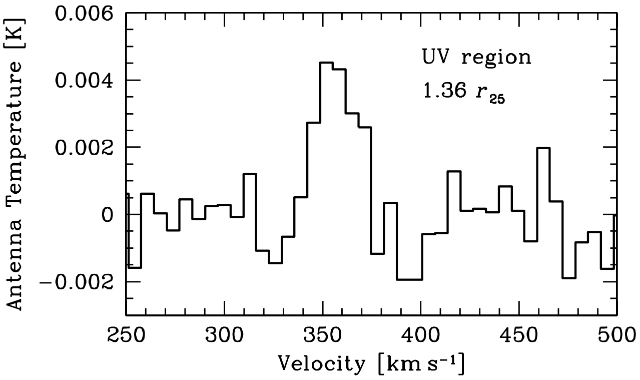

Fig. 3. CO(1–0) spectrum obtained by summing up all spectra at the 12 pointings used to map the bright UV region at $r_{\rm gal} = 1.36\,r_{25}$. There is a clear CO emission detection in this region of M 63 well beyond the optical radius. CO(2–1) remains undetected.

namely out to the isophotal radius $r_{25} = 354'' = 17.4$ kpc. A severe drop in the CO flux is nevertheless observed as a function of the galactocentric radius. Beyond r_{25} and out to $1.6\,r_{25}$, the limit of our CO search along the M 63 major axis, no CO emission is detected anymore (Table 1). Even by summing up all the spectra corresponding to all scans at the ten outermost pointings and by smoothing the resulting spectrum to a resolution of 9.7 km $\rm s^{-1}$, i.e., similar to the typical FWHM of CO(1–0) lines detected at the outermost pointings, no CO emission is observed. We do, however, derive a stringent 3σ upper limit on the integrated CO(1–0) line flux at $r_{\rm gal} > r_{25}$ of $F_{\rm CO(1-0)} < 0.06$ K km $\rm s^{-1}$, when assuming a line width of 10 km $\rm s^{-1}$. This is equivalent to a molecular gas mass of $M_{\rm H_2} < 3.9 \times 10^5\ M_\odot$. On the other hand, the CO(2–1) emission is securely detected only out to $r_{\rm gal} = 242''$, i.e., $0.68\,r_{25}$, in agreement with the CO(2–1) mapping by Leroy et al. (2009), while there are two very tentative detections at 2σ at the pointings $r_{\rm gal} = 0.93\,r_{25}$ and r_{25} (Table 1). The CO(2–1) line thus appears to be excited over about 2/3 of the optical disk. The corresponding CO luminosity ratios, $r_{2,1} = L'_{\rm CO(2-1)}/L'_{\rm CO(1-0)}$, can be found in Table 1 (Col. 10). They vary randomly between 0.13 and 0.24 (in the center of M 63) along the galactocentric radius, without showing any radial evolution. The absence of any clear detection of the CO(2–1) line beyond $r_{\rm gal} = 0.68\,r_{25}$ suggests that the subthermal excitation sets in around this galactocentric radius. However, this has to be considered with caution because the major axis pointings probe only a small portion of the M 63 disk at each radius and the Leroy et al. (2009) CO(2–1) map of the entire M 63 disk is not very deep and because there seems still to be plenty of star-forming regions at $r_{\rm gal} > 0.68\,r_{25}$ with high enough densities (locally) to thermalize the CO(2–1) line (see Fig. 1).

Whereas our survey for CO emission along the major axis of the M 63 disk seems to indicate that the molecular gas is confined to the isophotal radius r_{25} of the galaxy, we find a convincing CO(1–0) detection in the selected bright UV region at $r_{\rm gal} = 1.36\,r_{25}$. The sum of all spectra corresponding to all scans at the 12 pointings used to map the UV region leads to a CO(1–0) detection at 5.5σ with an integrated line flux $F_{\rm CO(1-0)} = 0.11 \pm 0.02$ K km $\rm s^{-1}$ (Fig. 3). This corresponds to a molecular gas mass of $M_{\rm H_2} = 7.1 \times 10^5\ M_\odot$. The CO(1–0) emission appears to be maximal at the offset (−22″; 0″), where it is detected at 3–4σ (Table 2). The CO(2–1) emission is, on the other hand, not detected down to an integrated line flux $F_{\rm CO(2-1)} < 0.06$ K km $\rm s^{-1}$, obtained when summing up all the spectra corresponding to all scans at the 12 pointings.

Table 3. Public ancillary data of M 63.

Band or line	Telescope	*FWHM* (″)	Reference
CO(2–1)	IRAM	13.4	Leroy et al. (2009)
FUV	GALEX	4.3	Gil de Paz et al. (2007)
NUV	GALEX	5.3	Gil de Paz et al. (2007)
Hα	KPNO	0.38	Kennicutt et al. (2008)
24 μm	*Spitzer*	6	Dale et al. (2009)
H I (21 cm)	VLA	6	Walter et al. (2008)

5. Discussion

A few hundred nearby galaxies have been the object of intensive surveys for molecular gas (e.g., Young & Scoville 1991; Young et al. 1995; Helfer et al. 2003; Leroy et al. 2009). However, for only a very few have deep CO searches in their outer disk regions been undertaken. Here, we show the existence of molecular gas up to the isophotal radius, r_{25}, and beyond in the nearby spiral galaxy M 63. This is the fourth such a detection of molecular gas in the outskirts after the spiral galaxies NGC 4414 (Braine & Herpin 2004), NGC 6946 (Braine et al. 2007), and M 33 (Braine et al. 2010). To analyze the impact of our observations in the context of star formation in the outer disk of M 63, we present the radial profiles of our CO observations along with complementary data of other star formation tracers (FUV, NUV, Hα, 24 μm) and H I, and we investigate the behavior of the Kennicutt-Schmidt relations across the galaxy and beyond r_{25} in the bright UV region. Characterizing the Kennicutt-Schmidt relation in the outer disk regions, namely in environments with low metallicities, gas temperatures, excitations, and gas densities, which are all properties hostile to star formation, is our main interest.

5.1. Radial profiles

To compare the CO distribution in M 63 along the major axis of its disk to H I and other star formation tracers' distributions, we built comparative radial profiles of the CO, H I, FUV, NUV, Hα, and 24 μm emission. Altogether they provide a complete view of the past and ongoing star formation that took or takes place in the galaxy and of the ingredients needed to sustain the star formation: molecular and atomic gas. The respective data are taken from the literature and are described in Table 3. In Fig. 4 we show the multiwavelength views of the bright UV region at $r_{\rm gal} = 1.36\,r_{25}$ with, from left to right, the NVU, 24 μm, and H I 21 cm emission.

As these data were obtained with different instruments and hence at various FWHM resolutions, we first convolved all these data to the resolution of our CO(1–0) data which is equal to the half-power beam width of the IRAM 30 m telescope at 3 mm, i.e., 22″. The images were then rotated by 20° in a north-to-west direction to have the major axis in the horizontal axis, and deprojected by correcting for a 55° inclination angle to bring the galaxy face-on. Finally, we did aperture photometry on these processed images with apertures of 22″ diameter using the "qphot" task of the "digiphot.apphot" package of IRAF[3],

---

[3] IRAF is distributed by the National Optical Astronomy Observatories, which are operated by the Association of Universities for Research in Astronomy, Inc., under cooperative agreement with the National Science Foundation.

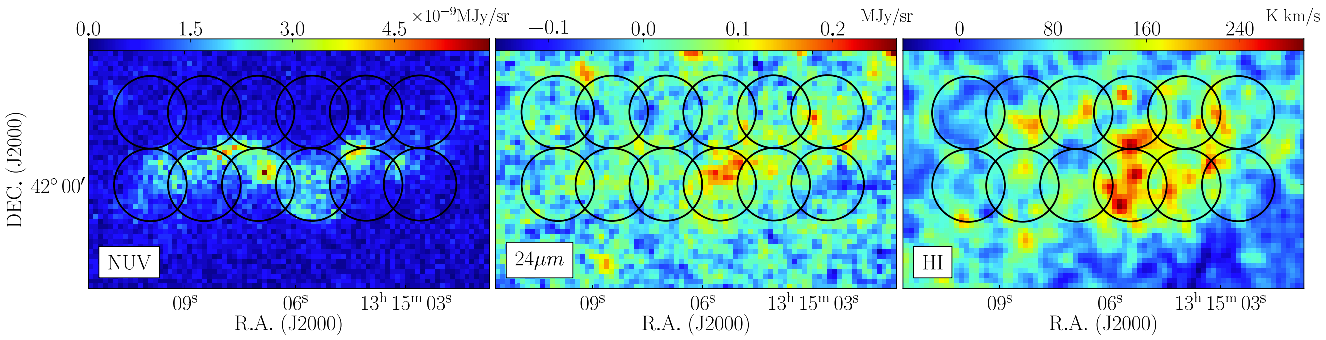

Fig. 4. Multiwavelength views of the bright UV region at $r_{\mathrm{gal}} = 1.36\,r_{25}$, showing from *left to right* the NUV, 24 μm, and H I 21 cm emission in flux units of 10^{-9} MJy sr^{-1}, MJy sr^{-1}, and K km s^{-1}, respectively, as indicated by the color bars. The circles of 22″ diameter refer to the positions of the 12 pointings used to map the CO(1–0) emission. The Hα emission is undetected in this external region of the M 63 galaxy.

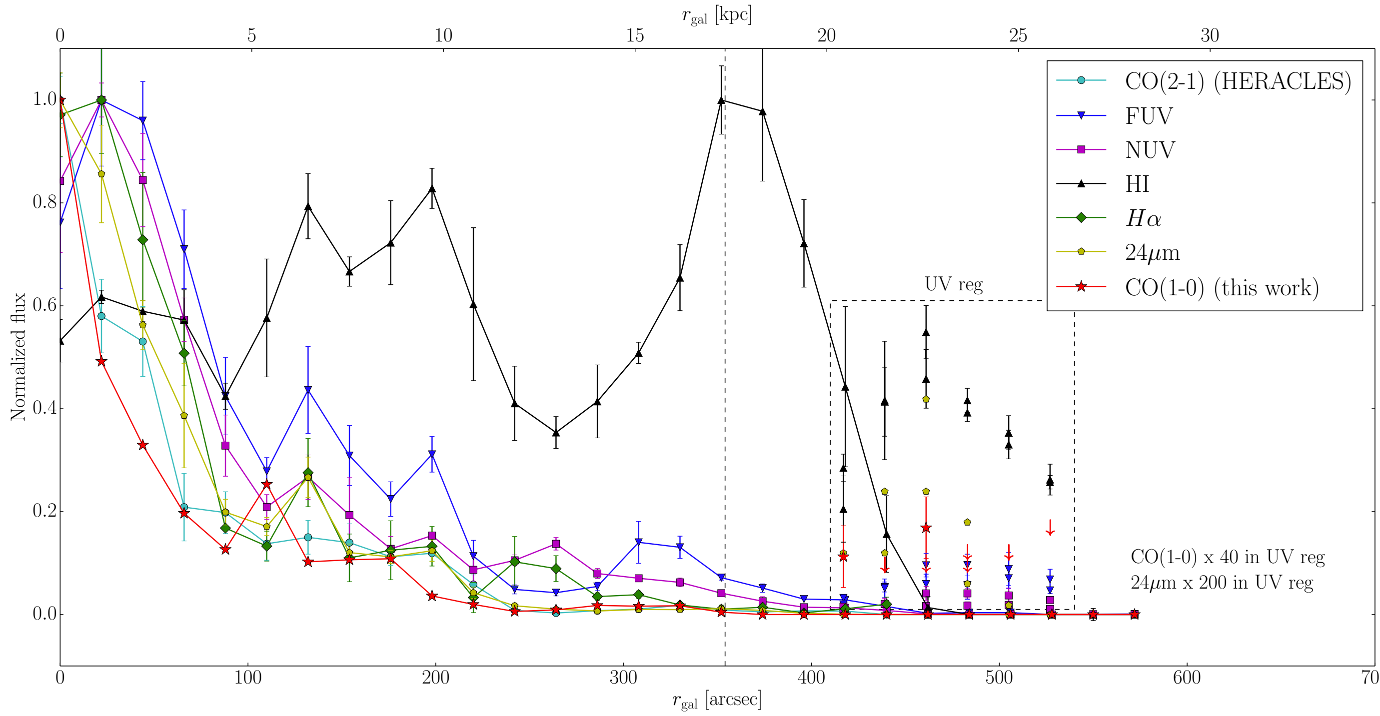

Fig. 5. Radial profiles of FUV, NUV, Hα, 24 μm, different star formation tracers, and H I taken from the literature (see Table 3), as measured along the major axis of the M 63 disk, which we compare to our CO(1–0) radial profile (red stars) and to the CO(2–1) radial profile from the HERACLES survey (Leroy et al. 2009). The measured fluxes are plotted in a normalized flux scale in order to allow relative comparisons. All the star formation tracers nicely follow the spiral arm structure at $r_{\mathrm{gal}} \simeq 130$, 200, and probably 260″. We observe a severe drop with the galactocentric radius for all star formation tracers, as well as for CO, such that close to the r_{25} limit (dashed line) and beyond all tracers and CO are practically absent with the exception of UV and H I. The CO emission is again detected in the external bright UV region. The measurements obtained in this UV region are shown in the dashed box at the correct galactocentric radii. The CO(1–0) and 24 μm fluxes are multiplied by a factor of 40 and 200, respectively, to make them visible. The double data points plotted at each r_{gal} correspond to the parallel pointings used to map the UV region (see Table 2). This external UV region has relatively high FUV and NUV emissions and is dominated by H I.

and we subtracted an average sky value measured away from the galaxy. The photometric measurements were performed at the 27 positions of the radial cut along the M 63 major axis used for the CO radial mapping, as well as at the 12 positions used to map CO in the external bright UV region, following the same spacing and pointings exactly.

The resulting CO(1–0), CO(2–1), FUV, NUV, H I, Hα, and 24 μm radial profiles along the M 63 radial cut are shown in Fig. 5 (connected data points), where the measured fluxes are plotted in a normalized flux scale to allow relative comparisons. All the profiles nicely follow the spiral structure observed at galactocentric radii $r_{\mathrm{gal}} \simeq 130$, 200, and probably 260″. They all show a severe drop with the galactocentric radius, except the profile of the atomic gas, which shows a completely different behavior. We observe that close to the r_{25} limit, the star formation tracers and CO begin to vanish considerably, and beyond the r_{25} limit, they all are practically absent with the exception of the faint UV emission. The H I emission is very strong beyond the r_{25} limit. This shows the importance of looking for molecular gas beyond the optical limit, where evidence of star formation is clearly brought by the UV emission.

While the CO emission is not detected beyond the r_{25} limit in the M 63 major axis map, it is again detected in the external UV region at $r_{\mathrm{gal}} = 1.36\,r_{25}$. The corresponding CO(1–0) fluxes, multiplied by a factor of 40 to make them visible (showing the depth of our data), with H I and other star formation tracer fluxes as measured in the UV region, are also shown in Fig. 5. The FUV and NUV emissions are observed in all pointings over the external UV region, while the Hα emission is undetected and a faint 24 μm emission, whose fluxes were multiplied by a factor of 200 to make them visible, is observed in only eight pointings (see also Fig. 4). It is interesting to point out that the FUV and NUV fluxes in the external UV region are similar to those at the pointing at r_{25}, the galactocentric limit where CO is still detected along the M 63 major axis. Beyond r_{25}, the FUV and NUV fluxes decrease and get weaker than in the external UV region. This suggests a tight correlation between the UV flux, namely the intensity of star formation and the CO flux that should trace the amount of molecular gas, since the CO emission starts to be detected at a given UV flux level. If correct, the CO emission is not detected beyond r_{25} along the major axis mapping simply because the amount of CO, corresponding to the molecular gas needed to sustain the star formation that is taking place there, falls below our detection threshold. Consequently, it is likely that molecular gas is present in the outer regions of the M 63 disk at least as long as the XUV is present.

The considerably larger amount of H I observed in the external UV region relative to CO leads us to speculate that H I is more likely a precursor of H_2 rather than a product of photodissociation due to UV radiation. However, the situation might be more complicated in reality. The main complication we may invoke is the reliability of CO as a proxy of H_2. As discussed in Sect. 4 and shown in Fig. 5, the absence of a clear CO(2–1) line detection beyond $r_{gal} = 0.68\, r_{25}$, with a CO luminosity ratio, $r_{2,1}$, below ~0.1 (see Table 1), may betray a decrease in the excitation temperature with the galactocentric radius. If this is the case, it may be that even if substantial H_2 is present in the outer regions of the M 63 disk, the CO lines may be quite weak, hence remain undetected.

In Fig. 6 we plot the radial profiles of the star formation efficiency (SFE) and the H_2-to-H I surface density ratio. The SFE is the star formation rate (SFR) per unit of molecular gas or the inverse of the gas depletion timescale, i.e., the time required for present-day star formation to consume the gas reservoir. It is calculated here as SFE $= \Sigma_{SFR}/\Sigma_{H_2}$. The various surface densities are computed using Eqs. (1) to (3). In the radial cut we only consider the pointings up to the isophotal radius, r_{25}, where we obtained convincing CO detections (17 pointings), and in the UV region we retain pointings with 24 μm detections only (8 pointings) in order to accurately estimate the star formation rate density. We observe that the SFE, as measured over the radial cut of M 63, is roughly constant as a function of the galactocentric radius out to the r_{25} limit. This is in line with the findings by Leroy et al. (2008), which we now extend out to the isophotal radius. Beyond r_{25}, the two SFE detections tend to show a drop in the SFE in the bright UV region, but upper limits in the other data points prevent us from drawing definitive conclusions. The H_2-to-H I surface density ratio shows a smooth decrease with the galactocentric radius, such that the inner regions of the M 63 disk are H_2-dominated, while the regions at $r_{gal} > 0.5\, r_{25}$ end up to be H I-dominated. This transition between a "mostly-H_2" and a "mostly-H I" interstellar medium (ISM) is found to be a well-defined function of local conditions according to Leroy et al. (2008), occurring at characteristic galactocentric radius, stellar and gas surface densities, hydrostatic gas pressure, and orbital timescale. At the r_{25} limit and beyond, we observe a further and more severe drop of the H_2-to-H I surface density ratio. Nevertheless, the behavior of the radial profiles of the SFE and the H_2-to-H I surface density ratio may well be inverted, if the trend toward an increasing CO-to-H_2 conversion factor with the galactocentric radius, as shown by Sandstrom et al. (2013, see their Fig. 7) for M 63 over the radial cut out to $r_{gal} \sim 0.7\, r_{25}$, is confirmed.

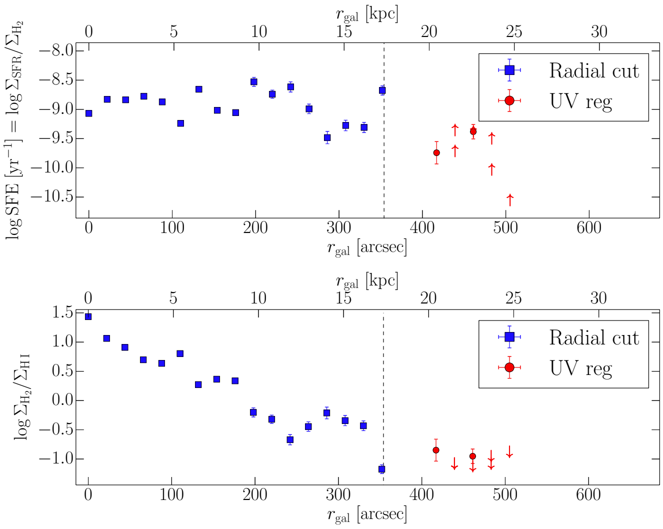

Fig. 6. Radial profiles of the star formation efficiency (*upper panel*) and the H_2-to-H I surface density ratio (*bottom panel*). The SFE is defined here as the star formation rate per unit of molecular gas. The blue squares correspond to the 17 pointings used to map CO along the M 63 major axis (the radial cut) out to the isophotal radius, r_{25} (dashed line), and the red circles correspond to the 8 pointings with 24 μm emission detection used to map CO over the bright UV region at $r_{gal} = 1.36\, r_{25}$. The double data points plotted for the UV region at each r_{gal} correspond to the parallel pointings used to map this region (see Table 2).

5.2. Kennicutt-Schmidt relations

Our acquired CO measurements offer the opportunity to analyze the Kennicutt-Schmidt relations across the optical disk of the M 63 galaxy and, in particular, close to and beyond the isophotal radius, r_{25}. This exercise is especially of interest in the bright UV region located in the outer disk of M 63 at the galactocentric radius $r_{gal} = 1.36\, r_{25}$, whose stellar emission is solely dominated by the UV emission, so where the star formation rate, metallicity, gas temperature, excitation, and gas density are potentially lower. For this purpose, we use the photometric measurements obtained in Sect. 5.1 for the FUV, 24 μm, and H I data. At each pointing of the CO radial mapping and the CO mapping of the bright UV region, we compute the star formation rate surface density, Σ_{SFR}, the atomic gas surface density, $\Sigma_{H\,I}$, and the molecular gas surface density, Σ_{H_2}. We can question how these surface densities determined over single pointings along the radial major axis cut are representative of surface densities that Leroy et al. (2008) obtained by performing azimuthal averages over the entire disk of M 63. The comparison of the respective molecular gas surface densities as a function of the galactocentric radius is excellent. The SFR surface densities for the radial cut show an offset toward higher values, but the respective Σ_{SFR} radial profiles are the same. Only the atomic gas surface density measurements seem to severely diverge between the radial cut and the azimuthal averages. This difference comes from the fact that the radial cut along the major axis crosses a spiral arm like structure, which is very bright in H I and covers an H I emission peak in the outer parts of the radial profile. This certainly also explains the higher Σ_{SFR} we observe for the radial cut, where the star formation activity is slightly enhanced.

Table 4. Best-fitting bisector linear Kennicutt-Schmidt relations obtained for M 63 in log space.

	This work						Bigiel et al. 2008		
	Radial cut out to r_{25}			UV region at 1.36 r_{25}			Radial cut out to 0.68 r_{25}		
	$\log A$	N	σ	$\log A$	N	σ	$\log A$	N	σ
H_2	–1.93	1.06	0.29	0.17†	3.0†	–	–2.22	0.92	0.10
H I + H_2	–2.43	1.73	0.31	–2.20	4.7	0.35	–2.63	1.58	0.22

Notes. The Kennicutt-Schmidt relations are best parametrized by power laws of the form $\Sigma_{\rm SFR} = A(\Sigma_{\rm gas})^N$, which in log space translates into linear relations. † Only indicative $\log A$ and N values, since they rely only on two data points, which makes them very uncertain.

The SFR surface density is determined using the calibration from Leroy et al. (2008):

$$\Sigma_{\rm SFR}(M_\odot\ {\rm yr}^{-1}\ {\rm kpc}^{-2}) =$$
$$8.1 \times 10^{-2} F_{\rm FUV}({\rm MJy\ sr}^{-1}) + 3.2 \times 10^{-3} F_{24\,\mu{\rm m}}({\rm MJy\ sr}^{-1}), \quad (1)$$

which includes the FUV flux to measure the unobscured star formation through the emission of O and B stars, and the 24 μm flux that traces the obscured FUV emission that is re-emitted in the far-IR by dust grains. The atomic gas surface density is measured with the calibration of Bigiel et al. (2010):

$$\Sigma_{\rm H\,I}(M_\odot\ {\rm pc}^{-2}) = 0.020 F_{\rm H\,I}({\rm K\ km\ s}^{-1}), \quad (2)$$

which includes a factor of 1.36 to reflect the presence of helium. Finally, the molecular gas surface density (see Tables 1 and 2) is calculated with our integrated CO(1–0) line fluxes using the calibration of Leroy et al. (2008):

$$\Sigma_{\rm H_2}(M_\odot\ {\rm pc}^{-2}) = 4.4 \cos(i) F_{\rm CO(1-0)}({\rm K\ km\ s}^{-1}), \quad (3)$$

where the "standard" Galactic CO-to-H_2 conversion factor, $X_{\rm CO} = 2\times10^{20}\ {\rm cm}^{-2}\ ({\rm K\ km\ s}^{-1})^{-1}$ (Dickman et al. 1986), as well as the factor of 1.36 to account for helium are adopted. The inclination correction by an angle $i = 55°$ is taken into account. This correction is also considered in the SFR and atomic gas surface densities when deprojecting the FUV, 24 μm, and H I images (see Sect. 5.1).

We compare the star formation rate surface densities with the atomic and molecular gas surface densities separately in the two top panels of Fig. 7. The two plots show that the gas surface density of M 63 in its radial cut is dominated by the molecular gas, whereas the bright UV region is strongly dominated by the atomic gas, as also observed in Fig. 6 (bottom panel). Interestingly, the H I surface density of the UV region is very similar to the one observed along the radial cut, in contrast to its molecular gas surface density, which is significantly lower. Finally, in the bottom panel of Fig. 7 we show the star formation rate surface density as a function of the total gas surface density, $\Sigma_{\rm H\,I+H_2}$, namely the sum of both $\Sigma_{\rm H\,I}$ and $\Sigma_{\rm H_2}$.

To characterize the star formation in M 63, we use the Kennicutt-Schmidt (K-S) relation that relates the SFR surface density to the gas surface density. In all plots of Fig. 7, we fit a power law of the form $\Sigma_{\rm SFR} = A(\Sigma_{\rm gas})^N$, which in log space translates into a simple linear relation. The coefficient A traces the absolute star formation efficiency (Kennicutt 1998), and the exponent N relates the star formation rate to the gas density present and tells us how close the two variables are to linearity. We use the least-square bisector method, which is suitable for two independent variables (Isobe et al. 1990), for the fit in log space and leave $\log A$ and N as free parameters. It is important to note that for the fitting procedure alone (not the plotting), we rescaled $\Sigma_{\rm gas}$ by a factor of 10, such that $\Sigma_{\rm gas}/10\ M_\odot\ {\rm pc}^{-2}$. We made this rescaling to minimize the covariance of $\log A$ and N in the fit[4] and to make our results comparable to those of Bigiel et al. (2008) for M 63. They used the same FUV and H I data as we did, but the CO data were taken from the HERACLES CO(2–1) database (Leroy et al. 2009) with a 11″ resolution and a CO(2–1)/CO(1–0) line ratio of 0.8. Our CO(1–0) data reach much deeper sensitivity than the HERACLES CO(2–1) data, which is essential for properly characterizing the K-S relations over all the optical disk and especially beyond the r_{25} limit.

The best-fitting bisector linear relations, $\log\Sigma_{\rm SFR} = \log A + N\log\Sigma_{\rm gas}$, obtained independently for the K-S relation over the full radial cut out to r_{25} and the UV region in the outer disk of M 63 are shown in Fig. 7. The errors we provide on $\log A$ and N are 1σ quotes of the nearly Gaussian distributions of $\log A$ and N obtained through Monte-Carlo simulations of 5000 data sets created from the original data, with random values generated within their error bars. The scatter in our fits typically are on the order of 0.3 dex. The corresponding K-S relation results are presented in Table 4 for both $\Sigma_{\rm gas} = \Sigma_{\rm H_2}$ and $\Sigma_{\rm gas} = \Sigma_{\rm H\,I+H_2}$, and are compared to the respective K-S relations found by Bigiel et al. (2008) over the radial cut of the M 63 disk out to $r_{\rm gal} = 0.68\,r_{25}$ only. The K-S relations obtained over the radial cut have very comparable slopes (in log space) $N \sim 1.0$ for $\Sigma_{\rm H_2}$ and $N \sim 1.6$ for $\Sigma_{\rm H\,I+H_2}$, with our slopes systematically slightly steeper. They also have comparable coefficients $\log A \sim -2.0$ for $\Sigma_{\rm H_2}$ and $\log A \sim -2.5$ for $\Sigma_{\rm H\,I+H_2}$, with our coefficients systematically smaller by about 0.2–0.3 dex, but still within the fit scatter. The one-to-one linearity of the K-S relation between the SFR surface density and the molecular gas surface density is really solid, meaning that the gas is being consumed at a nearly constant rate, as expected for $\Sigma_{\rm H_2}$.

When comparing these results to the K-S relations of the UV region in the outer disk of M 63 at the galactocentric radius $r_{\rm gal} = 1.36\,r_{25}$, we note that they are significantly different. The slope $N = 4.7$ (in log space) of the K-S relation for $\Sigma_{\rm H\,I+H_2}$ is considerably steeper in the external UV region. A similar trend is observed for $\Sigma_{\rm H_2}$. It is true that this relies on two data points, but if we trust our 3σ upper limits on $\Sigma_{\rm H_2}$, we can hardly expect to reconcile these external UV region measurements with the K-S relations observed over the radial cut, more especially as the derived star formation rate surface densities are very reliable. It is very likely that the CO-to-H_2 conversion factor adopted over the external UV region is underestimated, given the low metallicity expected in the outskirts of M 63 as supported by the metallicity gradient inferred in M 63 (see Sect. 2) and the observed trend for an increase in $X_{\rm CO}$ with decreasing metallicity (Sandstrom et al. 2013; Bolatto et al. 2013). While this may induce a shift in the external UV region data points toward higher gas surface densities, the slopes of the K-S relations for

---

[4] This rescaling has no influence on the results of the exponent N, so only the coefficient A will need to be corrected by the factor of 10.

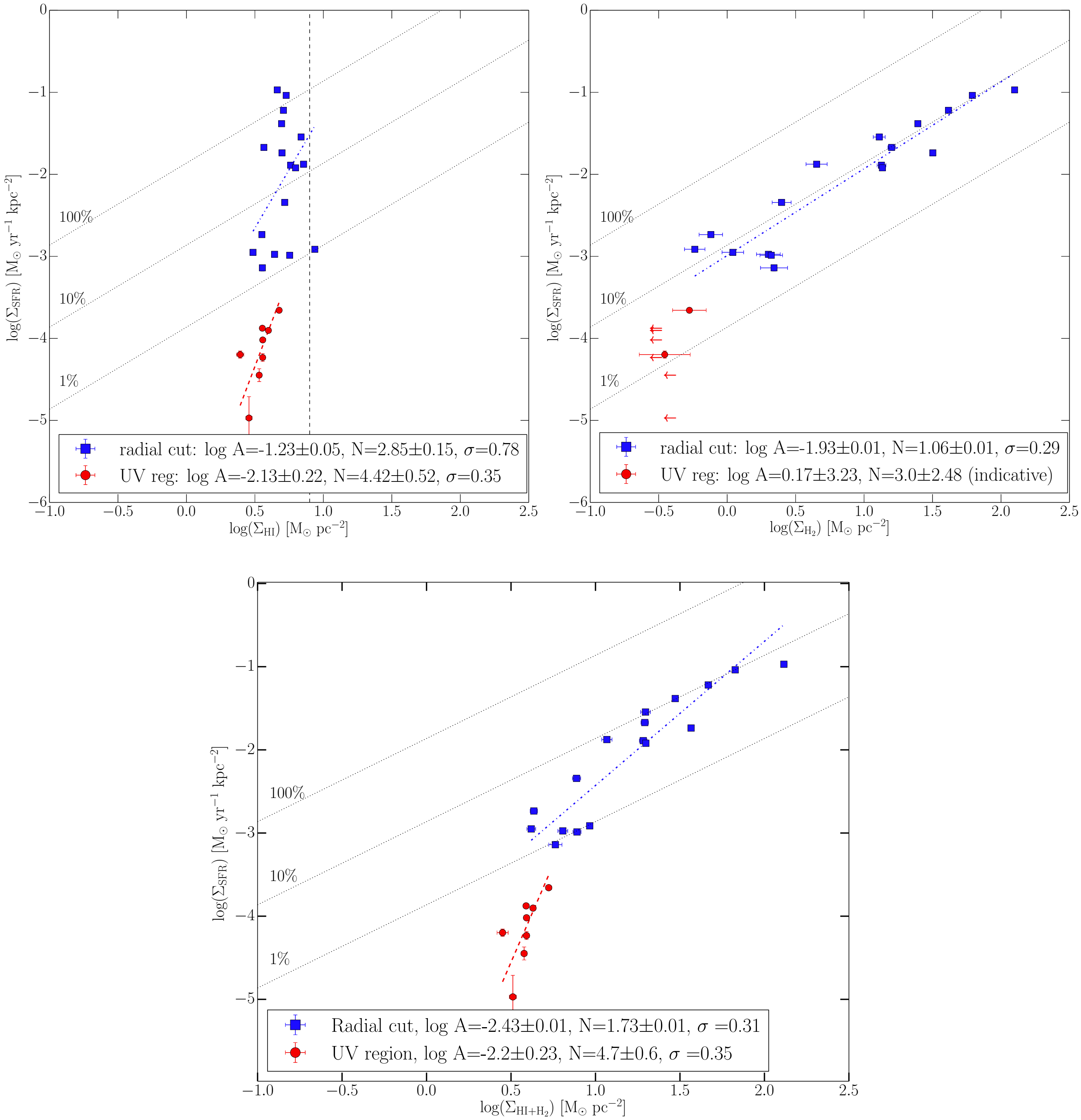

Fig. 7. Kennicutt-Schmidt relations that relate the SFR surface density to the gas surface density plotted for $\Sigma_{\rm H\,I}$ (*top-left panel*), $\Sigma_{\rm H_2}$ (*top-right panel*), and $\Sigma_{\rm H\,I+H_2}$ (*bottom panel*). The blue squares correspond to the 17 pointings used to map CO along the M 63 major axis (the radial cut) out to the isophotal radius, r_{25}, and the red circles correspond to the 8 pointings with 24 μm emission detection used to map CO over the bright UV region at $r_{\rm gal} = 1.36\,r_{25}$. The K-S relation is best parametrized by a power law of the form $\Sigma_{\rm SFR} = A(\Sigma_{\rm gas})^N$, which in log space translates into a linear relation. The best-fitting bisector linear K-S relations are derived separately for the radial cut (blue dashed-dotted lines) and for the UV region (red dashed lines). The corresponding coefficients log A and slopes N can be found in the labels of each panel. The black dotted lines represent “isochrones” of constant star formation efficiencies, indicating the level of $\Sigma_{\rm SFR}$ needed to consume 100%, 10%, and 1% of the total amount of gas within 10^8 years. The vertical dashed line in the *top-left panel* corresponds to the $\Sigma_{\rm H\,I} \sim 9\ M_\odot\ {\rm pc}^{-2}$ threshold at which the atomic gas saturates (Bigiel et al. 2008).

$\Sigma_{\rm H\,I+H_2}$ and $\Sigma_{\rm H_2}$ will remain unchanged, unless there is a significant $X_{\rm CO}$ gradient over the external UV region. As a result, a broken K-S power law between the inner and outer regions of the M 63 disk seems to robustly emerge. It suggests that the regime of star formation drastically changes beyond the isophotal radius, r_{25}. Indeed, the exponents N observed for the K-S relations in the external UV region show a nonlinear SFR regime, in clear contrast to the quasi-linear SFR regime in the inner regions of the disk. What triggers the "quenching" of star formation in the outer regions of the M 63 disk and, consequently, the severe deviation from the commonly accepted star formation relation as traced by the K-S relations observed along the radial cut of M 63? We can invoke the flaring of the outer gas layers or, more speculative, the possible presence of high turbulence providing support against gravitational collapse as suggested by Longmore et al. (2013).

To better appreciate the change in the star formation regime between the inner and outer regions of the M 63 disk, in Fig. 7 we also plot "isochrones" of constant star formation efficiencies, indicating the levels of $\Sigma_{\rm SFR}$ needed to consume 100%, 10%, and 1% of the total amount of gas (corrected by a factor of 1.36 to account for helium) within 10^8 years. These isochrones can also be interpreted as constant gas depletion timescales (i.e., the time needed to consume the total amount of gas) of 10^8 yr, 10^9 yr, and 10^{10} yr from top to bottom. We can see that when the total gas is considered (H I + H_2), the SFE settles the gas consumption within 10^8 years to 1% to 10% for the radial cut of M 63, whereas the external UV region has a much lower SFE with less than 1% of the gas converted into stars within 10^8 years. The drop in the star formation efficiency beyond the isophotal radius, r_{25}, can also be appreciated in Fig. 6 (upper panel). The SFE could even be lower in the external UV region, since the CO-to-H_2 conversion factor may, in reality, be up to 100 times more (in the extreme case) than the "Galactic" value (Bolatto et al. 2013) and so are the computed $\Sigma_{\rm H_2}$ values, depending on the metallicity of the external UV region, which may well be as low as 10% to 20% of the local Galactic ISM[5]. Consequently, the star formation still occurs in the outer regions of the M 63 disk, but at very low efficiency, significantly lower than in the inner regions of the disk.

6. Summary and conclusions

Deep CO(1–0) and CO(2–1) observations obtained on the IRAM 30 m telescope of the M 63 spiral galaxy characterized by an XUV disk extending out to 2.5 times the optical equivalent radius were presented. We performed both a CO mapping along the major axis of the M 63 disk from the center out to the galactocentric radius $r_{\rm gal} = 572'' = 1.6\, r_{25}$ and over a bright UV region in the outer disk of M 63 at the galactocentric radius $r_{\rm gal} = 1.36\, r_{25}$. Our objective was to search for CO emission and hence for molecular gas in the outer regions of the M 63 disk beyond the optical radius, where evidence of star formation is brought by both the extended UV emission and high H I column densities observed in these regions. We highlighted the importance of a CO detection in regions far away from the center of the galaxy, where the metallicity, gas temperature, excitation, and gas density are supposed to be lower and where stars have more difficulty to form. To complement our CO observations, we used FUV, NUV, Hα, 24 μm, and H I data from the literature. This allowed us to investigate the Kennicutt-Schmidt relations across the galaxy and beyond the isophotal radius, r_{25}, in the bright UV region. Our main results are as follows.

1. The CO(1–0) emission is clearly detected along the major axis of the M 63 disk out to the isophotal radius, r_{25}, but not beyond. However, the CO(1–0) is again detected in the bright UV region in the outer disk of M 63 at $r_{\rm gal} = 1.36\, r_{25}$. This is the fourth molecular gas detection in the outskirts of nearby spiral galaxies. The CO(2–1) emission is, on the other hand, confined to $r_{\rm gal} = 0.68\, r_{25}$ and thus suggests subthermal excitation in the outer regions of the M 63 disk.
2. The radial profiles of the CO emission and other star formation tracers (Fig. 5) show a severe drop with the galactocentric radius, in contrast to the atomic gas. Close to the r_{25} limit, CO and the star formation tracers begin to vanish considerably, and beyond r_{25}, they all are practically absent with the exception of the faint UV emission and H I. The UV region at $r_{\rm gal} = 1.36\, r_{25}$, in which the CO emission is detected, is characterized by FUV and NUV emission fluxes similar to the fluxes observed at r_{25}, but stronger than the fluxes observed at $r_{\rm gal} > r_{25}$ along the M 63 major axis. This probably reflects a tight correlation between the CO and UV fluxes, namely between the intensity of star formation and the amount of molecular gas, so it strongly suggests that the absence of CO detection at $r_{\rm gal} > r_{25}$, where the XUV is weaker, is simply the result of the CO detection threshold that is still too high.
3. The external UV region is characterized by a very high H I flux with respect to the measured CO flux. This leads us to speculate that H I is more likely the precursor of H_2 rather than the product of UV photodissociation, since it seems to dominate in quantity. This is, however, true as long as substantial H_2 is not hidden in the outer disk regions of M 63, which may be the case as we observe hints for an excitation temperature decrease at large galactocentric radii, which may lead to very weak CO lines.
4. With the integrated CO line flux measurements and the complementary data from the literature, we derive SFR, H I, and H_2 surface densities all along the major axis of the M 63 disk and in the external UV region. We observe that the gas surface density along the radial cut is dominated by the molecular gas, whereas in the UV region it is dominated by the atomic gas. The best-fit Kennicutt-Schmidt relations, $\Sigma_{\rm SFR} = A(\Sigma_{\rm gas})^N$, show a broken power law from the inner to the outer regions of the M 63 disk (Fig. 7). Indeed, the almost linear K-S relation (with a slope of nearly 1 in log space) observed over the radial cut, in the inner regions of the disk characterized by high gas densities, cannot be extrapolated to the outer disk regions. The latter are characterized by a nonlinear SFR regime (with a K-S slope much higher than 1 in log space), perhaps owing to the flaring of the outer gas layers. This is the first time that the K-S relation is quantified in the outskirts of a spiral galaxy, i.e., in low gas density environments. At a molecular gas surface density as low as $\Sigma_{\rm H_2} = 0.35\, M_\odot$ pc^{-2}, well below all the determined H_2 surface densities referenced in spiral galaxies so far (Bigiel et al. 2008, 2011), star formation still occurs spontaneously.
5. The change in the star formation regime between the inner and outer regions of the M 63 disk can also be appreciated by the difference in their star formation efficiencies. Indeed, along the major axis of the disk out to the isophotal radius the SFE settles the gas consumption within 10^8 years from 1% to 10%, whereas in the external UV region much less than 1% of the gas is converted into stars within 10^8 years. Consequently, star formation still occurs in the outer regions of the disk, but at very low efficiency.

Acknowledgements. C.V. wishes to acknowledge support from CNRS and CONICYT through an agreement signed on December 11, 2007. We warmly thank the IRAM 30 m telescope staff for their support during the observations. We thank the anonymous referee for her/his very careful and constructive report.

---

[5] When extrapolating the metallicity gradient determined for M 63 (see Sect. 2), we get a metallicity of 20% of the local Galactic ISM at $r_{\rm gal} = 1.36\, r_{25}$, the galactocentric radius of the bright UV region.

References

Alberts, S., Calzetti, D., Dong, H., et al. 2011, ApJ, 731, 28
Allen, R. J. 1996, Cold dust and Galaxy Morphology, eds. D. L. Block, & J. M. Greenberg, Astrophys. Space Sci. Lib. (Dordrecht: Kluwer Academic Publishers), 209, 50
Allen, R. J., Atherton, P. D., & Tilanus, R. P. J. 1986, Nature, 319, 296
Allen, R. J., Heaton, H. I., & Kaufman, M. J. 2004, ApJ, 608, 314
Battaglia, G., Fraternali, F., Oosterloo, T., & Sancisi, R. 2006, A&A, 447, 49
Bigiel, F., Leroy, A., Walter, F., et al. 2008, AJ, 136, 2846
Bigiel, F., Leroy, A., Walter, F., et al. 2010, AJ, 140, 1194
Bigiel, F., Leroy, A. K., Walter, F., et al. 2011, ApJ, 730, L13
Bolatto, A. D., Wolfire, M., & Leroy, A. K. 2013, ARA&A, 51, 207
Braine, J., & Herpin, F. 2004, Nature, 432, 369
Braine, J., Ferguson, A. M. N., Bertoldi, F., & Wilson, C. D. 2007, ApJ, 669, L73
Braine, J., Gratier, P., Kramer, C., et al. 2010, A&A, 520, A107
Combes, F., & Pineau Des Forets, G. 2000, Molecular Hydrogen in Space (Cambridge: Cambridge University Press)
Crosthwaite, L. P., Turner, J. L., Buchholz, L., Ho, P. T. P., & Martin, R. N. 2002, AJ, 123, 1892
Cuillandre, J.-C., Lequeux, J., Allen, R. J., Mellier, Y., & Bertin, E. 2001, ApJ, 554, 190
Dale, D. A., Cohen, S. A., Johnson, L. C., et al. 2009, ApJ, 703, 517
de Blok, W. J. G., & Walter, F. 2003, MNRAS, 341, L39
Dickman, R. L., Snell, R. L., & Schloerb, F. P. 1986, ApJ, 309, 326
Dong, H., Calzetti, D., Regan, M., et al. 2008, AJ, 136, 479
Ferguson, A. M. N., Wyse, R. F. G., Gallagher, J. S., & Hunter, D. A. 1998, ApJ, 506, L19
Gil de Paz, A., Madore, B. F., Boissier, S., et al. 2005, ApJ, 627, L29
Gil de Paz, A., Boissier, S., Madore, B. F., et al. 2007, ApJS, 173, 185
Helfer, T. T., Thornley, M. D., Regan, M. W., et al. 2003, ApJS, 145, 259
Henry, R. B. C., & Worthey, G. 1999, PASP, 111, 919
Isobe, T., Feigelson, E. D., Akritas, M. G., & Babu, G. J. 1990, ApJ, 364, 104
Kennicutt, Jr., R. C. 1989, ApJ, 344, 685
Kennicutt, Jr., R. C. 1998, ApJ, 498, 541
Kennicutt, Jr., R. C., Lee, J. C., Funes, S. J., et al. 2008, ApJS, 178, 247
Leroy, A. K., Walter, F., Brinks, E., et al. 2008, AJ, 136, 2782
Leroy, A. K., Walter, F., Bigiel, F., et al. 2009, AJ, 137, 4670
Longmore, S. N., Bally, J., Testi, L., et al. 2013, MNRAS, 429, 987
Lupton, R., Blanton, M. R., Fekete, G., et al. 2004, PASP, 116, 133
Martin, C. L., & Kennicutt, Jr., R. C. 2001, ApJ, 555, 301
Moustakas, J., Kennicutt, Jr., R. C., Tremonti, C. A., et al. 2010, ApJS, 190, 233
Nieten, C., Neininger, N., Guélin, M., et al. 2006, A&A, 453, 459
Pilyugin, L. S., & Thuan, T. X. 2005, ApJ, 631, 231
Sancisi, R., Fraternali, F., Oosterloo, T., & van der Hulst, T. 2008, A&ARv, 15, 189
Sandstrom, K. M., Leroy, A. K., Walter, F., et al. 2013, ApJ, 777, 5
Schruba, A., Leroy, A. K., Walter, F., et al. 2011, AJ, 142, 37
Smith, D. A., Allen, R. J., Bohlin, R. C., Nicholson, N., & Stecher, T. P. 2000, ApJ, 538, 608
Solomon, P. M., Rivolo, A. R., Barrett, J., & Yahil, A. 1987, ApJ, 319, 730
Solomon, P. M., Downes, D., Radford, S. J. E., & Barrett, J. W. 1997, ApJ, 478, 144
Thilker, D. A., Bianchi, L., Boissier, S., et al. 2005, ApJ, 619, L79
Walter, F., Brinks, E., de Blok, W. J. G., et al. 2008, AJ, 136, 2563
Young, J. S., & Scoville, N. 1982, ApJ, 258, 467
Young, J. S., & Scoville, N. Z. 1991, ARA&A, 29, 581
Young, J. S., Xie, S., Tacconi, L., et al. 1995, ApJS, 98, 219

2.2 2013 observations

Motivated by the successful results obtained in M63, new CO observations were done in the external parts of several XUV disk galaxies. Such galaxies were selected for having large disks of UV emission, beyond their r_{25} limit, previous CO detection in their centers (Holwerda et al. 2012, Young et al. 1995), and a low inclination angle to avoid projection problems. With this criteria, three spiral galaxies were selected: NGC628, NGC3344 and NGC2403, choosing the brightest points in FUV-NUV as targets to be observed in CO(1–0) and CO(2–1) (Figure 2.13 and Table 2.8). Details of these galaxies, including positions, distances, r_{25} limits and integration times during the observations are presented in Table 2.7.

For this project a total of 40 hours were granted between January 31^{th} and February 4^{th} 2013. Atmospheric conditions were good (pwv between 1.2 and 2.6 mm), but due to strong winds ∼40% of the time was lost. A total of 26.6 hrs were observed, including overheads.

2.2.1 Data reduction and Results

The data were recorded with the WILMA and FTS correlators, which give a spectral resolution of 2 MHz and 195 kHz respectively. At 115 GHz, these resolutions translate into 5.2 km/s for WILMA and 0.5 km/s for FTS, and at 230 GHz, the corresponding values are 2.6 km/s and 0.25 km/s respectively.

The data reduction was done with CLASS, in the same way as the reductions of M63. Each spectra of both backend were carefully inspected, and bad scans were removed.

Baselines were subtracted with polynomials of order 0 and 1 depending on the source, and antenna temperatures were corrected by the telescope beam efficiency (B_{eff}) and forward efficiency (F_{eff}) to obtain main beam temperatures with B_{eff} and F_{eff} equal to 0.78 and 0.94 respectively for 115 GHz, and to 0.59 and 0.92 for 230 GHz.[6]

Spectra were smoothed with the hanning method to degrade the velocity resolution until obtain a value no greater than 1/3 of the FWHM line. Finally, a simple gaussian line was fitted to the line candidate. The CLASS fit returns the velocity position of the line, its FWHM, the peak temperature and the integrated line intensity.

Unfortunately, and probably due to the bad weather conditions, no CO detections were found beyond the r_{25} limit of each galaxy. Apart from confirming the CO detections in the centers of NGC2403 and NGC3344, only one detection was found in the point NGC3344-5 located at 2.6 kpc from the center of the galaxy (Figure 2.14). Details of line parameters of such detections are presented in Table 2.9.

---

[6] http://www.iram.es/IRAMES/mainWiki/Iram30mEfficiencies

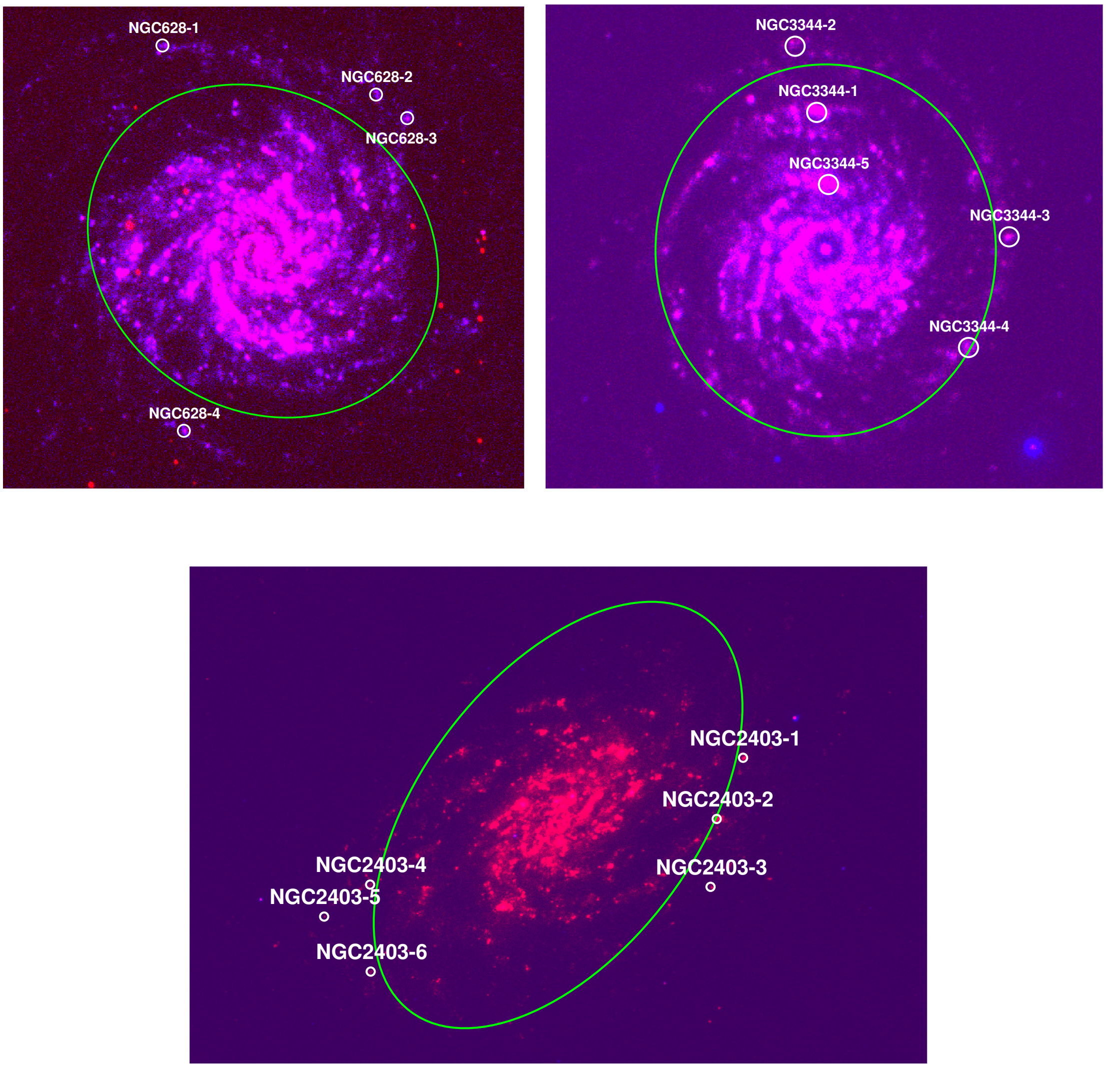

Figure 2.13: Targets selected for NGC628 (*top left*), NGC3344 (*top right*) and NGC2403 (*bottom*) in GALEX FUV-NUV composite images (FUV in red and NUV in blue, Gil de Paz et al. 2007a). The green ellipse marks the r_{25} limit. Circles are $22''$ in diameter, as the CO(1–0) FWHM. Observations were done as single pointing observation in each one of these targets.

Table 2.7. Galaxies selected for XUV observations in 2013.

Galaxy	RA(J2000)[a] $[^{hr}:^{m}:^{s}]$	DEC(J2000)[a] $[^{deg}:^{m}:^{s}]$	d[a] [Mpc]	r_{25}[a] [arcmin]	int. time [hrs]
NGC628	01:36:41.8	15:47:00.5	11	5.0±0.1	···
NGC2403	07:36:51.4	65:36:09.2	3.2	10.0±0.1	0.7
NGC3344	10:43:31.2	24:55:20.0	6.9	3.4±0.1	10.9

[a] Information taken from Gil de Paz et al. (2007a).

Note. — Due to bad weather conditions NGC628 could not be observed.

Table 2.8. Targets description for XUV observations 2013.

Target	RA(J2000) $[^{hr}:^{m}:^{s}]$	DEC(J2000) $[^{deg}:^{m}:^{s}]$	int. time [hrs]	detection
NGC2403-1	07:35:31.42	65:38:40.78	0.4	no
NGC3344-1	10:43:31.80	24:57:57.58	1.6	no
NGC3344-2	10:43:33.62	24:59:13.33	0.9	no
NGC3344-3	10:43:15.59	24:55:35.02	4.0	no
NGC3344-4	10:43:19.02	24:53:28.29	3.3	no
NGC3344-5	10:43:30.81	24:56:35.00	0.6	yes

Table 2.9. Line parameters for detections in XUV observations 2013.

Source	line	resol. [km/s]	v_0 [km/s]	dv [km/s]	T_{mb} [mK]	rms [mK]	I_{CO} [K km/s]	M_2 [$\times 10^6 M_\odot$]
NGC2403	CO(1–0)	4	126.0±1.5	40.3±3.5	60	10	2.58±0.19	1.04
⋯	CO(2–1)	2	1425.4±1.0	32.4±2.3	48	8.4	1.65±0.10	⋯
NGC3344	CO(1–0)	4	583.7±2.4	64.1±5.8	32	7.3	2.18±0.17	4.08
⋯	CO(2–1)	4	1878.6±0.9	56.9±2.5	72	6.4	4.39±0.15	⋯
NGC3344-5	CO(1–0)	4	643.6±0.7	20.2±1.5	55	5.6	1.18±0.08	2.2
⋯	CO(2–1)	4	1939.3±1.1	23.3±2.3	37	5.8	0.92±0.08	⋯

Note. — Data for NGC2403 and NGC3344 correspond to their galactic centers. H_2 masses were calculated with Equation 1.4, i e. $M_{H_2}[M_\odot] = 4.4\pi R^2[pc] I_{CO(1-0)}$[K km/s], with the radius R measured as the CO(1–0) beamsize radius (11″) at the distances of the galaxy, from Table 2.7.

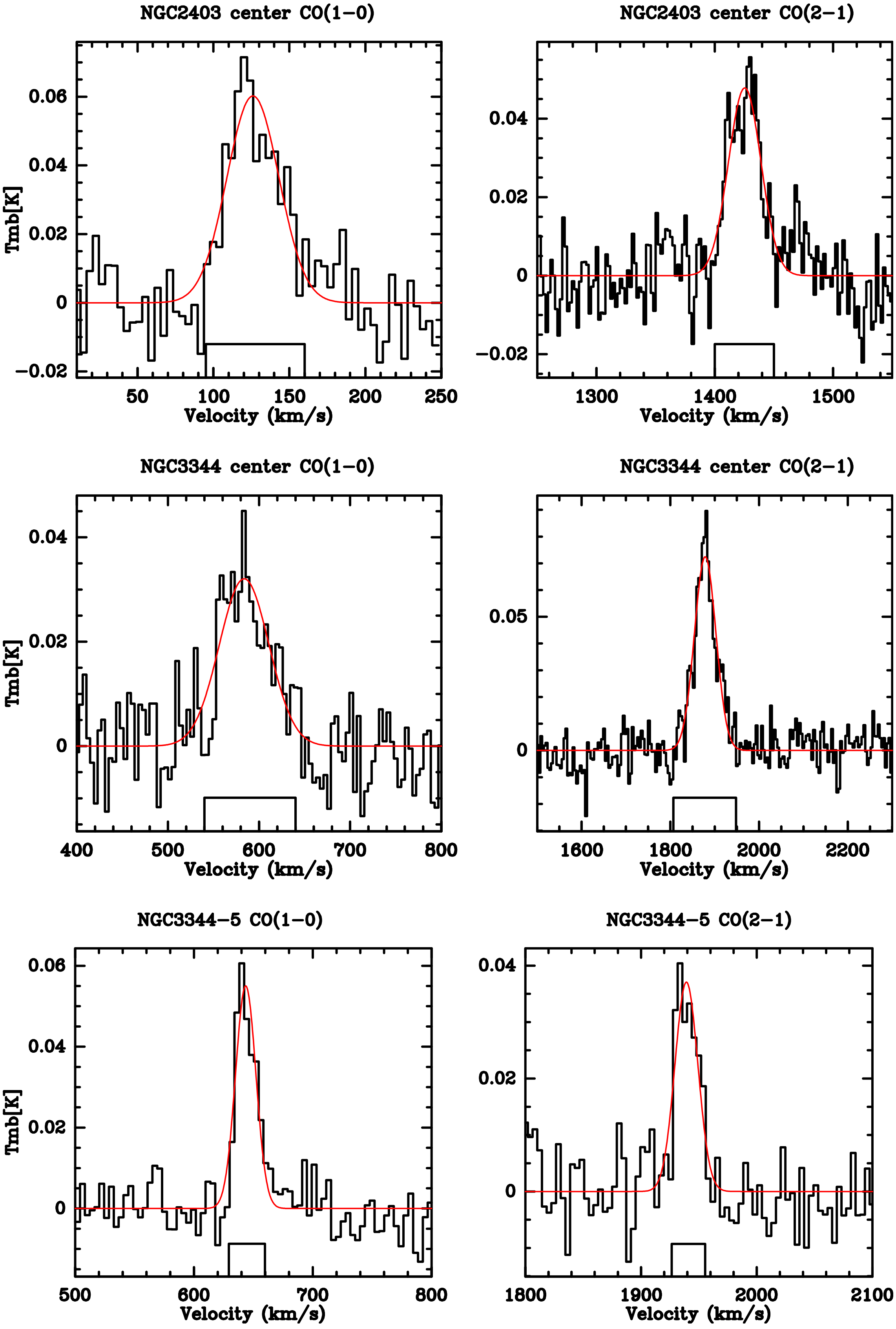

Figure 2.14: Spectra results for XUV observations 2013.

Table 2.10. 3σ upper limits of CO(1–0) emission for sources with no detection in 2013 observations.

Source	rms [mK]	I_{CO} [K km/s]	M_{H_2} [$\times 10^5 M_\odot$]
NGC2403-1	3.4	<0.31	<1.25
NGC3344-1	1.6	<0.14	<2.62
NGC3344-2	1.9	<0.17	<3.18
NGC3344-3	1.1	<0.10	<1.87
NGC3344-4	1.2	<0.11	<2.06

Note. — Rms values correspond to T_{mb} scale, and were calculated in smoothed spectra of ~30 km/s resolution. I_{CO} upper limits calculated assuming a velocity line width of 30 km/s.

For the remaining sources though, we calculated 3σ upper limits for the CO(1–0) emission, from the rms values of the spectra, and assuming a velocity width of 30 km/s. Such limits, along with their corresponding mass estimation, are listed in Table 2.10

2.2.2 Stacking

In regions where the CO is hard to detect due to its faintness, it is not surprising that no detection was found beyond the r_{25} limits, especially in bad weather conditions. But we cannot assure that the CO is not present. All we can say is that the S/N is too low to confirm a detection.

One way to overpass this problem is through stacking of the CO spectra. By averaging the spectra within a given region, we can increase the S/N and verify that faint emission is in fact an astronomical signal (Schruba et al. 2011). It is important to note that when stacking the spectra of different targets in the same galaxy we are loosing position information, but gaining crucial S/N. If a detection appears after the stacking of several spectra obtained at different positions, we can affirm that the detection is an average value inside a given range of radii, r_{min} and r_{max}, where the targets are located.

Now, in order to stack the spectra and average them, first we need to align them all to the same central velocity. So the most convenient thing to do is to center all the spectra to $v = 0$. To do this shifting in velocity we first need to know the velocity at which we would expect to find the source. Such velocities can be determined through HI velocity maps, where we can locate the position of our targets and identify the corresponding velocity. After the shifting in Δv of each spectra taken in one galaxy, we average all the spectra centered at $v = 0$ and obtain one spectra per galaxy. Figure 2.15 shows this procedure done for NGC3344, were sources 1 through 4 were

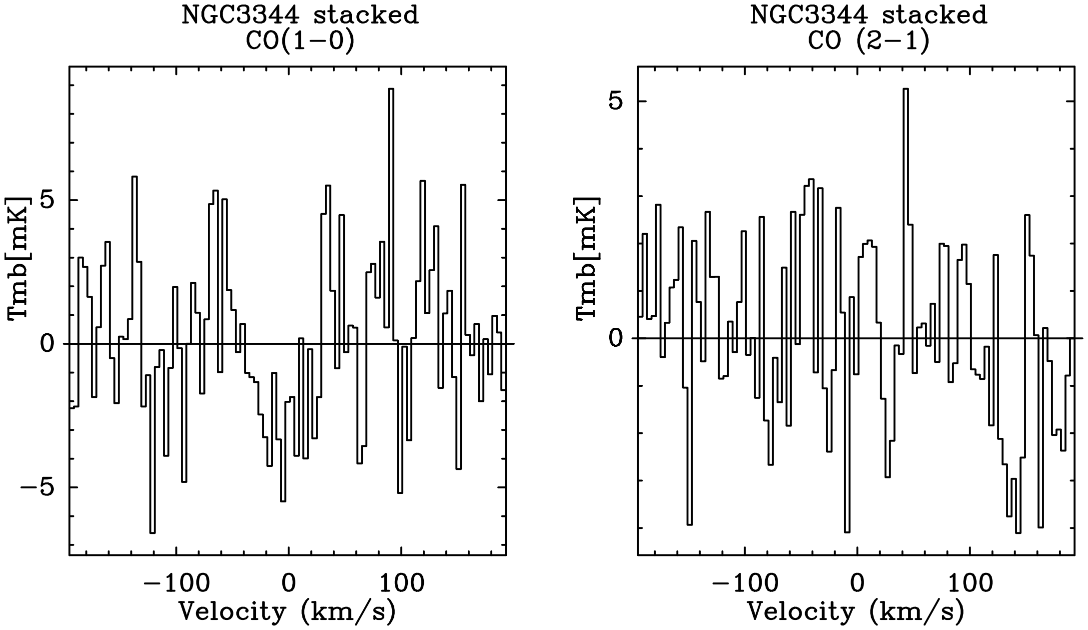

Figure 2.15: Stacking of CO spectra for NGC3344, sources 1 through 5. The velocity shifting of the spectra was done by using the HI velocities from Verdes-Montenegro et al. (2000). The stacked spectra have a resolution of 4 km/s. The rms values of the spectra are 2.82 and 1.85 mK for CO(1–0) and CO(2–1) respectively.

shifted and averaged all together. Unfortunately no detection was found either after this technique. This stacking was not done for NGC2403 because only one source could be observed (with no detection) apart from the galaxy center.

2.3 M83

The last work done in the XUV topic for this thesis was in the nearby spiral galaxy M83, including exclusive ALMA data from Cycle-2. Due to the very recent delivery of these data (March 2015), this is a work still in progress.

M83 (NGC 5236) is a remarkable example of a nearby spiral galaxy with an extended XUV disk reaching 2.3 times the optical major axis radius $R_{25} = 6.09' = 8.64$ kpc (Gil de Paz et al. 2007a). Figure 2.18 shows the GALEX NUV and FUV color-composite image of M 83. An extensive population of UV-bright star-forming regions (tracing O and B stars) and stellar clusters is revealed. The NUV and FUV surface-brightness profiles show the smooth decrease of the XUV emission out to 28 kpc in the equivalent radius $(a \times b)^{1/2}$. Located at a distance of 4.88 Mpc (Paturel et al. 2003), this SAB(s)c galaxy is expected to be representative of a large class of spirals, having no immediate neighbours with which it could interact. The 21 cm observations of M 83 also show the presence of a very large, gaseous disk extending out to 56 kpc (e.g. Tilanus & Allen 1993). The extent of this HI emission can be appreciated in Figure 2.18 in red contours. This provides another evidence of the presence of molecular gas out to large galactocentric radii, since recent studies have demonstrated that strong H I emission is on average a good tracer of regions rich in

Figure 2.16: ALMA interferometer at Llano Chajnantor in Chile. Credit: ALMA (ESO/NAOJ/NRAO)

molecular gas (e.g. Crosthwaite et al. 2002, Nieten et al. 2006).

2.3.1 Instrumentation and Observations

The Atacama Large Millimeter Array (ALMA) is the largest ground-based astronomical project in existence. Located at 5000 mts above sea level in Llano Chajnantor at the Atacama desert in Chile (Figure 2.16), it is the best interferometer in the world, in terms of sensitivity and resolution. With its 66 high-precision antennas spread over distances of up to 16 km, it studies the light coming from the coldest parts of the universe, at millimeter and sub-millimeter wavelengths, shedding light on our origins. It is nowadays the most sought-after radiotelescope in the south hemisphere, and thanks to its unprecedented sensitivity, it is ideal for the search of molecular gas in the faintest regions of XUV disk galaxies.

With its 8 spectral bands it has a frequency coverage between 84 and 950 GHz, equivalent to 0.32 and 3.57 mm in wavelength scale (Figure 2.17).

For this project we selected the band 6 to observe CO(2–1) at 229.67 GHz, as well as 3 continuum bands, centered at 232.5, 218.4 and 216.5 GHz.

For choosing the target for these observations we used the same selection criteria as for the other XUV galaxies in this chapter, i.e, by analysing the FUV, NUV and atomic gas maps, we select the regions with peaks of emission in UV and HI, beyond the optical radius. This is how we selected the region at $13^h37^m03.6^s$, $-29°59^m47.6^s$ shown in Figure 2.18, enclosed in a green rectangle of $3'$x$1.5'$ and located at $r_{gal} = 7.85' = 11$kpc. Unlike our previous IRAM-30 mt observations, where we were limited to do single ON+OFF pointings in order to reach the S/N needed in a reasonable amount of integration time, with ALMA we can take advantage of its much better sensitivity, and map the entire region within just an hour of observations.

The selected region was observed during ∼1 hour on March 2, 2014, in very good weather conditions (pwv ∼1.3 mm). The 12m array was used, with 34 antennas and a maximum baseline of 558.2 m. The map was done with 121 pointings separated by $12.9''$, and with an integration time of 10.8 sec in each one of them.

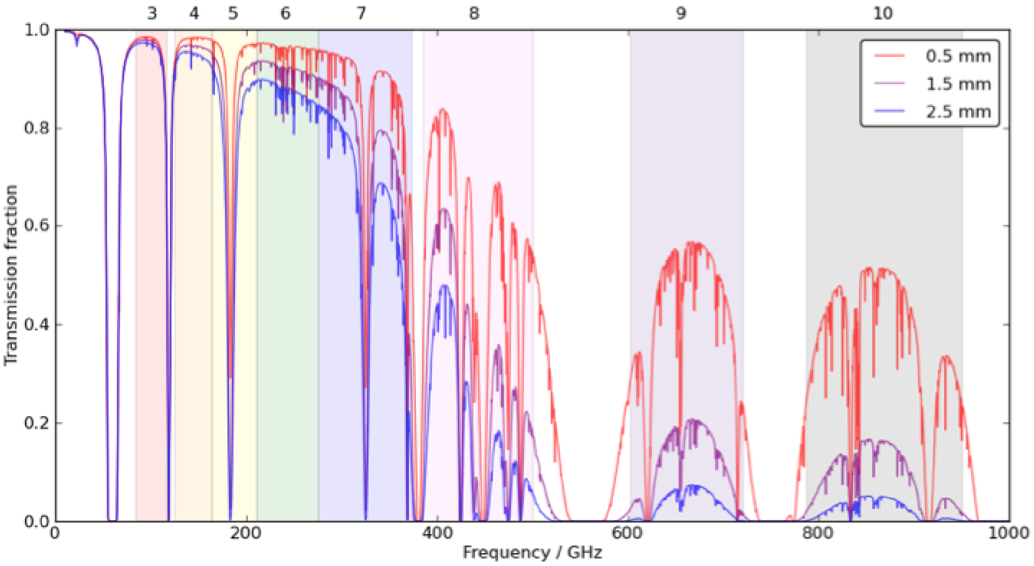

Figure 2.17: Atmospheric transmissions at 0.5, 1.5 and 2.5 mm of pwv for the 8 ALMA bands. Band 6 was used in this project to observe CO(2–1) at 229.67 GHz.

The initial goal of achieving an rms of 11.1 mJy was reached and surpassed up to 10.3 mJy, with an angular resolution of 1.6″ and a spectral one of 1.94 MHz (2.5 km/s).

2.3.2 Results

The data was reduced using the CASA[7] package, version 4.2.2. Approximately 36% of the data was flagged, which is considered normal for 12m Array data.

A CO(2–1) data cube was created with natural weighting, with a velocity range of ∼15 to ∼1015 km/s, a channel spacing of 2.5 km/s and an rms of 10.3 mJy per channel. Unfortunately, according to the observing results sent by the ALMA staff, and after a first inspection of the data cube, no CO(2-1) emission has been found yet in the selected region in M83 (Figure 2.19). It is possible that no CO(2–1) emission is present due to a low metallicty and gas density, possibly due to gas flaring in this region so far away from the center of the galaxy, and so vulnerable to external factors. This still is a work in progress though, and the are some possible candidates for clumps that could be real (see Figure 2.20) and will be analyzed in the near future, with more elaborated algorithms of search for weak emission.

Only one weak point source was detected in continuum, with a flux <2 mJy. This is a rather unexpected continuum source at such a low frequency, and it is probable

---

[7] the Common Astronomy Software Applications is developed by an international consortium of scientists based at the National Radio Astronomical Observatory (NRAO), the European Southern Observatory (ESO), the National Astronomical Observatory of Japan (NAOJ), the CSIRO Australia Telescope National Facility (CSIRO/ATNF), and the Netherlands Institute for Radio Astronomy (ASTRON) under the guidance of NRAO.

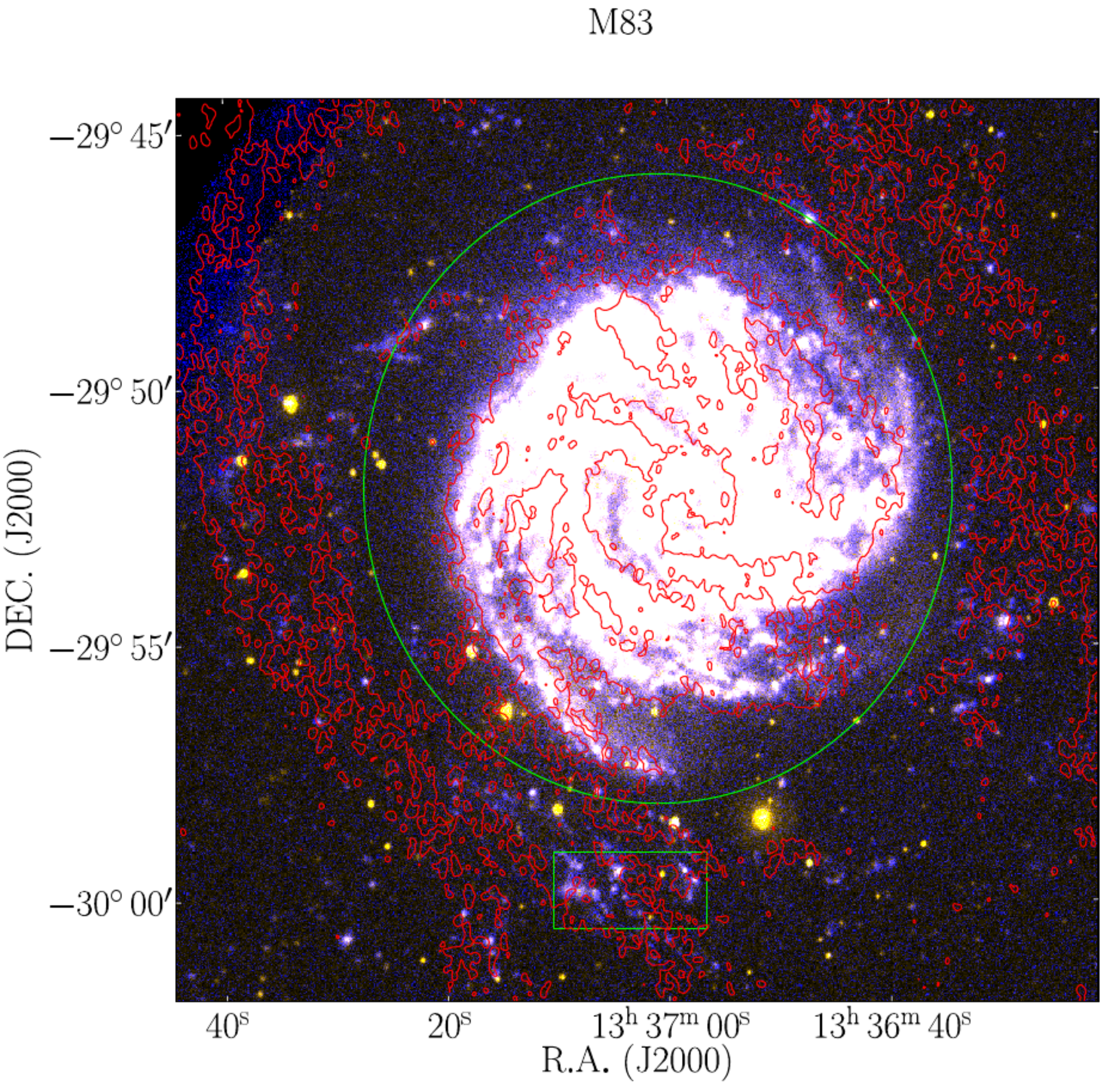

Figure 2.18: RGB composite color image of M83, with the NUV emission in red, FUV in blue and a combination of both in green. The arcsinh function has been applied to this image which allows to show faint objects while simultaneously preserving the structure of brighter objects in the field, such as the spiral arms of large galaxies (Lupton et al. 2004). The red contours shows the HI emission taken from the THINGS survey (Walter et al. 2008). The green ellipse shows the optical limit ($r_{25} = 6.09' = 8.64$ kpc). The green rectangle ($3' \times 1.5'$) marks the region selected to observe, located at $r_{gal} = 7.85' = 11$kpc, which is bright in UV and HI emission.

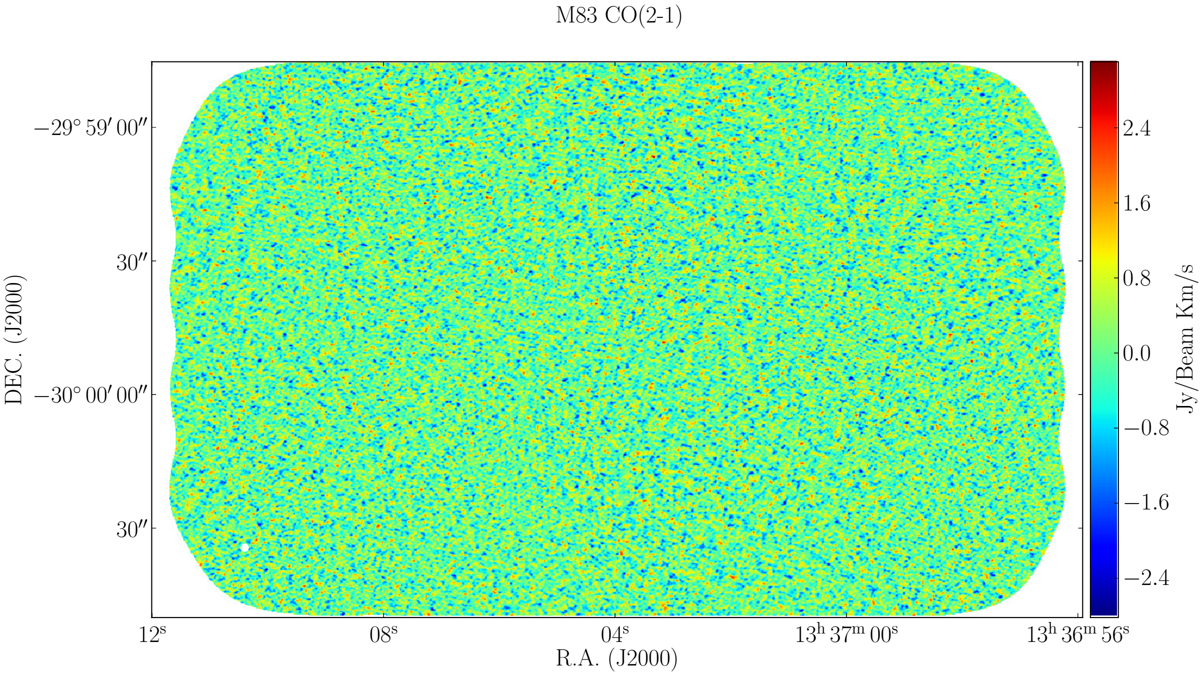

Figure 2.19: Intensity map from CO(2–1) data cube. The white circle on the lower left side indicates the 1.6″ beamsize

that a background source, such as a quasar, might be the responsible. This will be check in the near future of this work. The continuum map (Figure 2.21) has an rms of 0.19 mJy and synthesized beamsize of 0.78″×0.60″.

2.3.3 Star formation rate

To calculate the SFR taking place in this region, we used complementary data for NUV and FUV (Gil de Paz et al. 2007a), HI (Walter et al. 2008) and 24μm emission (Bendo et al. 2012). These maps are presented in Figure 2.22

Same as for M63, we used the FUV and 24μm emission to calculated the SFR surface density, which includes the FUV flux to measure the unobscured and recent star formation through the emission of O and B stars, and the 24 μm flux that traces the obscured FUV emission that is re-emitted in the FIR by dust grains. From Leroy et al. (2008):

$$\Sigma_{\rm SFR}[{\rm M_\odot yr^{-1} kpc^{-2}}] = (8.1\times10^{-2} {\rm I_{FUV}}[{\rm MJy\ sr^{-1}}] + 3.2\times10^{-3} {\rm I_{24\mu m}}[{\rm MJy\ sr^{-1}}])\times\cos({\rm i}) \tag{2.4}$$

where i corresponds to the inclination angle of the galaxy, 24°.

We reprojected the FUV map from Figure 2.22 to the same resolution and spatial grid of the 24μm, and created a $\Sigma_{\rm SFR}$ map following Eq. 2.4, pixel by pixel. This

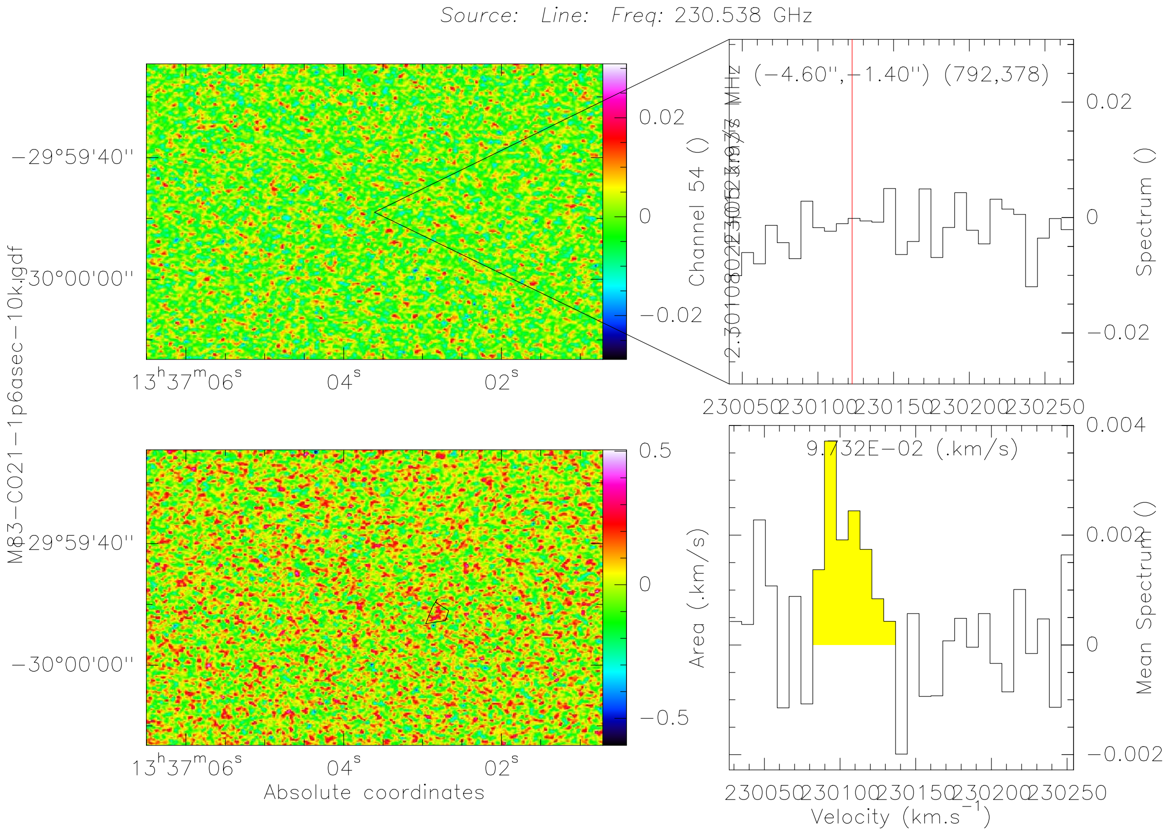

Figure 2.20: Hint of a possible clump in the CO(2–1) data cube of M83. It will be analyzed more carefully in the near future, with a special algorithm of search for weak emission.

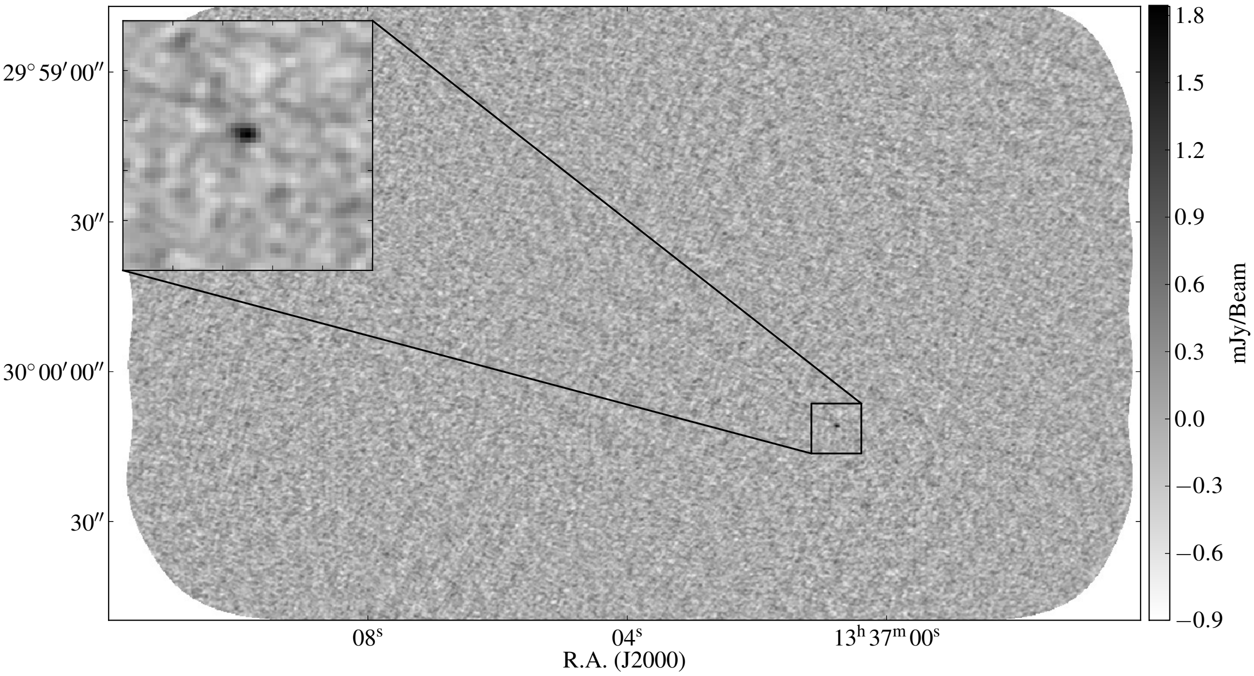

Figure 2.21: Continuum map of M83 with a weak detection on a point source (<2mJy). The rms of the map is 0.19 mJy.

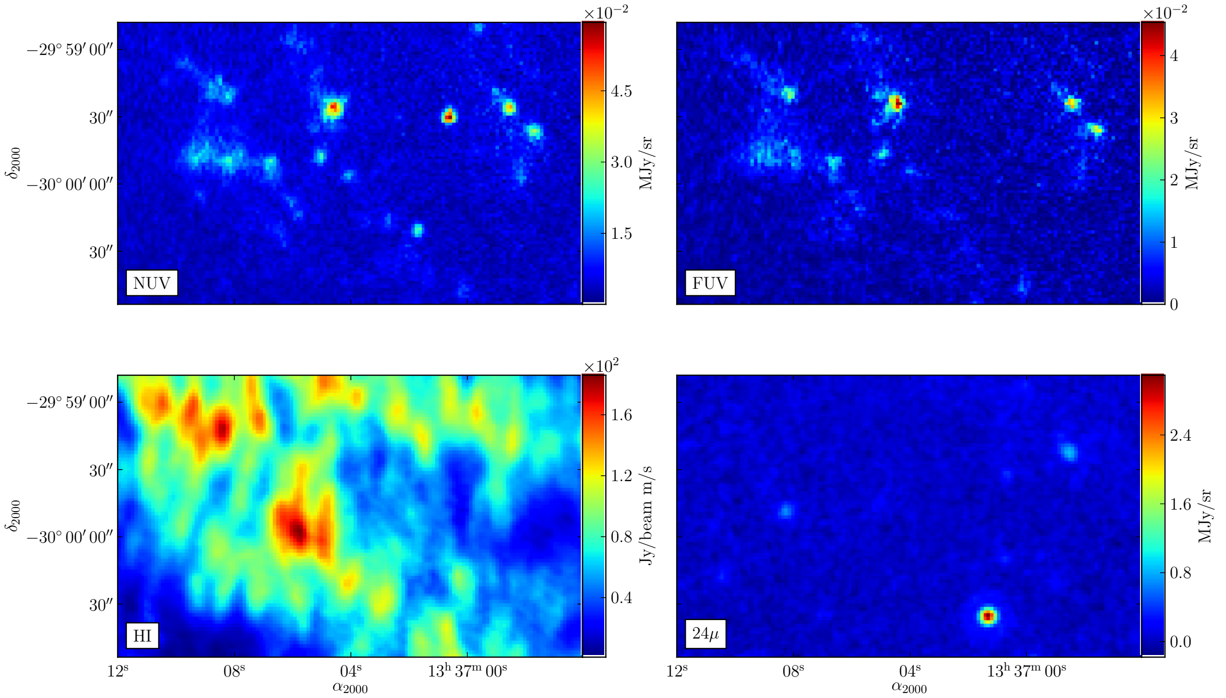

Figure 2.22: Complementary data for M83, with NUV, FUV, HI and 24μm maps.

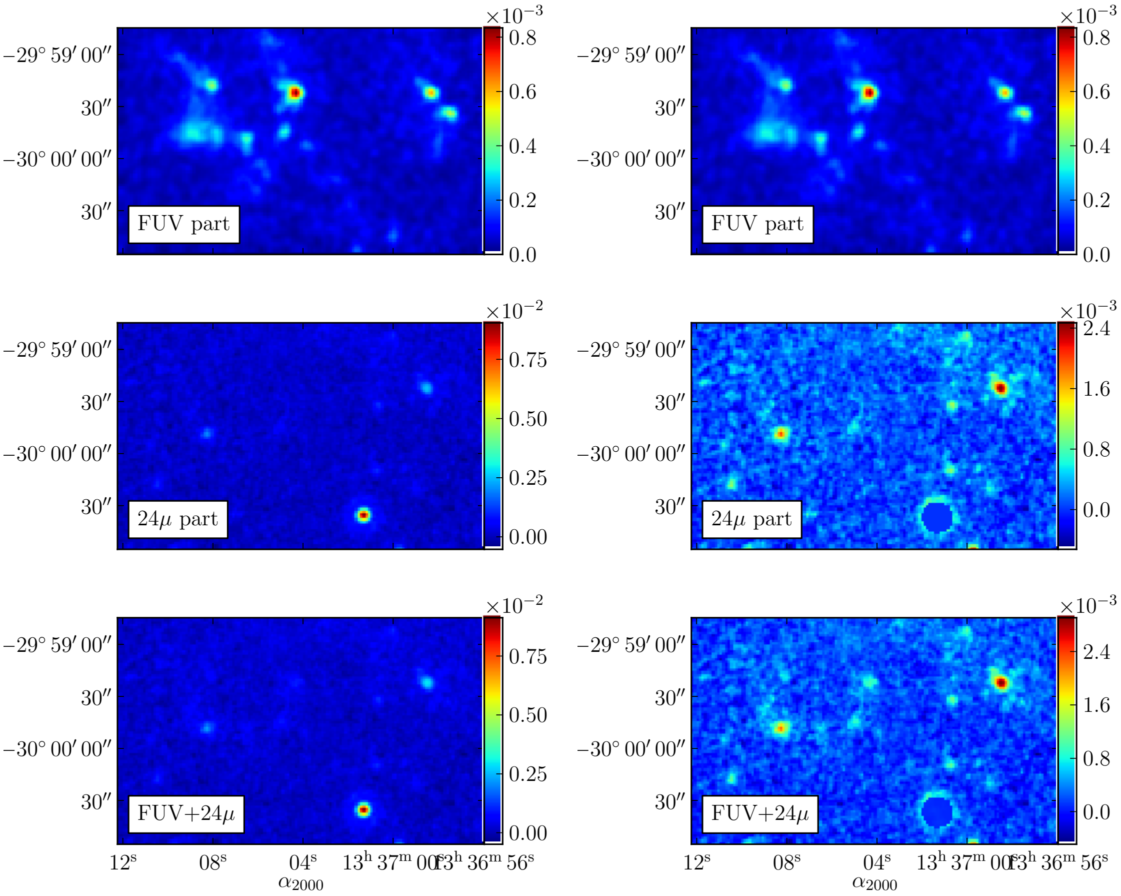

Figure 2.23: $\Sigma_{\rm SFR}$ in units of $\rm M_{\odot}yr^{-1}kpc^{-2}$ (calculated with Eq. 2.4), for the FUV contribution only (top), the 24μm (middle) and the combination of both (bottom). Right side panels have a bright foreground point source subtracted, to de-saturate the image.

map is presented in Figure 2.23 (left panels), where we show the $\Sigma_{\rm SFR}$ with the FUV contribution only, with the 24μm, and the combination of both.

In Figure 2.23 we noted a very bright and point source at 24μm that was saturating the image, probably a source in the foreground, not part of the galaxy. We masked this source in the maps of the right panels, and could appreciate much better the spatial distribution on the $\Sigma_{\rm SFR}$ across the entire region mapped. The $\Sigma_{\rm SFR}$ is mainly dominated by the 24μm emission.

Chapter 3

Ram-Pressure stripping

Contents

3.1 Virgo cluster **78**

3.2 Observations **80**

3.3 Data Reduction and spectral line fitting **80**

3.4 Results **85**

3.5 Star formation efficiency **85**

3.5.1 HI photometry 87

3.5.2 Hα data 87

3.5.3 K-S relation 92

3.6 Publication **93**

For a long time we have known that galaxies are not isolated systems. On the contrary, they are highly influenced by their surrounding medium. This can be directly seen in our local universe, where galaxies that belong to dense clusters have different properties than the ones in a more isolated medium, even when they have the same size, mass or age. In particular, one of the most interesting differences relies on their gas content, since there has been long observational evidence that spiral galaxies in clusters have less neutral atomic hydrogen than galaxies of the same morphological type in the field (Haynes & Giovanelli 1984).

No doubt this HI deficiency is strongly related to the fact that those galaxies belong to a dense galaxy cluster, where galaxies are ruled by the cluster's dynamics, and can easily interact with each other. In fact, in overdense cluster environments, galaxies are significantly transformed, through tidal interactions with other galaxies or with the cluster as a whole (e.g. Merritt 1984, Tonnesen et al. 2007), and interactions with the intra-cluster medium (ICM), which strips them from their gas content. This effect is most likely to be the result of ram-pressure, i.e the force that any body, in this case a galaxy, feels when moving through a fluid, like the ICM. This ram-pressure stripping (RPS) process has been described by Gunn & Gott (1972), who discussed what might happen if there would be any intergalactic gas left after a cluster had collapsed. The interstellar material in a galaxy would feel the ram-pressure of the ICM as it moves through the cluster. If this ram-pressure force is larger than the restoring gravitational force of the disk, the gas of the outer disk of the galaxy would be stripped off. Even more, they estimate that for a galaxy moving at a typical velocity of ∼1700 km/s in the Coma cluster, the ISM would be stripped in one pass. This would explain why so few normal spiral galaxies are seen in nearby clusters, and so many gas poor, non star forming disk galaxies (Spitzer & Baade 1951).

The RPS has also been simulated by many groups (Quilis et al. 2000, Vollmer et al. 2001, Roediger & Hensler 2005; Jáchym et al. 2007), showing the feasibility of gas stripping due to ram-pressure, and evidence of stripping has been observed in many cases (Kenney et al. 2004; Chung et al. 2007; Sun et al. 2007, Vollmer et al. 2008) in several galaxies of the nearby clusters Virgo and Abell 3627.

RPS and/or tidal interactions can disperse the interstellar gas (ISM) of galaxies at large distance, up to 100kpc scales, as shown by the spectacular tail of ionized gas in Virgo (Kenney et al. 2008), but what is the fate of the stripped gas? According to the time-scale of the ejection, the relative velocity of the ICM-ISM interaction, and the environment, it could be first seen as neutral atomic gas (Chung et al. 2009, Scott et al. 2012, Serra et al. 2013), then ionized gas detected in Hα (Gavazzi et al. 2001, Cortese et al. 2007, Yagi et al. 2007, Zhang et al. 2013), and is finally heated to X-ray gas temperatures (e.g. Machacek et al. 2005, Sun et al. 2010). In rarer cases, it can be seen as dense and cold molecular gas, detected as carbon monoxyde (CO) emission (Vollmer et al. 2005, Dasyra et al. 2012, Jáchym et al. 2014). The presence of these dense molecular clumps might appear surprising, since the RPS should not be able to drag them out of their galaxy disks (Nulsen 1982; Kenney & Young 1989). However they could reform quickly enough in the tail. The survival of these clouds in the hostile ICM environment, with temperature 10^7 K and destructive X-rays (e.g., Machacek et al. 2004; Fabian et al. 2006; Tamura et al. 2009) is a puzzle, unless they are self-shielded (e.g. Dasyra et al. 2012, Jáchym et al. 2014). The presence of cold molecular gas is also observed in rich galaxy clusters, with cool cores. Here also a multi-phase gas has been detected, in CO, H_α, X-rays and also the strongest atomic cooling lines (Edge et al. 2010). Ionized gas, together with warm atomic and molecular gas and cold molecular gas clouds coexist in spatially resolved filaments around the brightest cluster galaxy, such as in the spectacular prototype Perseus A (Conselice et al. 2001; Salomé et al. 2006, 2011; Lim et al. 2012).

The survival of molecular clouds was also observed by Braine et al. (2000) in several tidal tails, and in particular in the interacting system Arp 105 (dubbed the Guitar), embedded in the X-ray emitting medium of the Abell 1185 cluster (Mahdavi et al. 1996). Again, the formation in situ of the molecular clouds is favored (Braine et al. 2000). In the Stephan's Quintet compact group, where X-ray gas and star formation have been observed in between galaxies (O'Sullivan et al. 2009), the shock has been so violent (1000 km/s) that H_2 molecules are formed and provide the best cooling agent, through mid-infrared radiation (Cluver et al. 2010). In this shock, multi-phases of gas coexist, from cold dense molecular gas to X-ray gas.

Does this gas form stars? In usual conditions, inside galaxy disks, the star formation is observed to depend essentially on the amount of molecular gas present (e.g. Bigiel et al. 2008; Leroy et al. 2013). A Kennicutt-Schmidt (K-S) relation is observed, roughly linear, between the surface densities of star formation and molecular gas, leading to a depletion time-scale of 2 Gyr. But this relation does not apply in special regions or circumstances, such as galaxy centers (Casasola et al. 2015), outer parts of galaxies and extended UV disks (Dessauges-Zavadsky et al. 2014), or low surface brightness galaxies (Boissier et al. 2008). Little is known on star formation in gas clouds stripped from galaxies in rich clusters. Boissier et al. (2012) have put constraints on this process, concluding to a very low star formation efficiency, lower by an order of magnitude than what is usual in galaxy disks, and even lower than outer parts of galaxies or in low surface brightness galaxies. It is interesting to better constrain this efficiency, given the large amount of intracluster light (ICL) observed today (e.g. Feldmeier et al. 2002, Mihos et al. 2005). These stars could come from tidal stripping of old stars formed in galaxy disks, or also a large fraction could have formed in situ, from ram-pressure stripped gas. More intracluster star formation could have formed in the past (DeMaio et al. 2015). The origin of the ICL could bring insight on the relative role of galaxy interactions during the cluster formation, or cluster processing after relaxation.

3.1 Virgo cluster

One of the best laboratories to study the interaction between galaxies is the Virgo Cluster. Located at ∼18 Mpc and with a mass of 1.2×10^{15} $M_\odot$ (Fouqué et al. 2001), it hosts more than a thousand spiral and elliptical galaxies, such as M87, M86 and M49. Many of its galaxies interact with each other in merging or collissional processes, or interact with the ICM, which strips them from their gas content. Such is the case in particular of the group of galaxies close to M86, which shows an spectacular bridge of ionized gas connecting M86 with NGC4438, and a kpc scale plume of atomic gas being stripped from NGC4388 (Figure 3.1).

This tail northeast of NGC4388 is one of the best ram-pressure tail to probe molecular gas survival and the star formation efficiency, where X-ray gas has been mapped (Iwasawa et al. 2003) and young stars have been found (Yagi et al. 2013). It is located at about 400 kpc in projection from the cluster center M87. NGC 4388 is moving at a relative velocity redshifted by 1500km/s with respect to M87, and more than 2800 km/s with respect to the M86 group. This strong velocity may explain the violent RPS, the high HI deficiency of NGC 4388 (Cayatte et al. 1990) and the large ($\sim$ 35kpc) emission-line region found by Yoshida et al. (2002), northeast of the galaxy. The ionized gas has a mass of 10^5 $M_\odot$, and is partly excited by the ionizing radiation of the Seyfert 2 nucleus in NGC 4388. The RPS plume is even more extended in HI (Oosterloo & van Gorkom 2005), up to 110 kpc, with a mass of 3.4 x 10^8 $M_\odot$. Gu et al. (2013) have found neutral gas in absorption in X-ray, with column densities 2-3×10^{20} cm^{-2}, revealing that the RPS tail is in front of M86. The high ratio between hot and cold gas in the clouds means that significant evaporation

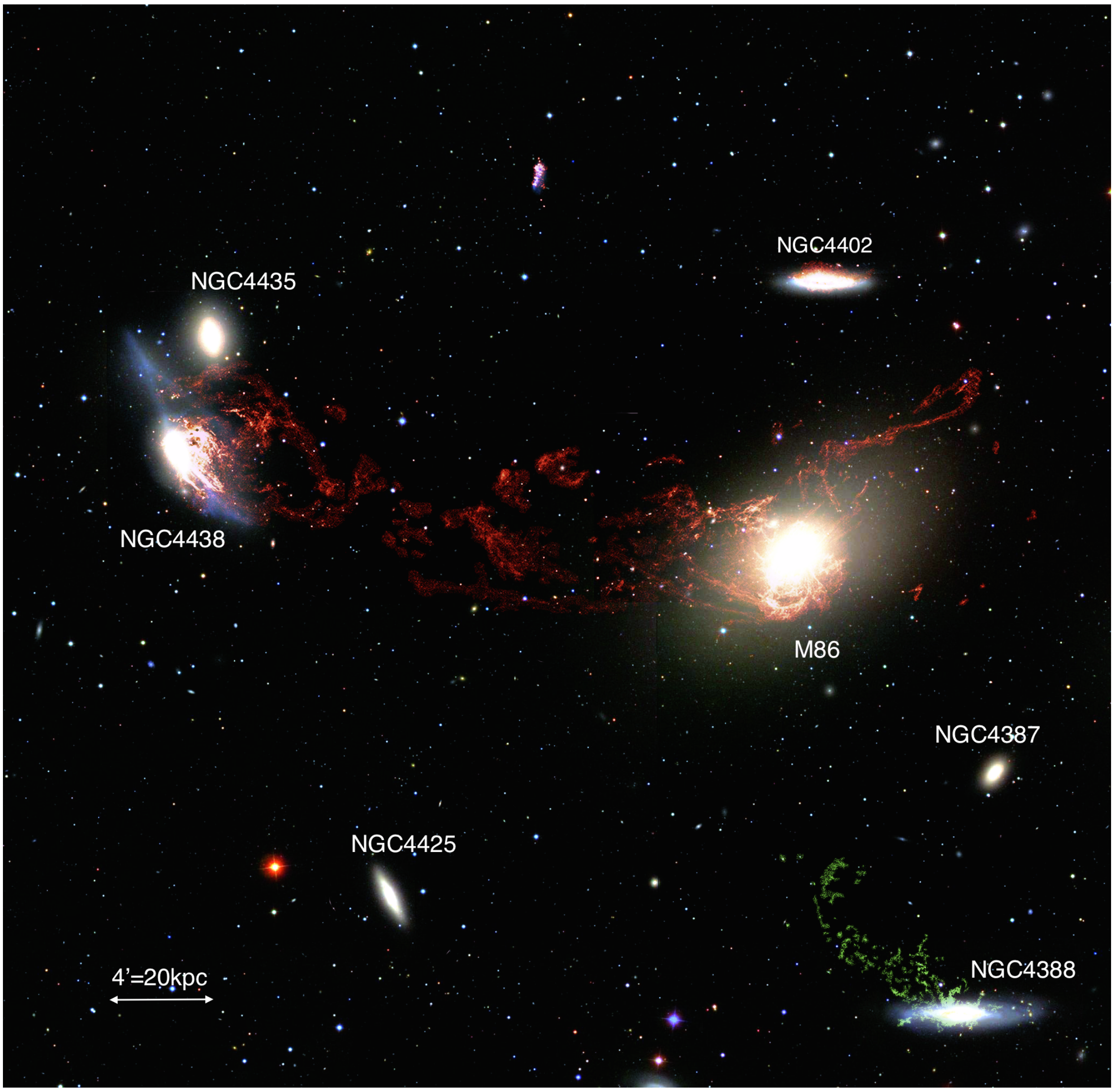

Figure 3.1: Hα + NII image of the Virgo cluster from Kenney et al. (2008). In red: low velocity emission <500 km/s. In green: high velocity emission >2000 km/s.

has proceeded. Yagi et al. (2013) find star-forming regions in the plume at 35 and 66 kpc from NGC 4388, with solar metallicity and age 6 Myrs. Since these stars are younger than the RPS event, they must have formed in situ.

The aim of the work presented in this chapter is to probe the presence of molecular gas in the stripped tail northeast of NGC4388, and study its star formation efficiency. Section 3.2 presents the IRAM-30m CO observations, with their corresponding data reduction and line fitting in Section 3.3. Results are presented in Section 3.4 and the gas star formation efficiency discussed in Section 3.5. Finally, the publication of this work submitted to A&A is presented in Section 3.6.

3.2 Observations

Observation in the HI stream connecting M86 and NGC4388 were done in two runs. The first one as part of project 195-13 (with 28 hrs of observations) took place during December 5-8th 2013 in excellent weather conditions, with a τ <0.1 and a pwv between 0.1 and 3 mm. The second run was part of project 075-14, with 47 hrs of observations during June 25-30th 2014. The weather conditions in this run were poor to average, with a τ between 0.2 and 0.6, and a pwv between 3 and 10 mm.

The targets for the first run were chosen in the regions along the HI stream for having a match of HI, Hα and 250μm emission, to trace atomic gas, ionized gas and dust respectively. With this criteria six sources were selected and observed (Figure 3.2).

All these targets are listed in Table 3.1, including their coordinates, heliocentric velocities, and the integration time spent on them.

These observations resulted in two $\sim$6σ detections of CO(2–1) , in Source-1 and HaR-2 (Figure 3.3 bottom).

HaR-2 is a source of particular interest since it is so far away from NGC4388 ($\sim$70 kpc), were molecular gas in unexpected, and it has also shown a strong detection in Hα with the Subaru Telescope (Yagi et al. 2013), therefore this source was chosen as a central target for the 2014 observations, selecting five more targets close to it, and where the HI emission seemed brighter (see upper right box in Fig 3.2).

3.3 Data Reduction and spectral line fitting

The data were reduced using the CLASS software from the GILDAS package. First, a careful inspection of all scans was done, to remove the bad ones. The approved scans of the same source, CO line and backend were averaged with a normal time weighting, to obtain one spectra. Then, each spectra was inspected individually, and in both of its polarizations, to identify a possible CO emission line. If a detection was found in the spectra of both backends, the best spectra was chosen (in terms of spectral resolution and S/N) as the final one. The selected

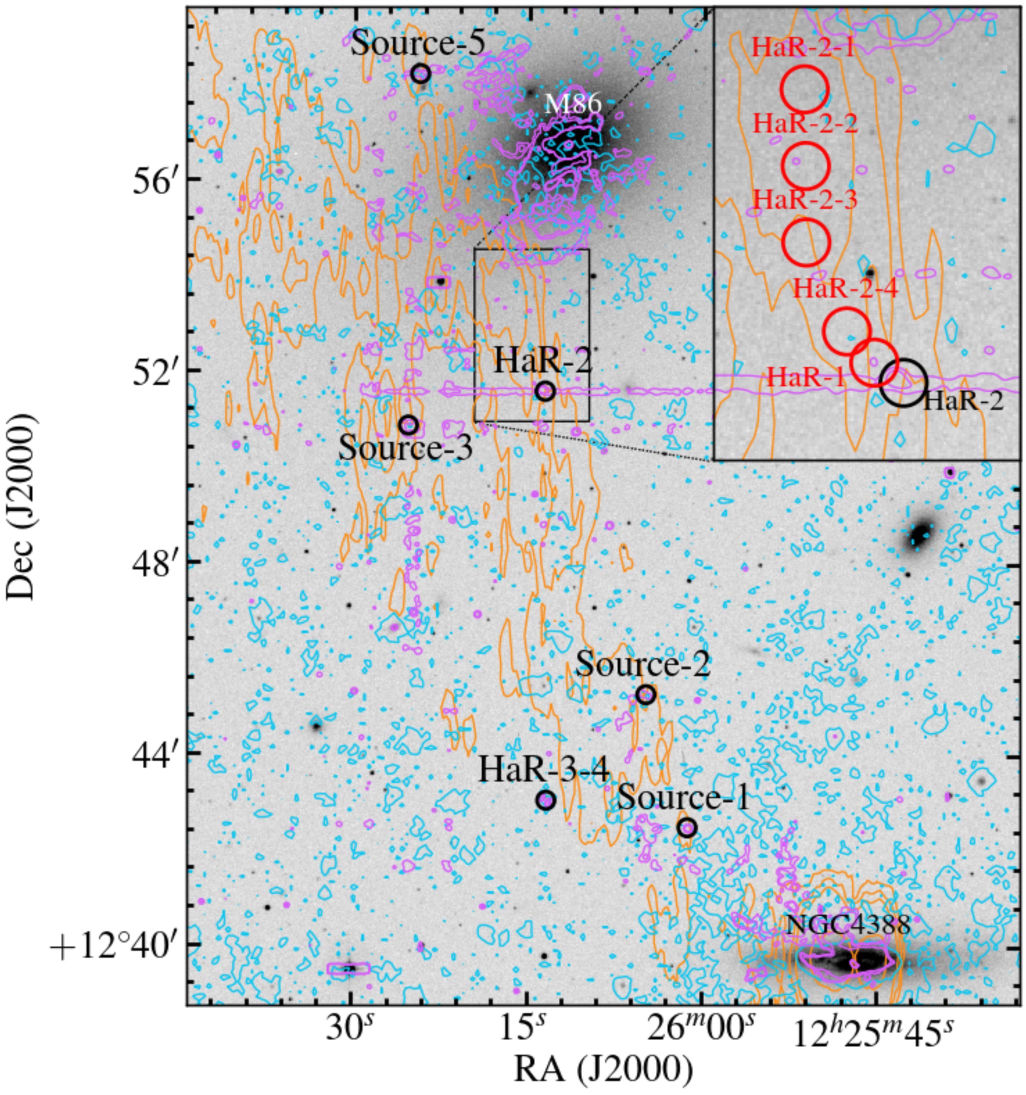

Figure 3.2: Targets observed in the Virgo Cluster. Orange: HI contours levels at 1, 5, 10 and 50 $\times 10^{19} cm^{-2}$ from Oosterloo & van Gorkom (2005). Purple: Hα contours levels at 5, 11 and 50 e^{-}/sec (Kenney et al. 2008). Cyan: 250μm contour levels at 0.01 and 0.1 Jy/beam (Davies et al. 2012). In zoomed regions: targets selected close to HaR-2 for run 075-14.

Table 3.1. Targets and Observations.

Source	RA(J2000) $[^{hr}:^{m}:^{s}]$	DEC(J2000) $[^{deg}:^{m}:^{s}]$	hel. vel. [km/s]	ON+OFF [hrs]
Source-1	12:26:01.3	12:42:30.1	+2500	4.2
Source-2	12:26:04.9	12:45:16.7	+2500	2.9
Source-3	12:26:25.4	12:50:53.6	+2200	3.1
Source-5	12:26:24.5	12:58:14.6	+2000	3.9
HaR-2	12:26:13.7	12:51:36.9	+2230	7.2
HaR-3-4	12:26:13.5	12:43:03.7	+2500	3.8
HaR-2-1	12:26:16.9	12:53:55.6	+2230	4.5
HaR-2-2	12:26:16.9	12:53:19.3	+2230	5.6
HaR-2-3	12:26:16.9	12:52:43.1	+2230	6.2
HaR-2-4	12:26:15.5	12:52:01.1	+2230	8.0
HaR-1	12:26:14.6	12:51:46.4	+2230	3.8
NGC4388	12:25:46.6	12:39:44.0	+2550	1.2

Note. — Sources in the first 6 rows correspond to run 195-13, and last 6 rows to run 075-14 (although source HaR-2 was observed in both runs). NGC4388 was observed for calibration purposes. Heliocentric velocities are referencial, taken from Oosterloo & van Gorkom (2005).

spectra with CO emission are presented in Figures 3.3 and 3.4, which contain both polarizations, horizontal and vertical, combined.

Baselines were subtracted with polynomials of order 0 and 1 depending on the source, and antenna temperatures were corrected by the telescope beam efficiency ($\mathrm{B_{eff}}$) and forward efficiency ($\mathrm{F_{eff}}$) to obtain main beam temperatures:

$$T_{\mathrm{mb}} = \frac{F_{\mathrm{eff}}}{B_{\mathrm{eff}}} T_a^* \tag{3.1}$$

with $\mathrm{B_{eff}}$ and $\mathrm{F_{eff}}$ equal to 0.78 and 0.94 respectively for 115 GHz, and to 0.59 and 0.92 for 230 GHz.[1]

Spectra were smoothed with the hanning method to degrade the velocity resolution until obtain a value no greater than 1/3 of the FWHM line.

Finally, a simple gaussian line was fitted to the line candidate. The CLASS fit return the velocity position of the line, its FWHM, the peak temperature and the integrated line intensity.

Such spectra and fitting results for sources with CO detection are presented in Figures 3.3 and 3.4, and then in Table 3.3.

---

[1] http://www.iram.es/IRAMES/mainWiki/Iram30mEfficiencies

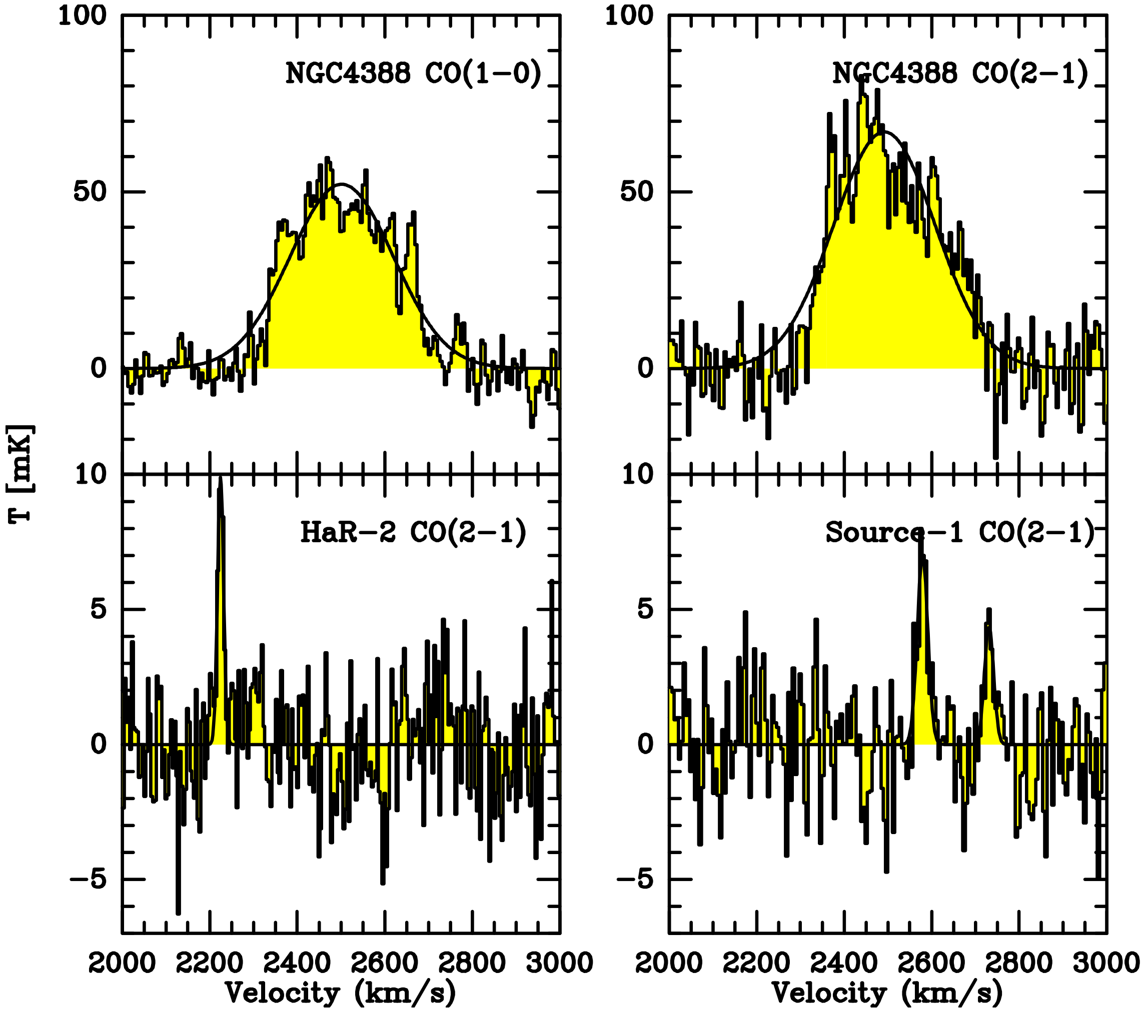

Figure 3.3: Top: CO(1–0) and CO(2–1) spectra for the center of NGC4388, observed for calibration purposes. Bottom: CO(2–1) spectra for HaR-2 and Source-1, taken in the first observing run 195-13. The temperature scale corresponds to main beam temperature (T_{mb}).

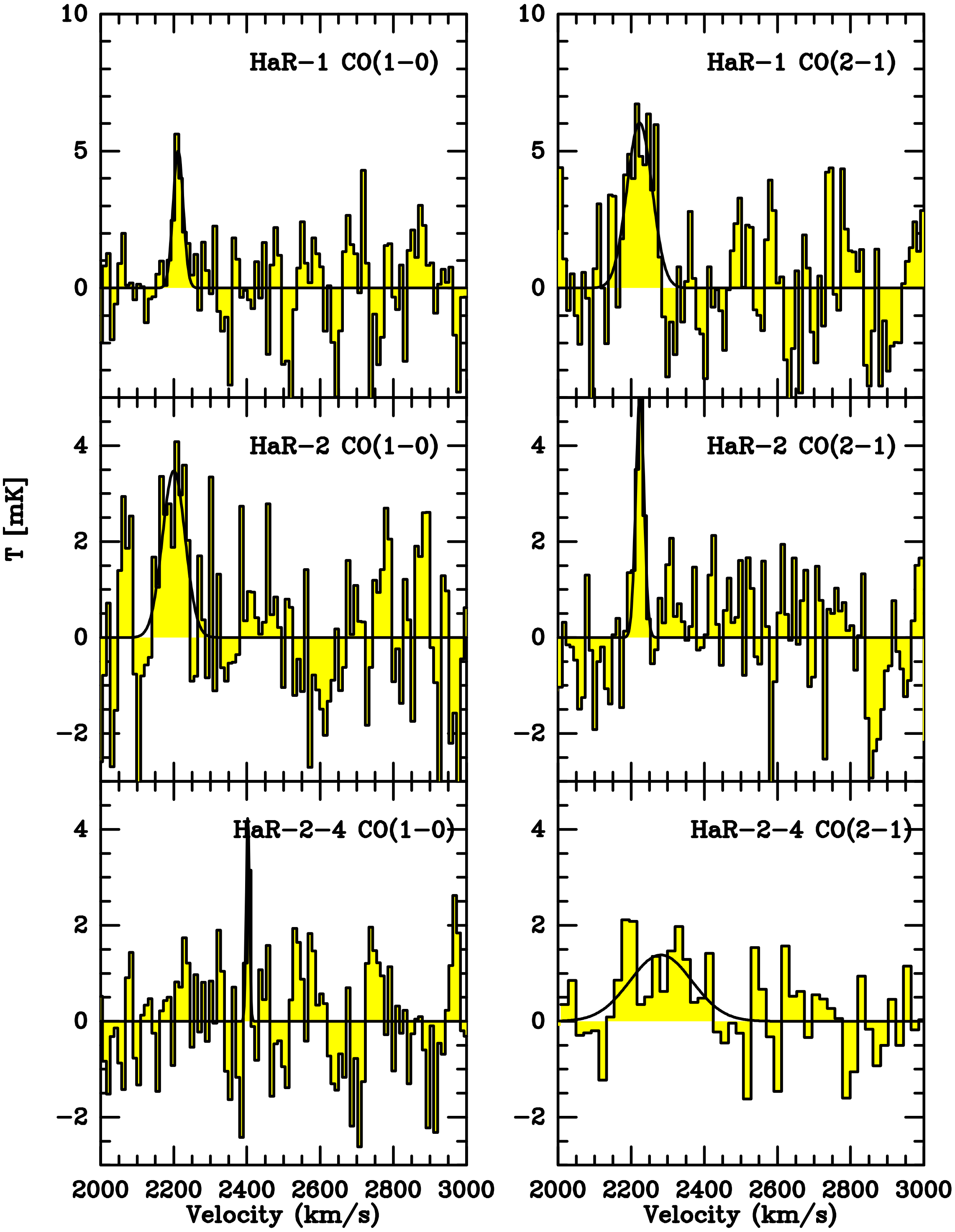

Figure 3.4: Final CO spectra for HaR-2, HaR-1 and HaR-2-4 from run 075-14. Only HaR-2 in CO(2–1) has data combined from both runs. The temperature scale corresponds to T_{mb}.

Table 3.2. CO(1–0) upper limits at 3σ for sources with no detection.

Source	int. time [min]	rms [mK]	I_{CO} [K km/s]	M_{H_2} [$10^6 M_\odot$]	Σ_{H2} [$M_\odot pc^{-2}$]
Source-2	173	1.2	<0.11	<1.21	<0.48
Source-3	186	1.0	<0.09	<0.99	<0.40
Source-5	231	1.2	<0.11	<1.21	<0.48
HaR-3-4	229	1.0	<0.09	< 0.99	<0.40
HaR-2-1	269	1.1	<0.10	<1.10	< 0.44
HaR-2-2	334	1.1	<0.10	<1.10	<0.44
HaR-2-3	374	0.6	<0.05	<0.55	<0.22

Note. — We assumed a Δv of 30 km/s to calculate the I_{CO}.

3.4 Results

As a result of this second run, we could confirm the CO detection in HaR-2, and obtain two more, in HaR-1 and HaR-2-4 (Figure 3.4). Given the large distances of these sources to NGC4388 (~70 kpc), it is not likely that the molecular gas was stripped from the galaxy, and must have formed in situ in the HI gas plume. Details of these detections and their fitting results are presented in Table 3.3. The range of linewidths found for these detections is quite large, between 10 and 200 km/s, and their main beam temperatures were found to be between 1 and 10 mK. H_2 masses were derived from the CO(1–0) line intensity folwing Eq. 1.4, with a Galactic CO conversion factor of 2.0×10^{20} $cm^{-2}(K\ km/s)^{-1}$ and a correction factor of 1.36 to account for heavy elements. For the 3 sources with CO(1–0) detected, these masses were found to be between 0.6 and 3 $\times 10^6$ $M_\odot$

For the rest of the sources, with no visible CO detections, 3σ upper limits for I_{CO} where calculated from their rms values, assuming a $\Delta v = 30$ km/s . Such limits are presented in Table 3.2.

3.5 Star formation efficiency

To estimate how fast is the gas being transformed into stars, we compare the SFR surface density versus the gas surface density in a K-S relation, to understand the efficiency of this star formation process. Since these are low gas density regions, we can expect a large amount of gas in atomic phase, larger than in molecular phase. Therefore both components, atomic and molecular, need to be taken into account when estimating a total amount of gas to be converted into stars.

Molecular gas can be directly estimated from the CO(1-0) line intensity, obtained from our observations. If we consider Eq. 1.4 and average the HI mass in the source's area, i.e $M_{HI}/\pi\Omega^2$, we obtain the H_2 surface density:

Table 3.3. CO detections in the Virgo Cluster.

Source	line	backend	int. time [min]	v_0 [km/s]	FWHM [km/s]	resol. [km/s]	T_{mb} [mK]	rms [mK]	I_{CO} [K km/s]	M_{H_2} [$10^6 M_\odot$]
HaR-2	CO(2–1)	FTS	268	2224.9±1.2	16.2 ±2.9	4	9.9	2.0	0.17± 0.03	· · ·
Source-1(1)	CO(2–1)	WILMA	232	2579.2±2.3	28.7±6.1	5.2	7.0	2.5	0.21±0.04	· · ·
Source-1(2)	CO(2–1)	WILMA	232	2731.3±4.0	25.1±12.4	5.2	4.3	2.5	0.12±0.04	· · ·
HaR-2	CO(1–0)	WILMA	318	2200.3±8.6	72.6±15.9	10.4	3.5	2.1	0.27±0.06	3.24
· · ·	CO(2–1)	WILMA	586	2224.3±2.7	26.6±7.2	10.5	5.0	1.8	0.14±0.03	· · ·
HaR-1	CO(1–0)	WILMA	229	2212.2±4.5	32.8±13.8	10.4	5.0	2.3	0.18±0.05	2.11
· · ·	CO(2–1)	WILMA	229	2223.2±7.8	80.9±15.15	10.4	6.0	3.2	0.52± 0.09	· · ·
HaR-2-4	CO(1–0)	WILMA	665	2402.6±2.3	10.4±62.1	10.4	4.2	1.5	0.47±0.02	0.57
· · ·	CO(2–1)	WILMA	665	2281.7±26.4	200.4±45.3	20.8	1.4	2.8	0.29±0.07	· · ·
NGC4388	CO(1–0)	WILMA	87	2501.7±2.7	278.6±5.9	5.2	52.2	5.7	15.47±0.30	186
· · ·	CO(2–1)	WILMA	82	2492.0±3.5	273.3±7.4	5.2	67	9.4	19.49±0.49	· · ·

H_2 masses were directly calculated from the CO(1–0) emission using Eq.1.4, using a source radius R equivalent to the CO(1–0) beamsize radius at the distance for the source (17.5 Mpc from Mei et al. 2007).

Note. — First three rows correspond to observing run 195-13. Both components shown in Figure 3.3 for Source-1 are listed. H_2 masses were calculated as $M_{H_2}[M_\odot]=4.4\pi R^2[\mathrm{pc}]\ I_{CO}[\mathrm{K\ km/s}]$, which uses a Galactic CO conversion factor of 2.0×10^{20} [$\mathrm{cm}^{-2}(\mathrm{K\ km/s})^{-1}$] and a correction factor of 1.36 to account for He. A distance to the Virgo Cluster of 17.5 Mpc (Mei et al. 2007) was used to calculate the CO(1–0) beam radius as source radius. HaR-2 includes data taken in the first run only for CO(1–0), and data combined from both runs for CO(2–1).

$$\Sigma_{H_2}[M_\odot pc^{-2}] = 4.4 I_{CO(1-0)}[K\ km\ s^{-1}] \tag{3.2}$$

These values are listed in column 2 of Table 3.4 for the sources with CO(1–0) detections, including upper limits for the sources with no CO detection using Table 3.2.

3.5.1 HI photometry

The mass of atomic gas can be directly estimated from the HI column density (N_{HI}), which integrated inside the source's area gives the amount of HI atoms present in that area. Thus, by multiplying by the hydrogen mass:

$$M_{HI} = \mu m_H \int N_H dA \tag{3.3}$$

where $\mu = 1.36$ is the correction factor to account for heavy elements and m_H is the mass of one hydrogen atom ($8.4\times10^{-58} M_\odot$). Since the area differential is related with the solid angle differential as $d\Omega = dA/D^2$, then

$$M_{HI} = \mu m_H D^2 \int N_H d\Omega \tag{3.4}$$

where the solid angle Ω used here corresponds to the CO(1–0) beamsize radius of $11''$. To measure the HI mass for the sources in our sample, we used the HI column density map of Oosterloo & van Gorkom (2005) for the plume northeast of NGC4388 (Figure 3.5). The corresponding integrated column densities are listed in column 3 of Table 3.4.

Finally, the HI surface density is calculated by averaging the HI mass in the surface area to be considered, i.e $\Sigma_{HI} = M_{HI}/\Omega$, where Ω is the CO(1–0) beam solid angle at the distance of the source (i.e $\Omega = 2.74 \times 10^6$ pc^2 at D=17.5 Mpc). This surface densities are presented in column 4 of Table 3.4.

3.5.2 Hα data

The Hα emission seen in the plume northeast of NGC4388 shows evidence of star forming regions (HII regions). Therefore it can be used to estimate the rate at which the gas is being converted into stars. The SFR can be calculated directly from the Hα luminosity by following Kennicutt & Evans (2012):

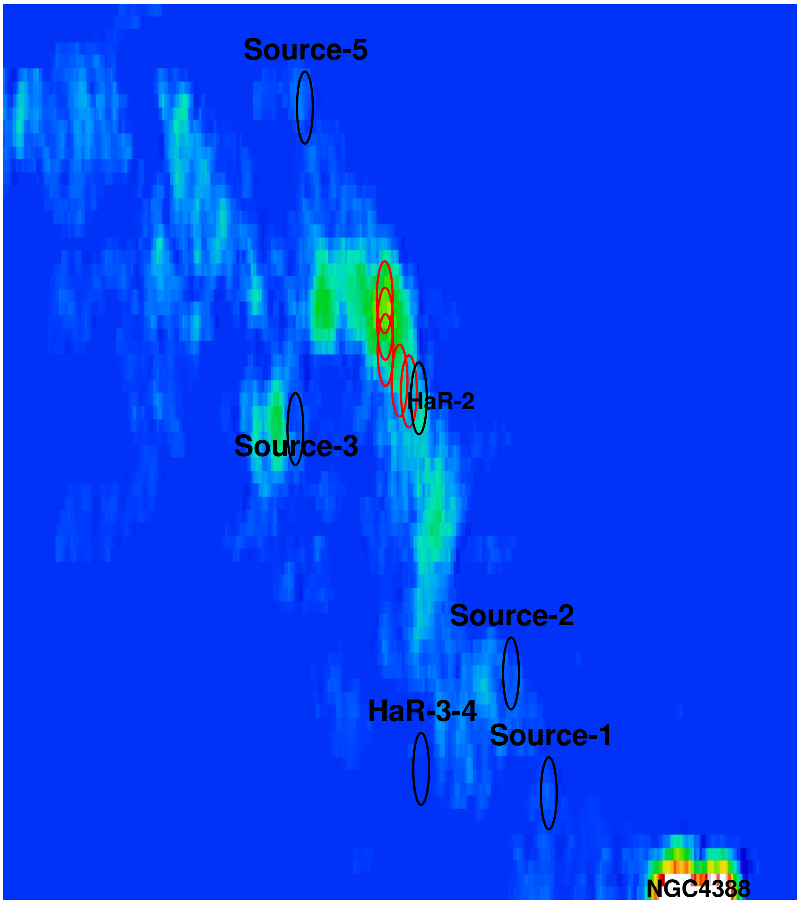

Figure 3.5: HI column density map from Oosterloo & van Gorkom (2005) taken with the Westerbork radiotelescope. Our sources are marked in the same way as in Figure 3.2. Aperture photometry was done for all sources inside apertures of 22″ diameter, which here look as ovals since the image has rectangular pixels.

Table 3.4. K-S relation values.

Source	Σ_{H_2} [$M_\odot pc^{-2}$]	$\int N_{HI} d\Omega$ [$10^{12} cm^{-2}$]	Σ_{HI} [$M_\odot pc^{-2}$]	$\log(L_{H_\alpha})$ [erg s^{-1}]	$\log(\Sigma_{SFR})$ [$M_\odot yr^{-1} kpc^{-2}$]	$\tau_{dep}(H_2)$ [yr]
Source-1	0.93	0.33	0.40	<35.51	< -6.19	$>1.4\times10^{12}$
Source-2	<0.48	0.41	0.50	<35.51	< -6.19	···
Source-3	<0.40	0.56	0.68	<35.51	< -6.19	···
Source-5	<0.48	0.60	0.69	37.51	-4.20	$<7.7\times10^{9}$
HaR-2	1.18	2.12	2.5	37.10	-4.61	4.8×10^{10}
HaR-3-4	<0.40	···	···	37.75	-3.96	$<3.6\times10^{9}$
HaR-2-1	<0.44	5.56	6.77	<35.51	< -6.19	···
HaR-2-2	<0.44	5.13	6.24	<35.51	< -6.19	···
HaR-2-3	<0.22	3.67	4.46	<35.51	< -6.19	···
HaR-2-4	2.09	3.08	3.74	< 35.51	< -6.19	$>3.2\times10^{12}$
HaR-1	0.77	2.05	2.49	35.89	-5.82	5.1×10^{11}

Note. — Surface densities consider a solid angle Ω=2.74 kpc^2, equivalent to the CO(1–0) beam-size at the distance of the source (17.5 Mpc fom Mei et al. 2007). Depletion times are calculated as $\tau_{dep} = \Sigma_{H_2}/\Sigma_{SFR}$.

$$\log \text{SFR} = \log \text{L}_{H_\alpha}[\text{erg s}^{-1}] - 41.27 \tag{3.5}$$

which uses the initial mass function (IMF) of Kroupa & Weidner (2003). Once again, if we average this value over the surface area to be taken into account, we obtain the SFR surface density: Σ_{SFR} = SFR/Ω, with Ω the CO(1–0) beam solid angle.

H_α luminosities for HaR-1, HaR-2 and HaR-3-4 were obtained from Yagi et al. (2013) with the Subaru Prime Focus Camera. Such values are presented in column 5 of Table 3.4 with their corresponding Σ_{SFR} in column 6 following Eq. 3.5

For the remaining sources in our sample we used the Hα+[NII] map of the Virgo cluster from Kenney et al. (2008), presented in Figure 3.6. We used the Hα luminosities of HaR-2, HaR-3 and HaR-4 of Yagi et al. (2013) to calibrate the Hα+[NII] emission to Hα intensities, assuming that all HII regions have the same NII/Hα ratio.

With this calibration, and using an aperture photometry of 1″ diameter (similar to the seeing of the observations of Yagi et al. 2013) we calculated an $L_{H\alpha}$ for Source-5 (Table 3.4). For the rest of the sources with no visible emission, we calculated upper limits from the noise level of the map, estimated in 4.8×10^{-7}erg s^{-1}cm^{-2}sr^{-1}. Inside a 1″ aperture and at the distance of 17.5 Mpc, this limit translates to 3.24×10^{35} erg s^{-1}. Then by using Eq. 3.5 and the averaging the SFR in the CO(1–0) beam solid angle Ω, we obtain an upper limit of 6.49×10^{-7} $M_\odot yr^{-1} kpc^{-2}$.

All these values are presented in Table 3.4

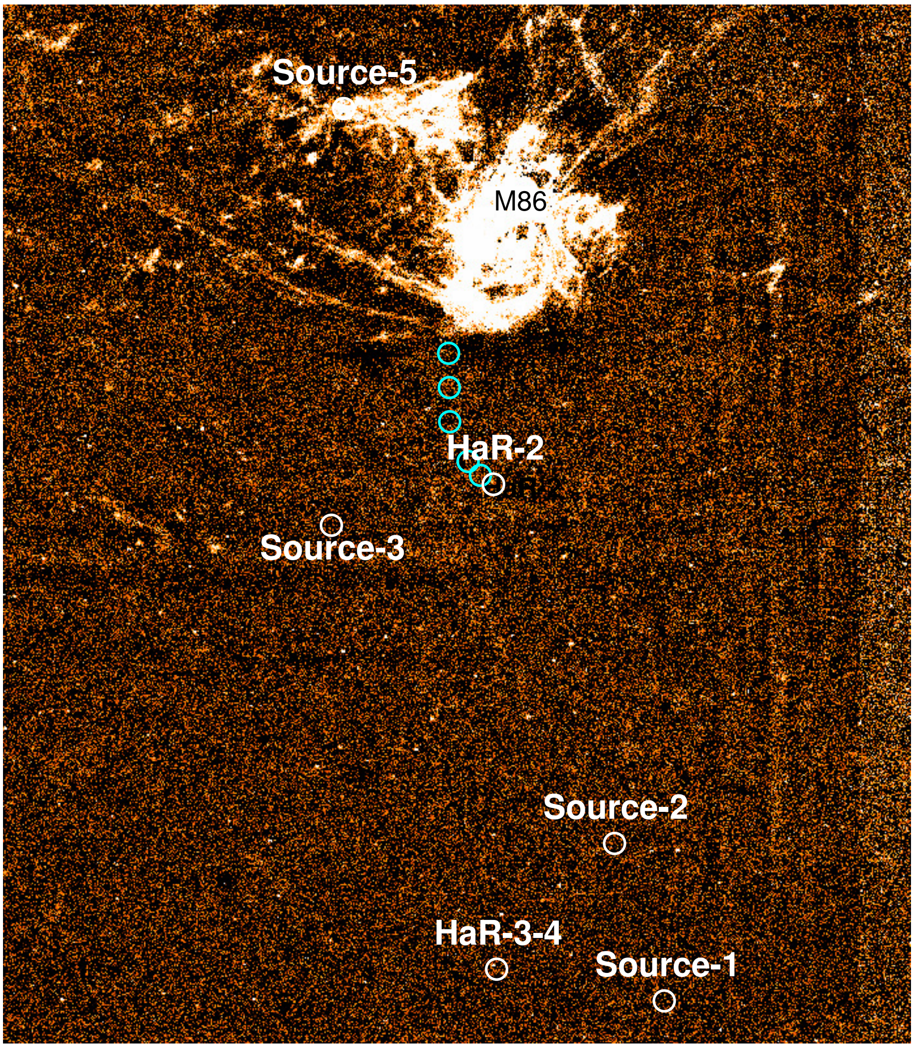

Figure 3.6: Hα+[NII] map of the Virgo cluster from Kenney et al. (2008) taken with the KPNO telescope. Our sources are marked in the same way as in Figure 3.2. Circles in this image are $22''$ width, but the aperture photometry was done in a $1''$ aperture, to be consistent with the H_α data from Yagi et al. (2013). This map was calibrated with Yagi's data and used to calculate the L_α of Source-5, as well as the upper limits for Source-1, Source-2, Source-3, HaR-2-1, HaR-2-2, HaR-2-3 and HaR-2-4 from the map's noise level.

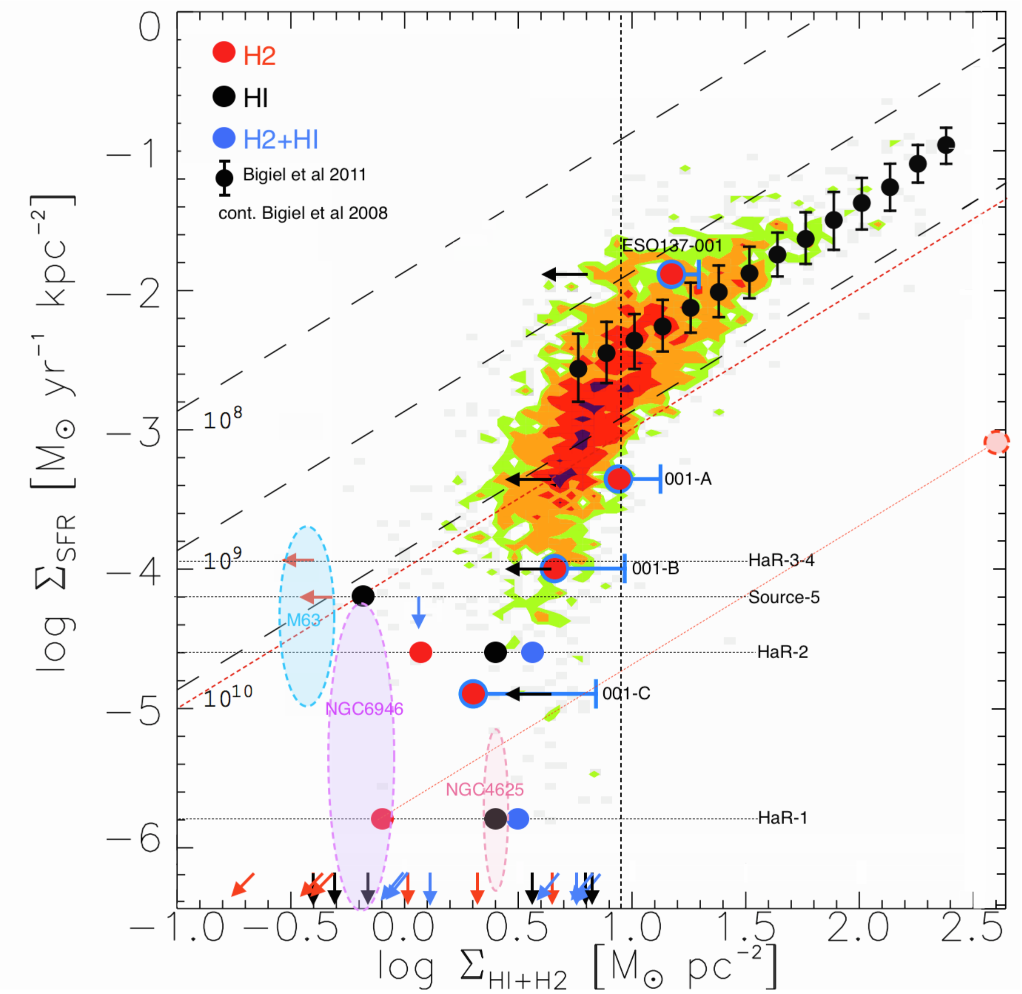

Figure 3.7: K-S relation for sources in Table 3.4, with filled circles and arrows for values and upper limits respectively. Red markers consider only H_2 for Σ_{gas}, black ones only HI, and blue ones the sum of both. Figure adapted from Jáchym et al. (2014), where their sources ESO137-001, 001-A, 001-B and 001-C have been plotted in a similar way than ours: red circles for H_2 gas, black left arrows for HI upper limits, and blue "error bars" to account for both gas components. Colored contours account for the spiral galaxies from Bigiel et al. (2008) (green, orange, red and purple for 1, 2, 5 and 10 sampling points per 0.05 dex respectively). Black markers with error bars correspond to the running medians in Σ_{SFR} as a function of σ_{H_2} of 30 nearby galaxies from Bigiel et al. (2011). Shaded ovals represent the data from the outer parts of XUV disk galaxies: NGC4625 and NGC6946 from Watson et al. (2014) (priv. communication), and M63 (NGC5055) from Dessauges-Zavadsky et al. (2014), taking only H_2 into account in all of them. The dashed vertical line shows the 9 $M_\odot pc^{-2}$ threshold at which the atomic gas saturates. Dashed inclined lines represent "isochrones" of constant star formation efficiencies, indicating the depletion times τ_{dep} of 10^8, 10^9 and 10^{10} years to consume all the gas. The dashed red isochrone marks a depletion time equal to the age of the universe, as one Hubble time (13.8 Gyr). A representative shift of the HaR-1 marker for Σ_{H_2} is drawn, to show the "effective" molecular gas density at which stars would formed in this region if we consider a beam correction factor of +2.68 in log space, to convert our 22″ beam to a ∼1″ beam as in the H_α data.

3.5.3 K-S relation

The SFR surface densities are plotted as a function of the gas surface densities to construct a K-S relation in Figure 3.7, using the values from Table 3.4. We have plotted separately, the atomic and molecular gas component of $\Sigma_{\rm gas}$, along with the combination of both, in red, black and blue markers respectively. Arrows denote the upper limits values from Table 3.4. In this Figure, adapted from Jáchym et al. (2014), we can compare our sources with with theirs in the Norma Cluster, as well as with the sample of spiral galaxies from Bigiel et al. (2008) (in coloured contours), and the sample of 30 nearby galaxies from Bigiel et al. (2011), plotted as the running medians of $\Sigma_{\rm SFR}$ as a function of $\Sigma_{\rm H_2}$, and with a typical depletion time ($\tau_{\rm dep}$) of ~2.3 Gyr. Additionally, shaded regions have been included to represent regions from the outskirts of XUV disk galaxies. NGC4625 and NGC6946 data was taken from Watson et al. (2014) (priv. communication), including IRAM-30m CO observations, and H_α luminosities measured within a 6″ aperture. M63 (NGC5055) data corresponds to the bright UV region located at $1.35r_{25}$ in Dessauges-Zavadsky et al. (2014), with IRAM 30-m CO data, and a SFR measured from the FUV and 24μm emission.

"Isochrones" of constant star formation efficiencies are also shown to indicate the depletion times of 10^8, 10^9 and 10^{10} years to consume all the gas, including an additional red isochrone to mark the age of the universe as one Hubble time (i.e $\tau_{\rm dep} = 13.8$Gyr).

Contrary to the photometry done in the HI data, the H_α data was not measured in a 22″ diameter aperture, as the CO(1–0) FWHM, but in an aperture of 1″ in diameter, similar to the seeing of those observations. Since we are averaging this Hα emission in a 22″ aperture to calculate the $\Sigma_{\rm SFR}$, we could be diluting the real surface density of the gas being converted into stars. To correct for this beam dilution, we have shifted in a representative way one of the points in Figure 3.7 to a fictitious $\Sigma_{\rm H_2}$, corresponding to a source's solid angle of 1″ in diameter. This correction translates in a +2.68 shift in log space, and is a representation of the real gas surface density at which stars would be formed, but always with the same $\tau_{\rm dep}$.

From Figure 3.7 we can see that our sources have extremely low SFRs in comparison with the nearby spiral galaxies, and are only comparable with the most outer clumps in the H_α/X-ray tail of the ISM stripped galaxy ESO137-001 in the Norma Cluster (Jáchym et al. 2014) and the XUV disk galaxies from Watson et al. (2014) and Dessauges-Zavadsky et al. (2014). We calculated the corresponding depletion times, i.e the amount of time needed to consume all the gas available to be converted into stars ($\tau_{\rm dep} = \Sigma_{\rm gas}/\Sigma_{\rm SFR}$), obtaining values significantly large. For example, HaR-1 and HaR-2 have $\tau_{\rm dep}$ values of 2.1×10^{12} and 1.5×10^{11} years respectively, to consume all the amount of gas present (HI+H_2). These values transform into 1.6×10^{12} and 1.0×10^{11} years if we consider only the atomic gas component, and into 5.1×10^{11} and 4.8×10^{10} years if we consider only the molecular one. Such values are quite large in comparison with the typical $\tau_{\rm dep}$ of ~2 Gyrs for spiral galaxies, and are even larger than a Hubble time by up to 2 orders of magnitude. In Table 3.4, depletion times of H_2 that can be calculated are listed in column 7. These high values of $\tau_{\rm dep}$, much larger than the age of the universe, indicate that this molecular gas will no be converted into stars, but remain in a gaseous phase and later join the ICM.

The extremely low SF efficiency of our sources seems to fall off the linearity of the K-S relation for typical spiral galaxies at higher gas densities, a result previously reported in other low gas density environments, such as XUV disk galaxies (Dessauges-Zavadsky et al. 2014). Watson et al. (2014) presents a different conclusion for their results in XUVs, with a typical SFR in agreement with the K-S linear regime, but they take into account the 24μm emission in the SFR, and neglect the contribution of heavy elements in the $\Sigma_{\rm H_2}$. We see that when we correct by these differences to make their data analytically compatible with ours (i.e neglect the 24μm emission and correct for heavy elements), their data points in the K-S plot are comparable to ours.

Therefore, our results help to show that the linearity between the SFR and the gas surface density, so clear at high gas surface densities (> 9 M$_\odot$pc^{-2}) for normal spiral galaxies, cannot be extrapolated to lower densities, below the HI-H$_2$ threshold, where the star formation is extremely inefficient, and the molecular gas, even though present, does not necessarily form stars .

3.6 Publication

The corresponding publication of this work was submitted to A&A in May 2015 and is presented here.

Astronomy & Astrophysics manuscript no. virgo_ram_pressure
May 17, 2015 ©ESO 2015

Ram Pressure stripping in the Virgo Cluster

C. Verdugo[1], F. Combes[1, 2], K. Dasyra[1, 3], P. Salomé[1] and J. Braine[4]

[1] Observatoire de Paris, LERMA (CNRS:UMR8112), 61 Av. de l'Observatoire, F-75014, Paris, France e-mail: `celia.verdugo@obspm.fr`
[2] Collège de France, 11 Place Marcelin Berthelot, 75005 Paris, France
[3] Department of Astrophysics, Astronomy & Mechanics, Faculty of Physics, University of Athens, Panepistimiopolis Zografos 15784, Greece
[4] Univ. Bordeaux, Laboratoire d'Astrophysique de Bordeaux, (CNRS:UMR5804) 33270 Floirac, France

Received 2015; accepted 2015

ABSTRACT

Gas can be violently stripped from their galaxy disks in rich clusters, and be dispersed over 100kpc-scale tails or plumes. Young stars have been observed in these tails, suggesting they are formed in situ. This will contribute to the intracluster light, in addition to tidal stripping of old stars. We want to quantify the efficiency of intracluster star formation. We present CO(1–0) and CO(2–1) observations, made with the IRAM-30m telescope, towards the ram-pressure stripped tail northeast of NGC4388 in Virgo. HII regions found all along the tails, together with dust patches have been targeted. We detect molecular gas in 4 positions along the tail, with masses between 6x10^5 to 3x10^6 $M_\odot$. Given the large distance from the NGC 4388 galaxy, the molecular clouds must have formed in situ, from the HI gas plume. We compute the relation between surface densities of star formation and molecular gas in these regions, and find that the star formation has very low efficiency. The corresponding depletion time of the molecular gas can be up to 500 Gyr and more. Since this value exceeds a by far Hubble time, this gas will not be converted into stars, and will stay in a gaseous phase to join the intracluster medium.

Key words. Galaxies: evolution — Galaxies: clusters: Individual: Virgo — Galaxies: clusters: intracluster medium — Galaxies: interactions — Galaxies: ISM

1. Introduction

In overdense cluster environments, galaxies are significantly transformed, through tidal interactions with other galaxies or with the cluster as a whole (e.g. Merritt 1984, Tonnesen et al. 2007), and interactions with the intra-cluster medium (ICM), which strips them from their gas content. This ram-pressure stripping (RPS) process has been described by Gunn & Gott (1972) and simulated by many groups (Quilis et al. 2000, Vollmer et al. 2001, Roediger & Hensler 2005; Jáchym et al. 2007). Evidence of stripping has been observed in many cases (Kenney et al. 2004; Chung et al. 2007; Sun et al. 2007, Vollmer et al. 2008). RPS and/or tidal interactions can disperse the interstellar gas (ISM) of galaxies at large distance, up to 100kpc scales, as shown by the spectacular tail of ionized gas in Virgo (Kenney et al. 2008).

What is the fate of the stripped gas? According to the time-scale of the ejection, the relative velocity of the ICM-ISM interaction, and the environment, it could be first seen as neutral atomic gas (Chung et al. 2009, Scott et al. 2012, Serra et al. 2013), then ionized gas detected in Hα (Gavazzi et al. 2001, Cortese et al. 2007, Yagi et al. 2007, Zhang et al. 2013), and is finally heated to X-ray gas temperatures (e.g. Machacek et al. 2005, Sun et al. 2010). In rarer cases, it can be seen as dense and cold molecular gas, detected as carbon monoxyde (CO) emission (Vollmer et al. 2005, Dasyra et al. 2012, Jáchym et al. 2014). The presence of these dense molecular clumps might appear surprising, since the RPS should not be able to drag them out of their galaxy disks (Nulsen 1982; Kenney & Young 1989). However they could reform quickly enough in the tail. The survival of these clouds in the hostile ICM environment, with temperature 10^7 K and destructive X-rays (e.g., Machacek et al. 2004; Fabian et al. 2006; Tamura et al. 2009) is a puzzle, unless they are self-shielded (e.g. Dasyra et al. 2012, Jáchym et al. 2014). The presence of cold molecular gas is also observed in rich galaxy clusters, with cool cores. Here also a multi-phase gas has been detected, in CO, Hα, X-rays and also the strongest atomic cooling lines (Edge et al. 2010). Ionized gas, together with warm atomic and molecular gas and cold molecular gas clouds coexist in spatially resolved filaments around the brightest cluster galaxy, such as in the spectacular prototype Perseus A (Conselice et al. 2001; Salomé et al. 2006, 2011; Lim et al. 2012).

The survival of molecular clouds was also observed by Braine et al. (2000) in several tidal tails, and in particular in the interacting system Arp 105 (dubbed the Guitar), embedded in the X-ray emitting medium of the Abell 1185 cluster (Mahdavi et al. 1996). Again, the formation in situ of the molecular clouds is favored (Braine et al. 2000). In the Stephan's Quintet compact group, where X-ray gas and star formation have been observed in between galaxies (O'Sullivan et al. 2009), the shock has been so violent (1000 km/s) that H_2 molecules are formed and provide the best cooling agent, through mid-infrared radiation (Cluver et al. 2010). In this shock, multi-phases of gas coexist, from cold dense molecular gas to X-ray gas.

Does this gas form stars? In usual conditions, inside galaxy disks, the star formation is observed to depend essentially on the amount of molecular gas present (e.g. Bigiel et al. 2008; Leroy et al. 2013). A Kennicutt-Schmidt (K-S) relation is observed, roughly linear, between the surface densities of star for-

---

Send offprint requests to: C. Verdugo

mation and molecular gas, leading to a depletion time-scale of 2 Gyr. But this relation does not apply in special regions or circumstances, such as galaxy centers (Casasola et al. 2015), outer parts of galaxies and extended UV disks (Dessauges-Zavadsky et al. 2014), or low surface brightness galaxies (Boissier et al. 2008). Little is known on star formation in gas clouds stripped from galaxies in rich clusters. Boissier et al. (2012) have put constraints on this process, concluding to a very low star formation efficiency, lower by an order of magnitude than what is usual in galaxy disks, and even lower than outer parts of galaxies or in low surface brightness galaxies. It is interesting to better constrain this efficiency, given the large amount of intracluster light (ICL) observed today (e.g. Feldmeier et al. 2002, Mihos et al. 2005). These stars could come from tidal stripping of old stars formed in galaxy disks, or also a large fraction could have formed in situ, from ram-pressure stripped gas. More intracluster star formation could have formed in the past (DeMaio et al. 2015). The origin of the ICL could bring insight on the relative role of galaxy interactions during the cluster formation, or cluster processing after relaxation.

1.1. The tail northeast of NGC4388

One of the best ram-pressure tails to probe molecular gas survival under extreme conditions, and the star formation efficiency is the RPS tail north of NGC 4388 in the Virgo cluster south of M86, where X-ray gas has been mapped (Iwasawa et al. 2003) and young stars have been found (Yagi et al. 2013). It is located at about 400 kpc in projection from the cluster center M87. NGC 4388 is moving at a relative velocity redshifted by 1500km/s with respect to M87, and more than 2800 km/s with respect to the M86 group. This strong velocity may explain the violent RPS, the high HI deficiency of NGC 4388 (Cayatte et al. 1990) and the large (~ 35kpc) emission-line region found by Yoshida et al. (2002), northeast of the galaxy. The ionized gas has a mass of 10^5 $M_\odot$, and is partly excited by the ionizing radiation of the Seyfert 2 nucleus in NGC 4388. The RPS plume is even more extended in HI (Oosterloo & van Gorkom 2005), up to 110 kpc, with a mass of 3.4 x 10^8 $M_\odot$. Gu et al. (2013) have found neutral gas in absorption in X-ray, with column densities 2-3$\times10^{20}$ cm^{-2}, revealing that the RPS tail is in front of M86. The high ratio between hot and cold gas in the clouds means that significant evaporation has proceeded. Yagi et al. (2013) find star-forming regions in the plume at 35 and 66 kpc from NGC 4388, with solar metallicity and age 6 Myrs. Since these stars are younger than the RPS event, they must have formed in situ.

In the present paper we present CO detections in the ram-pressure stripped gas northeast of NGC 4388. In a previous paper, we have already found molecular gas in a ionized gas tail south of M86 (Dasyra et al. 2012), and discussed its survival conditions. We here study the link between new stars formed and molecular gas, to derive the star formation efficiency. In the RPS plume, a significant fraction of the Hα emission could originate from the ionized gas in the outer layers of molecular clouds (Ferland et al. 2009). This makes the Hα lumps good tracers of star formation in an RPS tail, to probe the efficiency of the process of formation of intracluster stars. Section 2 presents the IRAM-30m observations, Section 3 the results obtained, which are discussed in Section 4.

In the following, we assume a distance of 17.5 Mpc to the Virgo cluster (Mei et al. 2007).

2. Observations and data reduction

CO observations along the HI stream connecting NGC4388 and M86 were done with the IRAM 30-mt telescope at Pico Veleta, Spain, in two separate runs. The first run was part of the project 195-13, with 28 hours of observation, and took place between the 5th and 8th of December 2013, with excellent weather conditions (τ < 0.1 and a pwv between 0.1 and 3mm). The second run was project 075-14, with 47 hours of observations between June 25th-30th 2014, and had poor to average weather conditions (τ between 0.2 and 0.6 and a pwv between 3 and 10 mm).

All observations were done with the EMIR receiver in the E0/E2 configuration, allowing us to observe simultaneously CO(1–0) and CO(2–1) at 115.271 and 230.538 GHz respectively. The telescope half-power beam widths at these frequencies are 22″ and 11″ respectively. The observing strategy consisted in single ON+OFF pointings per each target, with wobbler switching.

Targets along the HI stream were selected for having a match of HI, Hα and 250μ emission (Figure 1). With this criteria 6 targets where selected for the first run 195-13, and are listed in Table 1 (first 6 rows). As a result of this run, only two sources showed CO detection: Source-1 and HaR-2. Since HaR-2 is of particular interest for being so far away from both galaxies and for having a strong Hα detection (Yagi et al. 2013), it was chosen as a central target around which other 5 extra targets were selected for the second run 075-14 (second half of Table 1), following the path of an HI peak (Figure 1 top right box)

Table 1. Targets and Observations

Source	RA(J2000) $[^{hr}:^{m}:^{s}]$	DEC(J2000) $[^{deg}:^{m}:^{s}]$	hel. vel. [km/s]	ON+OFF [hrs]
Source-1	12:26:01.3	12:42:30.1	+2500	4.2
Source-2	12:26:04.9	12:45:16.7	+2500	2.9
Source-3	12:26:25.4	12:50:53.6	+2200	3.1
Source-5	12:26:24.5	12:58:14.6	+2000	3.9
HaR-2	12:26:13.7	12:51:36.9	+2230	7.2
HaR-3-4	12:26:13.5	12:43:03.7	+2500	3.8
HaR-2-1	12:26:16.9	12:53:55.6	+2230	4.5
HaR-2-2	12:26:16.9	12:53:19.3	+2230	5.6
HaR-2-3	12:26:16.9	12:52:43.1	+2230	6.2
HaR-2-4	12:26:15.5	12:52:01.1	+2230	8.0
HaR-1	12:26:14.6	12:51:46.4	+2230	3.8
NGC4388	12:25:46.6	12:39:44.0	+2550	1.2

Notes. Sources in the first 6 rows correspond to run 195-13, and last 6 rows to run 075-14 (although source HaR-2 was observed in both runs). NGC4388 was observed for calibration purposes. Heliocentric velocities are referencial, taken from Oosterloo & van Gorkom (2005).

Concerning the spectral resolution of our data, during the observations both FTS and WILMA backends were used, simultaneously. The FTS backend has a spectral resolution of 195 kHz and a bandwidth of 32 GHz including both polarizations. At 115 GHz these values correspond to 0.5 and 83200 km/s, and at 230 GHz to 0.25 and 41600 km/s. As for the WILMA backend, we obtained a spectral resolution of 2 MHz and a bandwidth of 16 GHz. At 115 GHz this translates to 5.2 and 41600 km/s, and to 2.6 and 20800 km/s at 230 GHz.

The data were reduced using the CLASS software from the GILDAS package. First, a careful inspection of all scans was done, to remove the bad ones. The approved scans of the same source, CO line and backend were averaged with a normal time weighting, to obtain one spectra. Then, each spectra was in-

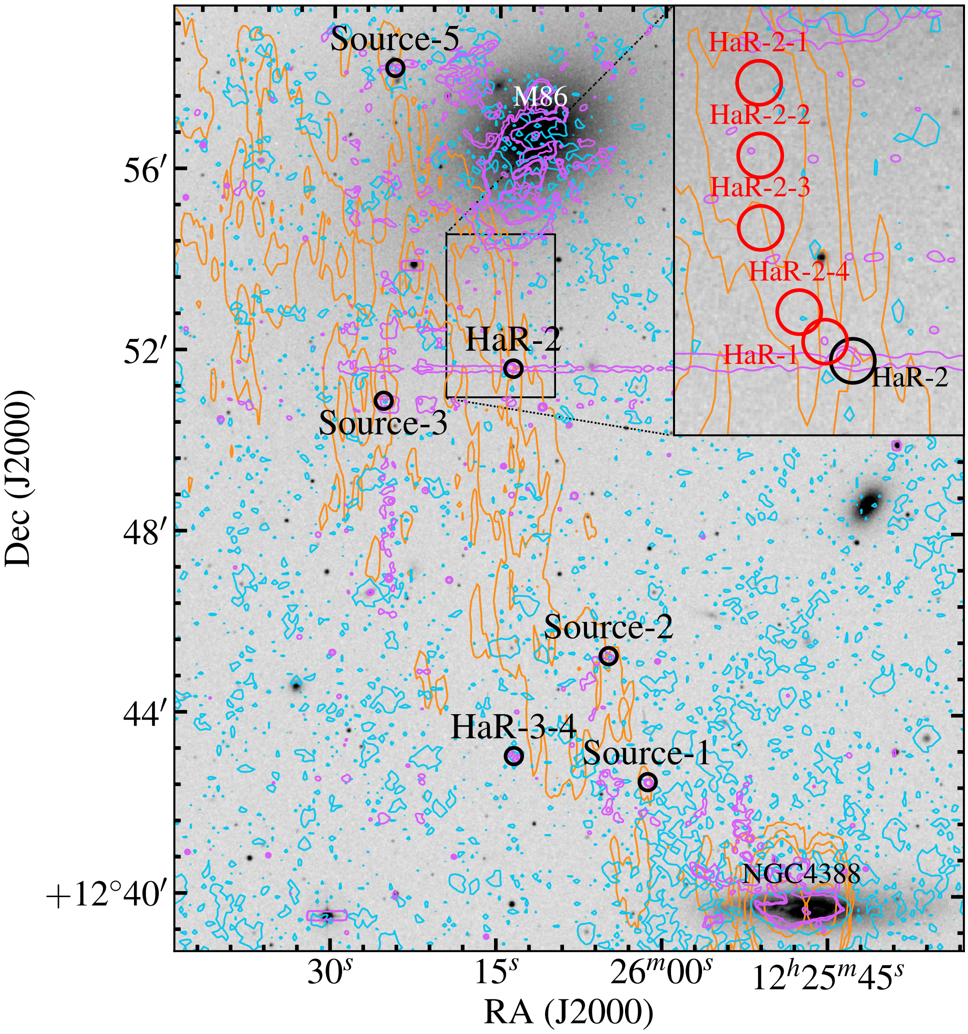

Fig. 1. Targets observed in the Virgo Cluster. Orange: HI contours levels at 1, 5, 10 and 50 $\times 10^{19} cm^{-2}$ from Oosterloo & van Gorkom (2005). Purple: Hα contours levels at 5, 11 and 50 e^{-}/sec (Kenney et al. 2008). Cyan: 250μm contour levels at 0.01 and 0.1 Jy/beam (Davies et al. 2012). In zoomed regions: targets selected close to HaR-2 for run 075-14 (red circles). Circles enclosing targets are 22″ width, as the CO(1–0) HPBW.

spected individually, and in both of its polarizations, to identify a possible CO emission line. If a detection was found in the spectra of both backends, the best spectra was chosen (in terms of spectral resolution and S/N) as the final one. The selected spectra with CO emission are presented in Figures 2 and 3, which contain both polarizations, horizontal and vertical, combined.

Baselines were subtracted with polynomials of order 0 and 1 depending on the source, and antenna temperatures were corrected by the telescope beam and forward efficiencies[1] to obtain main beam temperatures. Spectra were smoothed with the hanning method to degrade the velocity resolution until obtaining a value no greater than 1/3 of the FWHM line.

Finally, a simple gaussian line was fitted to the line candidate. The CLASS fit return the velocity position of the line, its FWHM, the peak temperature and the integrated line intensity.

Such spectra and fitting results for sources with CO detection are presented in Figures 2 (from the first run) and 3 (from second run) and then in Table 2. For the rest of the sources, with no visible CO detections, 3σ upper limits for I_{CO} where calculated from their rms values, assuming a Δv = 30 km/s . Such limits are presented in Table 3.

3. Results

After selecting the final spectra for every source with a visible detection and fitting their gaussian profiles, line parameters are calculated and presented in Table 2. H_2 masses were derived from the CO(1–0) line intensity, using a Galactic CO conversion factor of $2.0 \times 10^{20}[\mathrm{cm}^{-2}(\mathrm{K\ km/s})^{-1}]$ and a correction factor of 1.36 to account for heavy elements:

$$M_{H_2}[M_\odot] = 4.4\pi R^2[\mathrm{pc}]\ I_{CO(1-0)}[\mathrm{K\ km/s}] \tag{1}$$

---

[1] http://www.iram.es/IRAMES/mainWiki/Iram30mEfficiencies

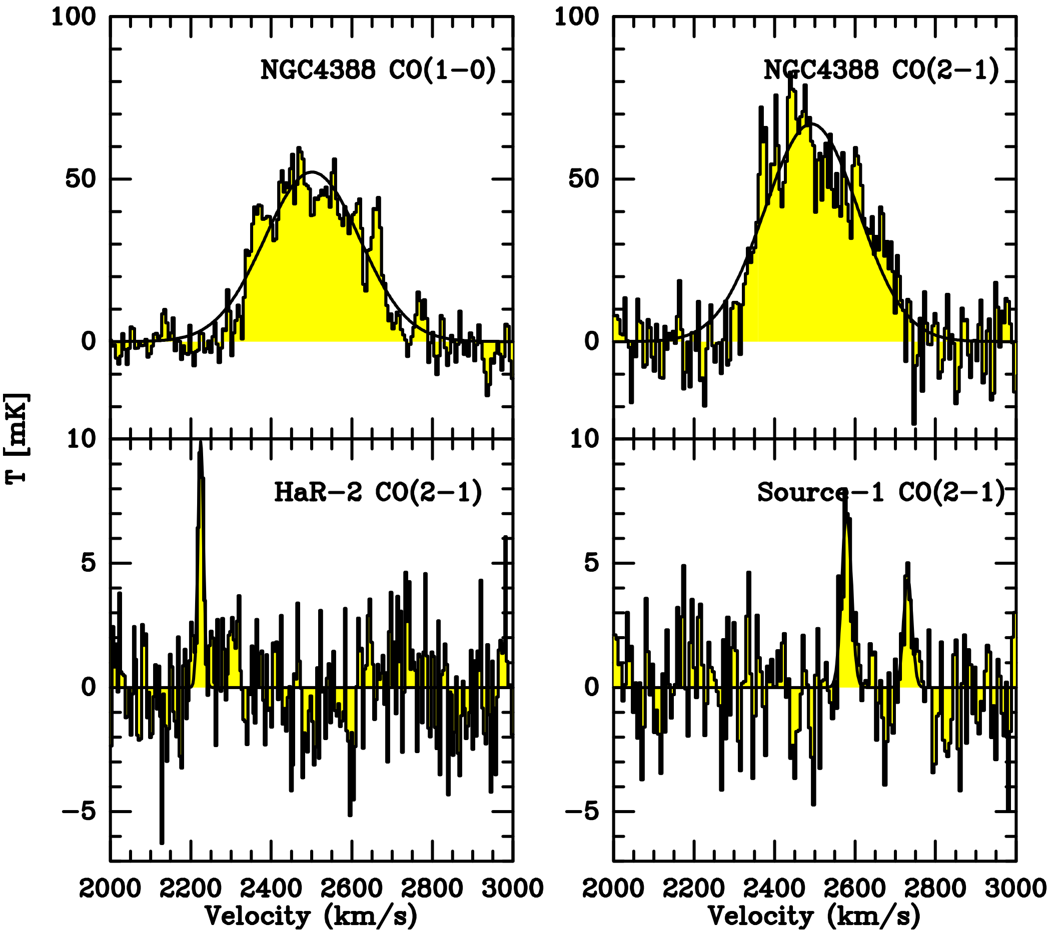

Fig. 2. Top: Spectra taken at the center of NGC4388, observed for calibration purposes. Bottom: Spectra from observing run 195-13 that showed CO emission. Spectra information and line parameters are presented in Table 2. The temperature scale corresponds to main beam temperature.

Table 2. CO detections and their line parameters.

Source	line	backend	int. time [min]	v_0 [km/s]	FWHM [km/s]	resol. [km/s]	T_{mb} [mK]	rms [mK]	I_{CO} [K km/s]	M_{H_2} [$10^6 M_\odot$]
HaR-2	CO(2–1)	FTS	268	2224.9±1.2	16.2 ±2.9	4	9.9	2.0	0.17± 0.03	
Source-1(1)	CO(2–1)	WILMA	232	2579.2±2.3	28.7±6.1	5.2	7.0	2.5	0.21±0.04	
Source-1(2)	CO(2–1)	WILMA	232	2731.3±4.0	25.1±12.4	5.2	4.3	2.5	0.12±0.04	
HaR-2	CO(1–0)	WILMA	318	2200.3±8.6	72.6±15.9	10.4	3.5	2.1	0.27±0.06	3.24
	CO(2–1)	WILMA	586	2224.3±2.7	26.6±7.2	10.5	5.0	1.8	0.14±0.03	
HaR-1	CO(1–0)	WILMA	229	2212.2±4.5	32.8±13.8	10.4	5.0	2.3	0.18±0.05	2.11
	CO(2–1)	WILMA	229	2223.2±7.8	80.9±15.15	10.4	6.0	3.2	0.52± 0.09	
HaR-2-4	CO(1–0)	WILMA	665	2402.6±2.3	10.4±62.1	10.4	4.2	1.5	0.47±0.02	0.57
	CO(2–1)	WILMA	665	2281.7±26.4	200.4±45.3	20.8	1.4	2.8	0.29±0.07	
NGC4388	CO(1–0)	WILMA	87	2501.7±2.7	278.6±5.9	5.2	52.2	5.7	15.47±0.30	186
	CO(2–1)	WILMA	82	2492.0±3.5	273.3±7.4	5.2	67	9.4	19.49±0.49	

Notes. First three rows correspond to observing run 195-13. Both components shown in Figure 2 for Source-1 are listed. H_2 masses were calculated as $M_{H_2}[M_\odot]=4.4\pi R^2[pc]\ I_{CO}[K\ km/s]$, which uses a Galactic CO conversion factor of 2.0×10^{20} $[cm^{-2}(K\ km/s)^{-1}]$ and a correction factor of 1.36 to account for heavy elements. A distance to the Virgo Cluster of 17.5 Mpc (Mei et al. 2007) was used to calculate the CO(1–0) beam radius as source radius. HaR-2 includes data taken in the first run only for CO(1–0), and data combined from both runs for CO(2–1).

where the source's radius R corresponds to the CO(1–0) beamsize radius at the distance of the source (17.5 Mpc from Mei et al. 2007).

3.1. Star formation efficiency

To estimate how fast is the gas being transformed into stars, we compare the SFR surface density versus the gas surface density in a K-S relation, to understand the efficiency of this star formation process. Since these are low gas density regions, we can expect a large amount of gas in atomic phase, greater than in molecular phase. Therefore both components, atomic and

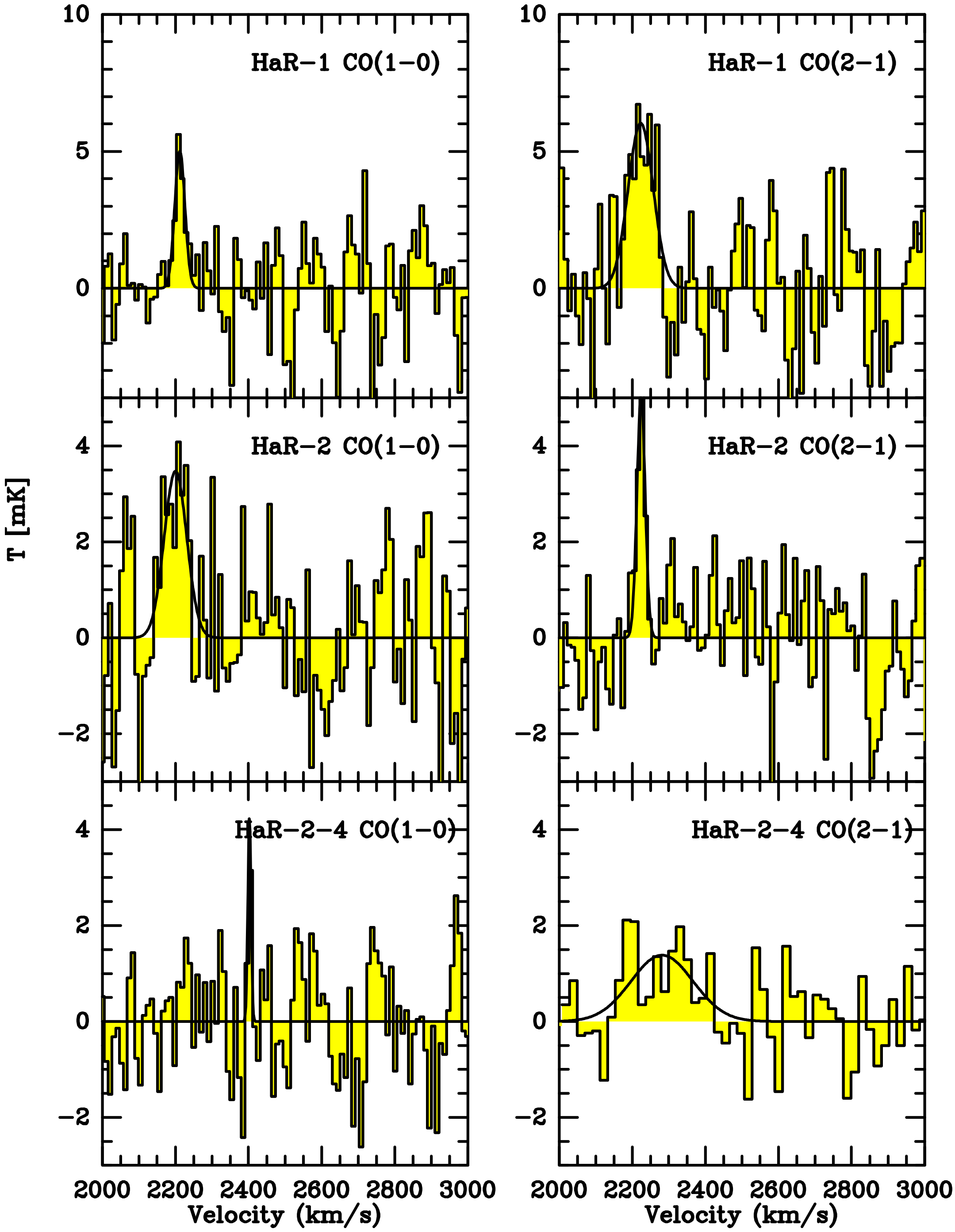

Fig. 3. Final CO spectra for HaR-2, HaR-1 and HaR-2-4 from run 075-14. Only HaR-2 in CO(2–1) has data combined from both runs. All spectra have both polarizations combined. Spectra information and line parameters are presented in Table 2. The temperature scale corresponds to main beam temperature.

Table 3. CO(1–0) upper limits at 3σ for sources with no detection.

Source	int. time [min]	rms mK	$I_{CO}{}^{a}$ [K km/s]	M_{H_2} [$10^6 M_\odot$]	Σ_{H2} [$M_\odot pc^{-2}$]
Source-2	173	1.2	<0.11	<1.21	<0.48
Source-3	186	1.0	<0.09	<0.99	<0.40
Source-5	231	1.2	<0.11	<1.21	<0.48
HaR-3-4	229	1.0	<0.09	< 0.99	<0.40
HaR-2-1	269	1.1	<0.10	<1.10	< 0.44
HaR-2-2	334	1.1	<0.10	<1.10	<0.44
HaR-2-3	374	0.6	<0.05	<0.55	<0.22

[a] We assumed a Δv of 30 km/s.

molecular, need to be taken into account when estimating a total amount of gas to be converted into stars.

Molecular gas can be directly estimated from the CO(1-0) line intensity, obtained from our observations. If we take Eq. 1, and we divide it by the source area (πR^2), we obtain the H_2 surface density:

$$\Sigma_{H_2}[M_\odot pc^{-2}] = 4.4 I_{CO(1-0)}[\mathrm{K\ km\ s^{-1}}] \quad (2)$$

These values are listed in column 2 of Table 4 for the sources with CO(1–0) detections, including upper limits for the sources with no CO detection using Table 3.

For the atomic gas component, we estimated the amount of HI from the HI column density map of the NGC4388 plume from Oosterloo & van Gorkom (2005). The HI mass is derived from the integrated amount of N_H inside the source solid angle:

$$M_{HI} = \mu m_H \int N_H dA = \mu m_H D^2 \int N_H d\Omega \quad (3)$$

Aperture photometry was done in the N_H map of Oosterloo & van Gorkom (2005), inside a circle of 11″ radius to obtain the integrated column density. These values are listed in column 3 of Table 4. Then, by dividing Eq. 3 by the CO(1–0) beam solid angle $\Omega = \pi R^2$, we obtain the HI surface densities Σ_{HI} listed in column 4 of Table 4.

Finally, we estimate the SFR surface density Σ_{SFR} directly from the H_α emission in these regions. From Kennicutt & Evans (2012):

$$\log SFR[M_\odot yr^{-1}] = \log L_{H_\alpha}[erg\ s^{-1}] - 41.27 \quad (4)$$

which, divided by the CO(1–0) beam solid angle Ω, gives the SFR surface density Σ_{SFR}. H_α luminosities for HaR-1, HaR-2 and HaR-3-4 were obtained from Yagi et al. (2013), and are listed in Table 4, along with the corresponding Σ_{SFR}. For the remaining sources we used the H_α map from Kenney et al. (2008), using an aperture photometry of ∼1″ in diameter, similar to the seeing of the H_α observations from Yagi et al. (2013). For the sources with no visible detection in this map, an upper limit was calculated form the noise level of Kenney's map, estimated in 4.8×10^{-7}erg s^{-1}cm^{-2}sr^{-1} .

The SFR surface densities are plotted as a function of the gas surface densities to construct a K-S relation in Figure 4, using the values from Table 4. We have plotted separately, the atomic and molecular gas component of Σ_{gas}, along with the combination of both, in red, black and blue markers respectively. Arrows denote the upper limits values from Table 4. In this Figure, adapted from Jáchym et al. (2014), we can compare our sources with with theirs in the Norma Cluster, as well as with the sample of spiral galaxies from Bigiel et al. (2008) (in coloured contours), and the sample of 30 nearby galaxies from Bigiel et al. (2011), plotted as the running medians of Σ_{SFR} as a function of Σ_{H_2}, and with a typical depletion time (τ_{dep}) of ∼2.3 Gyr. Additionally, shaded regions have been included to represent regions from the outskirts of XUV disk galaxies. NGC4625 and NGC6946 data was taken from Watson et al. (2014) (priv. communication), including IRAM-30m CO observations, and H_α luminosities measured within a 6″ aperture. M63 (NGC5055) data corresponds to the bright UV region located at $1.35r_{25}$ in Dessauges-Zavadsky et al. (2014), with IRAM 30-m CO data, and a SFR measured from the FUV and 24μm emission.

"Isochrones" of constant star formation efficiencies are also shown to indicate the depletion times of 10^8, 10^9 and 10^{10} years to consume all the gas, including an additional red isochrone to mark the age of the universe as one Hubble time (i.e τ_{dep} = 13.8Gyr).

Contrary to the photometry done in the HI data, the H_α data was not measured in a 22″ diameter aperture, as the CO(1–0) FWHM, but in an aperture of 1″ in diameter, similar to the seeing of those observations. Since we are averaging this H_α emission in a 22″ aperture to calculate the Σ_{SFR}, we could be diluting the real surface density of the gas being converted into stars. To correct for this beam dilution, as a representation we have shifted one of the points in Figure 4 to a fictitious Σ_{H_2}, corresponding to a source's solid angle of 1″ in diameter. This correction translates in a +2.68 shift in log space, and is a representation of the real gas surface density at which stars would be formed, but always with the same τ_{dep}.

From Figure 4 we can see that our sources have extremely low SFRs in comparison with the nearby spiral galaxies, and are only comparable with the most outer clumps in the H_α/X-ray tail of the ISM stripped galaxy ESO137-001 in the Norma Cluster (Jáchym et al. 2014) and the XUV disk galaxies from Watson et al. (2014) and Dessauges-Zavadsky et al. (2014). We obtain depletion times ($\tau_{dep} = \Sigma_{gas}/\Sigma_{SFR}$) significantly large. For example, HaR-1 and HaR-2 have τ_{dep} values of 2.1×10^{12} and 1.5×10^{11} years respectively, to consume all the amount of gas present (HI+H_2). These values transform into 1.6×10^{12} and 1.0×10^{11} years if we consider only the atomic gas component, and into 5.1×10^{11} and 4.8×10^{10} years if we consider only the molecular one. Such values are quite large in comparison with the typical τ_{dep} of ∼2 Gyrs for spiral galaxies, and are even larger than a Hubble time by up to 2 orders of magnitude. In Table 4, depletion times of H_2 that can be calculated are listed in column 7.

The extremely low SF efficiency of our sources seems to fall off the linearity of the K-S relation for typical spiral galaxies at higher gas densities, a result previously reported in other low gas density environments, such as XUV disk galaxies (Dessauges-Zavadsky et al. 2014). Watson et al. (2014) presents a different conclusion for their results in XUVs, with a typical SFR in agreement with the K-S linear regime, but they take into account the 24μm emission in the SFR, and neglect the contribution of heavy elements in the Σ_{H_2}. We see that when we correct by these differences to make their data analytically compatible with ours (i.e neglect the 24μm emission and correct for heavy elements), their data points in the K-S plot are comparable to ours.

4. Summary and Conclusions

From our molecular cloud and star formation study in the tail north of NGC 4388 in Virgo, we can draw the following conclusions:

1. CO(1–0) and CO(2–1) observations were done with the IRAM 30-m telescope in a total of 11 targets all along the ram-pressure stripped tail northeast NGC4388 in the Virgo Cluster, in order to probe the presence of molecular gas under extreme conditions. Such targets were selected for having strong peaks of HI and Hα emission.
2. Four of such positions showed CO detections, and 3 of them concentrated in the HaR-2 region, at a distance of ∼70 kpc of NGC4388, where molecular gas in unexpected. Given the large distances of these sources to NGC4388, it is not likely that the molecular gas was stripped from the galaxy, and must have formed in situ from the HI gas plume.
3. Gaussian line profiles were fitted to the spectra of the detections, finding a wide range of velocity dispersion (Δv∼10-80 km/s). The CO(1–0) line profiles were used to estimate molecular gas masses and surface densities. The amount of molecular gas in these 3 regions (HaR-1, HaR-2 and HaR-2-4) is very low (between 0.6 and 3 $\times10^6 M_\odot$), and their H_2 surface densities between 0.8 and 2 $M_\odot pc^{-2}$. These values are well below the HI-H_2 threshold, where the gas is mainly

Table 4. Kennicutt-Schmidt relation values.

Source	Σ_{H_2} $[M_\odot pc^{-2}]$	$\int N_{HI} d\Omega^a$ $[10^{12} cm^{-2}]$	Σ_{HI} $[M_\odot pc^{-2}]$	$\log(L_{H_\alpha})^b$ $[erg\ s^{-1}]$	$\log(\Sigma_{SFR})$ $[M_\odot yr^{-1} kpc^{-2}]$	$\tau_{dep}(H_2)$ [yr]
Source-1	0.93	0.33	0.40	<35.51	< -6.19	$>1.4\times10^{12}$
Source-2	<0.48	0.41	0.50	<35.51	< -6.19	—
Source-3	<0.40	0.56	0.68	<35.51	< -6.19	—
Source-5	<0.48	0.60	0.69	37.51	-4.20	$<7.7\times10^{9}$
HaR-2	1.18	2.12	2.5	37.10	-4.61	4.8×10^{10}
HaR-3-4	<0.40	—	—	37.75	-3.96	$<3.6\times10^{9}$
HaR-2-1	<0.44	5.56	6.77	<35.51	< -6.19	—
HaR-2-2	<0.44	5.13	6.24	<35.51	< -6.19	—
HaR-2-3	<0.22	3.67	4.46	<35.51	< -6.19	—
HaR-2-4	2.09	3.08	3.74	< 35.51	< -6.19	$>3.2\times10^{12}$
HaR-1	0.77	2.05	2.49	35.89	-5.82	5.1×10^{11}

Notes. Surface densities consider a solid angle Ω=2.74 kpc^2, equivalent to the CO(1–0) beamsize at the distance of the source (17.5 Mpc fom Mei et al. 2007).
$^{(a)}$ from Oosterloo & van Gorkom (2005).
$^{(b)}$ from Yagi et al. (2013) and Kenney et al. (2008).

atomic and very little is know about the SFR at such low gas densities, hence the importance of these detections.

4. Using complementary data from Yagi et al. (2013) and Kenney et al. (2008) for Hα and from Oosterloo & van Gorkom (2005) for HI, we computed Σ_{SFR} and Σ_{HI} to plot , in combination with Σ_{H_2}, a K-S relation. Our sources show an extremely low SFR (up to 2 order of magnitude lower than for typical spiral galaxies). For example, HaR-1 and HaR-2 have total gas depletion times of 2.1×10^{12} and 1.5×10^{11} years respectively. If we consider just the molecular gas component, these depletion times are 5.1×10^{11} and 4.8×10^{10} years. Furthermore, Source-1 and HaR-2-4 have H_2 depletion times even greater than 1.4 and 3.1 $\times10^{12}$ years respectively. These high values of depletion times exceed by far a Hubble time, thus indicating that this molecular gas will not form stars eventually, but remain in a gaseous phase and later join the ICM.
5. From Figure 4 we can see the linearity between the SFR and the gas surface density, so clear at high gas surface densities (> 9 M$_\odot$pc^{-2}) for normal spiral galaxies, cannot be extrapolated to lower densities, below the HI-H_2 threshold, where the star formation is extremely inefficient, and the molecular gas, even though present, does not necessarily form stars .

Acknowledgements. The IRAM staff is gratefully acknowledged for their help in the data acquisition. We thank J. Kenney for facilitating important H$_\alpha$ data. F.C. acknowledges the European Research Council for the Advanced Grant Program Number 267399-Momentum. We made use of the NASA/IPAC Extragalactic Database (NED), and of the HyperLeda database. C.V. acknowledges financial support from CNRS and CONICYT through agreement signed on December 11th 2007.

References

Bigiel, F., Leroy, A., Walter, F., et al. 2008, AJ, 136, 2846
Bigiel, F., Leroy, A. K., Walter, F., et al. 2011, ApJ, 730, L13
Boissier, S., Boselli, A., Duc, P.-A., et al. 2012, A&A, 545, A142
Boissier, S., Gil de Paz, A., Boselli, A., et al. 2008, ApJ, 681, 244
Braine, J., Lisenfeld, U., Due, P.-A., & Leon, S. 2000, Nature, 403, 867
Casasola, V., Hunt, L., Combes, F., & Garcia-Burillo, S. 2015, ArXiv e-prints [`arXiv:1503.00280`]
Cayatte, V., van Gorkom, J. H., Balkowski, C., & Kotanyi, C. 1990, AJ, 100, 604
Chung, A., van Gorkom, J. H., Kenney, J. D. P., Crowl, H., & Vollmer, B. 2009, AJ, 138, 1741
Chung, A., van Gorkom, J. H., Kenney, J. D. P., & Vollmer, B. 2007, ApJ, 659, L115
Cluver, M. E., Appleton, P. N., Boulanger, F., et al. 2010, ApJ, 710, 248
Conselice, C. J., Gallagher, III, J. S., & Wyse, R. F. G. 2001, AJ, 122, 2281
Cortese, L., Marcillac, D., Richard, J., et al. 2007, MNRAS, 376, 157
Dasyra, K. M., Combes, F., Salomé, P., & Braine, J. 2012, A&A, 540, A112
Davies, J. I., Bianchi, S., Cortese, L., et al. 2012, MNRAS, 419, 3505
DeMaio, T., Gonzalez, A. H., Zabludoff, A., Zaritsky, D., & Bradač, M. 2015, MNRAS, 448, 1162
Dessauges-Zavadsky, M., Verdugo, C., Combes, F., & Pfenniger, D. 2014, A&A, 566, A147
Edge, A. C., Oonk, J. B. R., Mittal, R., et al. 2010, A&A, 518, L46
Fabian, A. C., Sanders, J. S., Taylor, G. B., et al. 2006, MNRAS, 366, 417
Feldmeier, J. J., Mihos, J. C., Morrison, H. L., Rodney, S. A., & Harding, P. 2002, ApJ, 575, 779
Ferland, G. J., Fabian, A. C., Hatch, N. A., et al. 2009, MNRAS, 392, 1475
Gavazzi, G., Boselli, A., Mayer, L., et al. 2001, ApJ, 563, L23
Gu, L., Yagi, M., Nakazawa, K., et al. 2013, ApJ, 777, L36
Gunn, J. E. & Gott, III, J. R. 1972, ApJ, 176, 1
Iwasawa, K., Wilson, A. S., Fabian, A. C., & Young, A. J. 2003, MNRAS, 345, 369
Jáchym, P., Combes, F., Cortese, L., Sun, M., & Kenney, J. D. P. 2014, ApJ, 792, 11
Jáchym, P., Palouš, J., Köppen, J., & Combes, F. 2007, A&A, 472, 5
Kenney, J. D. P., Tal, T., Crowl, H. H., Feldmeier, J., & Jacoby, G. H. 2008, ApJ, 687, L69
Kenney, J. D. P., van Gorkom, J. H., & Vollmer, B. 2004, AJ, 127, 3361
Kenney, J. D. P. & Young, J. S. 1989, ApJ, 344, 171
Kennicutt, R. C. & Evans, N. J. 2012, ARA&A, 50, 531
Leroy, A. K., Walter, F., Sandstrom, K., et al. 2013, AJ, 146, 19
Lim, J., Ohyama, Y., Chi-Hung, Y., Dinh-V-Trung, & Shiang-Yu, W. 2012, ApJ, 744, 112
Machacek, M., Dosaj, A., Forman, W., et al. 2005, ApJ, 621, 663
Machacek, M. E., Jones, C., & Forman, W. R. 2004, ApJ, 610, 183
Mahdavi, A., Geller, M. J., Fabricant, D. G., et al. 1996, AJ, 111, 64
Mei, S., Blakeslee, J. P., Côté, P., et al. 2007, ApJ, 655, 144
Merritt, D. 1984, ApJ, 276, 26
Mihos, J. C., Harding, P., Feldmeier, J., & Morrison, H. 2005, ApJ, 631, L41
Nulsen, P. E. J. 1982, MNRAS, 198, 1007
Oosterloo, T. & van Gorkom, J. 2005, A&A, 437, L19
O'Sullivan, E., Giacintucci, S., Vrtilek, J. M., Raychaudhury, S., & David, L. P. 2009, ApJ, 701, 1560
Quilis, V., Moore, B., & Bower, R. 2000, Science, 288, 1617
Roediger, E. & Hensler, G. 2005, A&A, 433, 875
Salomé, P., Combes, F., Edge, A. C., et al. 2006, A&A, 454, 437
Salomé, P., Combes, F., Revaz, Y., et al. 2011, A&A, 531, A85
Scott, T. C., Cortese, L., Brinks, E., et al. 2012, MNRAS, 419, L19
Serra, P., Koribalski, B., Duc, P.-A., et al. 2013, MNRAS, 428, 370
Sun, M., Donahue, M., Roediger, E., et al. 2010, ApJ, 708, 946
Sun, M., Donahue, M., & Voit, G. M. 2007, ApJ, 671, 190
Tamura, T., Maeda, Y., Mitsuda, K., et al. 2009, ApJ, 705, L62
Tonnesen, S., Bryan, G. L., & van Gorkom, J. H. 2007, ApJ, 671, 1434
Vollmer, B., Beckert, T., & Davies, R. I. 2008, A&A, 491, 441
Vollmer, B., Braine, J., Combes, F., & Sofue, Y. 2005, A&A, 441, 473
Vollmer, B., Cayatte, V., Balkowski, C., & Duschl, W. J. 2001, ApJ, 561, 708
Watson, L. C., Martini, P., Lisenfeld, U., et al. 2014, in American Astronomical Society Meeting Abstracts, Vol. 223, American Astronomical Society Meeting Abstracts 223, 454.22
Yagi, M., Gu, L., Fujita, Y., et al. 2013, ApJ, 778, 91
Yagi, M., Komiyama, Y., Yoshida, M., et al. 2007, ApJ, 660, 1209
Yoshida, M., Yagi, M., Okamura, S., et al. 2002, ApJ, 567, 118
Zhang, B., Sun, M., Ji, L., et al. 2013, ApJ, 777, 122

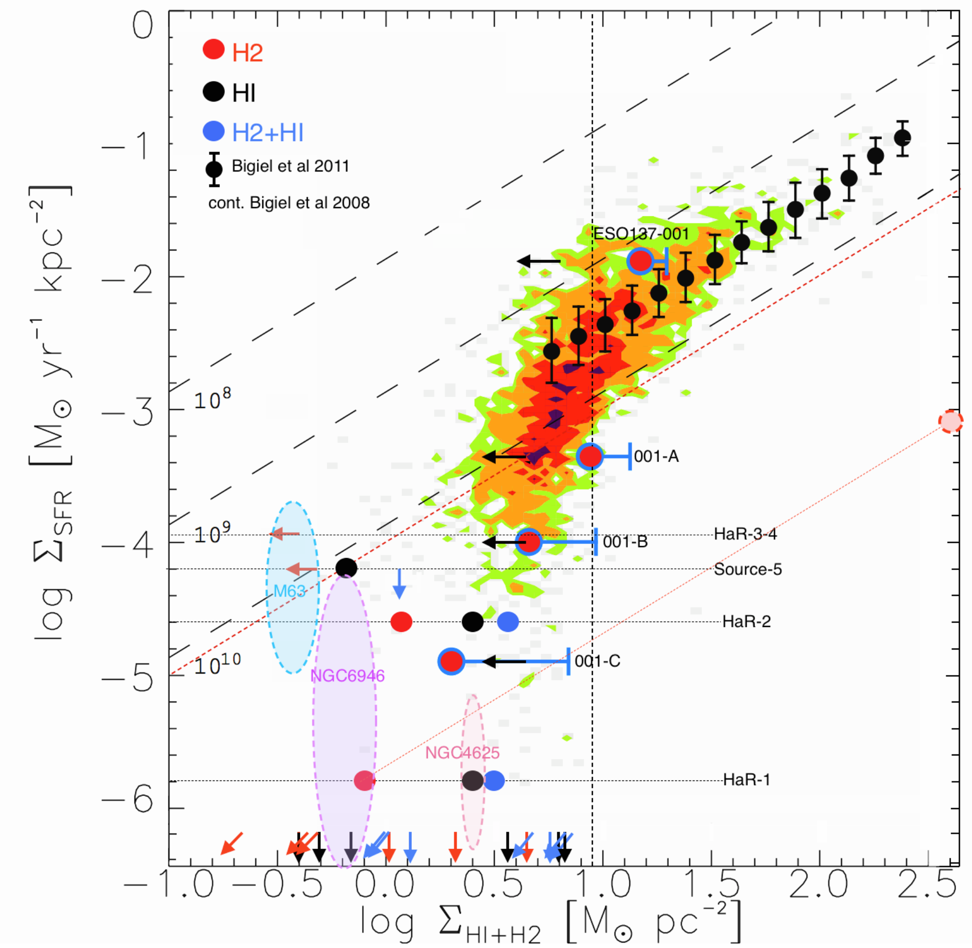

Fig. 4. K-S relation for sources in Table 4, with filled circles and arrows for values and upper limits respectively. Red markers consider only H_2 for Σ_{gas}, black ones only HI, and blue ones the sum of both. Figure adapted from Jáchym et al. (2014), where their sources ESO137-001, 001-A, 001-B and 001-C have been plotted in a similar way than ours: red circles for H_2 gas, black left arrows for HI upper limits, and blue "error bars" to account for both gas components. Colored contours account for the spiral galaxies from Bigiel et al. (2008) (green, orange, red and purple for 1, 2, 5 and 10 sampling points per 0.05 dex respectively). Black markers with error bars correspond to the running medians in Σ_{SFR} as a function of σ_{H_2} of 30 nearby galaxies from Bigiel et al. (2011). Shaded ovals represent the data from the outer parts of XUV disk galaxies: NGC4625 and NGC6946 from Watson et al. (2014) (priv. communication) , and M63 (NGC5055) from Dessauges-Zavadsky et al. (2014), taking only H_2 into account in all of them. The dashed vertical line shows the 9 $M_\odot pc^{-2}$ threshold at which the atomic gas saturates. Dashed inclined lines represent “isochrones” of constant star formation efficiencies, indicating the depletion times τ_{dep} of 10^8, 10^9 and 10^{10} years to consume all the gas. The dashed red isochrone marks a depletion time equal to the age of the universe, as one Hubble time (13.8 Gyr). A representative shift of the HaR-1 marker for Σ_{H_2} is drawn, to show the "effective" molecular gas density at which stars would formed in this region if we consider a beam correction factor of +2.68 in log space, to convert our 22″ beam to a ∼1″ beam as in the H_α data.

Chapter 4

Summary and Conclusions

This thesis presented the results of three years of work dedicated to obtain the degree of Doctor in Astronomy and Astrophysics of the Observatoire de Paris. It focused on star formation in low gas density and low metallicity environments, particularly in the search of carbon monoxide (CO) as a tracer of molecular gas (H_2), which is the main precursor of star formation. Due to the extreme conditions of such environments, the detection of CO in these places is very difficult, but plausible. In fact its presence is denoted by different signs of (scarce) star formation activity.

The importance of the regions studied in this thesis not only relies on determining constrains on the environmental conditions needed to form stars, but also on the resemblance of such regions with a younger universe, much hotter, with lower levels of gas density and content of heavy elements.

This was mainly an observational work, with CO observations at the IRAM 30m radio-telescope, and with complementary data of space and ground-based telescopes, to trace different stages of the star formation process. All this data was used to quantify the star formation activity and its efficiency, through Kennicutt-Schmidt (K-S) relations, which compares the SFR surface density versus the gas surface density. The goals of this work were to find molecular gas in places were it is unexpected due to hostile conditions, and use it, along with the complementary data, to characterize the star formation efficiency of the process, which is very unexplored at such low gas density regions.

XUV galaxies

The first topic explored in this thesis was on nearby XUV galaxies, i.e, galaxies with extended disks of UV emission, first revealed by the GALEX telescope (Gil de Paz et al. 2007a). Such disks extend up to the most external parts of spiral galaxies, beyond their optical radius (r_{25}), where gas densities and metallicities are low (Henry & Worthey 1999). Many of these regions lack Hα emission (e.g Thilker et al. 2005), the most common star formation tracer, but are rich in NUV and FUV emission coming from young O and B stars, indicating recent episodes of star formation, and the likely presence of the molecular gas out of which they must have been formed.

This thesis began in 2012 by resuming a work started in 2007 with CO observations on the nearby M63 galaxy, which has a remarkable disk of UV emission, extending up to 2.5 times its optical radius, as well as an extended disk of HI emission (Battaglia et al. 2006). Simultaneous CO(1–0) and CO(2–1) observations were done with the IRAM 30m telescope, using a linear arrange of 27 single ON+OFF pointings placed along the major axis of the galaxy, from the center of the galaxy up to a galactic radius (r_{gal}) of $1.6r_{25}$, and 12 pointings arranged in a rectangular configuration to map a small region bright in UV, located at $r_{gal} = 1.36r_{25}$. This mapping technique probed to be very efficient for detecting faint CO and achieving a good S/N. CO(1–0) emission was found in the observations along the radial axis, from the center of the galaxy up to the optical radius r_{25}, but not beyond. However, a CO(1–0) detection was found in the external bright UV region at $1.36r_{25}$. This is the fourth molecular gas detection in the outskirts of nearby spiral galaxies (after NGC4414 by Braine & Herpin 2004, NGC6946 by Braine et al. 2007 and M33 by Braine et al. 2010). The CO(2–1) emission is, on the other hand, confined to a galactic radius of $0.68r_{25}$. This result suggests subthermal excitation in the outer regions of the M63 disk.

A set of complementary data was used, including HI, Hα, 24μm, NUV, FUV and public CO, to compare the radial profiles of all this tracers to our CO observations. These radial profiles show a severe drop of emission with galactic radius, basically for all tracers except HI. Close to the r_{25} limit, all tracers begin to vanish considerably, and beyond r_{25}, they all are practically absent with the exception of the faint UV and HI emission. This is particularly seen at the location of the bright UV region, where the CO(1–0) detection was found, and where UV and HI emission, even though faint, still exist. This shows how UV and HI emission are good tracers to look for molecular gas (e.g Thilker et al. 2005, Gil de Paz et al. 2005, 2007a, Crosthwaite et al. 2002, Nieten et al. 2006). The UV region at $r_{gal} = 1.36r_{25}$, in which the CO emission is detected, is characterized by FUV and NUV emission fluxes similar to the fluxes observed at r_{25}, but stronger than the fluxes observed at $r_{gal} > r_{25}$ along the M63 major axis. This probably reflects a tight correlation between the CO and UV fluxes, namely between the intensity of star formation and the amount of molecular gas, so it strongly suggests that the absence of CO detection at $r_{gal} > r_{25}$ along the radial axis, where the XUV is weaker, is simply the result of the CO detection threshold that is still too high.

Additionally, the external UV region is characterized by a very high HI flux with respect to the measured CO flux. This leads us to speculate that HI is more likely the precursor of H_2 rather than the product of UV photodissociation, since it seems to dominate in quantity. This is, however, true as long as substantial H_2 is not hidden in the outer disk regions of M63, which may be the case as we observe hints for an excitation temperature decrease at large galactocentric radii, that could lead to very weak CO lines

SFRs were calculated for each pointing position of our observations, using the FUV and 24μm complementary data. In the same way, gas surface densities were calculated, using our observations to obtain $\Sigma_{\rm H_2}$, and the HI complementary data to calculate $\Sigma_{\rm HI}$, as well as the combination of both ($\Sigma_{\rm HI+H_2}$). These results were used to construct a K-S relation including all observing pointings in M63, i.e the ones along the major axis and the ones covering the external bright UV region. This is the first time that the K-S relation is quantified in the outskirts of a spiral galaxy, i.e., in low gas density environments, and we see that at a molecular gas surface density as low as $\Sigma_{\rm H_2} = 0.35 \rm M_\odot pc^2$. This value is well below all the determined $\rm H_2$ surface densities referenced in spiral galaxies so far (Bigiel et al. 2008, 2011), and still star formation occurs spontaneously.

Schmidt (1959) was the first to characterize the SFR density as a function of the gas density (both initially in volumic densities but soon translated into surface densities for observational reasons) through a power law of the form $\Sigma_{\rm SFR} = \rm A\Sigma_{gas}^N$, with the coefficient A directly related to the SFE, and the exponent N an indicator of the linearity of the relation. For the K-S relation obtained here, linear regressions of the form $\log(\Sigma_{\rm SFR}) = \log \rm A + N \log(\Sigma_{gas})$ were fitted to both data sets individually (radial profile and bright UV region), obtaining values of A and N for each one of them. We see a clear separation of these two sets of observations in the K-S plot, with the data points of major axis located above $\sim$10 $\rm M_\odot pc^{-2}$ (the HI-$\rm H_2$ threshold), and the points of the bright UV region located below this limit (Figure 2.12). We see that pointings along the major axis have their gas surface densities highly dominated by molecular gas, and follow an almost linear relation (N$\sim$1, in log space) when molecular gas is considered for $\Sigma_{\rm gas}$. On the other hand, pointings corresponding to the bright UV region have their gas surface densities mainly dominated by the atomic gas component, and follow a very non-linear (N$\sim$4) K-S relation. A clear broken power law is visible in the K-S plot between the two data sets, when the total gas surface density is considered ($\Sigma_{\rm HI+H_2}$), with an N slope of 1.7 for the pointings along the major axis, and 4.7 for the ones in the bright UV region. This discontinuity in the K-S relation indicates that the star forming processes, so well studied in the inner regions of galaxies, where gas densities are higher, are not the same, in terms of efficiency, to the ones in the less explored outer regions, with lower gas densities, and the relation cannot be extrapolated from inner to outer parts of galaxies.

This discontinuity can also be appreciated directly in the differences in SFE. Indeed, along the major axis of the disk out to the isophotal radius, the SFE settles the gas consumption within 10^8 years from 1% to 10%, whereas in the external UV region much less than 1% of the gas is converted into stars within 10^8 years. Consequently, star formation still occurs in the outer regions of the disk, but at very low efficiency, perhaps owing to the flaring of the outer gas layers.

Motivated by the successful results obtained for M63, new CO observations were done in a set of nearby galaxies with extended UV disks. Three XUV galaxies were selected for having extended disks of both UV and HI emission, well beyond their optical limits. ON+OFF single observing pointings were done in several targets with peaks of UV and HI emission, beyond the optical limits. Both lines, CO(1–0) and CO(2–1) were observed simultaneously with the IRAM 30m telescope, but no clear detection was found, probably because of a considerable loss of observing time due to bad weather conditions (strong winds). Weak emission was even searched for through a stacking technique, which enables us to increase the S/N of the data by averaging the spectra of all targets observed, at the same velocity (v=0). This is done via a velocity shift in each one of the spectra using HI complementary information. Unfortunately, no detection was found either, but faint emission is not completely discarded yet, and new search techniques and more elaborated stacking procedures will be applied in the near future to search for very faint emission. Nevertheless, 3σ upper limits were calculated from the rms noise levels of the spectra.

Finally, the last XUV galaxy studied was M83, which is a nearby and face-on galaxy, with an extended disk of both UV (Gil de Paz et al. 2007b) and HI (Walter et al. 2008) emisison. New ALMA CO(2–1) and continuum observations were done in an external region of the M83 galaxy, beyond its optical radius, in a small region very bright in both UV and HI (Figure 2.18). A $3''\times1.5''$ region was mapped within just an hour of observation, reaching an rms of 10.3 mJy per channel and a spectral resolution of 2.5 km/s. Unfortunately, apart from a very weak point source in continuum, no clear CO detection has been found yet. It is possible that no CO emission is present due to an extremely low metallicity and gas density, or possibly due to gas flaring in this region, so far away from the center of the galaxy, and so vulnerable to external factors. However, due to the recent delivery of the data, this is still work in progress. There seems to be some hints of faint clumps (Figure 2.20), with possible weak emission, and will be analyzed in a near future, with more elaborated search algorithms. Nevertheless, star formation activity is present. Maps of SFR surface density were created for the observed region, with FUV and 24μm complementary data, finding a $\Sigma_{\rm SFR}$ distribution mainly dominated by the 24μm emission (which traces the obscured FUV emission that is re-emitted by dust grains), and with values as high as 2.9×10^{-3} $M_{\odot}yr^{-1}kpc^{-2}$.

Ram-pressure stripping

The second part of this thesis was dedicated to investigate the effects of ram-pressure striping as a possible trigger of star formation, in regions far away from galaxies, with extremely low levels of gas density and metallicity, and where no star formation activity is expected.

The Virgo Cluster is an ideal laboratory to study this effect, since it harbors more than a thousand spiral and elliptical galaxies that interact with each other through merging and collisional processes, and with the cluster as a whole and the ICM through tidal interactions. For this particular work, the NGC4388 galaxy was chosen in the Virgo Cluster, for having a long tail of atomic gas (Oosterloo & van Gorkom 2005) stripped from the galaxy by the ICM. The HI tail extends more than 100 kpc from NGC4388 in direction to the M86 galaxy, and has previous detections of Hα (Yagi et al. 2013) and X-ray emission (Iwasawa et al. 2003).

Several observing targets where selected all along the tail, for having peaks of HI and Hα emission (from complementary data). Simultaneous CO(1–0) and CO(2–

1) observations were done with the IRAM 30m telescope, successfully finding 3 detections in a region which is bright in both HI and Hα emission, and located ~70 kpc away from NGC4388. Due to the high distance to the galaxy, and because ram-pressure is not expected to be able to drag such a dense gas, especially so far away, an H_2 formation in situ is most reasonable for this molecular gas.

For the sources with CO detections, a wide range of velocity dispersion (Δv $\sim$ $10 - 80$ km/s) was found. From Gaussian line fitting, CO(1–0) line profiles were obtained and used to estimate molecular gas masses and surface densities. The amount of molecular gas in these regions is very low (between 0.6 and 3 $\times 10^6 M_\odot$), and their H_2 surface densities between 0.8 and 2 $M_\odot pc^2$. These values are well below the HI-H_2 threshold, where the gas is mainly atomic and very little is known about the SFR at such low gas densities, hence the importance of these detections. For the remaining sources with no visible detection, 3σ upper limits where calculated from the rms noise levels of the spectra.

For the observed regions, Σ_{SFR} and Σ_{HI} where calculated from complementary Hα and HI data respectively, as well as Σ_{H_2} from our CO observations, to construct a K-S relation, including detections and upper limits. All these regions lay on the low gas density portion of the K-S plot, below the HI-H_2 threshold, and show an extremely low SFR (up to 2 orders of magnitude lower than for typical spiral galaxies). In the K-S plot, they are only comparable with the most outer clumps in the Hα/X-ray tail of the ISM stripped galaxy ESO137-001 in the Norma Cluster (Jáchym et al. 2014) and the XUV disk galaxies from Watson et al. (2014) and Dessauges-Zavadsky et al. (2014).

The inefficiency of the star forming processes in such regions can be directly seen in the extremely high depletion times, with some values even greater than 10^{12} years, exceeding by far a Hubble time. This suggests that this molecular gas will never be able to form stars, but remain in a gaseous phase and later join the ICM. Finally, we see that the observed sources follow a non-linear regime in the K-S plot. The linearity between the SFR and the gas surface density, so clear at high gas surface densities (> 9 $M_\odot pc^{-2}$) for normal spiral galaxies, once again cannot be extrapolated to lower densities, below the HI-H_2 threshold, where the star formation is extremely inefficient, and the molecular gas, even though present, does not necessarily form stars.

We conclude that CO observations in extremely low gas density regions can successfully trace molecular gas, when atomic gas and star formation tracers, such as UV, IR or Hα, are present. Furthermore, we see that H_2 formation in situ is possible, even in the most hostile environments. The detection of molecular gas helps us not only to confirm ongoing star formation, but allows us to quantify it and compare it to the star formation processes taking place in other regions, with different environmental conditions. Through analyses of Kennicutt-Schmidt relations, we see that star formation is different depending on the regions and conditions involved, since they show different SFEs. The aim of this thesis is to make a contribution to the less explored field of star formation under low density conditions. Thanks to an extended observational work, this research was able to give not only a quantification of star formation in the outer parts of spiral galaxies for the first time, but also helps to support the idea that star formation processes in low gas density environments are not the same as the ones at higher densities. Therefore, the Kennicutt-Schmidt relation and the star forming processes, so well studied at densities above $\sim$10 $M_{\odot}pc^{-2}$, cannot be extrapolated to lower densities.

Appendix

A.1 CO in low metallicity galaxies

This appendix includes an additional work on star formation at low metallicity environments, particularly in the WLM galaxy, with the first CO ever on a galaxy with such a low metallicity. I started to work in this collaboration during my master thesis, and finished during my first year of PhD.

A.1.1 Introduction

Searching for molecular gas in low metallicity galaxies always has an observational restriction due to its low emission. At low metallicity, any other element that is not hydrogen or helium is sparse, including carbon and oxygen, or any other elements that can trace molecular gas. In fact, before this work, CO had never been detected in galaxies in which the oxygen abundance relative to hydrogen is less than 20% of that of the Sun. But these galaxies do not lack completely of star formation, since there's evidence that they host young stars.

Wolf-Lundmark-Melotte (WLM) (Figure 1) is an isolated dwarf galaxy at a distance of 985 kpc, at the edge of the Local Group. It is a small, dwarf irregular (dIrr) galaxy with a metallicity of $0.13\mathrm{Z}_{\odot}$, a low SFR due to its size, and no previous evidence of the molecular gas that always accompanies young stars in larger galaxies.

Star forming gas was searched through CO(3–2) emission and continuum dust emission at 345 GHz with the Atacama Pathfinder Experiment (APEX) telescope in Chile. Both the Swedish Heterodyne Facility Instrument (SHeFI) and the APEX Bolometer Camera (LABOCA) were used, and the targets were selected for having peaks of 160μm (SPITZER) and HI (VLA) emission. The reason for choosing the band at 345 GHz is because dust measurements can be converted to a dust temperature and a dust mass, and, after applying a suitable gas-to-dust ratio, to a gas mass from which the H I mass can be subtracted to give the H_2 mass for comparison with CO.

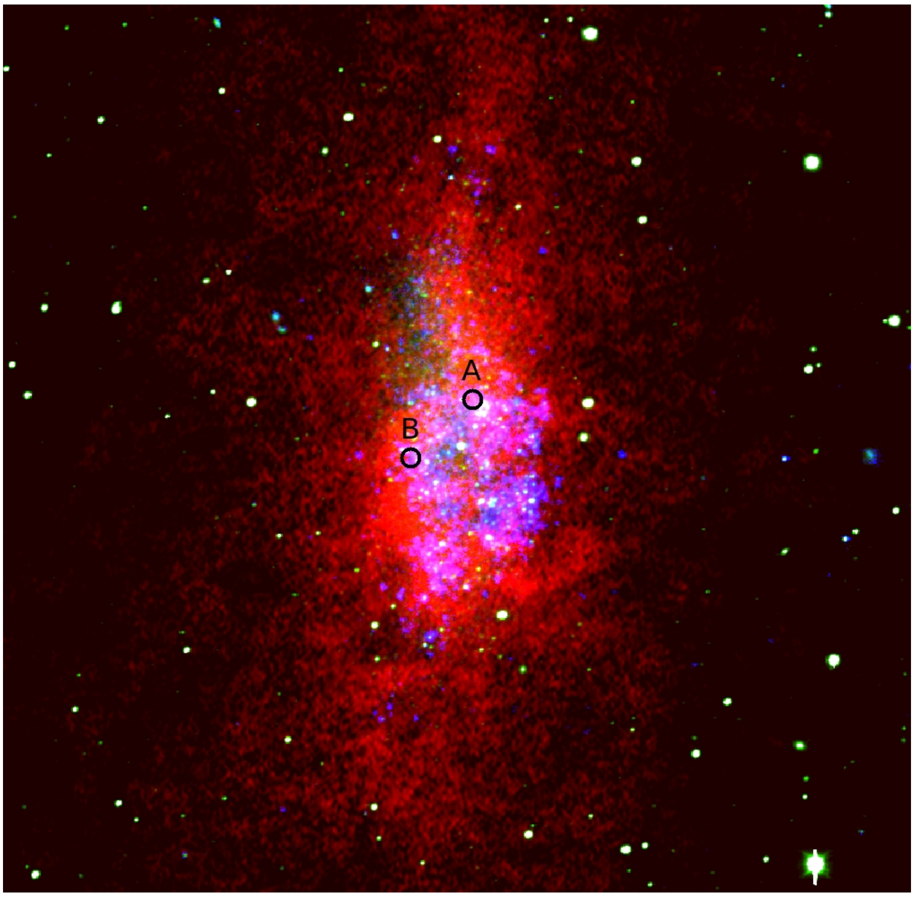

Figure 1: RGB image of WLM. Red: HI, green: V band, blue: FUV. Black circles denote the two positions where CO(3–2) was found: A position to the upper right, and B position to the lower left.

A.1.2 Results

Figure 1 shows WLM and the two regions, designated A and B, where CO(3–2) emission was detected. The peak CO brightness temperature in each detected region is ~0.01 - 0.015 K and the linewidth is 12 km s^{-1} (FWHM). Our observations with an 18″ aperture yields an intensity of 0.200 ± 0.046 K km s^{-1} and a luminosity of 1500 K km $s^{-1}pc^2$ for CO(3–2) in region A.

A large HI and FIR cloud that surrounds region A, designated region A1, was used to measure the dust temperature, $T_d = 15$ K, which was assumed to be the same throughout the region (the 160μm observation does not resolve region A, and so a more localized temperature measurement is not possible). This dust temperature was determined from the continuum emission, using the 870μm and 160μm fluxes, corrected for the CO(3-2) line and broadband free–free emission, to construct spectral energy distributions (SED). A modified black-body function was fitted to the SED, with dust emmissivity proportional to frequency to the power of the spectral emmissivity index β:

$$S_\nu \propto \nu^\beta B_\nu(T_d) \tag{1}$$

Local measurements (Planck Collaboration et al. 2011) suggest that $\beta = 1.78 \pm 0.08$, although a range is possible (Draine 2003, Galametz et al. 2012), depending on grain temperature and properties (Coupeaud et al. 2011). The 870μm flux was also corrected for an unexplained FIR and sub-millimeter excess that is commonly observed in other low-metallicity galaxies (Galametz et al. 2011, Verdugo 2012)

We made a χ^2 minimization fitting with the relation in Equation 1, using β=1.8 leaving T_d as the free paramenter. Additionally, we repeated the fitting with other values of β to show the dependency of the results on the spectral emmissivity index (Figure 2 shows an test example of such procedure).

Using this dust temperature for region A, the dust mass was calculated from an emissivity (Draine 2003) of $\kappa = 13.9$ cm^2 gm^{-1} at 140μm, and converted to 870μm with the same power-law index, β. The dust mass for region A is then

$$M_{\rm dust,A} = \frac{S_{870,A} D^2}{\kappa B_\nu(T_d)} \tag{2}$$

for flux $S_{870,A}$, distance D and black-body spectral function B_ν.

Dust mass is converted to gas mass using a factor equal to the gas–to–dust mass ratio, R_{GD}. An approximation (Leroy et al. 2011) is to assume the solar value (Draine et al. 2007) (1/0.007) increased by the inverse of the metallicity of WLM (0.13), which would give 1100. We use this approximation here, but introduce a scaling factor to the gas mass, $\delta_{GD} = R_{GD}/1100$; that is, the gas-to-dust ratio normalized by the solar value and scaled to the metallicity.

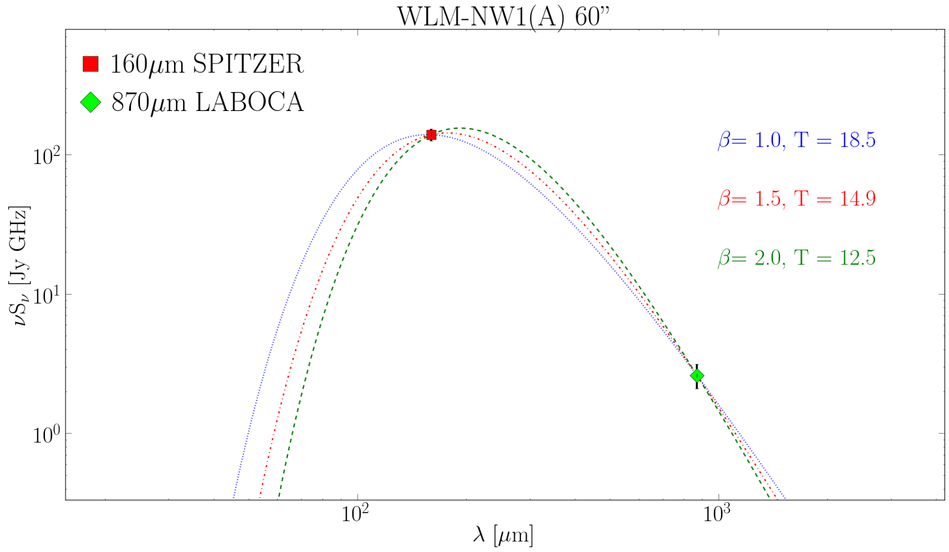

Figure 2: Example of a modified blackbody fitting procedure for region A in a 60″ aperture. Different values of β where tested. Each fit gives a result for T_d.

The total gas mass column density in a 22″ region around region A is ∼58 ± 15 $M_\odot$ pc^{-2} for $\beta = 1.8$. Atomic hydrogen contributes ∼27.3 ± 1.4 M$\odot$ pc^{-2}, and the remainder is ascribed to molecular H_2 traced by the observed CO.

The integral under the CO(3–2) line from region A is $I_{CO} = 0.200 \pm 0.046$ K km s^{-1}. This intensity has to be converted to CO(1–0) before comparing it with H_2 mass in the conventional way. We take as a guide (Nikolić et al. 2007) the value of CO(3–2)/CO(1–0) ∼ 0.80 in another low metallicity galaxy, the SMC (Dufour 1984) (where O/H = 20% of the solar value). The result, 0.25 K km s^{-1}, is combined with the H_2 mass column density to determine the conversion factor, α_{CO}, from CO(1–0) to H_2.

Taking the H_2 column density from the residual between the dust-derived total and the HI column density, 31 ± 15 $M_\odot$pc^{-2}, and dividing by the inferred CO(1–0) line integral of 0.25 K km s^{-1}, we obtain $\alpha_{CO} = 124 \pm 60$ $M_\odot$pc^{-2}K^{-1}km^{-1}s including He and heavy elements, with a range in α_{CO} from 34 to 271 as β varies from 1.6 to 2. The corresponding CO–to–H_2 conversion factor is $X_{CO} = (5.8 \pm 2.8)\times10^{21}$ cm^{-2}K^{-1}km^{-1}s. This value is used to calculate the H_2 mass in region B from its CO line intensity, giving a value of (1.2 ± 0.6) $\times10^5$ $M_\odot$.

The star-formation rate based on the Hα and FUV (Hunter et al. 2010) fluxes within an 18″ aperture centered on cloud A is (3.9–4.8) × $10^{-5}M_\odot$ yr^{-1}. Dividing these rates into the CO-associated molecular mass using $\alpha_{CO} = 124$ $M_\odot$ pc^{-2} K^{-1}km^{-1}s gives a CO molecular consumption time (for converting gas into stars) of 4.6–3.8 Gyr for region A. In region B, the star-formation rate from Hα and FUV fluxes is (1.7–12.6) × 10^{-5} $M_\odot$yr^{-1} and the CO molecular consumption time is 6.7–1.5 Gyr. These times are only slightly larger than the average value in spiral galaxies (Leroy et al. 2008), which is 2 Gyr, but they are ten times larger than the rate per molecule in local giant molecular clouds (Lada et al. 2012), which is a more direct analogy with our observations. The detection of CO in WLM suggests that star formation continues to occur in dense molecular gas even at lower metallicities than previously observed. The similarity between the metallicities of dIrr galaxies such as WLM and those of larger galaxies at high redshift (Mannucci et al. 2009) implies that we should be able to study star formation in young galaxies using the usual techniques.

A.1.3 Publication

This entirety of this work was published by Nature on March 2013, and is presented here.

LETTER

doi:10.1038/nature11933

Carbon monoxide in clouds at low metallicity in the dwarf irregular galaxy WLM

Bruce G. Elmegreen[1], Monica Rubio[2], Deidre A. Hunter[3], Celia Verdugo[2], Elias Brinks[4] & Andreas Schruba[5]

Carbon monoxide (CO) is the primary tracer for interstellar clouds where stars form, but it has never been detected in galaxies in which the oxygen abundance relative to hydrogen is less than 20 per cent of that of the Sun, even though such 'low-metallicity' galaxies often form stars. This raises the question of whether stars can form in dense gas without molecules, cooling to the required near-zero temperatures by atomic transitions and dust radiation rather than by molecular line emission[1]; and it highlights uncertainties about star formation in the early Universe, when the metallicity was generally low. Here we report the detection of CO in two regions of a local dwarf irregular galaxy, WLM, where the metallicity is 13 per cent of the solar value[2,3]. We use new submillimetre observations and archival far-infrared observations to estimate the cloud masses, which are both slightly greater than 100,000 solar masses. The clouds have produced stars at a rate per molecule equal to 10 per cent of that in the local Orion nebula cloud. The CO fraction of the molecular gas is also low, about 3 per cent of the Milky Way value. These results suggest that in small galaxies both star-forming cores and CO molecules become increasingly rare in molecular hydrogen clouds as the metallicity decreases.

Wolf–Lundmark–Melotte (WLM) is an isolated dwarf galaxy at the edge of the Local Group[4]. It has a low star-formation rate because of its small size and, like other dwarf irregular (dIrr) galaxies, shows no previous evidence[5] for the molecular gas that always accompanies young stars in larger galaxies[6]. One problem with the detection of molecules is that the dominant tracer of such gas is CO, and dIrr galaxies have low carbon and oxygen abundances relative to hydrogen. No galaxy with an O/H abundance less than 20% has been detected using CO as a tracer[7–9]. Far more abundant is molecular hydrogen (H_2), but this does not have an observable state of excitation at the low temperatures (~10–30 K) required for star formation.

To search for star-forming gas, we surveyed WLM for CO(J = 3–2) emission in rotational state J and for continuum dust emission at 345 GHz using the Atacama Pathfinder Experiment (APEX) telescope at Llano de Chajnantor, Chile, with the Swedish Heterodyne Facility Instrument[10] and the Large APEX Bolometer Camera[11] (LABOCA). We also used a map of dust emission at 160 μm from the Spitzer Local Volume Legacy Survey[12] and a map of atomic hydrogen re-reduced from the archives of the Jansky Very Large Array radio telescope. The dust measurements can be converted to a dust temperature and a dust mass, and, after applying a suitable gas-to-dust ratio, to a gas mass from which the H I mass can be subtracted to give the H_2 mass for comparison with CO.

Figure 1 shows WLM and the two regions, designated A and B, where we detected CO(3–2) emission, along with H I, far-infrared (FIR) and submillimetre images. Observed and derived parameters are listed in Tables 1 and 2, respectively. The peak CO brightness temperature in each detected region is ~0.01–0.015 K and the linewidth is ~12 km s^{-1} (full-width at half-maximum). Previous efforts to detect CO(J = 1–0) in WLM[5] partly overlapped region A with a 45″ aperture and determined a 5σ upper limit to the CO(1–0) intensity of 0.18 K km s^{-1}. Our observation with an 18″ aperture yields an intensity of 0.200 ± 0.046 K km s^{-1} for CO(3–2) in the same region. The difference arises because the CO cloud is unresolved even by our 18″ beam—we did not detect comparable CO(3–2) intensities in our searches adjacent to region A. The previous upper limit corresponds to a maximum CO(1–0) luminosity of 8,300 K km s^{-1} pc^2 inside 45″ (which corresponds to a beam diameter of 215 pc at WLM), whereas the cloud we detect has a CO(3–2) luminosity ~6 times smaller (1,500 K km s^{-1} pc^2). Likewise, the previous null detection[5] in CO(J = 2–1) claimed a 5σ upper limit that is about the same as our CO(3–2) detection, but their closest pointing differed from region A by ~70 pc (14″, or half the beam diameter for CO(2–1)), which could have been enough to take it off the CO cloud.

The 160-μm, 870-μm and H I peaks are slightly offset from the CO positions, indicating variations in temperature and molecular fraction. A large H I and FIR cloud that surrounds region A, designated region A1, was used to measure the dust temperature, T_d ~ 15 K, which was assumed to be the same throughout the region (the 160-μm observation does not resolve region A, and so a more localized temperature measurement is not possible). We determined T_d from the 870-μm and 160-μm fluxes corrected for the CO(3–2) line and broadband free–free emission (Table 1), assuming a modified black-body function with dust emissivity proportional to frequency to the power β. Local measurements[13] suggest that $\beta = 1.78 \pm 0.08$, although a range is possible[14,15], depending on grain temperature and properties[16]. The 870-μm flux was also corrected for an unexplained FIR and submillimetre excess that is commonly observed in other low-metallicity galaxies[17,18]. An alternate

Table 1 | Observations of WLM

Source	Region	Right ascension	Declination	Beam diameter (″)	Flux
CO(3–2)	A	0 h 1 min 57.32 s	−15° 26′ 49.5″	18	0.200 ± 0.046 K km s^{-1}
H I	A	0 h 1 min 57.32 s	−15° 26′ 49.5″	22	774 ± 40 mJy km s^{-1}
870 μm	A	0 h 1 min 57.32 s	−15° 26′ 49.5″	22	2.66 ± 0.53 mJy (0.11, 0.02)*
H I	A1	0 h 1 min 56.93 s	−15° 26′ 40.84″	45	4,170 ± 82 mJy km s^{-1}
870 μm	A1	0 h 1 min 56.93 s	−15° 26′ 40.84″	45	15.2 ± 3.0 mJy (0.11, 0.06)*
160 μm	A1	0 h 1 min 56.93 s	−15° 26′ 40.84″	45	136.2 ± 13.6 mJy (0.05)†
CO(3–2)	B	0 h 2 min 1.68 s	−15° 27′ 52.5″	18	0.129 ± 0.032 K km s^{-1}

* Quantities in parentheses are the CO(3–2) flux and the free–free emission, both in mJy, that were subtracted from the source flux before calculating the dust flux.
† Quantity in parentheses is the free–free emission, in mJy, that was subtracted from the source flux before calculating the dust flux. The average FIR excess factor[18] for the Small Magellanic Cloud (SMC) is 1.7, so we divide the CO-corrected and free–free-corrected 870-μm fluxes in the table by 1.7 to get the thermal dust flux.

---

[1] IBM Research Division, T.J. Watson Research Center, 1101 Kitchawan Road, Yorktown Heights, New York 10598, USA. [2] Departamento de Astronomía, Universidad de Chile, Casilla 36-D, Santiago, Chile. [3] Lowell Observatory, 1400 West Mars Hill Road, Flagstaff, Arizona 86001, USA. [4] Centre for Astrophysics Research, University of Hertfordshire, Hatfield AL10 9AB, UK. [5] Cahill Center for Astronomy and Astrophysics, California Institute of Technology, Pasadena, California 91125, USA.

©2013 Macmillan Publishers Limited. All rights reserved

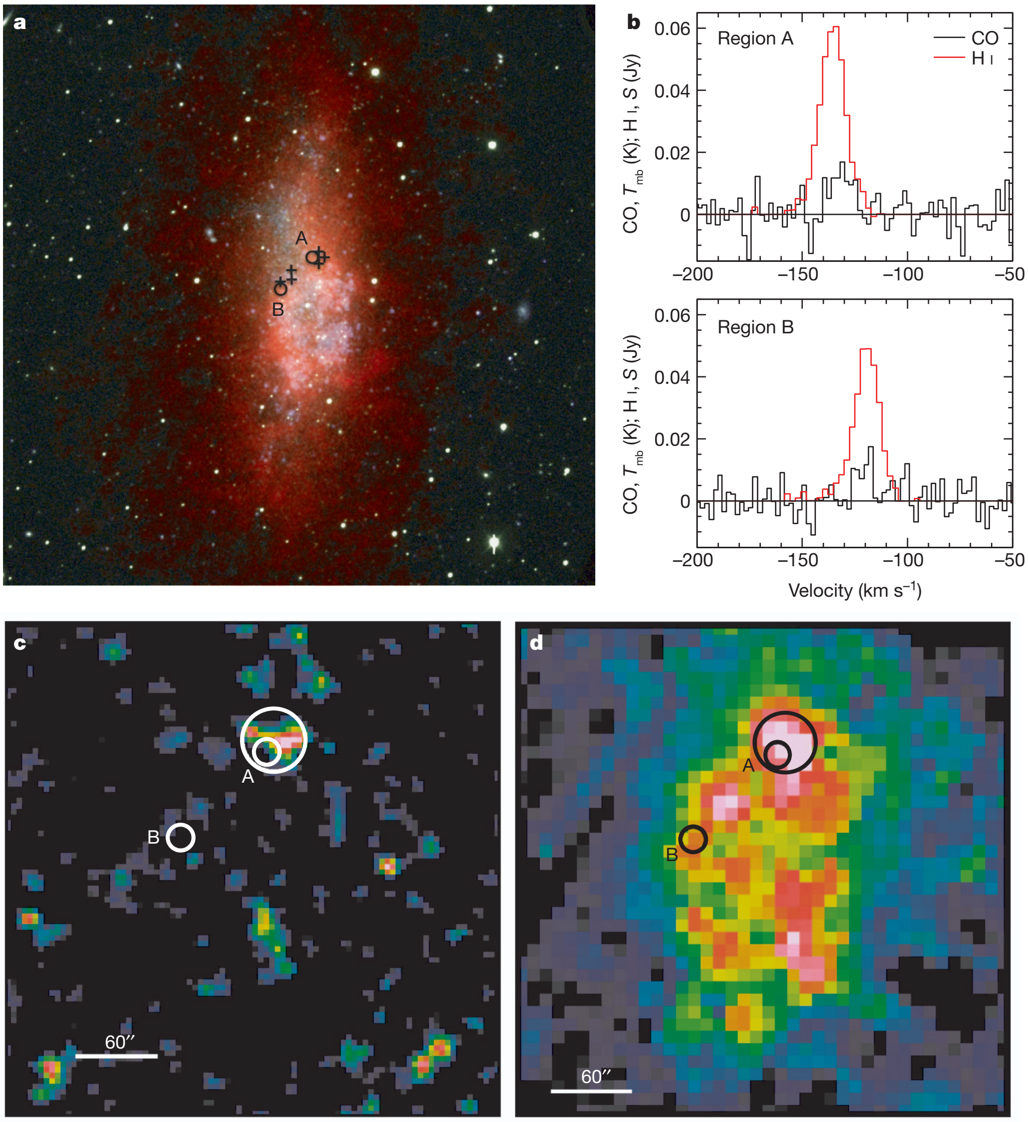

Figure 1 | Observations of the galaxy WLM. WLM is a small, gas-rich galaxy 985 ± 33 kpc from the Milky Way[4]. It contains $1.6\times10^7 M_\odot$ of stars[28], compared with $(6.4\pm0.6)\times10^{10} M_\odot$ in the Milky Way[29], and it forms new stars at a rate[23] of $0.006 M_\odot$ yr^{-1}, which is 12 times higher per unit stellar mass than the Milky Way[30]. **a**, Colour composite image: red, H I; green, V band; blue, GALEX far-ultraviolet. For H I the aperture was 7.6″ and the resolution was 2.6 km s^{-1}, and for CO(3–2) the aperture was 18″ (circles) and the resolution was 0.11 km s^{-1}, although the CO(3–2) spectra shown in the figure were smoothed to a resolution of 2.2 km s^{-1}. The CO detections are labelled; their exposure times were 218 min (region A) and 248 min (region B). Other regions searched with exposure times shorter by factors of ~2 to ~6 are indicated by plus signs; the presence of comparable CO mass in some of these other regions cannot be ruled out. **b**, Spectra of the two detections: velocities are relative to the local standard of rest; CO labels main-beam brightness temperature, T_{mb}, in kelvin; H I labels flux in Jy. **c**, False-colour image of the 870-μm observations made with LABOCA on APEX. **d**, False-colour Spitzer 160-μm image obtained from Spitzer archives. In **c** and **d**, the images show the same field of view and the small circles (22″ diameter, the resolution of LABOCA) show where CO was detected. The large circle is 45″ in diameter and surrounds a large H I and FIR cloud (region A1) where the dust temperature was measured.

Table 2 | Derived quantities for WLM

Source	Region	T (K)	Σ* ($M_\odot$ pc^{-2})	Mass ($M_\odot$)
$\beta = 1.8$, $\alpha_{CO} = 124 \pm 60$†				
Dust	A	14.7 ± 0.7‡	0.053 ± 0.014	$(4.6 \pm 1.2)\times10^2$
Gas§	A		$(58 \pm 15)\delta_{GD}$	$((5.1 \pm 1.3)\times10^5)\delta_{GD}$
H I‖	A		27.3 ± 1.4	$(2.4 \pm 0.1)\times10^5$
H_2	A		31 ± 15	$(1.8 \pm 0.8)\times10^5$
H_2¶	B		20 ± 10	$(1.2 \pm 0.6)\times10^5$
$\beta = 1.6$, $\alpha_{CO} = 34 \pm 34$†				
Dust	A	15.9 ± 0.8‡	0.032 ± 0.008	$(2.8 \pm 0.7)\times10^2$
Gas§	A		$(36 \pm 9)\delta_{GD}$	$((3.1 \pm 0.8)\times10^5)\delta_{GD}$
H_2	A		8.3 ± 9	$(0.5 \pm 0.5)\times10^5$
H_2¶	B		5.3 ± 6	$(0.3 \pm 0.3)\times10^5$
$\beta = 2$, $\alpha_{CO} = 271 \pm 97$†				
Dust	A	13.6 ± 0.6‡	0.087 ± 0.022	$(7.5 \pm 1.9)\times10^2$
Gas§	A		$(95 \pm 24)\delta_{GD}$	$((8.3 \pm 2.1)\times10^5)\delta_{GD}$
H_2	A		67 ± 24	$(3.9 \pm 1.4)\times10^5$
H_2¶	B		44 ± 16	$(2.5 \pm 0.9)\times10^5$

* Mass column density of gas or dust.

† The units of α_{CO} are $M_\odot$ pc^{-2} K^{-1} km^{-1} s. The uncertainty is dominated by the uncertainties in the 160-μm and 870-μm fluxes, as indicated by their error limits in Table 1. The error limits are approximately symmetric.

‡ The dust temperature in region A is assumed to be the same as the measured dust temperature in region A1.

§ $\delta_{GD} = R_{GD}/1{,}100$ is the gas-to-dust ratio, R_{GD}, normalized by the solar value and scaled to the metallicity of WLM. Lowering δ_{GD} lowers α_{CO}, but this does not seem reasonable: data suggests that the gas-to-dust mass ratio is ~5,000 for 12 + log(O/H) = 7.8 (ref. 27), and this implies larger values of δ_{GD} (~4.5) and α_{CO}. The gas mass and resulting α_{CO} value also depend on the assumed correction factor of 1.7 for submillimetre excess. With no correction for this excess, α_{CO} increases for all β values: at $\beta = 1.8$, $\alpha_{CO} = 370$. Solutions with no submillimetre excess correction and lower β values[19] can be found in Supplementary Information. In addition, α_{CO} depends on the assumed value of CO(3–2)/CO(1–0), which was taken to be 0.8 in Table 2; a value of CO(3–2)/CO(1–0) = 1 increases α_{CO} to 155 for $\beta = 1.8$.

‖ The H I mass column density is corrected for helium and heavy elements.

¶ The molecular mass for region B was calculated using the CO integrated intensity and the value of α_{CO} determined from region A.

©2013 Macmillan Publishers Limited. All rights reserved

combination of lower β with no submillimetre correction[19] gives similar results (Supplementary Information). The dust mass was calculated from an emissivity[14] of $\kappa = 13.9\,\mathrm{cm}^2\,\mathrm{gm}^{-1}$ at 140 μm, and converted to 870 μm with the same power-law index, β. The dust mass for region A is then $M_{\mathrm{dust,A}} = S_{870,\mathrm{A}}D^2/\kappa B_\nu(T_\mathrm{d})$ for flux $S_{870,\mathrm{A}}$, distance D and black-body spectral function B_ν.

Dust mass is converted to gas mass using a factor equal to the gas-to-dust mass ratio, R_{GD}. An approximation[8] is to assume the solar value[20] (1/0.007) increased by the inverse of the metallicity of WLM (0.13), which would give 1,100. We use this approximation here, but introduce a scaling factor to the gas mass, $\delta_{\mathrm{GD}} = R_{\mathrm{GD}}/1{,}100$; that is, the gas-to-dust ratio normalized by the solar value and scaled to the metallicity.

The results are in Table 2, assuming $\beta = 1.8$ as the fiducial value and comparing the results with those for $\beta = 1.6$ and 2 to illustrate the dependence of the results on β. Dust and gas mass correlate[15] with the assumed β value. The total gas mass column density in a 22′′ region around region A is $\sim 58 \pm 15 M_\odot\,\mathrm{pc}^{-2}$ for $\beta = 1.8$ ($M_\odot$, solar mass). Atomic hydrogen contributes $\sim 27.3 \pm 1.4 M_\odot\,\mathrm{pc}^{-2}$, and the remainder is ascribed to molecular $\mathrm{H_2}$ traced by the observed CO.

The integral under the CO(3–2) line from region A is $I_{\mathrm{CO}} = 0.200 \pm 0.046\,\mathrm{K\,km\,s^{-1}}$. This intensity has to be converted to CO(1–0) before comparing it with $\mathrm{H_2}$ mass in the conventional way. We take as a guide[21] the value of CO(3–2)/CO(1–0) ≈ 0.80 in another low-metallicity galaxy, the SMC[22] (where O/H = 20% of the solar value). The result, $0.25\,\mathrm{K\,km\,s^{-1}}$, is combined with the $\mathrm{H_2}$ mass column density to determine the conversion factor, α_{CO}, from CO(1–0) to $\mathrm{H_2}$. If α_{CO} can be calibrated as a function of metallicity, then CO observations can be used directly to infer the molecular gas content irrespective of the dust spectral energy distribution. Extensive compilations[7–9] show α_{CO} increasing strongly at lower metallicity, from $\sim 4 M_\odot\,\mathrm{pc}^{-2}\,\mathrm{K}^{-1}\,\mathrm{km}^{-1}\,\mathrm{s}$ in the Milky Way[8], where the metallicity[3] is $12 + \log(\mathrm{O/H}) = 8.69$, down to the previous CO detection limit[8] in the SMC, where $\alpha_{\mathrm{CO}} \approx 70 M_\odot\,\mathrm{pc}^{-2}\,\mathrm{K}^{-1}\,\mathrm{km}^{-1}\,\mathrm{s}$ at $12 + \log(\mathrm{O/H}) = 8.0$. Our observations of WLM[2] at a metallicity of $12 + \log(\mathrm{O/H}) = 7.8$ continue this trend.

Taking the $\mathrm{H_2}$ column density from the residual between the dust-derived total and the H I column density, $31 \pm 15 M_\odot\,\mathrm{pc}^{-2}$, and dividing by the inferred CO(1–0) line integral of $0.25\,\mathrm{K\,km\,s^{-1}}$, we obtain $\alpha_{\mathrm{CO}} = 124 \pm 60 M_\odot\,\mathrm{pc}^{-2}\,\mathrm{K}^{-1}\,\mathrm{km}^{-1}\,\mathrm{s}$ including helium and heavy elements, with a range in α_{CO} from 34 to 271 as β varies from 1.6 to 2. The corresponding factor, X_{CO}, for conversion from I_{CO} to $\mathrm{H_2}$ column density would be $(5.8 \pm 2.8) \times 10^{21}\,\mathrm{cm}^{-2}\,\mathrm{K}^{-1}\,\mathrm{km}^{-1}\,\mathrm{s}$, ranging from 1.5×10^{21} to 1.3×10^{22} as β varies between 1.6 and 2. There is a large uncertainty because of the unknown dust properties (β, κ, δ_{GD} and the submillimetre excess) and molecular excitation (CO(3–2)/CO(1–0)) in dIrr galaxies.

The star-formation rate based on the Hα and far-ultraviolet[23] fluxes within an 18′′ aperture centred on cloud A is $(3.9\text{–}4.8) \times 10^{-5} M_\odot\,\mathrm{yr}^{-1}$. Dividing these rates into the CO-associated molecular mass using $\alpha_{\mathrm{CO}} = 124\,M_\odot\,\mathrm{pc}^{-2}\,\mathrm{K}^{-1}\,\mathrm{km}^{-1}\,\mathrm{s}$ gives a CO molecular consumption time (for converting gas into stars) of 4.6–3.8 Gyr for region A. In region B, the star-formation rate from Hα and far-ultraviolet fluxes is $(1.7\text{–}12.6) \times 10^{-5} M_\odot\,\mathrm{yr}^{-1}$ and the CO molecular consumption time is 6.7–1.5 Gyr. These times are only slightly larger than the average value in spiral galaxies[24], which is ~2 Gyr, but they are ten times larger than the rate per molecule in local giant molecular clouds[25], which is a more direct analogy with our observations.

The detection of CO in WLM suggests that star formation continues to occur in dense molecular gas even at lower metallicities than previously observed. The similarity between the metallicities of dIrr galaxies such as WLM and those of larger galaxies at high redshift[26] implies that we should be able to study star formation in young galaxies using the usual techniques.

Received 24 October 2012; accepted 23 January 2013.

1. Krumholz, M. R. Star formation in atomic gas. *Astrophys. J.* **759,** 9 (2012).
2. Lee, H., Skillman, E. D. & Venn, K. A. Investigating the possible anomaly between nebular and stellar oxygen abundances in the dwarf irregular galaxy WLM. *Astrophys. J.* **620,** 223–237 (2005).
3. Asplund, M., Grevesse, N., Sauval, A. J. & Scott, P. The chemical composition of the sun. *Annu. Rev. Astron. Astrophys.* **47,** 481–522 (2009).
4. Leaman, R. *et al.* The resolved structure and dynamics of an isolated dwarf galaxy: a VLT and Keck spectroscopic survey of WLM. *Astrophys. J.* **750,** 33 (2012).
5. Taylor, C. L. & Klein, U. A search for CO in the Local Group dwarf irregular galaxy WLM. *Astron. Astrophys.* **366,** 811–816 (2001).
6. Bigiel, F. *et al.* A constant molecular gas depletion time in nearby disk galaxies. *Astrophys. J.* **730,** L13 (2011).
7. Taylor, C. L., Kobulnicky, H. A. & Skillman, E. D. CO emission in low-luminosity, H I-rich galaxies. *Astron. J.* **116,** 2746–2756 (1998).
8. Leroy, A. K. *et al.* The CO-to-$\mathrm{H_2}$ conversion factor from infrared dust emission across the Local Group. *Astrophys. J.* **737,** 12 (2011).
9. Schruba, A. *et al.* Low CO luminosities in dwarf galaxies. *Astron. J.* **143,** 138 (2012).
10. Vassilev, V. *et al.* A Swedish heterodyne facility instrument for the APEX telescope. *Astron. Astrophys.* **490,** 1157–1163 (2008).
11. Siringo, G. *et al.* The Large APEX BOlometer CAmera LABOCA. *Astron. Astrophys.* **497,** 945–962 (2009).
12. Dale, D. A. *et al.* The Spitzer Local Volume Legacy: survey description and infrared photometry. *Astrophys. J.* **703,** 517–556 (2009).
13. Planck Collaboration *et al.* Planck early results. XXV. Thermal dust in nearby molecular clouds. *Astron. Astrophys.* **536,** A25 (2011).
14. Draine, B. T. Interstellar dust grains. *Annu. Rev. Astron. Astrophys.* **41,** 241–289 (2003).
15. Galametz, M. *et al.* Mapping the cold dust temperatures and masses of nearby KINGFISH galaxies with Herschel. *Mon. Not. R. Astron. Soc.* **425,** 763–787 (2012).
16. Coupeaud, *et al.* Low-temperature FIR and submillimetre mass absorption coefficient of interstellar silicate dust analogues. *Astron. Astrophys.* **535,** A124 (2011).
17. Galametz, M. *et al.* Probing the dust properties of galaxies up to submillimetre wavelengths. II. Dust-to-gas mass ratio trends with metallicity and the submm excess in dwarf galaxies. *Astron. Astrophys.* **532,** A56 (2011).
18. Verdugo, C. *Sub-Millimeter Studies of Cold Dust and Gas in the Magellanic Clouds.* MSc thesis, Univ. Chile (2012).
19. Planck Collaboration. *Planck* early results. XVII. Origin of the submillimetre excess dust emission in the Magellanic Clouds. *Astron. Astrophys.* **536,** A17 (2011).
20. Draine, B. T. *et al.* Dust masses, PAH abundances, and starlight intensities in the SINGS galaxy sample. *Astrophys. J.* **663,** 866–894 (2007).
21. Nikolić, S., Garay, G., Rubio, M. & Johansson, L. E. B. CO and CS in the Magellanic Clouds: a χ^2-analysis of multitransitional data based on the MEP radiative transfer model. *Astron. Astrophys.* **471,** 561–571 (2007).
22. Dufour, R. J. The composition of H II regions in the Magellanic Clouds. *IAU Symp.* **108,** 353–360 (1984).
23. Hunter, D. A., Elmegreen, B. G. & Ludka, B. C. *GALEX* ultraviolet imaging of dwarf galaxies and star formation rates. *Astron. J.* **139,** 447–475 (2010).
24. Leroy, A. K. *et al.* The star formation efficiency in nearby galaxies: measuring where gas forms stars effectively. *Astron. J.* **136,** 2782–2845 (2008).
25. Lada, C. J., Forbrich, J., Lombardi, M. & Alves, J. F. Star formation rates in molecular clouds and the nature of the extragalactic scaling relations. *Astrophys. J.* **745,** 190 (2012).
26. Mannucci, F. *et al.* LSD: Lyman-break galaxies, stellar populations and dynamics – I. Mass, metallicity and gas at $z \sim 3.1$. *Mon. Not. R. Astron. Soc.* **398,** 1915–1931 (2009).
27. Engelbracht, C. W. *et al.* Metallicity effects on dust properties in starbursting galaxies. *Astrophys. J.* **678,** 804–827 (2008).
28. Zhang, H.-X., Hunter, D. A., Elmegreen, B. G., Gao, Y. & Schruba, A. Outside-in shrinking of the star-forming disks of dwarf irregular galaxies. *Astron. J.* **143,** 47 (2012).
29. McMillan, P. J. Mass models of the Milky Way. *Mon. Not. R. Astron. Soc.* **414,** 2446–2457 (2011).
30. Chomiuk, L. & Povich, M. S. Toward a unification of star formation rate determinations in the Milky Way and other galaxies. *Astron. J.* **142,** 197 (2011).

Supplementary Information is available in the online version of the paper.

Acknowledgements This work was funded in part by the US National Science Foundation through grants AST-0707563 and AST-0707426 to D.A.H. and B.G.E. M.R. and C.V. wish to acknowledge support from CONICYT (FONDECYT grant no. 1080335). M.R. was also supported by the Chilean Center for Astrophysics FONDAP grant no. 15010003. A.S. was supported by the Deutsche Forschungsgemeinschaft Priority Program 1177. We are grateful to M. Albrecht for help with the LABOCA data reduction and to L. Hill for making Fig. 1a. The National Radio Astronomy Observatory is a facility of the US National Science Foundation operated under cooperative agreement by Associated Universities, Inc.

Author Contributions B.G.E. coordinated the observational team, did the calculations for Table 2 and wrote the manuscript; M.R. was principal investigator for Chilean observing time on the APEX telescope and, with C.V., observed the galaxy in CO and at 870 μm, reduced the relevant data in Table 1 and did relevant calculations for Table 2; D.A.H. determined the observational strategy, selected WLM for study, chose the observing coordinates, extracted the H I spectra from the LITTLE THINGS data and prepared Fig. 1. E.B. was principal investigator on the APEX proposal using European time through ESO and coordinated the work on data uncertainties and background noise. A.S. made the WLM H I data cube from Jansky Very Large Array observations. All authors discussed the results and commented on the manuscript.

Author Information Reprints and permissions information is available at www.nature.com/reprints. The authors declare no competing financial interests. Readers are welcome to comment on the online version of the paper. Correspondence and requests for materials should be addressed to and requests for materials should be addressed to B.G.E. (bge@us.ibm.com).

©2013 Macmillan Publishers Limited. All rights reserved

Bibliography

Alberts, S., Calzetti, D., Dong, H. et al. *The Evolution of Stellar Populations in the Outer Disks of Spiral Galaxies*. ApJ, 2011. vol. 731, 28.

Allen, R. J., Atherton, P. D. & Tilanus, R. P. J. *Large-scale dissociation of molecular gas in galaxies by newly formed stars*. Nature, 1986. vol. 319, pp. 296–298.

Allen, R. J., Heaton, H. I. & Kaufman, M. J. *The Production of H I in Photodissociation Regions and a Comparison with CO (1-0) Emission*. ApJ, 2004. vol. 608, pp. 314–322.

Battaglia, G., Fraternali, F., Oosterloo, T. et al. *ion{H}{i} study of the warped spiral galaxy NGC 5055: a disk/dark matter halo offset?*. A&A, 2006. vol. 447, pp. 49–62.

Bauermeister, A., Blitz, L. & Ma, C.-P. *The Gas Consumption History to Redshift 4*. ApJ, 2010. vol. 717, pp. 323–332.

Bendo, G. J., Galliano, F. & Madden, S. C. *MIPS 24-160 μm photometry for the Herschel-SPIRE Local Galaxies Guaranteed Time Programs*. MNRAS, 2012. vol. 423, pp. 197–212.

Bigiel, F., Leroy, A., Walter, F. et al. *The Star Formation Law in Nearby Galaxies on Sub-Kpc Scales*. AJ, 2008. vol. 136, pp. 2846–2871.

Bigiel, F., Leroy, A., Walter, F. et al. *Extremely Inefficient Star Formation in the Outer Disks of Nearby Galaxies*. AJ, 2010. vol. 140, pp. 1194–1213.

Bigiel, F., Leroy, A. K., Walter, F. et al. *A Constant Molecular Gas Depletion Time in Nearby Disk Galaxies*. ApJ, 2011. vol. 730, L13.

Boissier, S., Boselli, A., Duc, P.-A. et al. *The GALEX Ultraviolet Virgo Cluster Survey (GUViCS). II. Constraints on star formation in ram-pressure stripped gas*. A&A, 2012. vol. 545, A142.

Boissier, S., Gil de Paz, A., Boselli, A. et al. *GALEX Observations of Low Surface Brightness Galaxies: UV Color and Star Formation Efficiency*. ApJ, 2008. vol. 681, pp. 244–257.

Bolatto, A. D., Wolfire, M. & Leroy, A. K. *The CO-to-H_2 Conversion Factor*. ARA&A, 2013. vol. 51, pp. 207–268.

Bouché, N., Murphy, M. T., Kacprzak, G. G. et al. *Signatures of Cool Gas Fueling a Star-Forming Galaxy at Redshift 2.3*. Science, 2013. vol. 341, pp. 50–53.

Braine, J., Ferguson, A. M. N., Bertoldi, F. et al. *The Detection of Molecular Gas in the Outskirts of NGC 6946*. ApJ, 2007. vol. 669, pp. L73–L76.

Braine, J., Gratier, P., Kramer, C. et al. *Molecular cloud formation and the star formation efficiency in M 33. Molecule and star formation in M 33*. A&A, 2010. vol. 520, A107.

Braine, J. & Herpin, F. *Molecular hydrogen beyond the optical edge of an isolated spiral galaxy*. Nature, 2004. vol. 432, pp. 369–371.

Braine, J., Lisenfeld, U., Due, P.-A. et al. *Formation of molecular gas in the tidal debris of violent galaxy-galaxy interactions*. Nature, 2000. vol. 403, pp. 867–869.

Carter, M., Lazareff, B., Maier, D. et al. *The EMIR multi-band mm-wave receiver for the IRAM 30-m telescope*. A&A, 2012. vol. 538, A89.

Casasola, V., Hunt, L., Combes, F. et al. *The resolved star-formation relation in nearby active galactic nuclei*. ArXiv e-prints, 2015.

Cayatte, V., van Gorkom, J. H., Balkowski, C. et al. *VLA observations of neutral hydrogen in Virgo Cluster galaxies. I - The Atlas*. AJ, 1990. vol. 100, pp. 604–634.

Chung, A., van Gorkom, J. H., Kenney, J. D. P. et al. *Virgo Galaxies with Long One-sided H I Tails*. ApJ, 2007. vol. 659, pp. L115–L119.

Chung, A., van Gorkom, J. H., Kenney, J. D. P. et al. *VLA Imaging of Virgo Spirals in Atomic Gas (VIVA). I. The Atlas and the H I Properties*. AJ, 2009. vol. 138, pp. 1741–1816.

Cluver, M. E., Appleton, P. N., Boulanger, F. et al. *Powerful H_2 Line Cooling in Stephan's Quintet. I. Mapping the Significant Cooling Pathways in Group-wide Shocks*. ApJ, 2010. vol. 710, pp. 248–264.

Combes, F. *Gas Accretion in Disk Galaxies*. M. S. Seigar & P. Treuthardt, eds., *Structure and Dynamics of Disk Galaxies*, vol. 480 of *Astronomical Society of the Pacific Conference Series*. p. 211.

Conselice, C. J., Gallagher, J. S., III & Wyse, R. F. G. *On the Nature of the NGC 1275 System*. AJ, 2001. vol. 122, pp. 2281–2300.

Cortese, L., Marcillac, D., Richard, J. et al. *The strong transformation of spiral galaxies infalling into massive clusters at z ˜ 0.2*. MNRAS, 2007. vol. 376, pp. 157–172.

Coupeaud, A., Demyk, K., Meny, C. et al. *Low-temperature FIR and submillimetre mass absorption coefficient of interstellar silicate dust analogues*. A&A, 2011. vol. 535, A124.

CROSTHWAITE, L. P., TURNER, J. L., BUCHHOLZ, L. et al. *CO in the Disk of the Barred Spiral Galaxy M83: CO (1-0), CO (2-1), and Neutral Gas*. AJ, 2002. vol. 123, pp. 1892–1912.

DALE, D. A., COHEN, S. A., JOHNSON, L. C. et al. *The Spitzer Local Volume Legacy: Survey Description and Infrared Photometry*. ApJ, 2009. vol. 703, pp. 517–556.

DASYRA, K. M., COMBES, F., SALOMÉ, P. et al. *Survival of molecular gas in Virgo's hot intracluster medium: CO near M 86*. A&A, 2012. vol. 540, A112.

DAVIES, J. I., BIANCHI, S., CORTESE, L. et al. *The Herschel Virgo Cluster Survey - VIII. The Bright Galaxy Sample*. MNRAS, 2012. vol. 419, pp. 3505–3520.

DEMAIO, T., GONZALEZ, A. H., ZABLUDOFF, A. et al. *On the origin of the intracluster light in massive galaxy clusters*. MNRAS, 2015. vol. 448, pp. 1162–1177.

DESSAUGES-ZAVADSKY, M., VERDUGO, C., COMBES, F. et al. *CO map and steep Kennicutt-Schmidt relation in the extended UV disk of M 63*. A&A, 2014. vol. 566, A147.

DICKMAN, R. L., SNELL, R. L. & SCHLOERB, F. P. *Carbon monoxide as an extragalactic mass tracer*. ApJ, 1986. vol. 309, pp. 326–330.

DOBBS, C. L., KRUMHOLZ, M. R., BALLESTEROS-PAREDES, J. et al. *Formation of Molecular Clouds and Global Conditions for Star Formation*. Protostars and Planets VI, 2014, pp. 3–26.

DONG, H., CALZETTI, D., REGAN, M. et al. *Spitzer Observations of Star Formation in the Extreme Outer Disk of M83 (NGC5236)*. AJ, 2008. vol. 136, 479.

DRAINE, B. T. *Interstellar Dust Grains*. ARA&A, 2003. vol. 41, pp. 241–289.

DRAINE, B. T., DALE, D. A., BENDO, G. et al. *Dust Masses, PAH Abundances, and Starlight Intensities in the SINGS Galaxy Sample*. ApJ, 2007. vol. 663, pp. 866–894.

DRAZINOS, P., KONTIZAS, E., BELLAS-VELIDIS, I. et al. *Indication of Hierarchical Star Formation in Spiral Galaxies*. 2013. pp. 36–47.

DUFOUR, R. J. *The composition of H II regions in the Magellanic Clouds*. S. van den Bergh & K. S. D. de Boer, eds., *Structure and Evolution of the Magellanic Clouds*, vol. 108 of *IAU Symposium*. pp. 353–360.

EDGE, A. C., OONK, J. B. R., MITTAL, R. et al. *Herschel observations of FIR emission lines in brightest cluster galaxies*. A&A, 2010. vol. 518, L46.

ELMEGREEN, D. M. & ELMEGREEN, B. *Hierarchical Star Formation in LEGUS Galaxies*. *American Astronomical Society Meeting Abstracts 224*, vol. 224 of *American Astronomical Society Meeting Abstracts*. p. 223.

FABIAN, A. C., SANDERS, J. S., TAYLOR, G. B. et al. *A very deep Chandra observation of the Perseus cluster: shocks, ripples and conduction*. MNRAS, 2006. vol. 366, pp. 417–428.

Feldmeier, J. J., Mihos, J. C., Morrison, H. L. et al. *Deep CCD Surface Photometry of Galaxy Clusters. I. Methods and Initial Studies of Intracluster Starlight*. ApJ, 2002. vol. 575, pp. 779–800.

Fouqué, P., Solanes, J. M., Sanchis, T. et al. *Structure, mass and distance of the Virgo cluster from a Tolman-Bondi model*. A&A, 2001. vol. 375, pp. 770–780.

Galametz, M., Kennicutt, R. C., Albrecht, M. et al. *Mapping the cold dust temperatures and masses of nearby KINGFISH galaxies with Herschel*. MNRAS, 2012. vol. 425, pp. 763–787.

Galametz, M., Madden, S. C., Galliano, F. et al. *Probing the dust properties of galaxies up to submillimetre wavelengths. II. Dust-to-gas mass ratio trends with metallicity and the submm excess in dwarf galaxies*. A&A, 2011. vol. 532, A56.

Gao, Y. & Solomon, P. M. *The Star Formation Rate and Dense Molecular Gas in Galaxies*. ApJ, 2004. vol. 606, pp. 271–290.

Gavazzi, G., Boselli, A., Mayer, L. et al. *75 Kiloparsec Trails of Ionized Gas behind Two Irregular Galaxies in A1367*. ApJ, 2001. vol. 563, pp. L23–L26.

Gil de Paz, A., Boissier, S., Madore, B. F. et al. *The GALEX Ultraviolet Atlas of Nearby Galaxies*. ApJS, 2007a. vol. 173, pp. 185–255.

Gil de Paz, A., Madore, B. F., Boissier, S. et al. *Discovery of an Extended Ultraviolet Disk in the Nearby Galaxy NGC 4625*. ApJ, 2005. vol. 627, pp. L29–L32.

Gil de Paz, A., Madore, B. F., Boissier, S. et al. *Chemical and Photometric Evolution of Extended Ultraviolet Disks: Optical Spectroscopy of M83 (NGC 5236) and NGC 4625*. ApJ, 2007b. vol. 661, pp. 115–134.

Gong, M. & Ostriker, E. C. *Prestellar Core Formation, Evolution, and Accretion from Gravitational Fragmentation in Turbulent Converging Flows*. ApJ, 2015. vol. 806, 31.

Gu, L., Yagi, M., Nakazawa, K. et al. *Multi-wavelength Studies of Spectacular Ram Pressure Stripping of a Galaxy: Discovery of an X-Ray Absorption Feature*. ApJ, 2013. vol. 777, L36.

Gunn, J. E. & Gott, J. R., III. *On the Infall of Matter Into Clusters of Galaxies and Some Effects on Their Evolution*. ApJ, 1972. vol. 176, p. 1.

Haynes, M. P. & Giovanelli, R. *Neutral hydrogen in isolated galaxies. IV - Results for the Arecibo sample*. AJ, 1984. vol. 89, pp. 758–800.

Helfer, T. T., Thornley, M. D., Regan, M. W. et al. *The BIMA Survey of Nearby Galaxies (BIMA SONG). II. The CO Data*. ApJS, 2003. vol. 145, pp. 259–327.

Henry, R. B. C. & Worthey, G. *The Distribution of Heavy Elements in Spiral and Elliptical Galaxies*. PASP, 1999. vol. 111, pp. 919–945.

Holwerda, B. W., Pirzkal, N. & Heiner, J. S. *Quantified H I morphology - VI. The morphology of extended discs in UV and H I*. MNRAS, 2012. vol. 427, pp. 3159–3175.

Hunter, D. A., Elmegreen, B. G. & Ludka, B. C. *Galex Ultraviolet Imaging of Dwarf Galaxies and Star Formation Rates*. AJ, 2010. vol. 139, pp. 447–475.

Isobe, T., Feigelson, E. D., Akritas, M. G. et al. *Linear regression in astronomy.*. ApJ, 1990. vol. 364, pp. 104–113.

Iwasawa, K., Wilson, A. S., Fabian, A. C. et al. *The X-ray nebula around the type 2 Seyfert galaxy NGC 4388*. MNRAS, 2003. vol. 345, pp. 369–378.

Jáchym, P., Combes, F., Cortese, L. et al. *Abundant Molecular Gas and Inefficient Star Formation in Intracluster Regions: Ram Pressure Stripped Tail of the Norma Galaxy ESO137-001*. ApJ, 2014. vol. 792, 11.

Jáchym, P., Palouš, J., Köppen, J. et al. *Gas stripping in galaxy clusters: a new SPH simulation approach*. A&A, 2007. vol. 472, pp. 5–20.

Kenney, J. D. P., Tal, T., Crowl, H. H. et al. *A Spectacular Hα Complex in Virgo: Evidence for a Collision between M86 and NGC 4438 and Implications for the Collisional ISM Heating of Ellipticals*. ApJ, 2008. vol. 687, pp. L69–L74.

Kenney, J. D. P., van Gorkom, J. H. & Vollmer, B. *VLA H I Observations of Gas Stripping in the Virgo Cluster Spiral NGC 4522*. AJ, 2004. vol. 127, pp. 3361–3374.

Kenney, J. D. P. & Young, J. S. *The effects of environment on the molecular and atomic gas properties of large Virgo cluster spirals*. ApJ, 1989. vol. 344, pp. 171–199.

Kennicutt, R. C., Calzetti, D., Aniano, G. et al. *KINGFISH – Key Insights on Nearby Galaxies: A Far-Infrared Survey with Herschel: Survey Description and Image Atlas*. PASP, 2011. vol. 123, pp. 1347–1369.

Kennicutt, R. C. & Evans, N. J. *Star Formation in the Milky Way and Nearby Galaxies*. ARA&A, 2012. vol. 50, pp. 531–608.

Kennicutt, R. C., Jr. *The star formation law in galactic disks*. ApJ, 1989. vol. 344, pp. 685–703.

Kennicutt, R. C., Jr. *Star Formation in Galaxies Along the Hubble Sequence*. ARA&A, 1998a. vol. 36, pp. 189–232.

Kennicutt, R. C., Jr. *The Global Schmidt Law in Star-forming Galaxies*. ApJ, 1998b. vol. 498, pp. 541–552.

Kennicutt, R. C., Jr., Lee, J. C., Funes, S. J., José G. et al. *An Hα Imaging Survey of Galaxies in the Local 11 Mpc Volume*. ApJS, 2008. vol. 178, pp. 247–279.

Kroupa, P. & Weidner, C. *Galactic-Field Initial Mass Functions of Massive Stars*. ApJ, 2003. vol. 598, pp. 1076–1078.

Lada, C. J., Forbrich, J., Lombardi, M. et al. *Star Formation Rates in Molecular Clouds and the Nature of the Extragalactic Scaling Relations*. ApJ, 2012. vol. 745, 190.

Leroy, A. K., Bolatto, A., Gordon, K. et al. *The CO-to-*H_2 *Conversion Factor from Infrared Dust Emission across the Local Group*. ApJ, 2011. vol. 737, 12.

Leroy, A. K., Walter, F., Bigiel, F. et al. *Heracles: The HERA CO Line Extragalactic Survey*. AJ, 2009. vol. 137, pp. 4670–4696.

Leroy, A. K., Walter, F., Brinks, E. et al. *The Star Formation Efficiency in Nearby Galaxies: Measuring Where Gas Forms Stars Effectively*. AJ, 2008. vol. 136, pp. 2782–2845.

Leroy, A. K., Walter, F., Sandstrom, K. et al. *Molecular Gas and Star Formation in nearby Disk Galaxies*. AJ, 2013. vol. 146, 19.

Lim, J., Ohyama, Y., Chi-Hung, Y. et al. *A Molecular Hydrogen Nebula in the Central cD Galaxy of the Perseus Cluster*. ApJ, 2012. vol. 744, 112.

Longmore, S. N., Bally, J., Testi, L. et al. *Variations in the Galactic star formation rate and density thresholds for star formation*. MNRAS, 2013. vol. 429, pp. 987–1000.

Lupton, R., Blanton, M. R., Fekete, G. et al. *Preparing Red-Green-Blue Images from CCD Data*. PASP, 2004. vol. 116, pp. 133–137.

Machacek, M., Dosaj, A., Forman, W. et al. *Infall of the Elliptical Galaxy NGC 1404 into the Fornax Cluster*. ApJ, 2005. vol. 621, pp. 663–672.

Machacek, M. E., Jones, C. & Forman, W. R. *Chandra Observations of NGC 4438: An Environmentally Damaged Galaxy in the Virgo Cluster*. ApJ, 2004. vol. 610, pp. 183–200.

Mahdavi, A., Geller, M. J., Fabricant, D. G. et al. *The Lumpy Cluster Abell 1185*. AJ, 1996. vol. 111, p. 64.

Mannucci, F., Cresci, G., Maiolino, R. et al. *LSD: Lyman-break galaxies Stellar populations and Dynamics - I. Mass, metallicity and gas at z ~ 3.1*. MNRAS, 2009. vol. 398, pp. 1915–1931.

Martin, C. L. & Kennicutt, R. C., Jr. *Star Formation Thresholds in Galactic Disks*. ApJ, 2001. vol. 555, pp. 301–321.

Mei, S., Blakeslee, J. P., Côté, P. et al. *The ACS Virgo Cluster Survey. XIII. SBF Distance Catalog and the Three-dimensional Structure of the Virgo Cluster*. ApJ, 2007. vol. 655, pp. 144–162.

Merritt, D. *Relaxation and tidal stripping in rich clusters of galaxies. II. Evolution of the luminosity distribution*. ApJ, 1984. vol. 276, pp. 26–37.

Mihos, J. C., Harding, P., Feldmeier, J. et al. *Diffuse Light in the Virgo Cluster*. ApJ, 2005. vol. 631, pp. L41–L44.

NARAYANAN, D., KRUMHOLZ, M., OSTRIKER, E. C. et al. *The CO-H_2 conversion factor in disc galaxies and mergers*. MNRAS, 2011. vol. 418, pp. 664–679.

NIETEN, C., NEININGER, N., GUÉLIN, M. et al. *Molecular gas in the Andromeda galaxy*. A&A, 2006. vol. 453, pp. 459–475.

NIKOLIĆ, S., GARAY, G., RUBIO, M. et al. *CO and CS in the Magellanic Clouds: a χ ˆ2-analysis of multitransitional data based on the MEP radiative transfer model*. A&A, 2007. vol. 471, pp. 561–571.

NULSEN, P. E. J. *Transport processes and the stripping of cluster galaxies*. MNRAS, 1982. vol. 198, pp. 1007–1016.

OOSTERLOO, T. & VAN GORKOM, J. *A large H I cloud near the centre of the Virgo cluster*. A&A, 2005. vol. 437, pp. L19–L22.

O'SULLIVAN, E., GIACINTUCCI, S., VRTILEK, J. M. et al. *A Chandra X-ray View of Stephan's Quintet: Shocks and Star Formation*. ApJ, 2009. vol. 701, pp. 1560–1568.

PATUREL, G., PETIT, C., PRUGNIEL, P. et al. *HYPERLEDA. I. Identification and designation of galaxies*. A&A, 2003. vol. 412, pp. 45–55.

PLANCK COLLABORATION, ABERGEL, A., ADE, P. A. R. et al. *Planck early results. XXV. Thermal dust in nearby molecular clouds*. A&A, 2011. vol. 536, A25.

POHLEN, M. & TRUJILLO, I. *The structure of galactic disks. Studying late-type spiral galaxies using SDSS*. A&A, 2006. vol. 454, pp. 759–772.

QUILIS, V., MOORE, B. & BOWER, R. *Gone with the Wind: The Origin of S0 Galaxies in Clusters*. Science, 2000. vol. 288, pp. 1617–1620.

ROEDIGER, E. & HENSLER, G. *Ram pressure stripping of disk galaxies. From high to low density environments*. A&A, 2005. vol. 433, pp. 875–895.

SALOMÉ, P., COMBES, F., EDGE, A. C. et al. *Cold molecular gas in the Perseus cluster core. Association with X-ray cavity, Hα filaments and cooling flow*. A&A, 2006. vol. 454, pp. 437–445.

SALOMÉ, P., COMBES, F., REVAZ, Y. et al. *A very extended molecular web around NGC 1275*. A&A, 2011. vol. 531, A85.

SÁNCHEZ ALMEIDA, J., ELMEGREEN, B. G., MUÑOZ-TUÑÓN, C. et al. *Star formation sustained by gas accretion*. A&A Rev., 2014. vol. 22, 71.

SANCISI, R., FRATERNALI, F., OOSTERLOO, T. et al. *Cold gas accretion in galaxies*. A&A Rev., 2008. vol. 15, pp. 189–223.

SANDSTROM, K. M., LEROY, A. K., WALTER, F. et al. *The CO-to-H_2 Conversion Factor and Dust-to-gas Ratio on Kiloparsec Scales in Nearby Galaxies*. ApJ, 2013. vol. 777, 5.

SCHMIDT, M. *The Rate of Star Formation.*. ApJ, 1959. vol. 129, p. 243.

Schruba, A., Leroy, A. K., Walter, F. et al. *A Molecular Star Formation Law in the Atomic-gas-dominated Regime in Nearby Galaxies*. AJ, 2011. vol. 142, 37.

Scott, T. C., Cortese, L., Brinks, E. et al. *Two long H I tails in the outskirts of Abell 1367*. MNRAS, 2012. vol. 419, pp. L19–L23.

Serra, P., Koribalski, B., Duc, P.-A. et al. *Discovery of a giant HI tail in the galaxy group HCG 44*. MNRAS, 2013. vol. 428, pp. 370–380.

Shlosman, I., Frank, J. & Begelman, M. C. *Bars within bars - A mechanism for fuelling active galactic nuclei*. Nature, 1989. vol. 338, pp. 45–47.

Smith, D. A., Allen, R. J., Bohlin, R. C. et al. *A New Probe of the Molecular Gas in Galaxies: Application to M101*. ApJ, 2000. vol. 538, pp. 608–622.

Solomon, P. M., Rivolo, A. R., Barrett, J. et al. *Mass, luminosity, and line width relations of Galactic molecular clouds*. ApJ, 1987. vol. 319, pp. 730–741.

Spitzer, L., Jr. & Baade, W. *Stellar Populations and Collisions of Galaxies.*. ApJ, 1951. vol. 113, p. 413.

Sun, M., Donahue, M., Roediger, E. et al. *Spectacular X-ray Tails, Intracluster Star Formation, and ULXs in A3627*. ApJ, 2010. vol. 708, pp. 946–964.

Sun, M., Donahue, M. & Voit, G. M. *Hα Tail, Intracluster H II Regions, and Star Formation: ESO 137-001 in Abell 3627*. ApJ, 2007. vol. 671, pp. 190–202.

Tamura, T., Maeda, Y., Mitsuda, K. et al. *X-ray Spectroscopy of the Core of the Perseus Cluster with Suzaku: Elemental Abundances in the Intracluster Medium*. ApJ, 2009. vol. 705, pp. L62–L66.

Thilker, D. A., Bianchi, L., Boissier, S. et al. *Recent Star Formation in the Extreme Outer Disk of M83*. ApJ, 2005. vol. 619, pp. L79–L82.

Tilanus, R. P. J. & Allen, R. J. *Spiral Structure of M83 - Distribution and Kinematics of the Atomic and Ionized Hydrogen*. A&A, 1993. vol. 274, p. 707.

Tonnesen, S., Bryan, G. L. & van Gorkom, J. H. *Environmentally Driven Evolution of Simulated Cluster Galaxies*. ApJ, 2007. vol. 671, pp. 1434–1445.

Verdes-Montenegro, L., Bosma, A. & Athanassoula, E. *A detailed study of the ringed galaxy NGC 3344*. A&A, 2000. vol. 356, pp. 827–839.

Verdugo, Celia. *Master's thesis: Sub-Millimeter Studies of Cold Dust and Gas in the Magellanic Clouds. MSc thesis, Univ. Chile*, 2012.

Vollmer, B., Braine, J., Combes, F. et al. *New CO observations and simulations of the NGC 4438/NGC 4435 system. Interaction diagnostics of the Virgo cluster galaxy NGC 4438*. A&A, 2005. vol. 441, pp. 473–489.

Vollmer, B., Braine, J., Pappalardo, C. et al. *Ram-pressure stripped molecular gas in the Virgo spiral galaxy NGC 4522*. A&A, 2008. vol. 491, pp. 455–464.

Vollmer, B., Cayatte, V., Balkowski, C. et al. *Ram Pressure Stripping and Galaxy Orbits: The Case of the Virgo Cluster*. ApJ, 2001. vol. 561, pp. 708–726.

WALTER, F., BRINKS, E., DE BLOK, W. J. G. et al. *THINGS: The H I Nearby Galaxy Survey*. AJ, 2008. vol. 136, 2563.

WATSON, L. C., MARTINI, P., LISENFELD, U. et al. *The Molecular Gas - Star Formation Connection in an Extended Ultraviolet (XUV) Disk*. *American Astronomical Society Meeting Abstracts 223*, vol. 223 of *American Astronomical Society Meeting Abstracts*. p. 454.22.

WU, J., EVANS, N. J., II, GAO, Y. et al. *Connecting Dense Gas Tracers of Star Formation in our Galaxy to High-z Star Formation*. ApJ, 2005. vol. 635, pp. L173–L176.

WYDER, T. K., MARTIN, D. C., BARLOW, T. A. et al. *The Star Formation Law at Low Surface Density*. ApJ, 2009. vol. 696, pp. 1834–1853.

YAGI, M., GU, L., FUJITA, Y. et al. *Multi-wavelength Studies of Spectacular Ram-pressure Stripping of a Galaxy. II. Star Formation in the Tail*. ApJ, 2013. vol. 778, 91.

YAGI, M., KOMIYAMA, Y., YOSHIDA, M. et al. *The Remarkable 60×2 kpc Optical Filament Associated with a Poststarburst Galaxy in the Coma Cluster*. ApJ, 2007. vol. 660, pp. 1209–1214.

YOSHIDA, M., YAGI, M., OKAMURA, S. et al. *Discovery of a Very Extended Emission-Line Region around the Seyfert 2 Galaxy NGC 4388*. ApJ, 2002. vol. 567, pp. 118–129.

YOUNG, J. S. & SCOVILLE, N. Z. *Molecular gas in galaxies*. ARA&A, 1991. vol. 29, pp. 581–625.

YOUNG, J. S., XIE, S., TACCONI, L. et al. *The FCRAO Extragalactic CO Survey. I. The Data*. ApJS, 1995. vol. 98, p. 219.

ZHANG, B., SUN, M., JI, L. et al. *The Narrow X-Ray Tail and Double Hα Tails of ESO 137-002 in A3627*. ApJ, 2013. vol. 777, 122.

ZHANG, Q. *Fragmentation of Molecular Clumps and Formation of Massive Cores*. *Dense Cores: Origin, Evolution, and Collapse*. p. 30201.

ZHANG, Q., WANG, K., LU, X. et al. *Fragmentation of Molecular Clumps and Formation of a Protocluster*. ApJ, 2015. vol. 804, 141.